Certificate of Originality

I hereby declare that this submission is my own work and to the best of my knowledge it contains no material previously published or written by another person, nor material which to a substantial extent has been accepted for the award of any other degree or diploma at UNSW or any other educational institution, except where due acknowledgement is made in the thesis. Any contribution made to the research by others, with whom I have worked at UNSW or elsewhere, is explicitly acknowledged in the thesis.

I also declare that the intellectual content of this thesis is the product of my own work, except to the extent that assistance from others in the project's design and conception or in style, presentation and linguistic expression is acknowledged.

Mauro Cirano

Dedication

To my kind grandpa Giuseppe, my endless source of inspiration, a life example of such a combination of a pure heart and a wisdom mind. To my dear parents, Franco and Cleide and to my sister Monica, for their immeasurable love and for always providing me the support that I needed for pursuing my goals. Specifically related to my professional life, they were the first ones to believe in what was merely a kid's dream by that time, when I left home to obtain my first university degree. Last but not least, I owe this work to my wife Lilian and have no words to describe her infinite patience, friendship and love.

Acknowledgements

I am indebted to my supervisor, Dr. John Middleton for his support, guidance and enthusiasm during the course of this project. I deeply appreciate his patience to read, comment and correct whatever was necessary in my uncountable manuscripts, most of them written with a Portuguese language structure. It was thanks to his organised approach to supervision that the conclusion of this work has become far more enjoyable. I would also like to thank Dr. Guennadi Platov, a researcher associated to this project, who helped me a lot in the code development as well as all the other related programs.

I would like to thank the Brazilian funding agency, CNPq (PhD Scholarship number 200108/96-4) for my financial support during these years and the Australian Research Council (grant A39700800) for supporting this research.

Also I wish to thank Dr. Vince Lyne and Dr. George Cresswell, from CSIRO, Hobart, for providing access to the current meter and ADCP data sets. Thanks also to Dr. Robin Tokmakian and Dr. David Webb for making the POCM_4C and OCCAM global ocean model archive data sets available, to Dr. John Middleton and the Australian National University for the time allocation on the **VPP 300 Fujitsu** supercomputer and to the Australian Geological Survey Organisation for providing the high resolution bathymetry data.

I am extremely grateful to Mauricio Mata, for his comments, the helping hand with the data analysis and more importantly, his friendship. Thanks also to my colleagues of the Ocean Lab. group (Renato Ghisolfi, Jose Lima, Rique Alves, Peter Oke and Chris Aiken), my office mates (Simon Evans, Greg Buckley and Pritha Das) as well as all the staff at the School of Mathematics. Also, I wish to specially thank Anthony Macks and Ann-Marie Wong for reading and correcting some of my manuscripts, Dr. Matthew England for the discussion of the results and Dr. Peter Blennerhassett for his excellent job of postgraduate coordination.

Finally, I would like to express my appreciation to each and everyone, those who are not explicitly mentioned here and perhaps do not belong to the scientific community, but have happened to cross my life during these years and to some extent have taught me a special lesson during this period. They definitely have contributed in my search for happiness and have made these years both pleasurable and memorable.

Publication Details

Supporting publications:

Middleton, J. F. and M. Cirano, 1999: Wind-Forced Downwelling Slope Currents: a Numerical Study. *J. Phys. Oceanogr.*, **29(8)**, 1723-1743 (see Appendix A).

Middleton, J. F. and M. Cirano, 2000: A Boundary Current along Australia's Southern Shelves: the Flinders Current. (submitted to *J. of Geophys. Res.*) (see Section 2.3)

The following papers are based upon work presented in this thesis:

Cirano, M. and J. F. Middleton, 2000: Wintertime shelf-slope circulation at the eastern side of the Southeast Indian Ocean. *(in preparation)*

Cirano, M. and J. F. Middleton, 2000: Seasonal ocean circulation South of Australia: a first order description based on the results from OCCAM. *(in preparation)*

The following abstracts are based upon work presented in this dissertation:

Cirano, M. and J. F. Middleton, 1997: *An investigation of the shelf-slope circulation at the eastern end of the Great Australian Bight: preliminary modelling efforts*. Workshop on the oceanography of the South East Indian Ocean and Great Australian Bight (GAB), Adelaide, Australia.

Cirano, M., 1998: *An investigation of the shelf-slope circulation at the eastern end of the Great Australian Bight: preliminary modelling efforts*. AGU Ocean Science Meeting, San Diego, EUA.

Middleton, J. F., M. Cirano and G. Platov, 1998: *The Wind-Forced Circulation in the Great Australian Bight: Preliminary Modelling studies*. Princeton Ocean Model Users Meeting, Miami, EUA.

Cirano, M., J. F. Middleton and G. Platov, 1998: *Winter Time Shelf-Slope Circulation Within the Bight: Preliminary Results from a Numerical Model* . The South East Indian Ocean and Great Australian Bight USA/Australia Bilateral Workshop, Port Lincoln, Australia.

Cirano, M., J. F. Middleton, 2000: *The wintertime shelf-slope circulation along the eastern side of the Southeast Indian Ocean*. First Latin American School in Ocean and Climate Modelling, Concepcion, Chile.

Contents

List of Figures

List of Tables

List of Abbreviations

AAIW: Antarctic Intermediate Water

ACC: Antarctic Circumpolar Current

ADCP: Acoustic Doppler Current Profiler

AVHRR: Advanced Very High Resolution Radiometer

BBL: Bottom Boundary layer

CARS: Climatology of the Australasian Regional Seas

CC: Coastal Current

CTW: Coastal Trapped Wave

EAC: East Australian Current

ECMWF: European Centre for Medium-Range Weather Forecasts

ENSO: El Ninõ Southern Oscillation

FC: Flinders Current

FRAM: Fine Resolution Antarctic Model

GAB: Great Australian Bight

ITF: Indonesian Throughflow

LC: Leeuwin Current

LUC: Leeuwin Undercurrent

OCCAM: Ocean Circulation and Climate Advanced Model

POM: Princeton Ocean Model

SEIO: Southeast Indian Ocean

SML: Surface Mixed Layer

SST: Sea Surface Temperature

STF: Subtropical Front

UCDW: Upper Circumpolar Deep Water

UC: Undercurrent

ZC: Zeehan Current

Abstract

A numerical study is made of the wintertime circulation within the Southeast Indian Ocean (SEIO), encompassed between Cape Leeuwin in the west, the southern tip of Tasmania in the east and the Southern Ocean in the south. The downwelling favourable winds result in a continuous eastward Coastal Current (CC) extending from Cape Leeuwin to the eastern coast of Tasmania, where it forms a confluence with the south branch of the East Australian Current. An additional forcing mechanism for the CC is the Leeuwin Current in the western part of the domain. The study here is divided in two parts: (1) available data and the wintertime averaged results from the Ocean Circulation and Climate Advanced Model (OCCAM) are analysed to provide a first order description of the large-scale circulation; (2) a high resolution model (Princeton Ocean Model) is nested within OCCAM to examine the shelf-slope circulation within the eastern SEIO. The nested model is forced with climatological monthly average winds and several experiments were run to simulate the effects of surface fluxes of density, enhanced bottom friction and stronger winds. In summary, the shelf-slope circulation is governed by a surface south-eastward CC that carries around 2 Sv and reaches velocities of up to 50 cm s^{-1}, where the shelf is narrowest. The core of the current is generally constrained to the shelf-break region. Zonal winds and geostrophic control of the CC lead to a transport of 1 Sv through Bass Strait and a north-eastward jet that is directed into the strait between King Is. and Tasmania. Further south, the CC is poleward and known as the Zeehan Current (ZC). Between Cape Leeuwin and Tasmania and over the slope region, a westward current (the Flinders Current) is found at depths of 500-1000 m and has an associated transport of 5-7 Sv. The current is shown to result from a northward Sverdrup transport in the deep ocean. Meso-scale eddies are shown to result from baroclinic instability and have wavelengths of around 250 km and transports of 3-4 Sv, and can dominate the slope circulation. A comparison of the numerical results is also made with two current meter data sets and results show an interannual variability in the ZC strength, that is probably related to El Ninõ Southern Oscillation events.

Chapter 1

Introduction

"Each of us has a finite supply of energy. We draw upon it when we think hard, supervise a technical group, or go to sea. Often it takes the last ounce of effort to break through to something new. So watch your Plimsoll mark, and don't become too heavily laden with other things to do. You need to be able to turn quickly, change plans, backtrack, and when the moment comes, to drop everything else to pursue that flighty elusive new idea."

H. Stommel

In their review of the oceanography of the Australian shelves, Church and Craig (1998) noted that not even a first order description exists of the ocean circulation of the Great Australian Bight (GAB) (124-136°E). The scenario is not different if the analysis is extended to the Southeast Indian Ocean (SEIO) shown in Fig. 1.1. One of the major difficulties in the study of this region is its enormous dimension, with the longest east-west oriented shelf (apart from Antarctica) and a length of more than 2000 km. In addition, the region is remote, with few cities along the shoreline and limited access to the coast, which is generally characterised by vertical cliffs. Probably, these are some of the reasons why the area is so pristine and unstudied compared to other major continental shelves of the world.

The importance of the southern Australian shelf waters arises from the fact that it comprises around 25% of Australia's coastal environment and Exclusive Economic Zone. A better knowledge of the current system within the region will provide the basis for a better management strategies, particularly in understanding the ecology of locally important fisheries. A very good example of how fish make use of the prevailing currents comes from the population biology of the Southern bluefin tuna. *Thunnus maccoyii*, is fished in the southern oceans, from the southeast Atlantic across the southern Indian Ocean to east Tasmania and New Zealand. The species is known to be highly migratory

and is a commercially valuable fish used for the sashimi market. The spawning ground is south Java and off the northwest coast of Australia. Juveniles migrate south down the coast of Western Australia in the Leeuwin Current, gradually leaving the coastal and continental shelf areas of Western Australia and the GAB as 2 to 4 years-old, and swimming either westwards towards South Africa or eastwards towards Tasmania and New Zealand. Feeding adults, which are pelagic in waters between 30°S and 50°S, return when mature (from $\sim$ 8 years of age) to waters south of Java for spawning (Grewe et al., 1997).

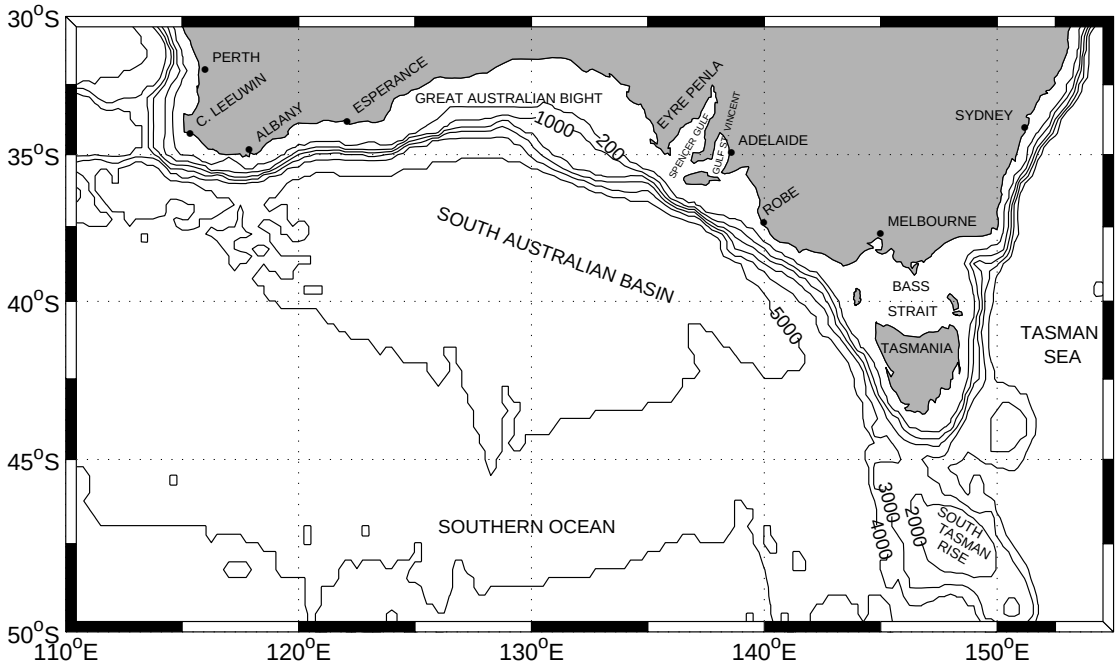

Figure 1.1: *Bathymetry for the SEIO and adjacent regions. Isobaths represent the 200, 1000, 2000, 3000, 4000 and 5000 m contours. The islands from left to right are the Kangaroo Is., the King Is. and the Fourneaux group.*

A better knowledge of advective processes, such as oceanic gyres, coastal currents, eddies, wind-driven currents and fronts will have a key impact in the success of coupled physical-biological models which could be used for larvae dispersion, for example. In order to focus all the efforts towards a better understanding of the SEIO system, a *bilateral USA-Australia workshop* was realized in 1998 and strategies to fulfill this lack of knowledge were discussed among the participants.

The motivation of this work is to study the dynamics of wind-forced downwelling favourable shelf-slope currents at the eastern side of the SEIO and its interaction with the large-scale circulation. To pursue this aim and considering that the wind system is highly seasonal for this area, the analysis will be concentrated on the wintertime season, when the alongshore winds throughout the region have an important downwelling component. The numerical results obtained will not only help to fulfill the lack of information regarding the climatological average circulation for the shelf-slope region, but will also provide an estimate of its interannual variability: results will be compared with two sets of current meter data from different years and from the western coast of Tasmania. As a secondary aim, the large-scale SEIO circulation will also be evaluated and a first order description provided.

The SEIO, as described in Hayes and Conolly (1972), encompasses Cape Leeuwin in west, the continental margin of southern Australia in the north and the Tasman rise in the east (Fig. 1.1). The continental shelves off Western Australia, the Robe region and western Tasmania are generally narrow (20-60 km) with steep continental slopes (5-8°). East of Esperance and within the GAB, the width of the continental shelf increases to values of 200 km. The continental slope here is only moderately steep with angles between 1° and 3°. Along the whole region, the continental slope connects to the South Australian Basin with an abyssal plain, maximum depth of 5500 m. South of the Eyre Peninsula, the continental slope is characterised by numerous transverse deep canyons (length of 50 km, width of 5 km) according to von der Borch (1968).

Of particular interest in terms of the coastline is the series of embayments that occur east of Eyre Peninsula. Spencer Gulf and the Gulf of St Vincent in South Australia and Bass Strait in the Victoria-Tasmanian region are the most prominent features. Bass Strait, with a maximum depth of 90 m, connects the waters of the SEIO to the Tasman Sea and has been studied by many authors (*e.g.* Baines et al., 1991; Middleton and Black, 1994; Evans and Middleton, 1998).

In terms of the circulation, a number of limited observational studies have pointed to the existence of a wintertime eastward current, that is trapped to the continental slope, and which flows uninterruptedly from Cape Leeuwin to the southern tip of of Tasmania. On its way to Tasmania the alongshore current gradually changes its orientation from

eastward (at the center of the SEIO) to poleward (off the western coast of Tasmania). The downwelling favourable alongshore winds in the SEIO may play a major role in the generation of this current, and indeed, during the summer when the winds reverse, evidence suggests that the eastward current reverses and significant regions of upwelling are found within the GAB and off Robe.

In Chapter 2, a review is made of the hydrography, surface fluxes of momentum, heat and freshwater and the limited current meter observations for the region. In addition, the average wintertime results from the Ocean Circulation and Climate Advanced Model (OCCAM) are examined and evaluated against the extant observations. The examination of the OCCAM results lead to three important steps. First, we find that Sverdrup dynamics is the cause of a subsurface alongshore current called the Flinders Current. The current is equatorward along the western coast of Tasmania and changes direction to be westward at the center of the SEIO. Second, the OCCAM results provide a first order description of the circulation for the surface and intermediate layers of the SEIO. Lastly, the OCCAM temperature and salinity fields are shown to be one of the most reliable climatologies to be used as an initial state for any regional modelling study (Appendix B).

Having a first order description of the large-scale circulation, we then move towards a study of the shelf-slope circulation. There are two major problems in modelling the circulation of SEIO. First, the bathymetry is very irregular. Second, the region is influenced by surrounding large-scale currents. To incorporate such currents and topographic variations a high resolution version of the Princeton Ocean Model (POM) was adopted but nested with the OCCAM global model. The development of this model is described in Chapter 3. The adopted final grid is a result of a series of curvilinear grids, where various configurations were tested. Since the grid is oriented along the slope region throughout the domain, it allows high resolution for this particular area without imposing a strong limitation to the CFL time-step. The use of cyclic boundary conditions at Bass Strait do not impose any constraint for the flow or waves, which are able to cross the region in both directions. Although the surrounding large-scale currents are prescribed, the use of a robust mixed boundary condition for the depth-integrated velocities allows correction of the associated transports when the regional model sea level is different from the

prescribed value from OCCAM.

In Chapter 4, the results of the nested regional model are analysed with a focus on the eastern part of the SEIO region. A description of the poleward surface (called Zeehan Current along the west Tasmanian coast) and subsurface current (the Flinders Current) is provided. One striking result of the nested model is the formation of eddies (wavelengths of $\sim$ 250 km) which are explained using baroclinic instability theory (Appendix C). Transport analyses show that these eddies make an important contribution to the generation of onshore and offshore flows (with associated transports of 3-4 Sv). The excursions of the density surfaces related to these eddies may also act as an important mechanism for the nutrient ventilation of the shelf waters, since for most of the year these waters are driven by downwelling rather than upwelling favourable winds.

Chapter 5 deals with the effect of surface heat and salt fluxes and the influence of tides and Coastal Trapped Waves through enhanced bottom friction (Appendix D). In Chapter 6, current meter data collected during 1988 and 1997-1998, and off west Tasmanian shelf-slope are compared with numerical model results. A comparison between the data sets also shows a strong interannual signature and possible causes for this signal, including El Ninõ Southern Oscillation (ENSO) events and local winds, are investigated.

Chapter 7 contains a summary of the results obtained and recommendations for future studies.

Chapter 2

Observations and OCCAM Results: a General Description of the Circulation and Hydrography

The main objective of this chapter is to review the hydrography, surface fluxes of momentum, heat and freshwater and the limited current meter observations at the SEIO region. In addition to this objective, the average wintertime results from OCCAM are also examined and evaluated against the extant observations and a first order description of the large-scale circulation is provided.

A description of the model is made first in section 2.1. The model results are discussed in section 2.2 along with the observations for the region. In summary, the downwelling favourable winds result in an eastward current near the coast that extends from Cape Leeuwin to the southern tip of Tasmania: off the west Tasmanian coast it is known as the Zeehan Current (ZC) and it has a poleward direction. The surface winds and cooling also result in a Surface Mixed Layer (SML) that deepens in the eastern part of the domain to depths of 400 m or more. Isopycnals are also downwelled towards the coast to a similar depth.

Below the eastward current and downwelled isopycnals, a westward current is found (the Flinders Current (FC)) that flows from the western coast of Tasmania to Cape Leeuwin. At the west coast of Tasmania the FC has an equatorward direction. The origin of this current is shown in section 2.3 to be the northward Sverdrup transport that results from the positive wind stress curl. The direction of the current and associated upwelled isopycnals are explained using arguments based on potential vorticity and mass conservation (the results from this section are taken from Middleton and Cirano (2000)).

Hydrographic observations, satellite images, and to an extent the averaged OCCAM results, also indicate the existence of filaments and eddies over the shelf-slope and for the entire region.

2.1 The OCCAM Global Model

OCCAM is a primitive equation numerical model based on the *z-level* Bryan-Cox-Semtner (Bryan, 1969; Semtner, 1974; Cox, 1984) general circulation model. The model uses a regularly spaced $1/4^\circ$ latitude-longitude Arakawa B grid and has 36 layers in the vertical with the first 8 layers in top 200 m. The choice to adopt OCCAM as the global model was based on inter-model comparisons (*e.g.* Parallel Ocean Climate Model (POCM) (Stammer et al., 1996), with a average horizontal resolution of $1/4^\circ$ and 20 levels). These results have shown that OCCAM would be more suitable since it has: (1) a more realistic SML; (2) higher resolution in the horizontal, since the equivalent grid spacing for POCM_4C at 40°S is 0.4° for the meridional direction and $\sim$ 0.3° for the zonal direction; (3) finer resolution in the vertical; (4) better estimate of transports for the surrounding currents and (5) more realistic water mass properties.

The model uses constant Laplacian diffusion and momentum terms to represent horizontal mixing. The horizontal diffusivity coefficient is 100 $m^2\ s^{-1}$ while the horizontal kinematic viscosity coefficient is 200 $m^2\ s^{-1}$. In the vertical, it uses Pacanowski and Philander (1981) for mixing tracers and a constant Laplacian mixing for velocities, where $K_M = 2 \times 10^{-4}\ m^2\ s^{-1}$ (see Webb et al. (1998) for further details).

The model was initialised with Levitus annual mean temperature and salinity fields (Levitus, 1982; Levitus et al., 1994; Levitus and Boyer, 1994), where it was run diagnostically for 4 years (initial spin-up phase). During this phase, a strong relaxation towards annual mean temperature and salinity fields from Levitus was imposed (scales of 30 days in the first layer and 360 days at other levels). Following this initial phase, the model was run prognostically for another 10 years and forced with monthly average wind stress climatology from the European Centre for Medium-Range Weather Forecasts (ECMWF) for the years of 1986 to 1988 inclusive (Siefridt and Barnier, 1993). The data was linearly interpolated in time, but the correct average stress was preserved using a methodology suggested by Killworth (1996). Heat and fresh water fluxes were calculated in order to relax the surface layer of the model towards the Levitus temperature and salinity monthly average values (the relaxation coefficient was 30 days).

The plot of the mean kinetic energy of the model presented in Webb et al. (1998) shows that the model starts to reach a seasonally varying equilibrium after the year 6 and from this stage until the end of the simulation (year 14), the total energy oscillates around a constant value. For this reason, the period between years 8 to 12 of the model run is the recommended period for analysis and outputs were archived every 15 days. However, since the main interest here is the mean climatological circulation, all variables were seasonally averaged over the 4 year period resulting in model data sets for the summer, autumn, winter and spring (austral seasons). These averaged data sets were provided by the Southampton Oceanography Centre (SOC).

A general feature of the OCCAM results is that for SEIO region, the temperatures in the top 200 m or so are generally 1-2°C warmer than indicated by the Climatology of the Australasian Regional Seas - CARS (Dunn et al., 2000) and Levitus data. However, a detailed comparison of the OCCAM and CARS temperature, salinity and density fields is made in Appendix B, and in general, the OCCAM fields are found to be of superior quality for the purposes of model initialisation.

There are few reasons that should be taken into account in order to properly justify why OCCAM appears to have a better representation of the seasonal climatology when compared with CARS. First of all, it is always important to remember that the Southern Ocean and the SEIO region are known in the oceanographic community for their lack of oceanographic data (*e.g.* Ridgway and Godfrey, 1997; Church and Craig, 1998). When the few data available is combined to built a climatological data set and considering that the local oceanographic properties are highly dependent on various time scales (such as the seasonal cycle and the latitudinal migration of the Subtropical Front (STF)), the immediate result is a number of inconsistencies in the thermohaline field. For example, CARS (see Appendix B) presents regions where there are "pools" of light water which do not exist in reality and are only a result of the non-linearity of the density equation due to the lack of data during the interpolation of the thermohaline field. Another advantage of having the climatology derived from a numerical model is that the momentum balance will always match the mass balance.

2.2 Circulation and Hydrography of the SEIO

During autumn and winter, the mean wind stress for the region is predominantly to the southeast (Fig. 2.1), resulting in a raising of coastal sea level and an eastward coastal current: the OCCAM wintertime solutions (Fig. 2.2a) indicate that such a current flows from Cape Leeuwin in the west to the east coast of Tasmania. To aid the discussion, the observations and OCCAM results for the western region of the domain will be considered first.

Western Region: Albany to Robe

The main current influencing the western side of the domain is the Leeuwin Current (LC), an anomalous eastern boundary current that flows along the Western Australian coast from at least 22°S down to Cape Leeuwin, when it turns eastward into the GAB. At the northern part it is broad and shallow (200 km by 50 m) and as it moves south it becomes deeper and narrower (less than 100 km wide), and basically confined to the shelf-break (Church et al., 1989).

The LC is characterised by high temperatures and relatively low salinity waters and has been studied by many authors (*e.g.* Batteen and Butler, 1998). Using current meter data at 29.5°S, Smith et al. (1991) estimated annual poleward mean currents of 10 cm s^{-1} at the shelf-edge and 30 cm s^{-1} for the upper slope. An equatorward Leeuwin Undercurrent (LUC) flowing between 250 and 450 m with an annual mean of 10 cm s^{-1} at a depth of 450 m was also observed. At the same location, but using CTD data, the authors estimated the geostrophic transport between 0-300 m to range from less than 2 Sv in summer to more than 5 Sv during autumn and winter.

The LC is primarily driven by an alongshore pressure gradient (Thompson, 1984; Godfrey and Ridgway, 1985), which is sufficient to oppose the prevailing northward winds, resulting in a poleward flow. Upon entering the bight, offshoots of the current, meanders and eddies are known to occur between 124°E, 129°E and even as far as the mid-bight at 134°E (Legeckis and Cresswell, 1981; Cresswell and Peterson, 1993). Such eddy activity is also evident in the time-averaged OCCAM solutions (Fig. 2.2).

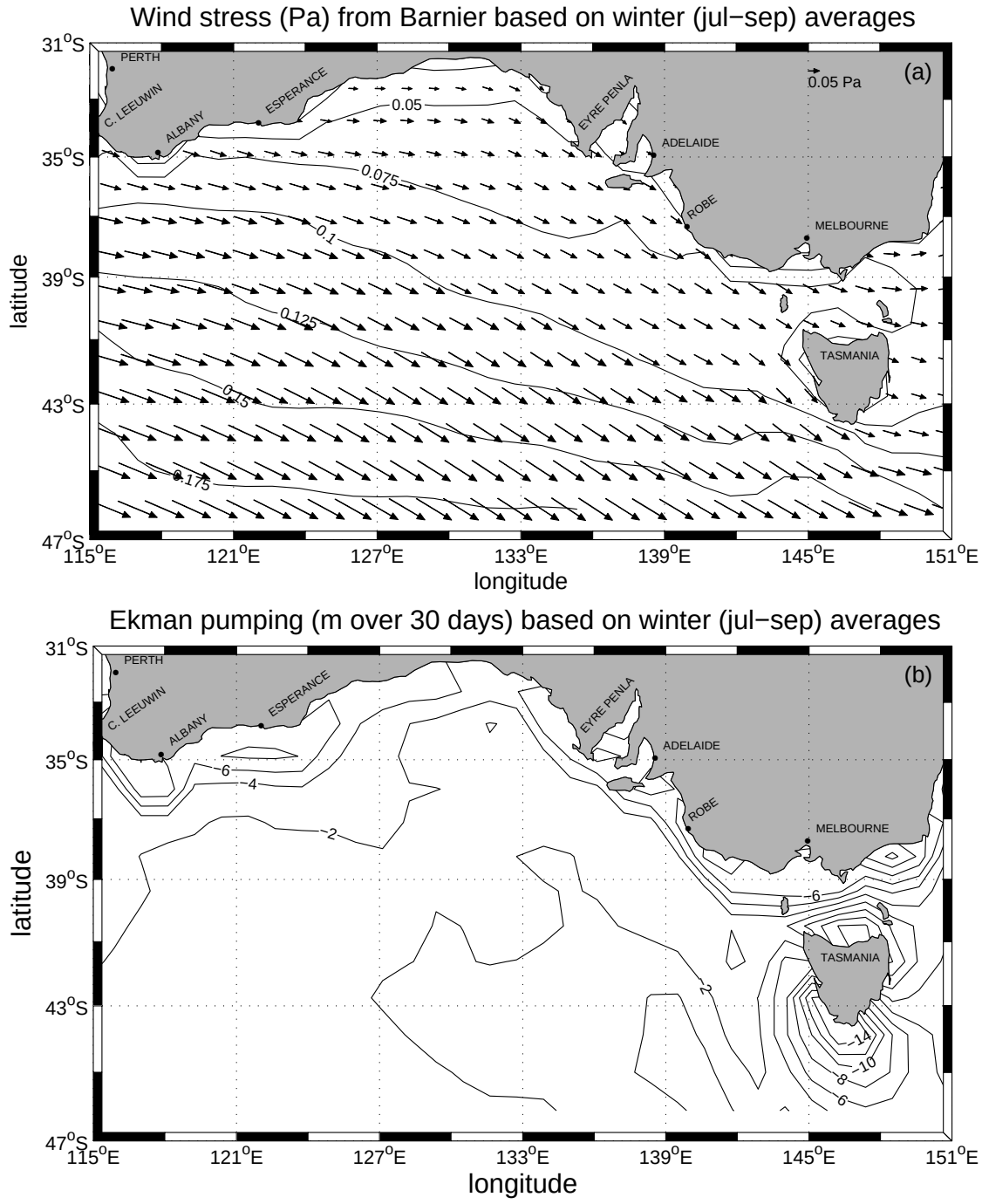

Figure 2.1: *(a) Seasonal averaged wind stress field for winter based on ECMWF from Siefridt and Barnier (1993) climatology. Contour lines represent the magnitude of the wind stress in intervals of 0.025 Pa. (b) Curl of the wind, here represented as the displacement due to Ekman pumping velocity over a period of 30 days. The contour interval is 2 m.*

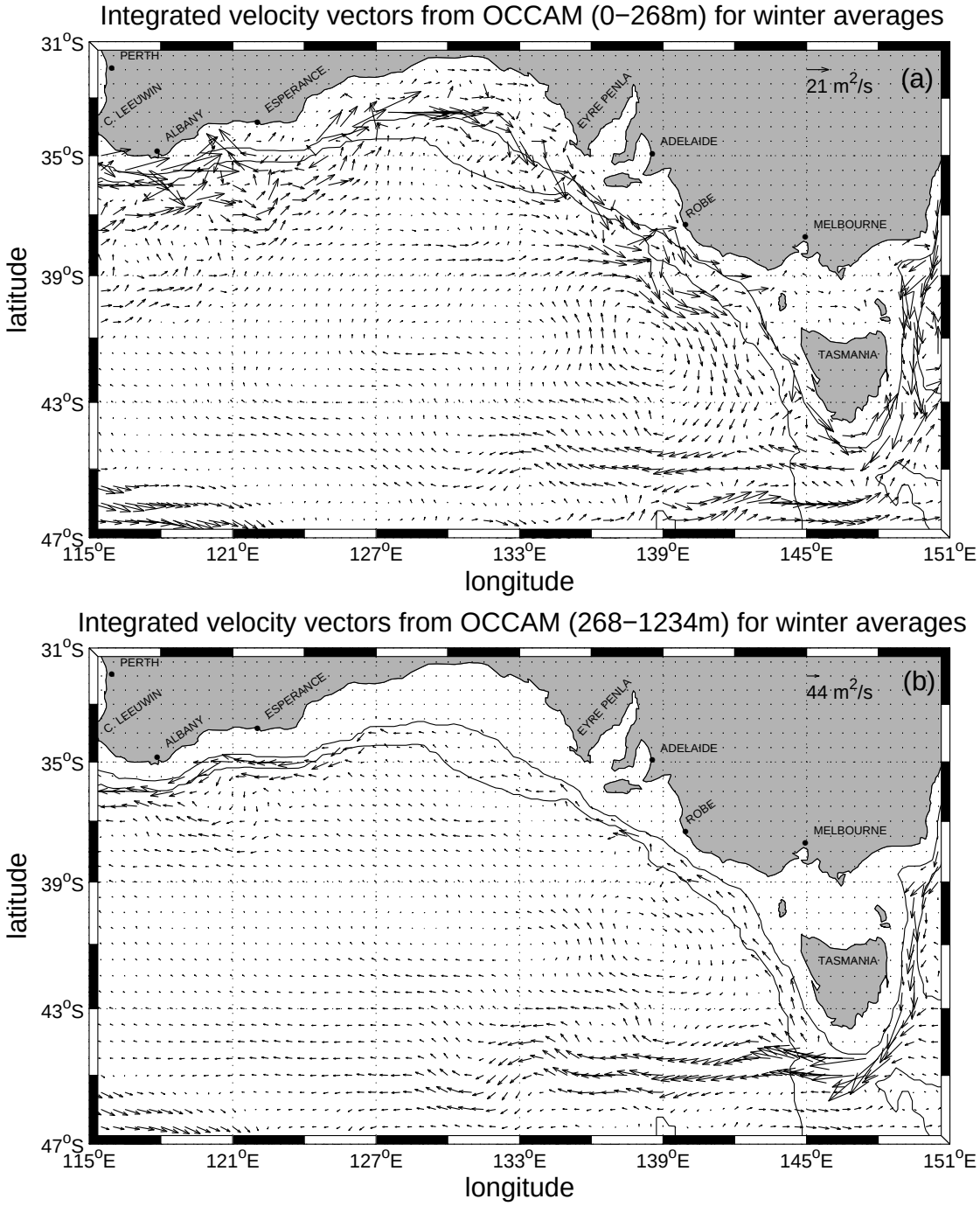

Figure 2.2: *(a) Integrated velocity vectors (m^2 s^{-1}) for the depth of 0-268 m and (b) for the depth of 268-1234 m. Solid lines are the 1000 and 4000 m isobaths.*

One topic of interest is the easternmost extent of the LC. Legeckis and Cresswell (1981) used satellite images to show that in July, there is evidence of a zonally oriented Sea Surface Temperature (SST) front between longitudes 122-136°E, and which was interpreted as the eastern extension of the LC. The extension lies predominantly on the shelf and the warmest water is 15.5°C. At Albany, the salinity for July had its lowest value of the year (35.5), which is again an indicative of the strongest peak in the LC flow.

Based on mean monthly values of SST and salinity, Rochford (1986) suggests that the LC enters the western shelf region in May and reaches its extreme eastern limit around 130°E by July. Using a Temperature and Salinity (TS) diagram analysis from a June cruise, the author also shows that there are 3 principal water masses within the region. (1) the warmest waters from the LC; (2) a very high salinity central bight water mass (which generally dominates the eastern shelf region of the GAB) and (3) the colder and lower salinity waters associated with the west wind drift water mass that is found across the entire southern portion of the region.

With the use of these water masses properties, Rochford (1986) showed that there is a clear distinction between the waters west and east of the head of GAB (130°E). Between 115°E and 130°E there is a tongue of warm water and almost constant salinity (35.7-35.8) that follows the shelf-break closely. On the other hand, east of 130°E, the warmest water was 1°C warmer than the warm tongue at 130°E, more haline (35.9-36.4) and is found all over the shelf.

A description of the annual cycle of SST in the GAB is given by Herzfeld (1997). The author used images for the period of March 1990 to September 1991. His hypothesis, in agreement with Rochford (1986), is that the warm wintertime strip of water found along the southern Australia's shelves is a combination of two water masses. The LC, flowing along the shelf-break, advects waters to about 130°E in late July/August, where it joins with the warm GAB water, that is broader and covers the shelf, and extends further east than 136°E. The author claims that the origin of this GAB water is a shallow strip of coastal water located at 124-129°E, where heating leads to the formation of a warm saline plume in the late summer and autumn. At these times, there is no signature of the LC in the region. Using an idealised version of the GAB bathymetry, Herzfeld and Tomczak (1997) also modelled the formation of such a plume.

During winter, the waters within the bight are subject to strong cooling ($\sim$ 100 W m^{-2}), as evidenced by the August average of the Southampton Oceanography Centre (SOC) heat flux climatology (Josey et al., 1996) (Fig. 2.3a). The da Silva et al. (1994) estimates of Evaporation-Precipitation (E-P) also shown in Fig. 2.3b indicate that evaporation exceeds precipitation on the western side of the bight, but not on the eastern side. These fluxes may be combined to yield the density change for the top meter of water over 30 days (Fig. 2.3c). This density change is useful, since when divided by the depth of the SML it yields the change in density of that column of water. Thus the density change of 15-20 kg m^{-3} in the first top meter indicated for the bight region would imply an equivalent increase in density of 0.15-0.20 kg m^{-3} over one month and for a 100 m deep SML.

Estimates of surface temperature and salinity obtained from the CARS atlas (Fig. 2.4) and OCCAM (Fig. 2.5) do show an eastward decrease in temperature into the bight. The CARS atlas also indicates the presence of a more haline water in the vicinity of the 130°E longitude, which is not so clear in the OCCAM results. Between the western and eastern end of the bight, the CARS results for density (Fig. 2.4c) indicate increases of $\sim$ 0.5 kg m^{-3}, a result that is not inconsistent with that estimated above from the fluxes.

Neither the CARS (Fig. 2.4) nor OCCAM (Fig. 2.5) results show the existence of the STF, the position of which is shown in Fig. 2.6 (Rintoul et al., 1997). For the region between 120-135°E, Tomczak et al. (2000) has shown that the front is characterised by enhanced gradients of temperature and salinity. The temperature and salinity range that characterises the front for this region, according to Tomczak and Pender (1998), is 12-14°C and 34.9-35 respectively. However, there is very high degree of density compensation and virtually no associated transport.

With the exception of the observations of the LC at the western coast of Australia, direct observations of currents for the shelf region west of the Eyre Peninsula are few. However, Godfrey et al. (1986) used steric height estimates relative to 450 db to infer the existence of a continuous wintertime eastward current over the 500 m isobath and from 115°E to 140°E. The data presented by Church et al. (1986) also shows that coastal sea level is indeed set-up throughout the bight during winter so that an eastward geostrophic current should exist near the coast. The six weeks of current meter data obtained off the Eyre

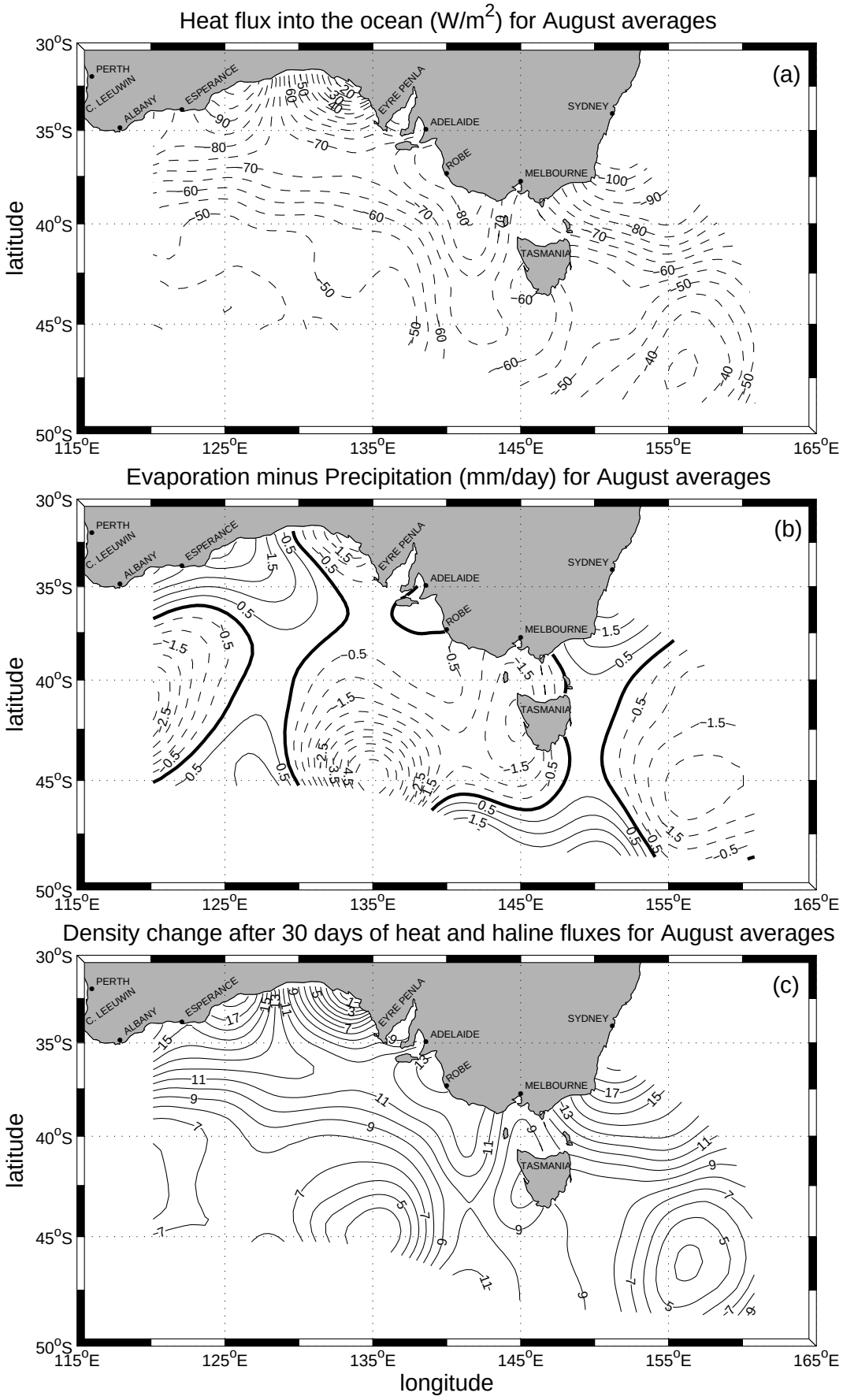

Figure 2.3: *(a) Heat fluxes from Josey et al. (1996). Positive contours represent fluxes into the ocean. (b) E-P fluxes from da Silva (1994). (c) Density change in the top 1 m (kg m^{-3}) after one month of the imposed (a) and (b) fluxes.*

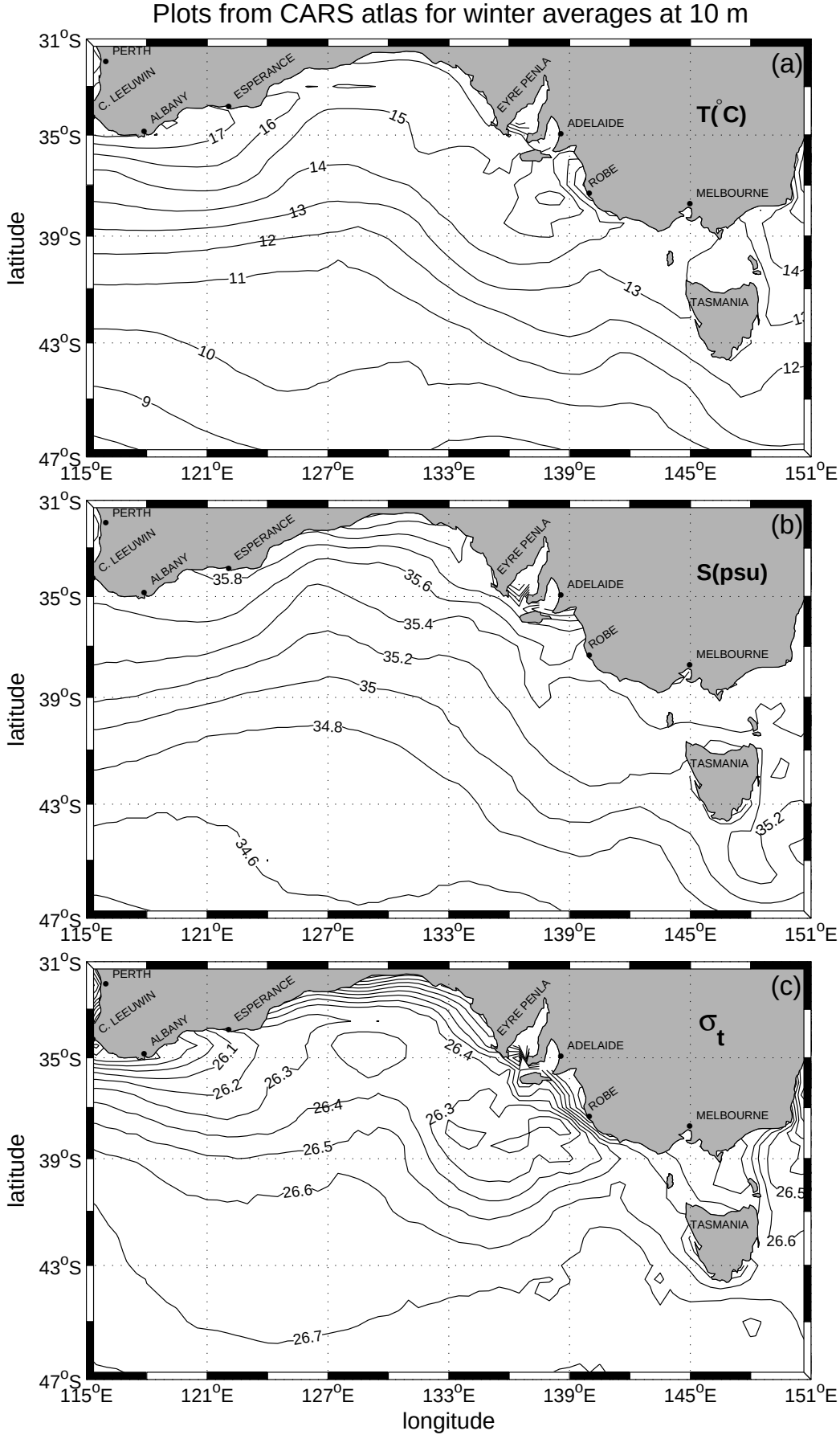

Figure 2.4: *Horizontal plots of (a) temperature, (b) salinity and (c) σ_t at 10 m from the CARS atlas.*

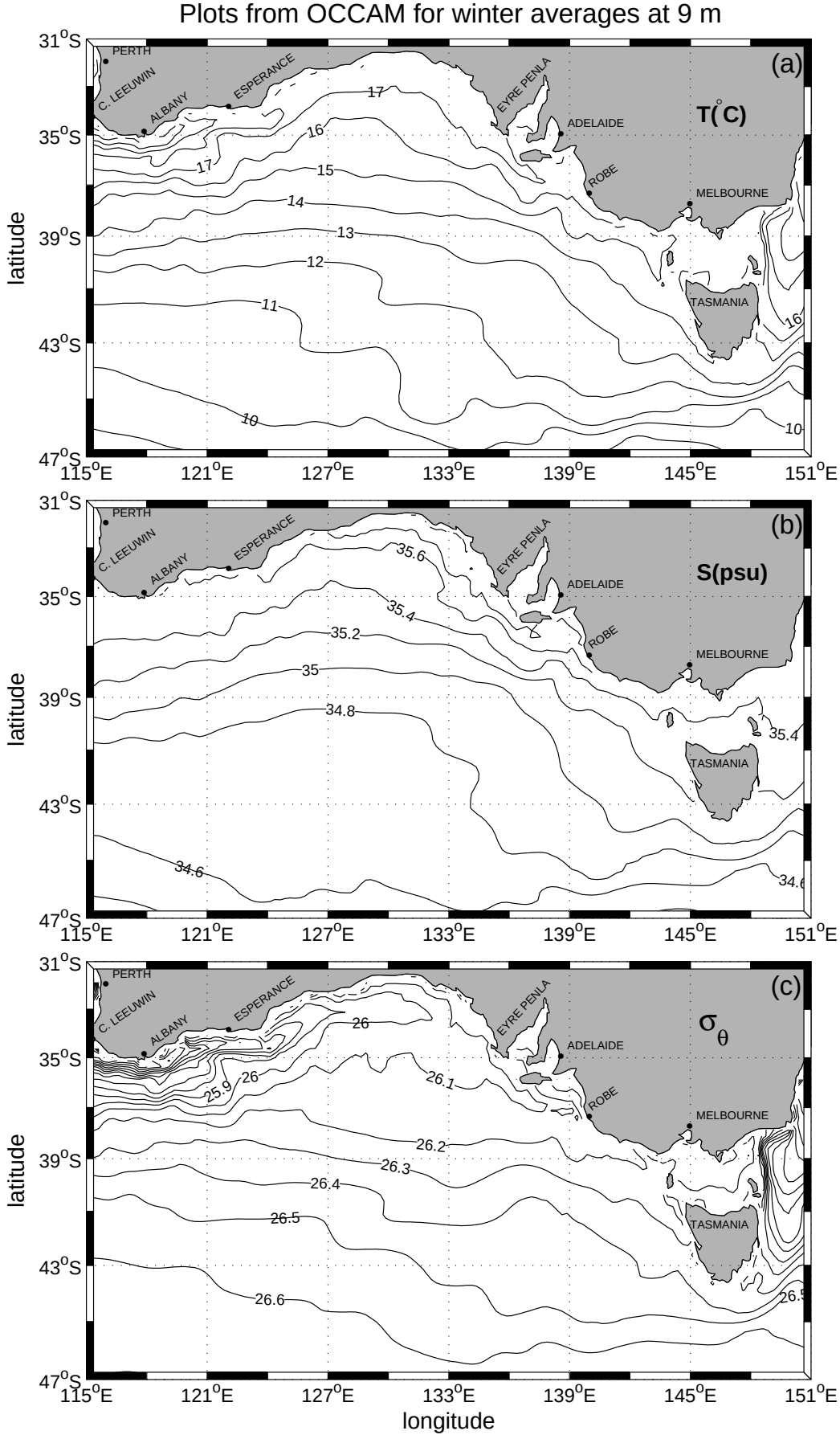

Figure 2.5: *Horizontal plots of (a) temperature, (b) salinity and (c) σ_θ at 9 m from OCCAM.*

Peninsula (Provis and Lennon, 1981) and in a depth of 200 m also indicate mean south-eastward currents of 16-19 cm s^{-1}. Farther to the east, current meter records obtained at the depth of 143 m and off Robe also demonstrate the existence of a south-eastward current with mean of 27 cm s^{-1} (Schahinger, 1987).

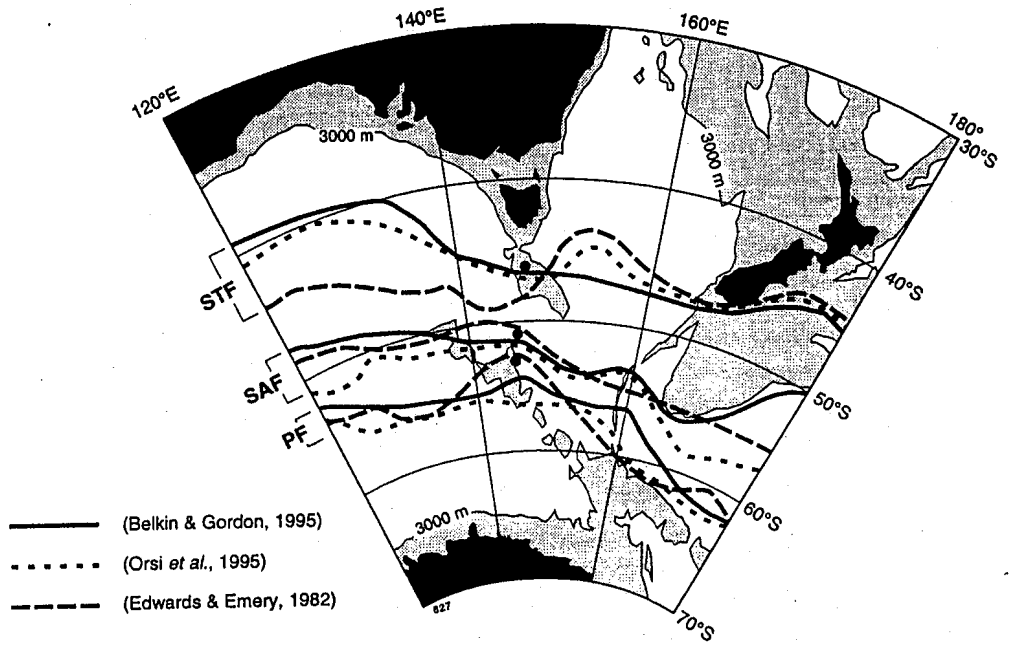

Figure 2.6: *Location of the Subtropical Front (STF), the Subantarctic Front (SAF) and the Polar Front (PF) south of Australia from Belkin and Gordon (1996), Orsi et al. (1995) and Edwards and Emery (1982). Extracted from Rintoul et al. (1997).*

Two meridional sections (122°E and 140°E) from OCCAM are presented in Fig. 2.7 and show that an eastward current may exist near the coast. Both sections also indicate that a westward current may exist below the eastward current and farther offshore and be of maximum amplitude at depths of 600 m. This depth corresponds to the middle of the permanent thermocline which is notably upwelled near the slope. A westward current is also shown in the integrated velocity results in Fig. 2.2b and was postulated by Bye (1983a) to result from the northward deep ocean Sverdrup transport that arises from the positive wind stress curl shown in Fig. 2.1b. Bye (1972) named it the Flinders Current and its structure, cause and associated upwelling will be examined in detail in section 2.3 below.

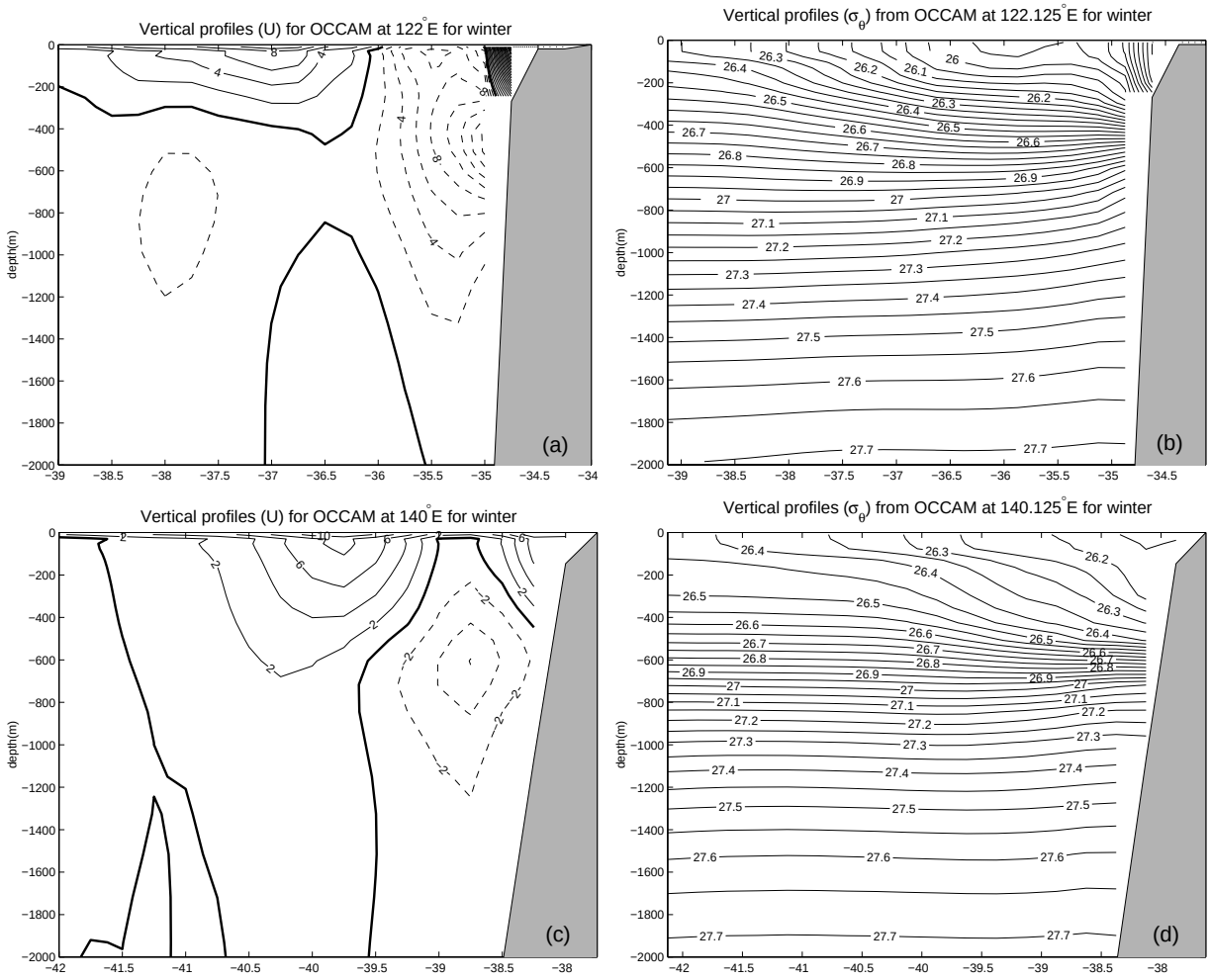

Figure 2.7: *Meridional sections for (a) zonal velocity (units cm s^{-1}) and (b) σ_θ at 122°E from OCCAM. (c) and (d) same as (a) and (b), but at 140°E. The solid (dashed) velocity contours indicate eastward (westward) flow.*

A second general feature illustrated by the meridional sections shown in Fig. 2.7 is the extensive downwelling of isopycnals and deep SML (100-200 m). The depth of the downwelling increases from about 200 m off Esperance (123°E) to almost 600 m off Robe (140°E). Such downwelling is thought to arise from the onshore surface Ekman flux and is found in the hydrographic data of CARS as well as in the cruise sections obtained by Rochford (1986) shown here in Fig. 2.8, where for the mid-bight, isotherms are downwelled to 250 m.

The OCCAM results in Fig. 2.2a would also suggest that the eastward current over the slope is subject to filaments and eddy formation. Evidence for this was obtained by Legeckis and Cresswell (1981), who noted the presence of offshore filaments and jets of

warm water off Esperance (124°E), Eucla (129°E) and the Eyre Peninsula (134°E). Such filament formation would appear to extend to the west coast of Tasmania as indicated by the wintertime SST images composed with the 8 days average from the Advanced Very High Resolution Radiometer (AVHRR) Pathfinder in Fig. 2.9. Surface drifters deployed between 128°E and 138°E also demonstrate the existence of such filaments or eddies with scales of 50-100 km (Godfrey et al., 1986).

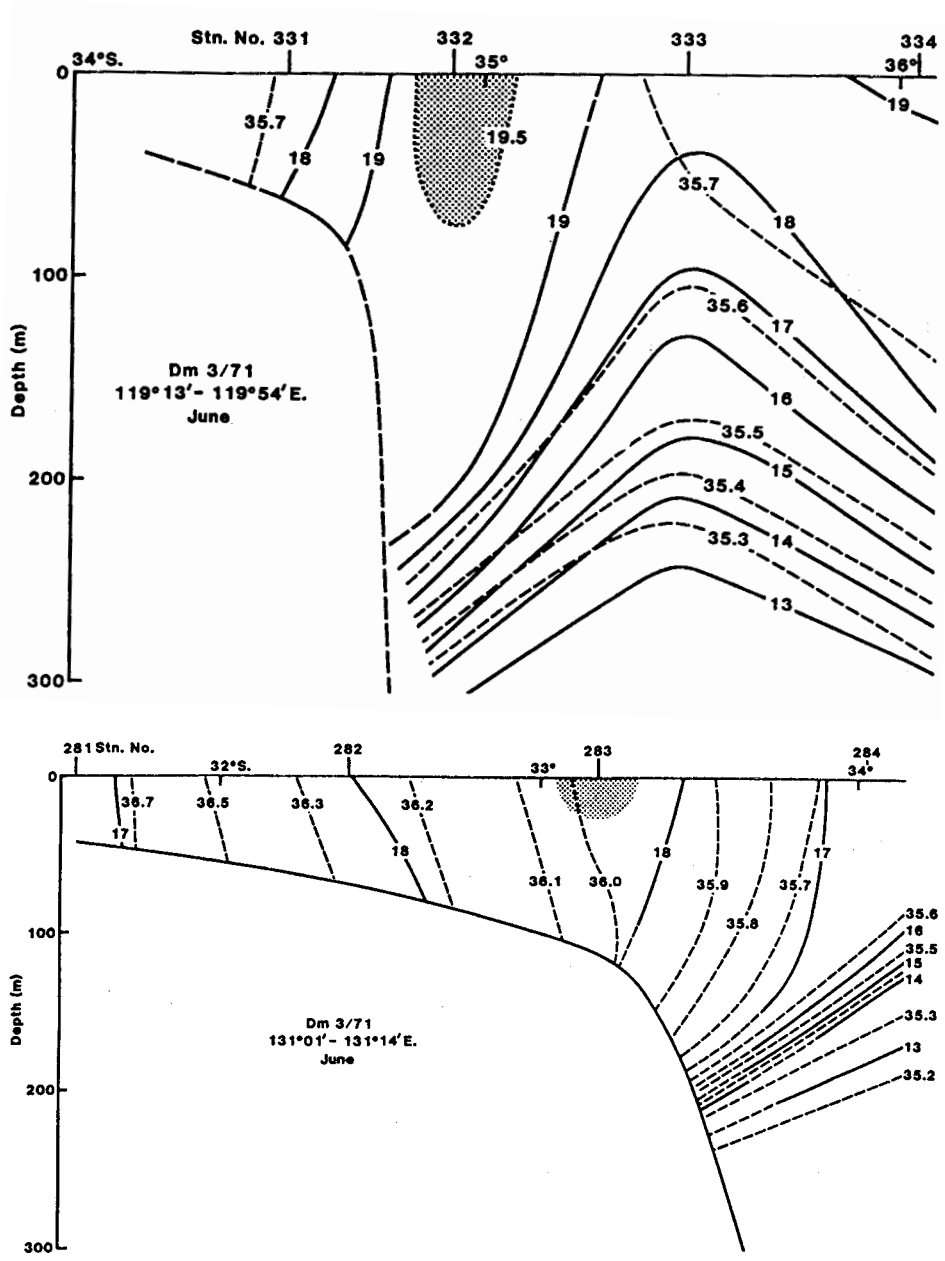

Figure 2.8: *Temperature and salinity sections extracted from Rochford (1986) at (a) 119°E and (b) 131°E.*

also show that there is a net southward movement of shelf water along the western coast of Tasmania.

The OCCAM zonal section taken at 42°S and off the west coast of Tasmania (Fig. 2.10a) does show a poleward current of 10 cm s^{-1} and a northward undercurrent ($\sim$ 4 cm s^{-1}). In agreement with the CTD sections of Lyne and Thresher (1994) and Cresswell (2000), the OCCAM results (Fig. 2.10b) also show the existence of a 200-400 m deep SML near the coast, deep downwelling at depths above 600 m and upwelling at greater depths.

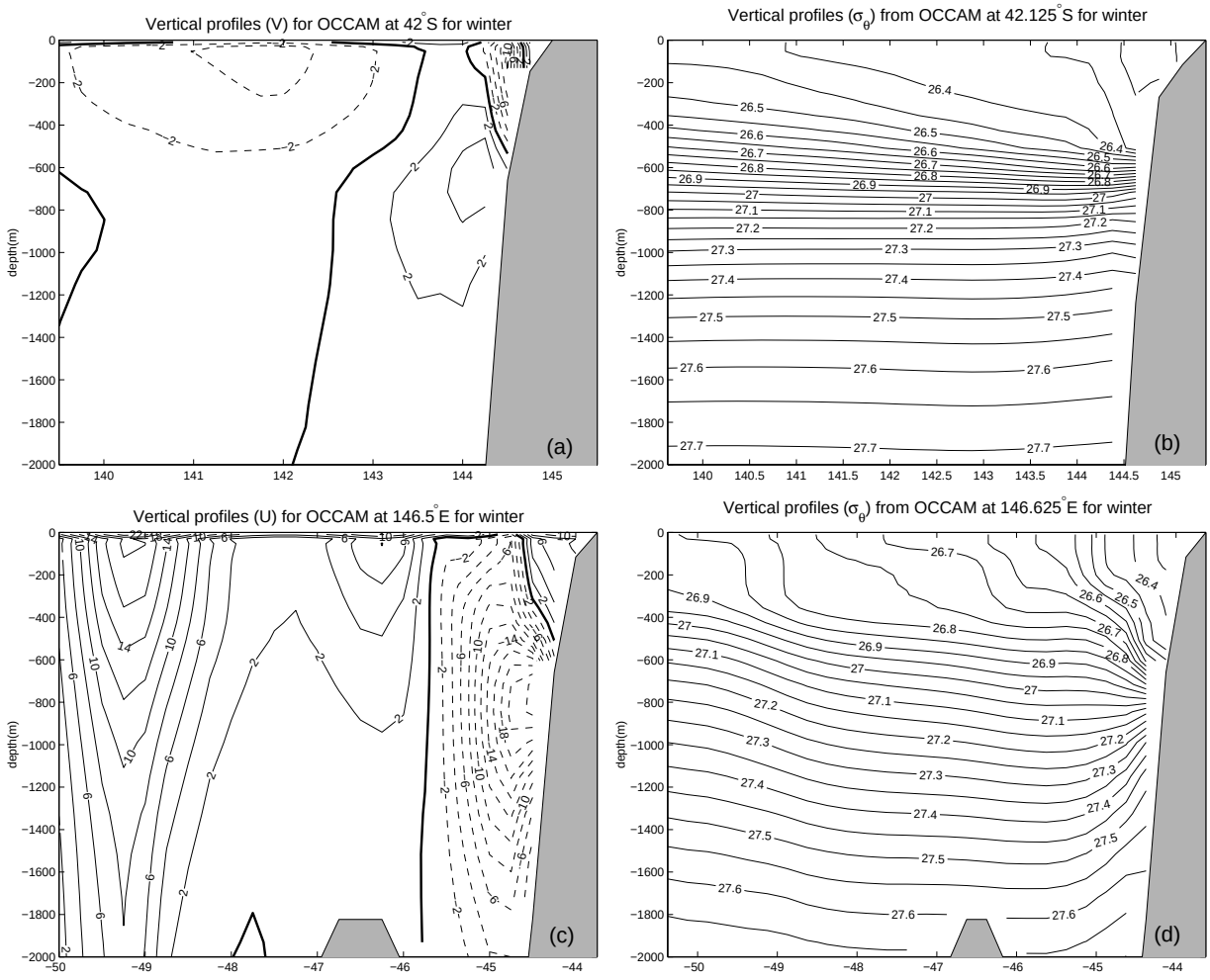

Figure 2.10: *Zonal section for (a) meridional velocity (units cm s^{-1}) and (b) σ_θ at 42°S off western Tasmania. Meridional section for (c) zonal velocity (units cm s^{-1}) and (d) σ_θ at 146.5°E south of Tasmania. Solid (dashed) velocity contours in (a) indicate northward (southward) flow and in (c) eastward (westward) flow.*

The OCCAM integrated velocity vectors presented in Fig. 2.2a show that such a current may flow around Tasmania until the point where it joins the south branch of the remaining

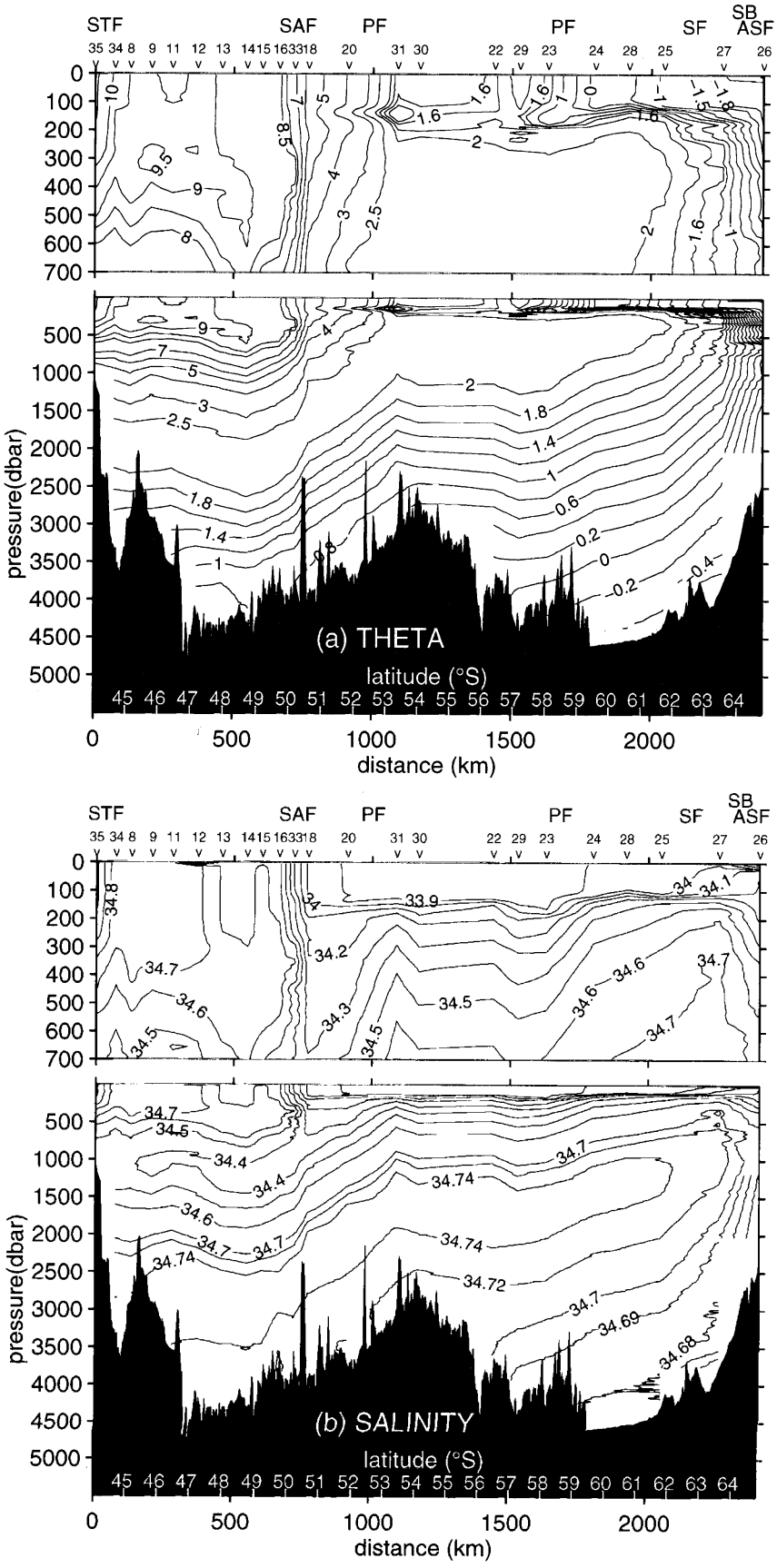

Figure 2.12: *(a) Wintertime temperature and (b) salinity sections south of Tasmania extracted from Rintoul and Bullister (1999) at 146°E.*

to depths of 400 m while upwelling is found at depths below 800 m or so. Note that the region south of Tasmania has the largest wind stress curl for the region (Fig. 2.1b). The downward displacement by Ekman pumping after 30 day of the imposed winds would be of order 10-15 m. A detailed description of the transports through this section are discussed in section 2.4.

2.3 The Flinders Current and Sverdrup Dynamics

To examine the nature and cause of the FC it will be necessary to examine the OCCAM results for both winter and summer since the spin-up of the Sverdrup transport by baroclinic Rossby waves can exceed the seasonal time scale over which the wind fields change. The main difference between the two seasons with this regards is the direction of the coastal winds. Although they have similar magnitude (around 0.05 Pa), during summer, the winds near the coast reverse and become upwelling favourable as shown in Fig. 2.13a. However, during both seasons, the wind stress curl is positive ($\sim 10^{-7}$ Pa m^{-1}) and leads to downwelling favourable Ekman pumping throughout most of the region.

Features evident in the plot of the transport streamfunction during summer (Fig. 2.13b) include the south branch of the EAC (southeast corner) and a general anticyclonic motion in the west that is associated with the anticyclonic forcing apparent in the wind stress. Of interest here is the generally northward transport found throughout the domain, and the westward flow along the 4000 m isobath that begins near Robe in the east.

Transport results obtained from OCCAM for the four sections indicated in Fig. 2.14 are presented in Table 2.1a. For summer, the transport through the zonal section closest to the shelf (36°S) is about 10 Sv. Much of this is deflected to the left through the meridional section at 122°E.

Wintertime results for the streamfunction are presented in Fig. 2.15, and also show the flow to be generally directed towards the north, although a boundary current is less evident and the transports are weaker than in summer. From Table 2.1b, the northward transport at 36°S is about 4 Sv and again deflected into the westward flowing FC.

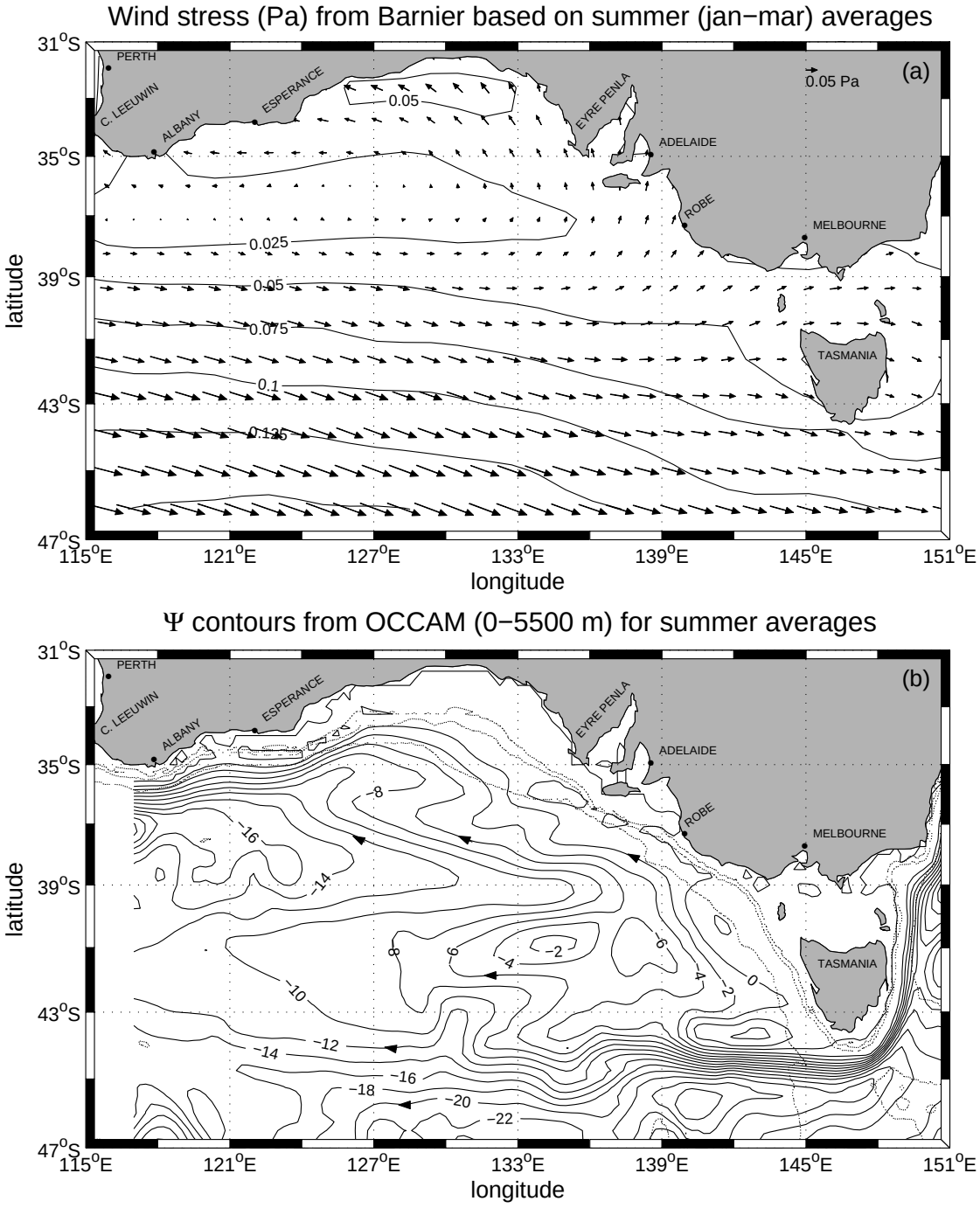

Figure 2.13: *(a) Seasonal averaged wind stress field for summer based on ECMWF from Siefridt and Barnier (1993) climatology. Contour lines represent the magnitude of the wind stress in intervals of 0.025 Pa. (b) The depth-integrated transport streamfunction obtained from the summer averaged OCCAM model results. (units Sv). The direction of the flow is indicated by the arrows. The light dashed lines are the 200, 1000 and 4000 m isobaths.*

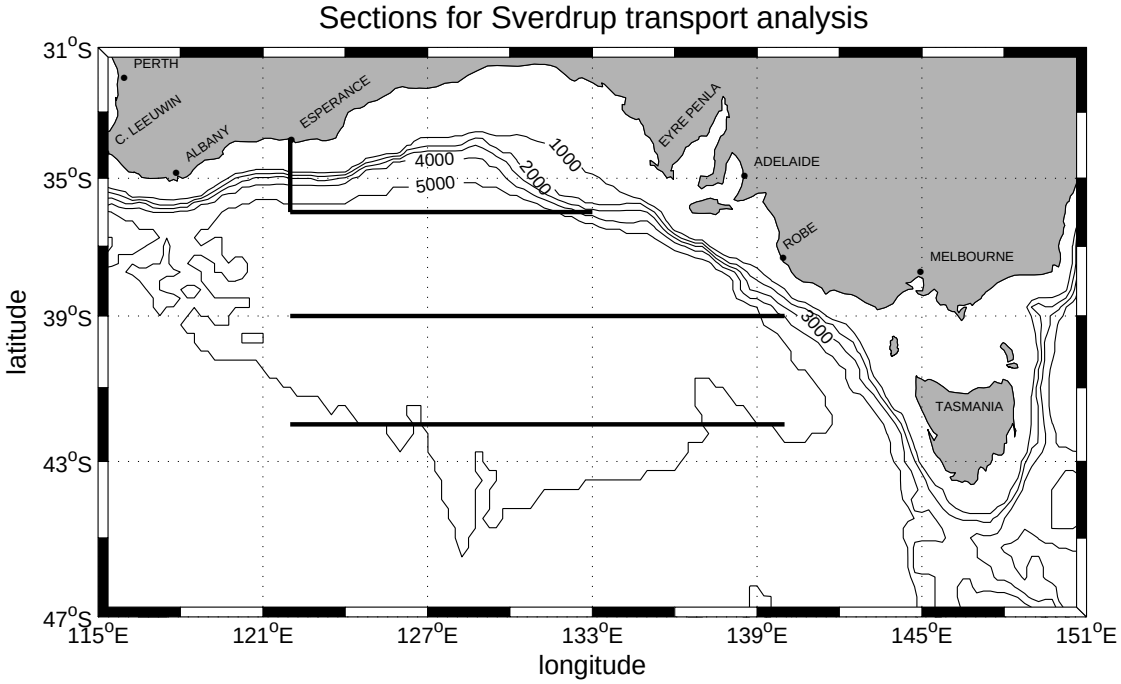

Figure 2.14: *Sections used to determine transports, here indicated by solid thick lines. The bathymetry of the region is represented by the 1000, 2000, 3000, 4000 and 5000 m isobaths.*

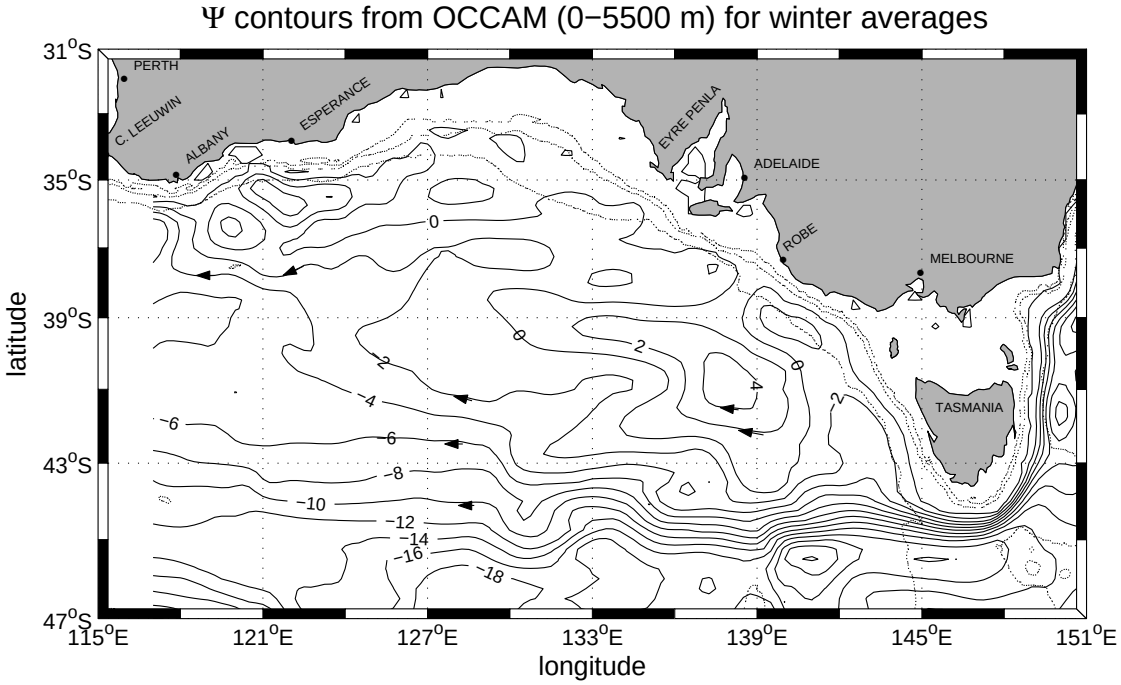

Figure 2.15: *As in Fig. 2.13b but for the wintertime results.*

The cross-shelf structure of the FC and associated density field were presented in Fig. 2.7a-b (a westerly section (122°E) where the boundary current is largest). The maximum westward speed is about 16 cm s^{-1} and occurs at a depth of 400 m. At and below this depth, the isopycnals are upwelled and the associated thermal wind shear acts to reduce the magnitude of the boundary current to near zero at a depth of 1200 m. Above 400 m, the isopycnals are downwelled as a result of the wind forcing and cooling. Results farther to the east at 140°E (Fig. 2.7c-d) are similar, although the magnitude of the FC is reduced to 4 cm s^{-1}.

Section	OCCAM	Sverdrup (flat)	Sverdrup (topog.)	Ekman
42°S	5.0	10.7	8.3	1.2
39°S	13.5	11.9	11.0	0.6
36°S	9.7	8.8	-1.2	-0.1
122°E	-10.6	-	-	-

Section	OCCAM	Sverdrup (flat)	Sverdrup (topog.)	Ekman
42°S	7.1	6.9	5.7	1.6
39°S	2.6	4.3	4.0	1.5
36°S	4.1	3.9	0.5	0.8
122°E	-4.8	-	-	-

Table 2.1: *(a) Summertime net transports (units Sv). For the zonal sections, positive values are to the north, while for the meridional section at 122°E, the negative values are to the west. (b) As in (a), but for the wintertime net transports (units Sv).*

The LC is absent during summer, although the density field and the FC are similar to that found during winter.

The likely explanation for the direction of the FC involves the dissipation of vorticity. Specifically, the surface Ekman pumping leads to a northward (Sverdrup) transport of fluid columns to where $|f|$ is smaller. The acquisition of anticyclonic potential vorticity is then dissipated near the boundary through frictional spin-down of the coastally intensified westward boundary current. (*e.g.* Pedlosky, 1987). [The spin-down of an eastward coastally intensified current would lead to the acquisition of anticyclonic vorticity.]

The Bottom Boundary Layer (BBL) of the FC is upwelling favourable, and presumably leads to the upward tilting of isopycnals that is found both in the OCCAM results and in the data of Levitus et al. (1994). Moreover, Cushman-Roisin (1994) points out that such an upwelling favourable BBL is necessary to take up the water that is elsewhere downwelled into the inviscid ocean interior by Ekman pumping at the surface.

To determine the origin of the OCCAM transports, we consider two approximations for the Sverdrup transport. The first is for a barotropic, flat bottom ocean

$$Hv_F = \frac{\mathbf{k} \cdot [\nabla \times \tau]}{\beta \rho} \tag{2.1}$$

where the x and y coordinates here are directed to the east and north, β is taken to be 2×10^{-11} m^{-1} s^{-1} and the density ρ is constant.

From Fig. 2.14 it is clear that the ocean depth does vary and as a second approximation we will assume that the ocean depth H is a function only of the northward meridional coordinate y. This assumption is by no means exact, but since this is largely the case, it has the advantage of simplifying the solution of the equations. So, it is important to remember that the topographic transports obtained are only approximate. However, the purpose here is to determine the nature of the Sverdrup transports and show that they are an important component of those found in the OCCAM model. Following Thompson et al. (1986), the topographic Sverdrup transport with $H = H(y)$ is

$$Hv = V_E + \frac{f\mathbf{k} \cdot [\nabla \times (\tau/f)]}{\rho(\beta - \beta_T)} \tag{2.2}$$

where $\beta_T = (f/h)dH/dy$ denotes the topographic vorticity gradient due to changes in ocean depth. The first term on the right side of Eq. (2.2) is V_E and represents the meridional surface Ekman transport. The second term on the right side of Eq. (2.2) represents the geostrophic flux associated with vortex squashing, and the equation may be rewritten in terms of the flat bottomed Sverdrup transport in Eq. (2.1) as

$$Hv = -\frac{\beta_T V_E}{\beta - \beta_T} + \frac{\beta H v_F}{\beta - \beta_T} \tag{2.3}$$

The Sverdrup transports given by Eqs. (2.1) and (2.2) represent steady state solutions

for a barotropic ocean that are set-up by the zonal passage of Rossby waves across the oceanic domain. However, differences between these and the OCCAM transports can arise since the winds vary seasonally and a steady state Sverdrup balance might not be achieved. The effects of stratification can also be important since the adjustment by the baroclinic modes can act to minimise near bottom currents and reduce the influence of topographic variations on the depth-integrated Sverdrup transport (Anderson and Killworth, 1977). As Gill (1982) states " the vertically integrated transport in stratified models is very similar to that found in flat bottom barotropic models."

A simple examination of these effects can be made by considering the time-scale that governs the adjustment to the steady Sverdrup solutions. For purely zonal winds, the scale is given by

$$T_B = B/c \tag{2.4}$$

and corresponds to the time taken for a Rossby wave, phase speed c, to propagate across the ocean basin, width B. For an eastward wind stress, with a meridional wavenumber l,

$$\tau^x = \tau_0 \cos(ly) \tag{2.5}$$

Anderson and Gill (1975) have shown that the steady Sverdrup solution is set up after the passage of the westward propagating Rossby waves. The phase speed for the long barotropic waves is given by $c = \beta l^{-2}$. For the case here $B = 2000$ km, and from Fig. 2.14 we take $l = 2\pi/2000$ km, so that $c \sim 2.0$ m s^{-1} and $T_B \sim 12$ days. The scale here is short compared to the seasonal scale of 180 days, so that a steady set-up of the barotropic component of the Sverdrup transport might be expected.

For the baroclinic modes, the fastest phase speed is $c_I = \beta a^2$ where a denotes the internal deformation radius. These waves act to displace the thermocline, redistribute the Sverdrup transport with depth, and make the near bottom currents small. For the OCCAM model, $a \sim 40$ km, the phase speed is small $c_I \sim 3.2$ cm s^{-1}, and the baroclinic time scale is large, $T_B \sim 2$ years.

However, the seasonal change in the zonal component of the wind stress poleward of 42°S is not large and the winds are predominantly zonal during summer and winter. For this component of the wind, a quasi-steady adjustment may be achieved by the baroclinic modes. In this case the effects of topographic slope would be minimised and the transports should be better described by those for a barotropic, flat bottom ocean in Eq. (2.1).

Now consider the net transports shown in Table 2.1. For each of the three zonal sections shown in Fig. 2.14, the local value of the slope dH/dy (and β_T), the Ekman and flat bottom Sverdrup transports were obtained, substituted into Eq. (2.3), and then integrated to determine the net topographic transport.

At 42°S, the ocean depth increases with y as shown in Fig. 2.14. Thus since f is negative, β_T is negative. The average value is -1.9×10^{-11} m^{-1} s^{-1}. From Eq. (2.2) above, the effective meridional change in planetary vorticity $\beta - \beta_T$ is larger, the beta effect is enhanced and the Sverdrup transport reduced from the flat bottom value. For a given wind stress curl, the transport is reduced since the change in latitude (and velocity) experienced by a fluid column is smaller due to the larger gradient of planetary vorticity $\beta - \beta_T$. When the topographic slope is included, the transport at 42°S decreases by about 20% for both seasons.

As noted, the likely adjustment by the baroclinic modes at 42°S would suggest that the OCCAM transports would be better estimated by the flat bottom Sverdrup transport in Eq. (2.1) although this is only true for winter. The summertime values are better estimated by the topographic transport in Eq. (2.3). However, all of the transports are of comparable magnitude (5-10 Sv) indicating that Sverdrup dynamics drive a substantial component of the northward flow found in OCCAM.

Now consider the results at 39°S, which lies in the middle of a large topographic "bowl" that extends over 5°of latitude or $\sim$ 550 km (Fig. 2.14). Since the topographic slope is small for such a large region, the relevant scale for spin-up is that of 12 days, based on barotropic wave propagation. Indeed, both the flat bottom and topographic Sverdrup transports are similar to those obtained from OCCAM and show a strong seasonal variation between summer ($\sim$ 12 Sv) and winter ($\sim$ 4 Sv).

At the northernmost section (36°S) the winds reverse between the seasons so that baroclinic adjustment based on Rossby wave propagation should not occur and the barotropic Sverdrup transport should be given by the topographic expression in Eq. (2.3). Indeed, the strong topographic slope (dH/dy $\sim -10^{-2}$) dominates the barotropic Sverdrup dynamics with the average sectional value of β_T being 18.1 $\times$ 10^{-11} m^{-1} s^{-1} and much larger than β. During summer, the topographic Sverdrup transport is directed to the south, while during winter, the net transport is weak and less than the onshore Ekman transport. That is, the geostrophic transport is directed to the south.

Surprisingly, the flat bottom estimates at 36°S are in much closer agreement with those obtained from OCCAM (The topographic Sverdrup transports are less than one eighth of the OCCAM values). The reason for this is that baroclinic effects are again important but now arise from the presence of the shelf rather than Rossby wave propagation.

To see this, consider first the cross-sectional results at 122°E shown in Fig. 2.7a,b. Below 400 m, seasonal variations of the density field are very small and significant upwelling occurs so as to take up water downwelled elsewhere at the surface by Ekman pumping. The resultant thermal-wind shear leads to a decrease in the magnitude of the FC with depth, so that the effects of bottom slope are small. A similar result pertains to the northward currents at 36°S. Below 400 m, the density field changes very little with season and the isopycnals slope up towards the east. Thermal wind shear acts to minimise the near-bottom northward currents and thus insulate the northward transport from the topographic slope. The northward transport is thus better predicted by the flat bottom Sverdrup balance in Eq. (2.1).

Depth-Integrated Vorticity Balance

In order to evaluate the magnitude of the terms in the depth-integrated vorticity equation, the mean from years 8 to 12 OCCAM outputs was obtained and the specific terms in Eq. (2.6) below were calculated using the methodology adopted by Wells and de Cuevas (1995). The terms in the depth-integrated vorticity equation can be written as:

$$\frac{\partial}{\partial t}\nabla^2\psi = \underbrace{-\beta\frac{\partial\psi}{\partial x}}_{1} + \underbrace{\nabla\times\tau^s}_{2} - \underbrace{\nabla\times\tau^b}_{3} - \underbrace{J[p_b,H]}_{4} + \underbrace{\nabla\times\mathbf{F}}_{5} + \underbrace{\nabla\times\mathbf{N}}_{6} \qquad (2.6)$$

where ψ ($Hu = -\partial\psi/\partial y$ and $Hv = \partial\psi/\partial x$) is the streamfunction, β the beta parameter, τ^s wind stress, τ_b bottom stress, p_b bottom pressure, **F** the vertical integral of lateral friction, **N** the vertical integral of nonlinear advection and H the depth of the ocean.

The left-hand side of Eq. (2.6) represents the time dependent term and the individual terms in the right-hand side can be referred as:

1 - APV: advection of planetary vorticity

2 - W_CURL: wind stress curl

3 - B_FRIC: bottom friction

4 - BPT: bottom pressure torque (JEBAR)

5 - LFT: lateral friction torque

6 - NLAV: nonlinear advection of vorticity

The vorticity balance was calculated for the 3 zonal sections shown in Fig. 2.14 and the results can be compared with those from section 2.3. The approach here is similar to that adopted by Saunders et al. (1999), who averaged the terms over selected sections. Here these are the zonal sections.

The results in Table 2.2 show that the most important terms in the overall balance are APV and W_CURL. Indeed, from the section at 42°S, where BPT or JEBAR is important, for all the other zonal sections the remaining terms are approximately one order of magnitude smaller than the W_CURL and APV terms. Even for the 42°S section, where the BPT is of some importance, the Sverdrup balance still represents more than 70% of the overall balance.

Section	APV	W_CURL	BPT	NLAV	LFT	B_FRIC	T_DEP
42°S	-7.24	10.14	-2.58	0.41	-0.49	-0.02	0.22
39°S	-9.43	10.03	-0.01	0.13	-0.36	-0.01	0.31
36°S	-10.16	12.19	-0.01	-0.69	-1.05	-0.02	0.31

Table 2.2: *Terms in the depth-integrated vorticity equation for the sections shown in Fig. 2.14. The last column represents the time dependent term. Units* 10^{-11} *m* s^{-2}.

In a conclusion, and as argued in section 2.3, the Sverdrup balance dominates the vorticity budget of the zonal sections described in Fig. 2.14 and is the mechanism responsible for the existence of the Flinders Current.

2.4 Spatial Distribution of Large-Scale Transports

To further examine the large-scale circulation indicated by the OCCAM results, the SEIO was divided into 7 boxes (Fig. 2.16), and the transports between boxes calculated for two distinct layers in the vertical. These layers were based on the TS distribution of the water masses shown in Fig. 2.17 and were chosen to represent the SML (0-268 m), and permanent thermocline and Antarctic Intermediate Water (AAIW) levels (268-1234 m) (Deeper circulation of the Upper Circumpolar Deep Water (UCDW) and the abyssal waters are not discussed). The purpose here is to develop a schematic cartoon (Fig. 2.18) which will allow for a description, in an idealised sense, of the pathways of circulation at the surface and intermediate depths.

Net Transports: 0-5500 m

Lets begin by examining the total integrated transports. Positive transports denote flow to the north or east and the results in Fig. 2.16 reveal three notable features. The first relates to the net transports in and out of the domain. The largest transport into the domain is 19.64 Sv and is associated with the Tasman Outflow (box 7). A total of 6.2 Sv flows out through the southern boundary. Of the remainder, 8.13 Sv leaves through the western domain and poleward of 42°S (box 3) and 4.47 Sv leaves equatorward of 39°S (box 1), as part of the Sverdrup dynamics explained on section 2.3.

The two other features are related to the circulation on the eastern side of the basin (boxes 4-7). The first is a 5 Sv or so transport (Fig. 2.15) that is associated with the cyclonic eddy centered upon (41°S, 138°E) with a radius of approximately 200 km (this feature will be called the Victorian Low). The second is the eastward transport of 0.28 Sv through Bass Strait. The value here is somewhat less than 0.49 Sv estimated from current meter data by Baines et al. (1991).

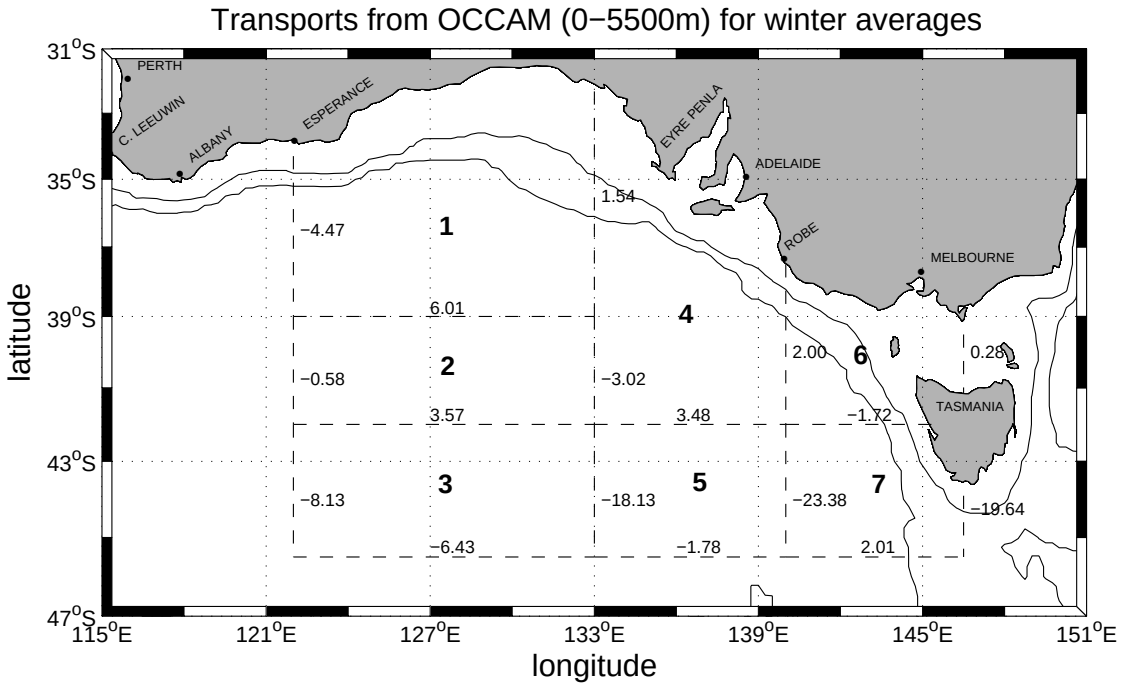

Figure 2.16: *Integrated transports (Sv) from surface to bottom, where bold numbers at the center of each cell represent the box number. At the edge of each cell positive values indicate eastward or northward transports. Solid lines are the 1000 and 4000 m isobaths.*

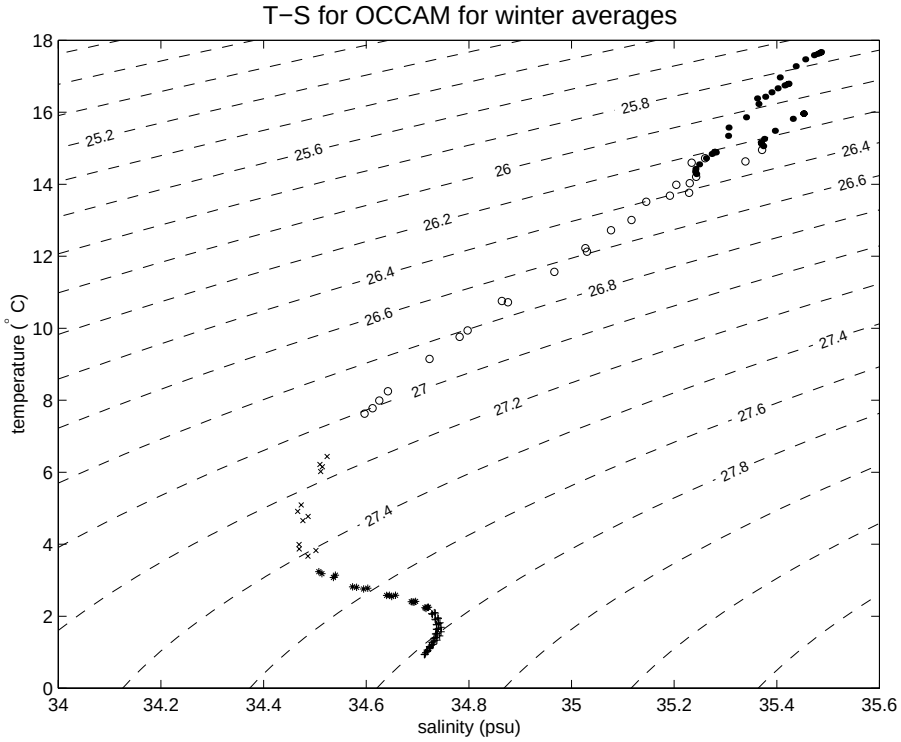

Figure 2.17: *TS diagram at selected points of box 1 on Fig. 2.16. Filled circles represent the SML level, empty circles represent the permanent thermocline level, x-marks represent the AAIW level, stars represent the UCDW level and crosses represent the remaining points below this level. Dashed lines are the isopycnal contours at 0.2 intervals.*

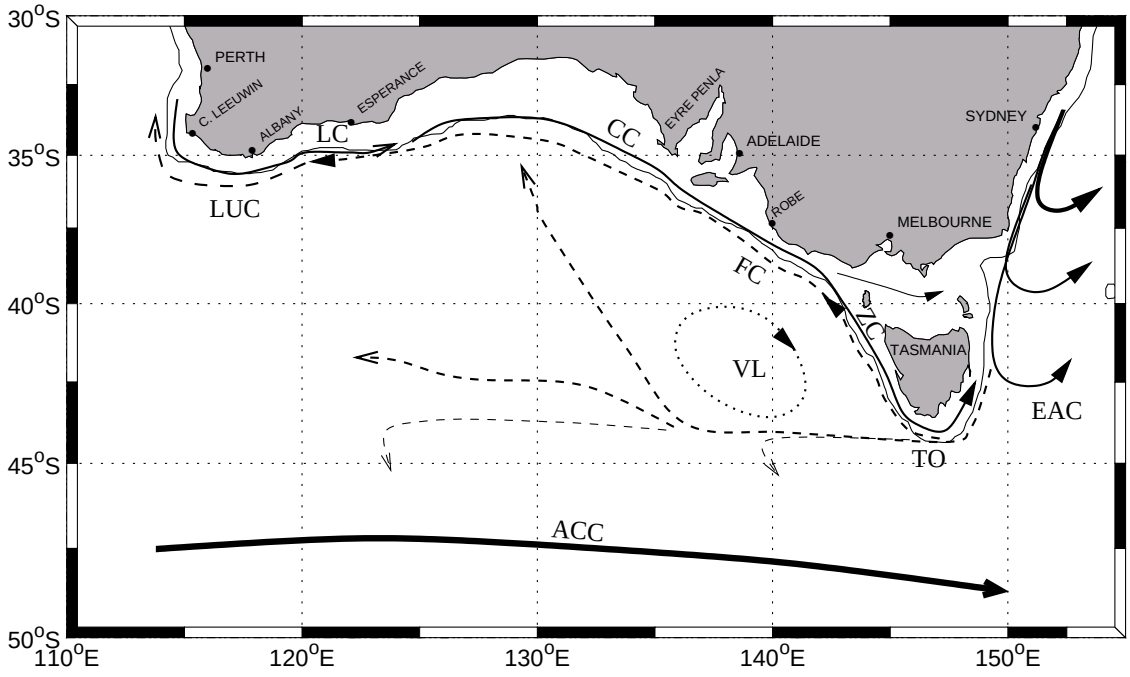

Figure 2.18: *Schematic wintertime circulation based on OCCAM results, where the solid lines represent surface currents (Leeuwin Current (LC), Coastal Current (CC), Zeehan Current (ZC) and East Australian Current (EAC)), dashed lines represent sub-surface currents (Leeuwin Undercurrent (LUC), Flinders Current (FC) and Tasman Outflow (TO)) and AAIW flow and dotted lines represent a cyclonic gyre (the Victorian Low (VL)). The 1000 m isobath is also plotted as a reference.*

The westward flow south of Tasmania has also been observed by many authors (*e.g.* Wyrtki, 1971; Bye, 1972; Reid, 1997). Godfrey (1989) used a Sverdrup model of the global depth-integrated flow forced with annual mean wind stress and found a westward transport of $\sim$ 20 Sv passing through the southern tip of Tasmania. Tomczak et al. (2000) calculated the geostrophic transport relative to 1200 m and found a westward transport of 16.4 Sv for a meridional section that extends from Tasmania to the latitude of 45°S. Based upon 6 repeated CTD sections between Tasmania and Antarctica, Rintoul and Sokolov (1999) calculated the net transport relative to optimal reference levels and found two distinct westward flows south of Tasmania. The first one was a variable outflow from the Tasman Sea with a transport of 8 ± 13 Sv between Tasmania and the South Tasman Rise ($\sim$ 46°S). The authors found that the strength of this westward flow appears to be controlled by meridional shifts in the latitude of zero wind stress curl, where equatorward displacements of the zero curl line would lead to a weak westward

flow. Based on the mean position of the zero curl line, they speculate that the mean transport of the outflow is likely to be about 20 Sv. The second portion of the transport, between 46°S and the Subantarctic Front ($\sim$ 53°S) was a stronger and more persistent westward flow, which is part of an anticyclonic circulation cell carrying 22$\pm$8 Sv, confined between 135°E and 145°E.

Transports within the SML: 0-268 m

Within the SML (Fig. 2.19), the results indicate a generally northward flow as well as an eastward transport near the coast. While the transport of 2.98 Sv entering box 1 is no doubt driven in part by the LC, the otherwise eastward and northward transports within the SML are mainly wind driven.

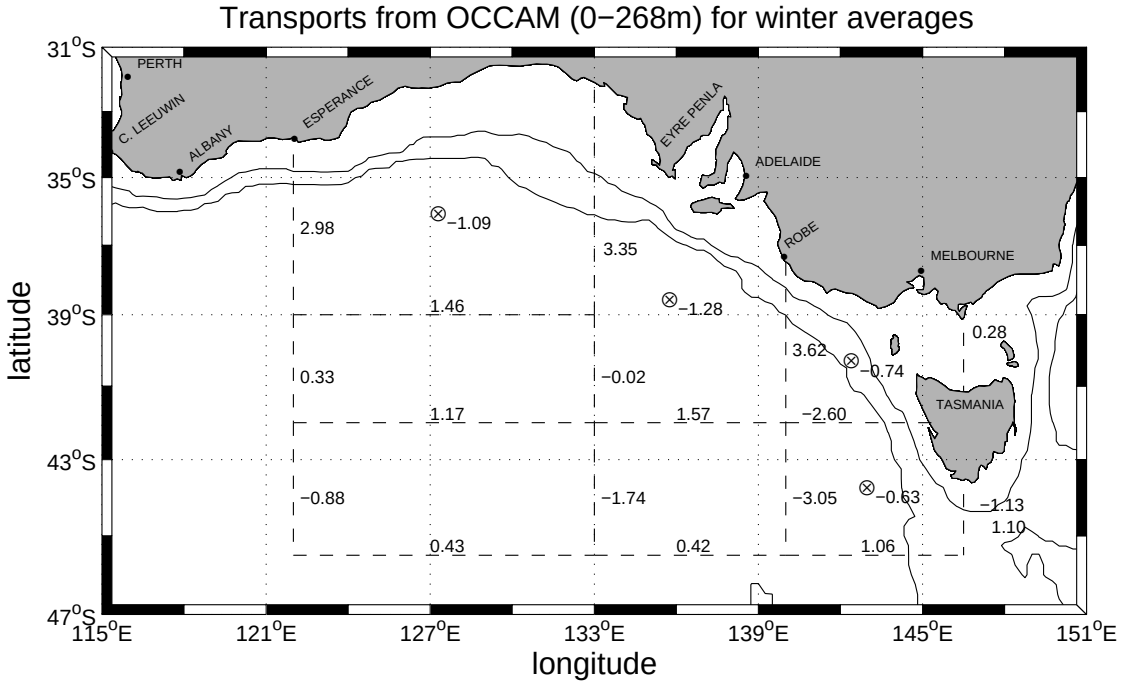

Figure 2.19: *Integrated transports (Sv) for the SML (0-268 m). Vertical transports higher than 0.2 Sv are represented by negative values for downwelling (⊗) and positive values for upwelling (○). Solid lines are the 1000 and 4000 m isobaths.*

The mean wind field is generally parallel to the coastline (Fig. 2.1a) and has a positive curl for the whole region (Fig. 2.1b). As a consequence, it raises the sea level at the coast (Fig. 2.20) generating an eastward coastal jet and also leads to downwelling everywhere. Indeed, for the coastal boxes (box 1, 4, 6 and 7) the total downwelling for the Ekman layer (Fig. 2.21) is 2.55 Sv or 85 % of the total of 2.95 Sv.

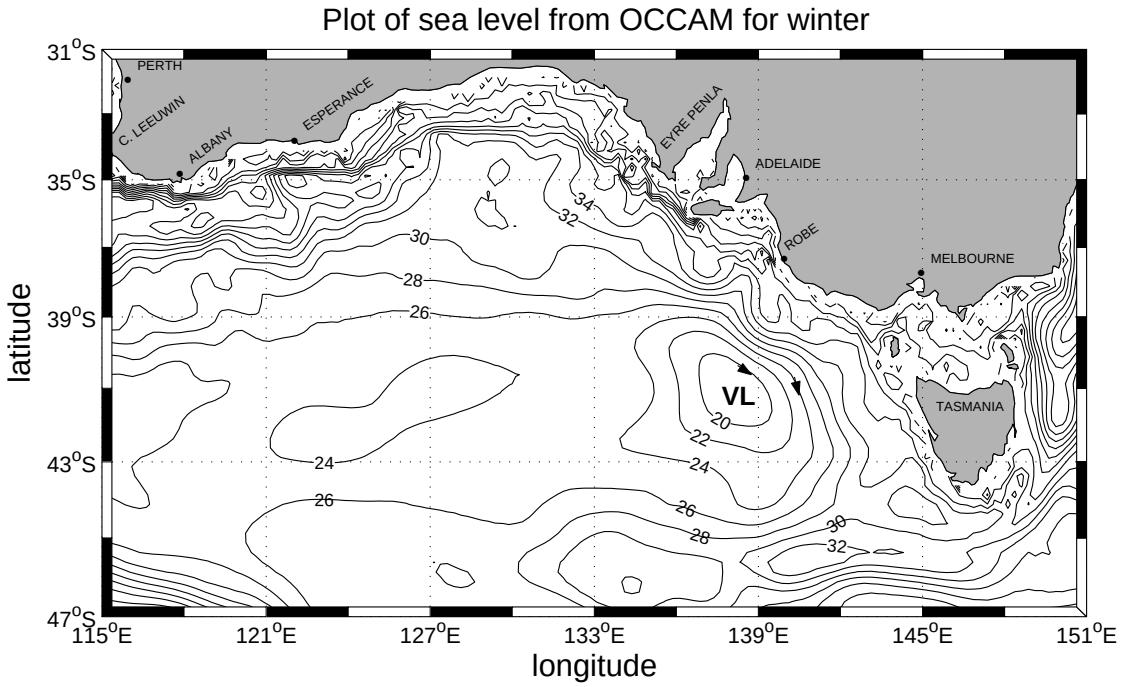

Figure 2.20: *Sea level for OCCAM. The contour interval is 2 cm. The arrows represent the movement associated with the Victorian Low (VL).*

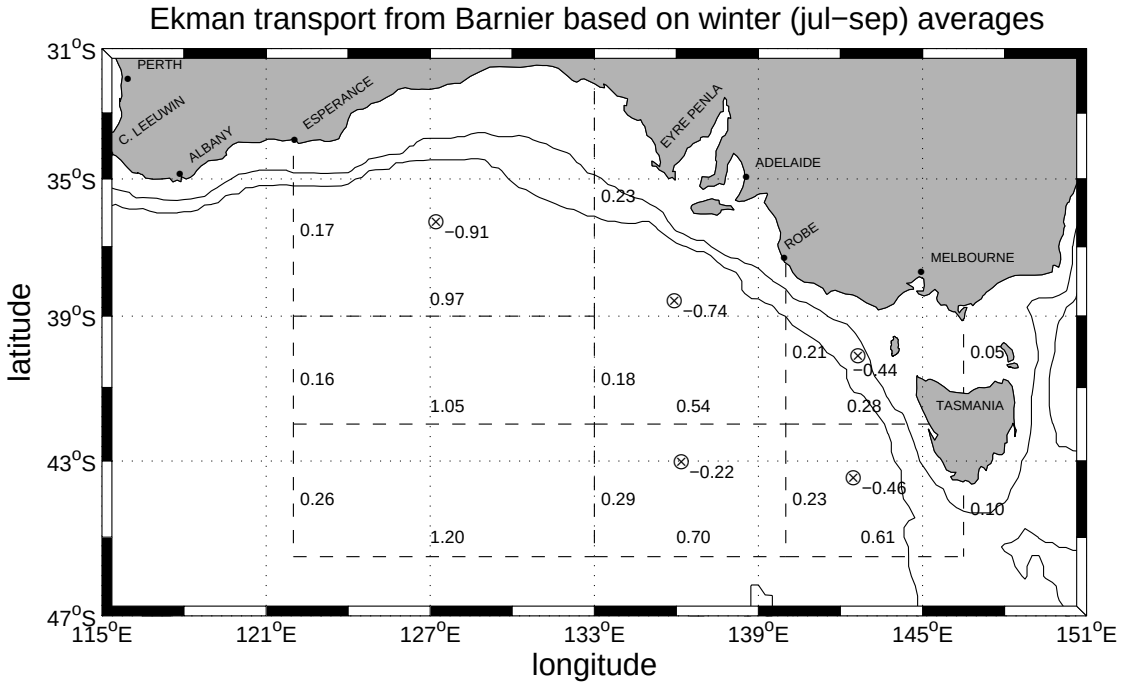

Figure 2.21: *Associated Ekman transport due to the wind stress field from Siefridt and Barnier (1993) in Fig. 2.1a. Negative values (⊗) represent the convergence in the Ekman layer. Solid lines are the 1000 and 4000 m isobaths.*

Similar results are obtained from OCCAM (Fig. 2.19), indicating that much of the downwelling within the SML is determined by the Ekman layer (Fig. 2.21). For the SML coastal boxes, 3.75 Sv is downwelled (2.55 Sv for the Ekman layer) while for all boxes, the total is 4.09 Sv (2.95 Sv for the Ekman layer).

Of the 3.6 Sv that passes Robe at the shelf-slope region, only 1.4 Sv leaves the region either through Bass Strait (0.28 Sv) or south of Tasmania (1.1 Sv). (The transports indicated on the right side of box 7 are for the eastward flowing ZC (1.1 Sv) and westward Tasman Outflow (-1.13 Sv)). The remainder of the 3.6 Sv passing Robe forms part of the Victorian Low (Fig. 2.20). The possible cause of this low is the velocity shear induced by the combined effects of the poleward currents off Victoria and Tasmania and westward currents south of Tasmania. The eastern side of the gyre is illustrated by the 42°S section shown in Fig. 2.10a-b. The thermal wind shear associated with the sloping (downwelled) isopycnals reduce the magnitude of the currents to less than 2 cm s^{-1} at depths below 600 m or so.

As will be seen in the solutions presented in chapter 4, the gyre is reproduced after 6 days of forcing in the high resolution POM. Localised Ekman pumping does not seem to be important to the formation of the low since there is no local anomaly in this field (Fig. 2.1b) for the region.

Transports at intermediate layers: 268-1234 m

For the permanent thermocline and AAIW level (Fig. 2.22), the circulation is quite distinct from that found within the SML. Over the continental slope there is a north-westward undercurrent (Fig. 2.2b) that is built up due to downwelling from the SML (3.75 Sv for boxes 1, 4, 6 and 7) and upwelling from the layer below (0.68 Sv for the same boxes). The vortex squashing leads to northward Sverdrup transport and westward flow with some 9.68 Sv passing south of Esperance (box 1).

Apart from the slope circulation, the two other important features are the effects of the Victorian Low at intermediate layers, with an associated transport of $\sim$ 3 Sv, and the westward circulation due to the Tasman Outflow. At latitudes higher than 42°S this transport gradually decreases as it flows westward, but even at the longitude of 122°E and for box 3, it still accounts for a transport of 5.5 Sv.

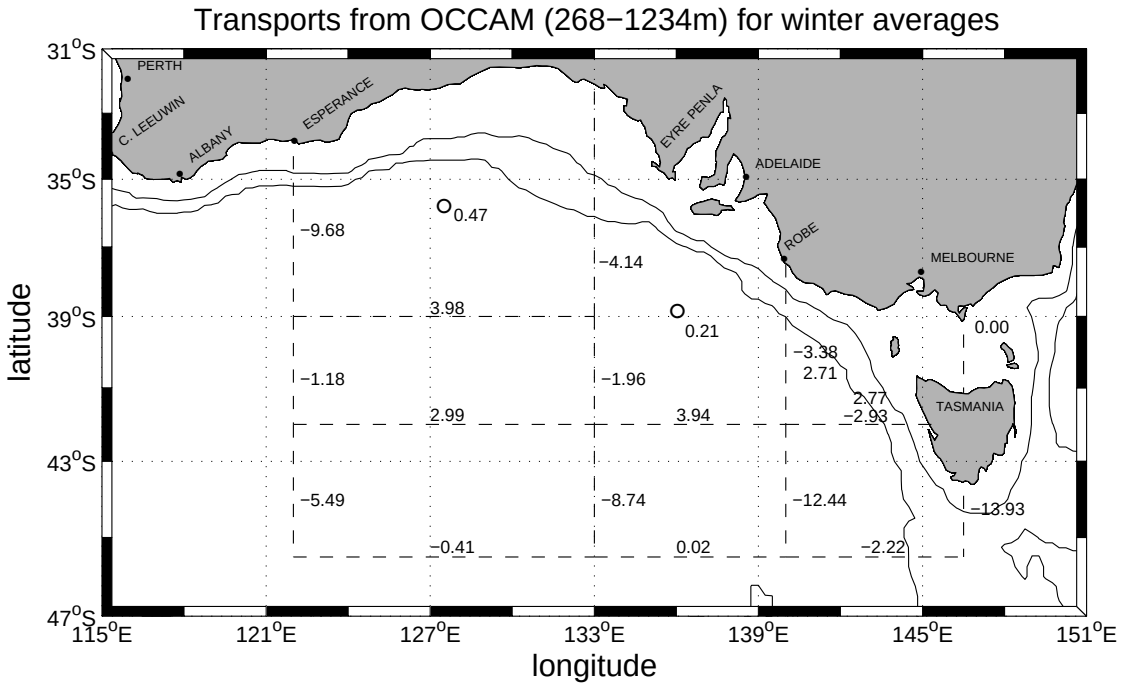

Figure 2.22: *Same as Fig. 2.19, but for the level of the permanent thermocline and AAIW level (268-1234 m). Upwelling from the bottom of this layer is represented by (○).*

The large westward transport of 16.35 Sv through boxes 1-3 is in agreement with that found by Schodlok et al. (1997). At 120°E and north of the latitude of 45°S, they found a westward flow of 7.5 ± 1.2 Sv just for the AAIW level (here the transport through the permanent thermocline, which is in the same direction, is also considered). The authors defined two distinct components of the flow, one which is related to the shelf-slope region and the other at higher latitudes and which is similar to that found from the OCCAM results in Fig. 2.2b.

Chapter 3

A Regional Scale Model: Implementation

There are two major problems in modelling the circulation of the SEIO. First, the bathymetry is very irregular, characterised by a wide shelf at the centre of the GAB and narrow shelves and steep slopes along the Western Australia, Robe and western Tasmania (Fig. 1.1). Second, the region is influenced by surrounding large-scale currents. To incorporate such currents and topographic variations a high resolution version of the Princeton Ocean Model (POM) (Blumberg and Mellor, 1987; Mellor, 1998) was adopted, but nested with the OCCAM global model (which would allow for the representation of the larger scale currents). The global model will provide the integrated transports at the boundaries of the regional model as well as the initial temperature and salinity fields.

The following sections describe the details of the regional model, as well as its implementation.

3.1 The Regional Model

POM is a *sigma* coordinate model, which is freely available at the POM home page (http://www.aos.princeton.edu/WWWPUBLIC/htdocs.pom) and a complete description of the model can be found in Blumberg and Mellor (1987) and Mellor (1998). The main attributes of the model are as follows:

- The vertical mixing coefficients are determined from an embedded second moment turbulence closure sub-model (Mellor, 1973; Mellor and Yamada, 1974, 1982);
- The horizontal grid uses curvilinear orthogonal coordinates and an Arakawa C grid;
- The horizontal time differencing is explicit and the vertical differencing is implicit. The latter eliminates time constraints arising from the vertical coordinate, allowing fine resolution in both the surface and bottom boundary layers;

- The model has a free surface and a split time step. The depth-averaged solutions are obtained using a time step based on the *Courant-Friedrichs-Levy* (CFL) condition and the external wave speed, while the three-dimensional solutions are obtained using a longer time step based on the CFL condition and the associated internal wave speed;
- Complete thermodynamics have been implemented.

Denoting the orthogonal Cartesian coordinates system by (x^*, y^*, z) and assuming the hydrostatic and Boussinesq approximations, the equations to be solved are:

- The momentum equations:

$$\frac{\partial \mathbf{u}}{\partial t} + (\mathbf{u} \cdot \nabla_h)\mathbf{u} + w\frac{\partial \mathbf{u}}{\partial z} + \mathbf{k} \times f\mathbf{u} = -\frac{1}{\rho_0}\nabla_h p + \frac{\partial}{\partial z}\left(K_M \frac{\partial \mathbf{u}}{\partial z}\right) + \mathbf{F} \quad (3.1)$$

$$\rho g = -\frac{\partial p}{\partial z} \quad (3.2)$$

- The conservation equation for potential temperature and salinity:

$$\frac{\partial \theta}{\partial t} + (\mathbf{u} \cdot \nabla_h)\theta + w\frac{\partial \theta}{\partial z} = \frac{\partial}{\partial z}\left(K_H \frac{\partial \theta}{\partial z}\right) + F_\theta \quad (3.3)$$

$$\frac{\partial S}{\partial t} + (\mathbf{u} \cdot \nabla_h)S + w\frac{\partial S}{\partial z} = \frac{\partial}{\partial z}\left(K_H \frac{\partial S}{\partial z}\right) + F_S \quad (3.4)$$

- The continuity equation:

$$\nabla_h \cdot \mathbf{u} + \frac{\partial w}{\partial z} = 0 \quad (3.5)$$

- The equation of state :

$$\rho = \rho(\theta, S, p) \quad (3.6)$$

where:

$\mathbf{u}$ $\equiv$ horizontal velocity vector with components u and v (m s^{-1})

∇_h $\equiv$ horizontal gradient operator $\left(\mathbf{i}\frac{\partial}{\partial x^*} + \mathbf{j}\frac{\partial}{\partial y^*}\right)$

w $\equiv$ vertical velocity (m s^{-1})

f $\equiv$ Coriolis parameter (s^{-1})

ρ,ρ_0 $\equiv$ *in situ* density and reference density (kg m^{-3})

p $\equiv$ pressure (N m^{-2})

K_M $\equiv$ vertical eddy diffusivity of momentum (m^2 s^{-1})

K_H $\equiv$ vertical eddy diffusivity of heat and salinity (m^2 s^{-1})

$\mathbf{F}$ $\equiv$ horizontal diffusion terms of momentum for F_{x^*} and F_{y^*}

$F_{\theta,S}$ $\equiv$ horizontal diffusion terms of heat and salinity

g $\equiv$ gravitational acceleration (m s^{-2})

θ $\equiv$ potential temperature

S $\equiv$ salinity (PSU)

Equations (3.1)-(3.5) can be rewritten in *sigma* coordinates (x, y, σ) using the transformation proposed by Phillips (1957)

$$(x, y, \sigma) = \left(x^*, y^*, \frac{z - \eta}{H + \eta}\right) \tag{3.7}$$

where $\eta(x, y, t)$ is the sea level elevation, $H(x, y)$ is the bottom topography and $D \equiv H + \eta$. The *sigma* coordinate ranges from $\sigma = 0$ at $z = \eta$ to $\sigma = -1$ at $z = -H$ and has a transformed vertical velocity (ω) which is the velocity component normal to the *sigma* surfaces. The transformation to the Cartesian vertical velocity is:

$$w = \omega + u\left(\sigma\frac{\partial D}{\partial x} + \frac{\partial \eta}{\partial x}\right) + v\left(\sigma\frac{\partial D}{\partial y} + \frac{\partial \eta}{\partial y}\right) + \sigma\frac{\partial D}{\partial t} + \frac{\partial \eta}{\partial t} \tag{3.8}$$

Using a time split technique, depth-averaged velocities $(\overline{u}, \overline{v})$ and η are calculated at every external time step (Δt_{ext}), while the three-dimensional fields (u, v, θ, S) are only calculated at longer internal time intervals (Δt_{int}). The external mode calculation uses a vertical integrated set of equations similar to equations (3.1) and (3.5), while for the internal mode the equations are similar to equations (3.1)-(3.6). All equations mentioned above were transformed to a *sigma* coordinate system with the use of equation (3.7)

and a detailed description of them can be found in Mellor (1998). The equation of state (3.6) used in the model was adapted by Mellor (1991).

3.2 Adaptation of the Regional Model

3.2.1 The Grid and the Spin-up Process

The approach for developing this regional grid followed two premises. First, it should be representative of the basin circulation and second, it should keep open boundaries away from the region of interest. The three geographic limits for the grid (Fig. 3.1) were selected according to the analysis of integrated transports from OCCAM. The Western and Eastern Boundaries were located in regions apart from the main eddy activity generated by the associated Leeuwin Current (LC) and East Australian Current (EAC) and the Southern Boundary was located just north of the main core of the Antarctic Circumpolar Current (ACC).

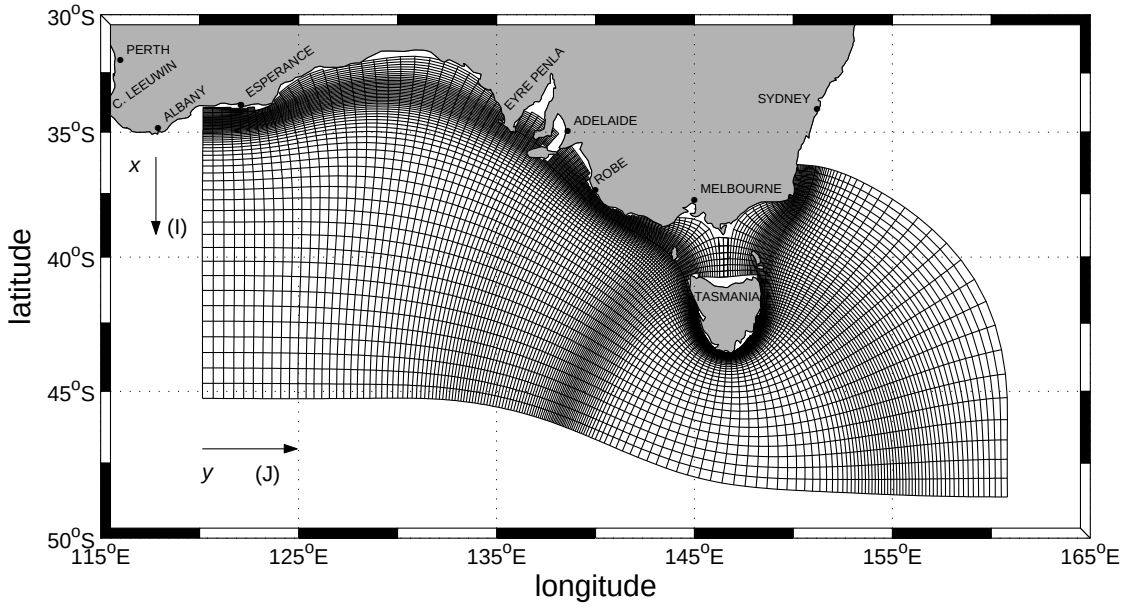

Figure 3.1: *The horizontal curvilinear grid (63 × 173).*

Since the bathymetry of the region is complicated, a horizontal curvilinear grid with high resolution over the shelf-slope region was applied (Fig. 3.1). The bathymetry was based on $1/120^{\circ}$ data set from the *Australian Geological Survey Organisation*. A cyclic

boundary condition was also applied within Bass Strait, to mimic the propagation of the information through this region. The minimum depth of the model was set to 20 m while the maximum was 5400 m.

The horizontally curvilinear grid (Fig. 3.1) has 63 cells in the offshore direction (x axis) and 173 cells in the alongshore direction (y axis). For the region of interest, between Kangaroo Is and the western shelf of Tasmania, the alongshore grid cells vary between 10-20 km and the offshore grid cells vary between 2-7 km.

The vertical grid has 32 *sigma* layers, with logarithmic distribution on the top 10 layers and linear distribution on the remaining layers (Fig. 3.2).

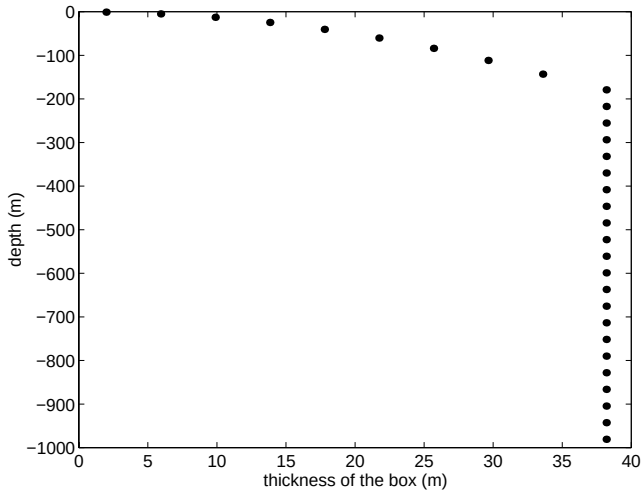

Figure 3.2: *Resolution of the vertical grid for a point located at a depth of 1000 m.*

Regarding the spin-up process, the regional model was run for a period of 2 months. The reasons for that is because: (1) the main interest is the coastal and shelf-slope dynamics which spin up on time scale of months (*e.g.* Middleton and Cirano, 1999) and over time scales due to the passage of Coastal Trapped Waves (CTW) and Kelvin waves; (2) the model was run out to 90 days (and results were similar to those of 60 days). In addition, plots of mean kinetic energy were also showing an equilibrium state; (3) the non-linear eddies, which will be shown in the discussion of the results, grow over 30-60 days time scales and (4) winds and boundary conditions change seasonally and therefore it is pointless to apply constant winds for a longer time.

3.2.2 The Horizontal Diffusion and Bottom Stress Formulation

The horizontal kinematic viscosity coefficient (A_M) and the horizontal diffusivity coefficient (A_H) are both equal to 100 m^2 s^{-1} and bottom drag (C_d) has a value of 0.0025.

The effects of CTW and tides will also be incorporated into the model through the drag law for bottom stress, $\tau_b = \rho_0 C_d \mathbf{u}(|\mathbf{u}|^2 + 2\sigma^2{}_{CTW} + 2\sigma^2{}_{TIDES})^{1/2}$, where σ_{CTW} and σ_{TIDES} are the *rms* bottom speed of the associated CTW and tidal currents (*e.g.* Wright and Thompson, 1983; Evans and Middleton, 1998). A detailed description of the tidal model is given in Platov and Middleton (2000) while the CTW model is described in Appendix D.

3.2.3 Boundary Conditions

The region of interest is surrounded by many currents and a common approach is to specify the associated inflow/outflows for the regional model using a larger scale global model (*e.g.* Mellor and Ezer, 1991; Oey and Chen, 1992b; Ezer and Mellor, 1994). Here, the set of boundary conditions adopted for the depth-averaged velocities and elevation were based on those of Palma and Matano (1998), who used a combination of an active boundary condition for the normal velocity and a passive boundary condition for the tangential velocity and sea level (Chapman, 1985). The discrete form of the scheme, at the eastern boundary may be written as:

- normal velocity

$$\overline{v}_B^{n+1} = V_0 + \frac{c_0}{H}\left(\eta_{B-1}^{n+1} - \eta_0\right) \tag{3.9}$$

$V_0,\ \eta_0$	$\equiv$	prescribed depth-averaged velocity and sea level from OCCAM
$c_0 = \sqrt{gH}$	$\equiv$	shallow water wave speed
B	$\equiv$	boundary point
n	$\equiv$	time step

- depth-averaged tangential velocity and sea level

$$\phi_B^{n+1} = \frac{\phi_B^n + r\phi_{B-1}^{n+1}}{1+r}, \text{ where } r = \frac{\Delta t_{ext}}{\Delta y} c_0 \tag{3.10}$$

For the three-dimensional fields, a combination of Orlanski boundary conditions (Orlanski, 1976; Chapman, 1985) for the normal velocities and advective boundary conditions for tangential velocities, temperature and salinity were used. The discrete form of these schemes are defined as:

- normal velocity

$$v_B^{n+1} = \frac{\{v_B^{n-1}(1-r) + 2rv_{B-1}^n\}}{(1+r)} \text{ , where} \tag{3.11}$$

$$r = \begin{cases} 1 & \text{if } C_n \geq 1 \\ C_n & \text{if } 0 < C_n < 1 \\ 0 & \text{if } C_n \leq 0 \end{cases} \quad \text{and } C_n = \frac{v_{B-1}^{n-1} - v_{B-1}^{n+1}}{v_{B-1}^{n+1} + v_{B-1}^{n-1} - 2v_{B-2}^{n-1}}$$

- tangential velocities, temperature and salinity

$$\phi_B^{n+1} = \phi_B^n - \frac{\Delta t_{int}}{\Delta y} V_1 r, \text{ where } r = \begin{cases} \phi_B^n - \phi_{B-1}^n & \text{if } V_1 \text{ is an outflow} \\ \phi_0 - \phi_B^n & \text{if } V_1 \text{ is an inflow} \end{cases} \tag{3.12}$$

$V_1 \equiv$ normal velocity at the boundary point

$\phi_0 \equiv$ OCCAM values for scalars and zero for tangential velocities

The prescribed velocity and elevation for the depth-averaged quantities, are based on the output of the OCCAM model and are kept constant in time. The adjustment of the regional model to the imposed transports is shown in Fig. 3.3. As can be seen, the model transports are very close to those of OCCAM after 30 days of model run.

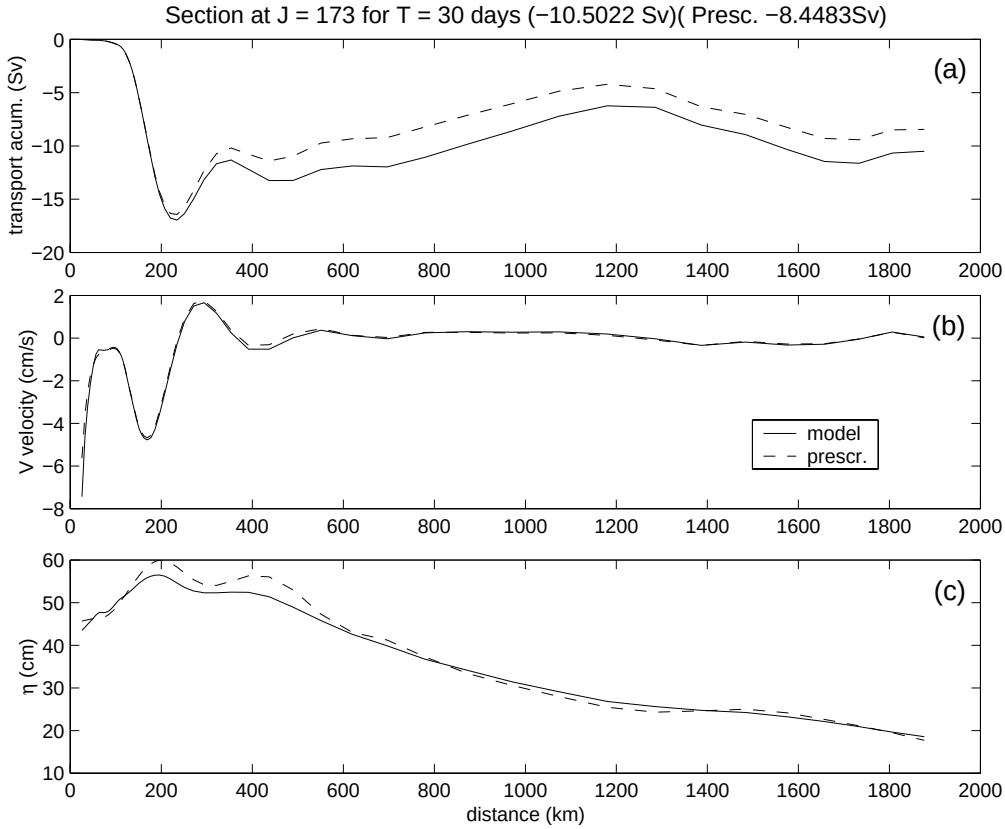

Figure 3.3: *(a) Plot of the accumulated transport, (b) velocity and (c) elevation for the eastern boundary. The solid lines represents the model values at day 30 and at the boundary, while the dashed lines represent the prescribed values from OCCAM.*

3.2.4 The 2 Grid-Point Instabilities

The results of the nested regional model, particularly along the slope, exhibited weak 2 grid-point instabilities. Middleton and Cirano (1999) solved a similar problem (where the instabilities do not evolve rapidly in time) using a once a day Shapiro filter for the alongshore direction and for all variables. In their study, there were no alongshore variations in the topography and the filter for sea level was written as:

$$\eta_{i,j} = (1-\gamma)\eta_{i,j} + 0.5\gamma(\eta_{i,j-1} + \eta_{i,j+1}) \ , \text{ where } \gamma = 0.5 \tag{3.13}$$

For the realistic bathymetry here, the design of a similar filter is more complicated. Even using a curvilinear grid, which tends to follow isobaths, one cannot guarantee that adjacent points on the alongshore direction will have the same depth. To counteract this

problem the filter was applied at the adjacent z-levels instead of *sigma* levels as shown in Fig. 3.4 by interpolating in the vertical.

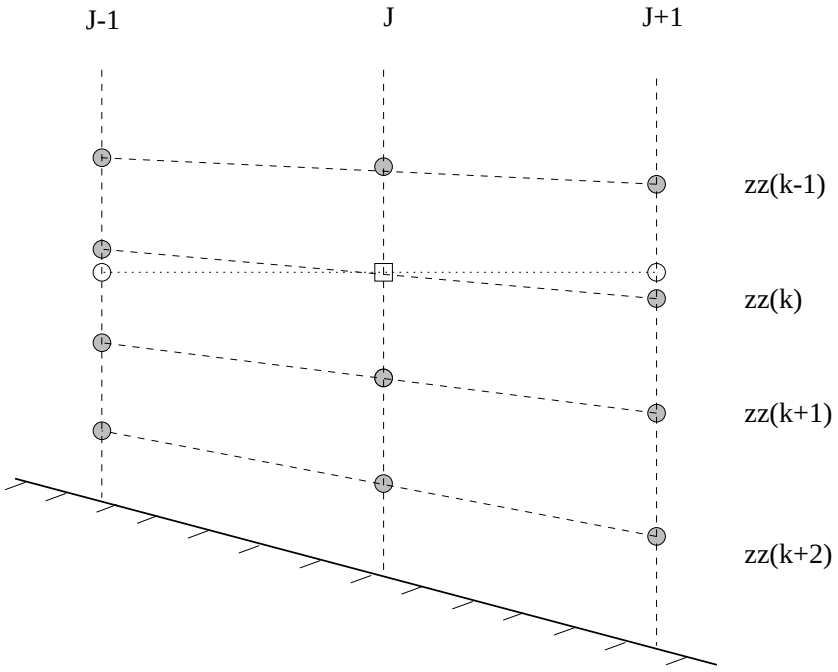

Figure 3.4: *Diagram of the z-level (dotted line) Shapiro filter in the J direction. The gray circles represent the points along the sigma coordinate (dashed lines) and unfilled circles represent the points resulting from the vertical interpolation. The square represents the sigma point at which the Shapiro filter is applied using adjacent interpolated values.*

An additional problem is that the alongshore grid does not follow isobaths (Fig. 3.5e). This may be seen from Fig. 3.5e, where the depth H is plotted as a function of the alongshore coordinate J. Thus a filter in the J direction will lead to filtering in the cross-isobath direction. As a crude test of the effects of using this filter, results (Fig. 3.7) are compared with those obtained without any filter (Fig. 3.5) and with a filter in both I and J directions (Fig. 3.6).The filters were applied every 10 days.

Surface, mid-depth, bottom and depth-averaged values of the cross-shelf velocities are shown and a comparison of results shows that the application of the filter does noticeably reduce the 2 grid-point instabilities shown in Fig. 3.5, while preserving the larger scale variability. The results obtained by filtering in both directions (Fig. 3.6) and in J direction alone (Fig. 3.7) are also similar, suggesting that the more severe cross-isobath filtering that results in the former case has little impact on the results.

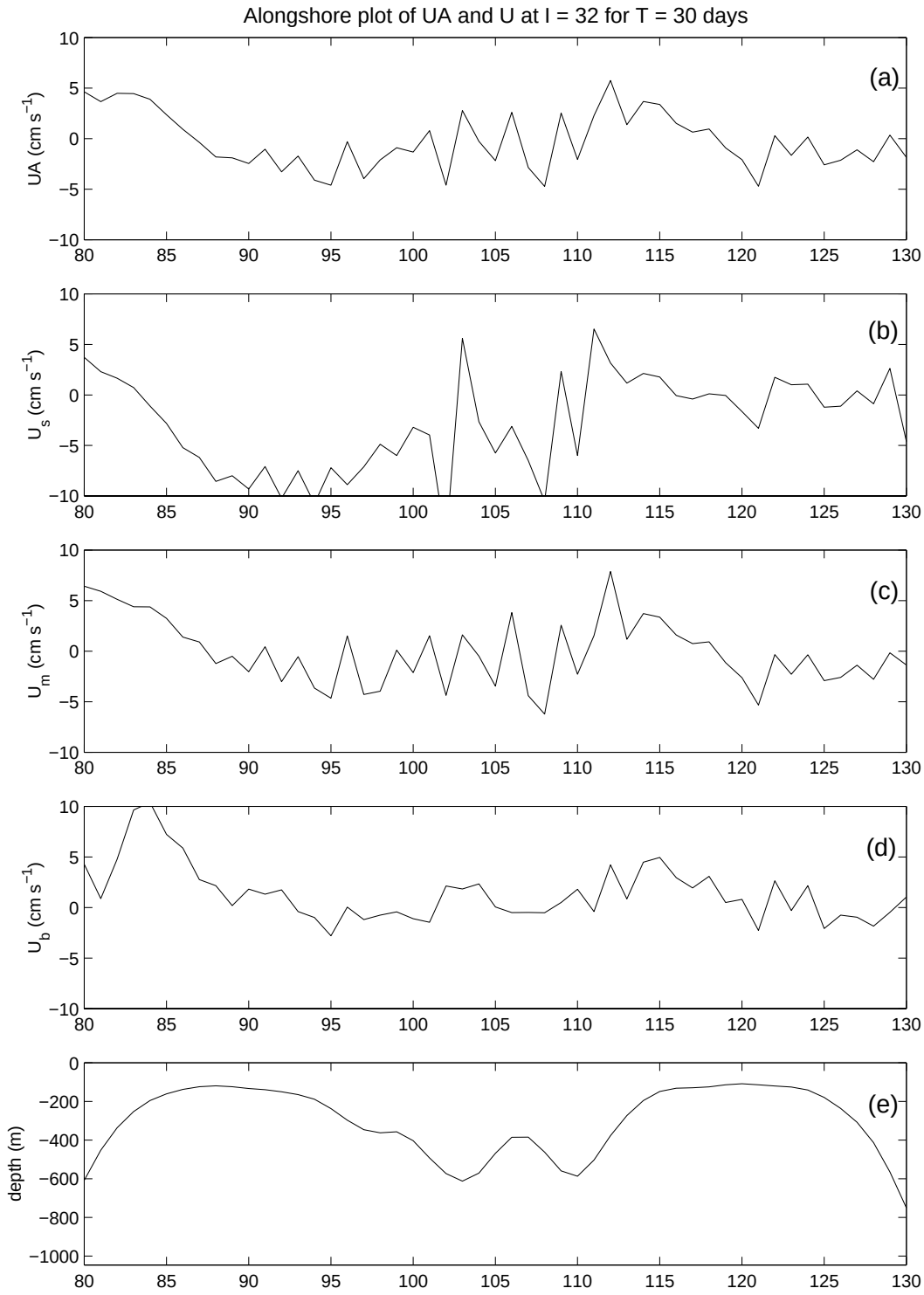

Figure 3.5: *Alongshore plot of the unfiltered u component of the velocity (a) depth-integrated, b) surface, c) mid-depth and d) bottom) at I=32 (solid lines), from J=80 to 130 (along the Tasmanian coast) at day 30. The bottom panel e) shows the associated local depth for these points.*

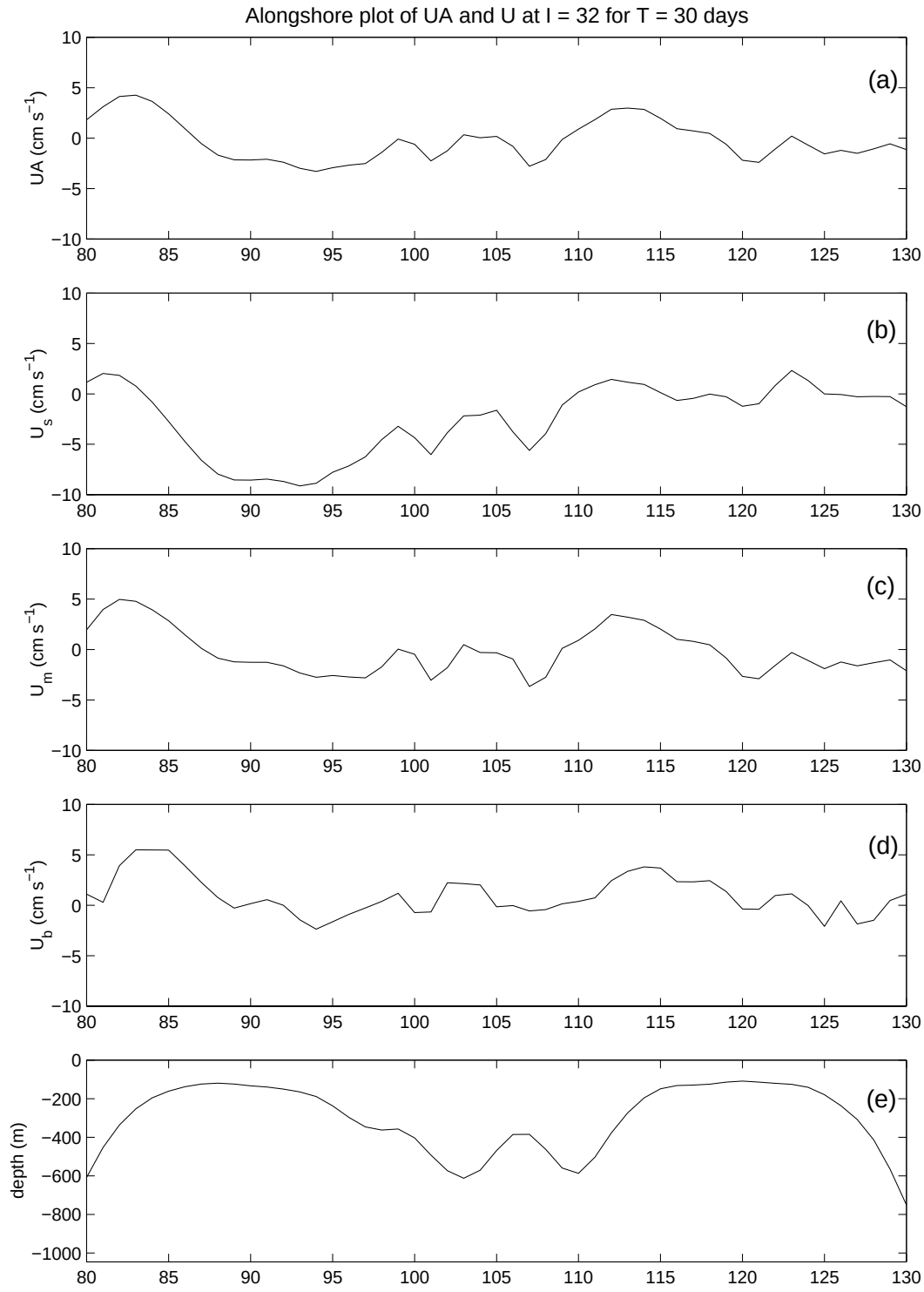

Figure 3.6: *As in Fig. 3.5, but applying the Shapiro filter once every 10 days for both directions.*

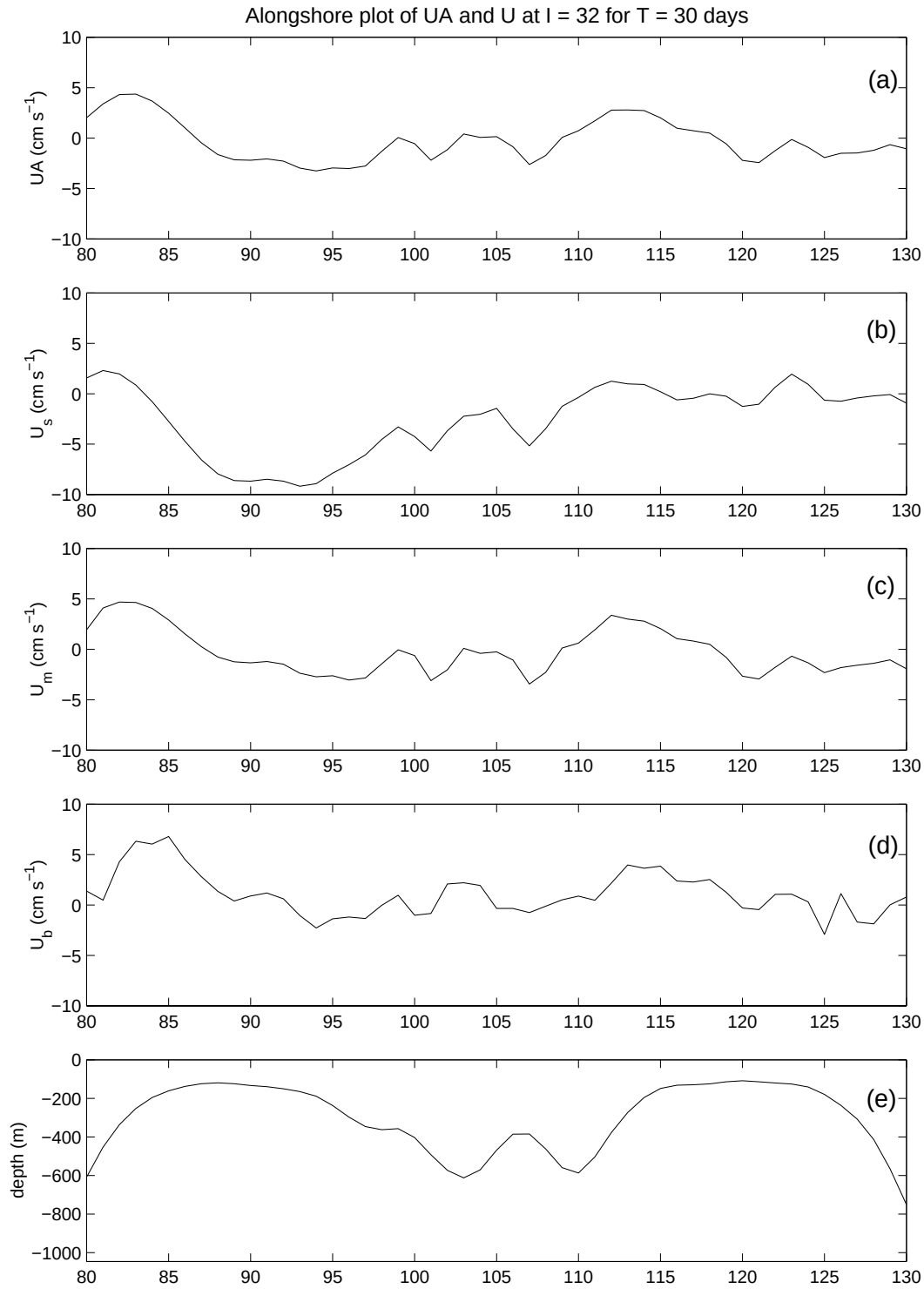

Figure 3.7: *As in Fig. 3.5, but applying the Shapiro filter once every 10 days just for J direction.*

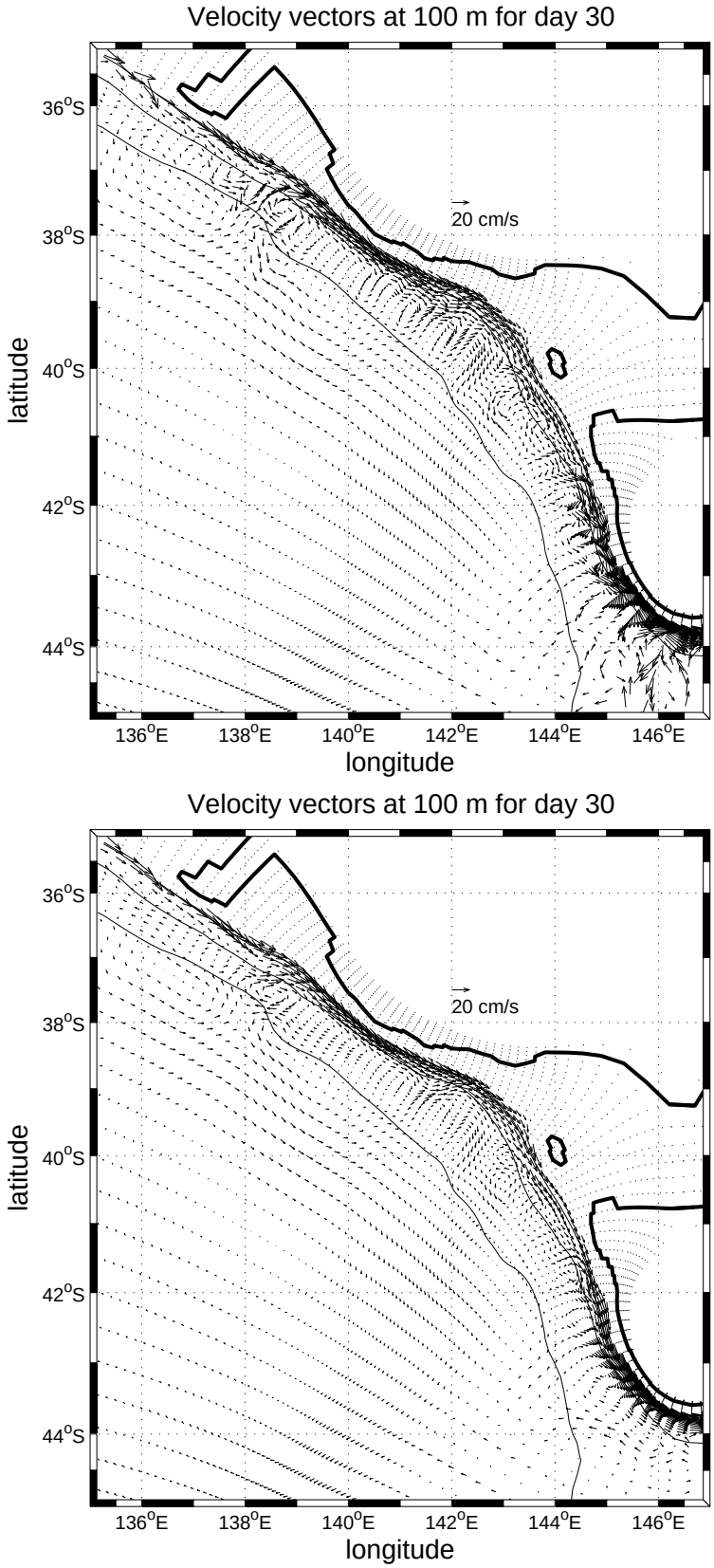

Figure 3.8: *Horizontal velocity field at 100 m at day 30 without the use of a Shapiro filter (top panel) and with Shapiro filter applied just for J direction (bottom panel). Solid lines are the 200, 1000 and 4000 m isobaths.*

Comparison of the horizontal velocity field (Fig. 3.8) also shows that the filtering procedure, while eliminating undesirable 2 grid-point instabilities, can preserve important small scale such as the eddies located off Robe.

3.2.5 The Pressure Gradient Error Evaluation

One of the disadvantages of *sigma* coordinate models is that interpolation errors can arise in the evaluation of the horizontal component of the pressure gradient (due to density) next to steep topography (*e.g.* Haney, 1991; Mellor et al., 1994, 1998; Chu and Fan, 1997). The problem is illustrated in Fig. 3.9, where from the Arakawa-C grid adopted, a horizontal gradient is required at the site of the square box. The grey circles denote sites were scalars are calculated. While a value of the scalar can be simply interpolated onto the right side of the square box, the problem is what to do on the left side so that a horizontal derivative can be estimated. Fortunately, there are various ways to reduce or even eliminate this problem. Song (1998) reviewed the main methods of calculating this term and divided them in four different strategies: (1) evaluate the pressure gradient in z-coordinates; (2) subtraction of the mean density field before calculating the pressure gradient; (3) use of higher-order methods, such as 4th order approximations and (4) conservation of integral properties.

Mellor et al. (1994), using POM, adopted the first two strategies and formulated an error correction for the pressure gradient, which results from the difference between the pressure gradient calculated in z-coordinates (first term in Eq. 3.14) and the one calculated in POM (second term in Eq. 3.14). The error is evaluated at the beginning of the run and a correction term is then added during the calculation of the pressure gradient in *sigma* coordinates. The error formulation can be defined as the difference between the pressure gradient in z and *sigma* coordinates:

$$\epsilon(x,\sigma) = \frac{\partial b^*}{\partial x^*} - \left(\frac{\partial b}{\partial x} - \frac{\sigma}{H}\frac{\partial H}{\partial x}\frac{\partial b}{\partial \sigma} \right) \tag{3.14}$$

where $b = \rho g/\rho_0$ is the buoyancy

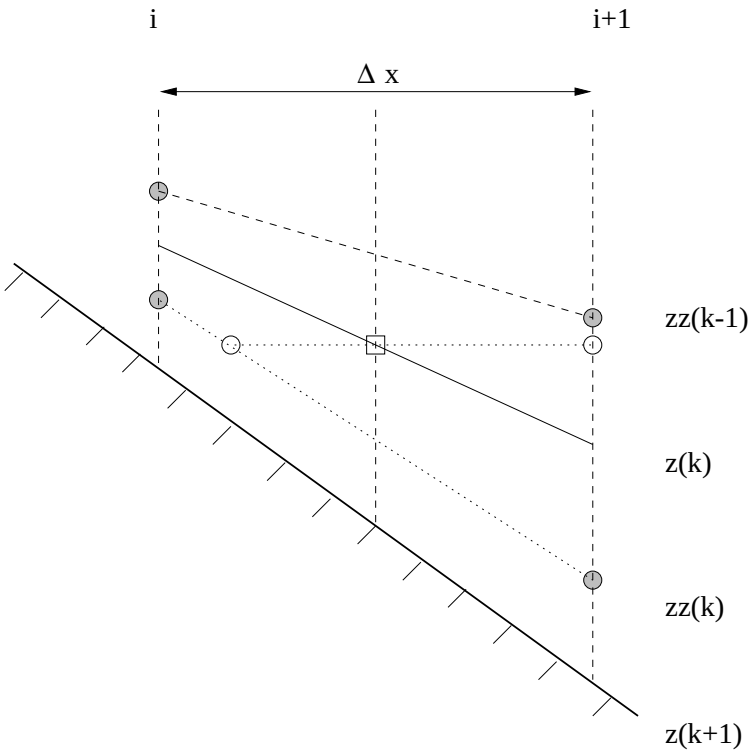

Figure 3.9: *Diagram of the pressure gradient calculation when interpolation is used. The gray circles represent θ, S or ρ points, unfilled circles represent the points resulting from the interpolation along dotted lines and density gradients are denoted by squares. The z levels represent the sigma layers, where z(k+1) is the bottom topography.*

In the case here, a similar procedure was adopted, but with two modifications. The first is that the error was allowed to vary in time, being recalculated every 10 days. Second, for regions where the left side point could not be obtained by vertical interpolation, the formulation from Fortunato and Baptista (1996) was adopted and an interpolation between adjacent bottom points was performed (Fig. 3.9).

3.2.6 The Forcing Fields

As noted, the initial thermohaline structure and the prescribed integrated velocities and elevation at the boundaries, come from the OCCAM model. Wind stress for the regional model is obtained from Trenberth et al. (1989) rather than Siefridt and Barnier (1993) (both data sets use ECMWF winds), since the first is based on a longer data set (monthly means from 1980 to 1989) and would be more representative of climatological values (Fig. 3.10). Heat and salt fluxes are those described in Chapter 2 (Fig. 2.3). All

data sets mentioned above are represented by monthly averages, where Trenberth et al. (1989) has a grid resolution of 2.5° × 2.5° and da Silva et al. (1994) and Josey et al. (1996) have grid resolutions of 0.5° × 0.5° and 1° × 1° respectively.

Horizontal interpolation and extrapolation of these fields onto the regional model grid was achieved using a technique of objective analyses similar to that adopted by Levitus (1982). The value for a field variable for each grid point (G_{ij}) is computed as the sum of a first guess (F_{ij}) and a correction term (C_{ij}), where a search radius criteria (R) is used to select points of the data set. The interpolated results were obtained from 4 successive iterations, with decreasing search radius. Sensitivity tests have shown that the smallest search radius (R_0) should not be less than 1.5 times the grid resolution of data set. The first iteration had a $7R_0$ search radius, decreasing to $5R_0$, $3R_0$ and finally R_0. Now let r be the distance between a given s-th data set grid point (i_s, j_s), (i, j) the point to be interpolated/extrapolated and n the number of points found within a certain search radius R. The equations for the interpolation can then be defined by:

$$G_{ij} = F_{ij} + C_{ij} \tag{3.15}$$

$$C_{ij} = \frac{\sum_{a=1}^{n} W_s Q_{i_s,j_s}}{\sum_{a=1}^{n} W_s}, \text{ where } W_s = e^{-4r^2/R^2} \tag{3.16}$$

$$Q_{ij} = O_{ij} - F_{ij} \tag{3.17}$$

At the first iteration, F_{ij} in Eqs. (3.15) and (3.17) is set to zero and G_{ij} is calculated only based on C_{ij}, where O_{ij} represents the original raw point of the data set. After that, F_{ij} in Eq. (3.17) is set equal to the value of G_{ij} from Eq. (3.15) calculated at the previous iteration.

To ensure that the net OCCAM transports are conserved along the regional model boundaries, a function of transport per length rather than depth-averaged velocity was interpolated. The values of depth-averaged velocity along the regional model boundaries were then obtained by dividing this function by the local depth.

For the three-dimensional thermohaline fields, the interpolation was first done for the horizontal POM grid and then a spline interpolation was made onto the *sigma* coordinate.

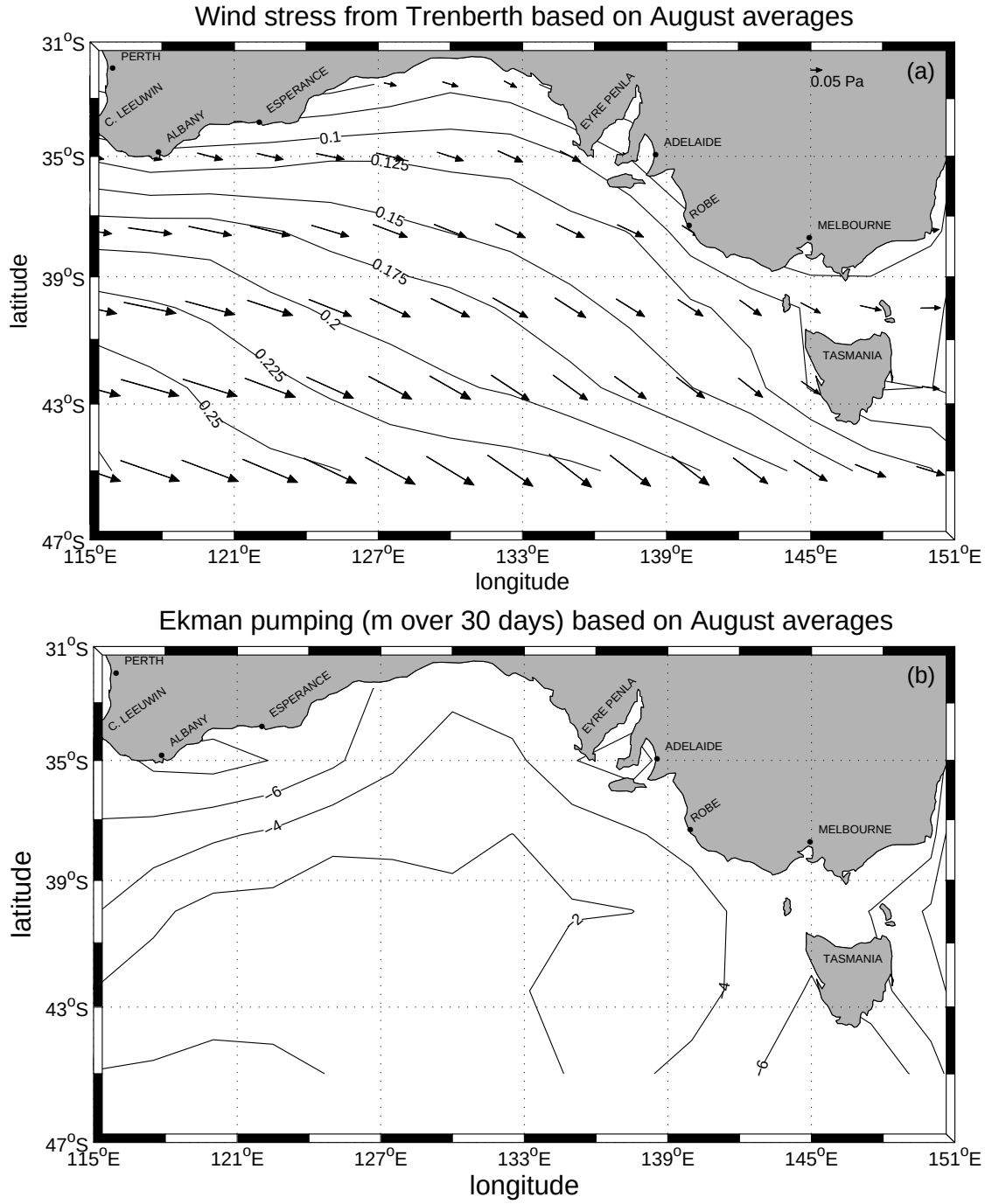

Figure 3.10: *(a) Monthly averaged wind stress field for August based on ECMWF from Trenberth et al. (1989) climatology. Contour lines represent the magnitude of the wind stress in intervals of 0.025 Pa. (b) Curl of the wind, here represented as the displacement due to Ekman pumping velocity over a period of 30 days. The contour interval is 2 m.*

The Brunt-Väisälä (N^2) frequency was calculated for all points. Where the vertical profiles of temperature and salinity combined resulted in negative static stability, these fields were adjusted to neutral static stability.

Results from the nested model are expected to differ from those obtained with OCCAM since: (1) the resolution is higher; (2) the forcing functions differ slightly from those used in OCCAM and (3) the bathymetry is more accurate. Since these difference are likely to be confined to the top 400 m or so, the temperature and salinity fields of the nested model were relaxed towards the OCCAM values (T_0, S_0) by inclusion of the Newtonian terms (Oey and Chen, 1992a) in the equations for temperature and salinity,

$$\begin{aligned} \frac{d}{dt}[T,S] &= \gamma([T_0,S_0]-[T,S]) \\ \text{where} \qquad \gamma &= \frac{1-e^{z/500}}{8.6\times 10^5} \end{aligned} \tag{3.18}$$

is equal to $1/(22$ days) at depth of 400 m and zero at the surface. Thus, the near surface fields are free to evolve away from the initial OCCAM values, while those at depth are always nudged towards the OCCAM climatology.

The surface fluxes of heat, salt and density are presented in Fig. 2.3 and the initial three-dimensional thermohaline fields will be presented in Chapter 4.

To avoid the generation of spurious inertial oscillations, the boundary forcings, surface forcing fields and gradients of temperature and salinity were ramped in from zero over a period of 5 inertial days. Since the main interest is on sub-inertial frequencies, the output from the model was also averaged over 2 days (*e.g.* Thompson, 1983) prior to presentation.

3.2.7 Proposed Experiments and Data Analysis

Although the analysis of the results discussed on Chapter 4 will be determined from a basic experiment, several parameters will be varied and the result discussed in Chapters 5 and 6 in order to evaluate the sensitivity of the model. The parameters include the

effects of heat and salt fluxes, the influence of CTW and tides through bottom stress enhancement and the effect of stronger winds. Table 3.1 summarises the experiments.

experiment	Parameters		
	winds	H and E-P fluxes	Bottom friction
basic-case	ECMWF clim - Aug (Fig. 3.10)	no	quadratic
1	ECMWF clim - Aug (Fig. 3.10)	yes	quadratic
2	ECMWF clim - Aug (Fig. 3.10)	no	CTW/tides
3	ECMWF(1988) - Jun (Fig. 6.9)	no	quadratic
4	ECMWF(1988) - Jul (Fig. 6.10)	no	quadratic

Table 3.1: *List of the different experiments to evaluate the sensitivity of the regional model.*

Chapter 4

Shelf-Slope Circulation: the Basic Experiment

The results for the nested regional model (basic experiment) are analysed in the following sections. First, an overview of the circulation for the entire region is provided. The main idea is to compare the regional model large-scale features with those in the OCCAM model, and to examine the small scale features which are not reproduced in OCCAM. Second, a more detailed analysis, with focus on the eastern part of the SEIO region is performed. To pursue this aim, the region is divided in two areas, (1) the South Australian region and (2) the Victoria-Tasmanian region. A description of the surface and the subsurface currents as well as the mechanism responsible for the formation of eddies along the shelf-slope region is provided.

4.1 An Overview

Before focusing on the results for the eastern SEIO, we consider first some results obtained for the entire nested model region. In particular, the results for sea level (Fig. 4.1a) indicate the development of a well defined LC in the west and EAC along the eastern Australian seaboard. The "Victorian Low" found in the OCCAM results (Fig. 4.1b) is again reproduced, while closer to the shelf, a similar pattern of eddies is also apparent. It should be noted that sea level in the nested POM, is determined by the depth-integrated divergence equation and is not at any stage set by the sea level field of the OCCAM model. Thus, the similarity of the eddy patterns in each model solution suggests that they are not the result of the numerical schemes adopted, but rather a robust feature of the circulation of the region.

Nearest to the coast, the high resolution nested solutions do differ from those of OCCAM. For the Esperance cross-section obtained from POM (Fig. 4.2), the Coastal Current (CC) is spread over a wider shelf than in OCCAM (Fig. 2.7a,b), but with a maximum current speed (20 cm s^{-1}) that is about twice that in OCCAM. The FC is similar in both cases.

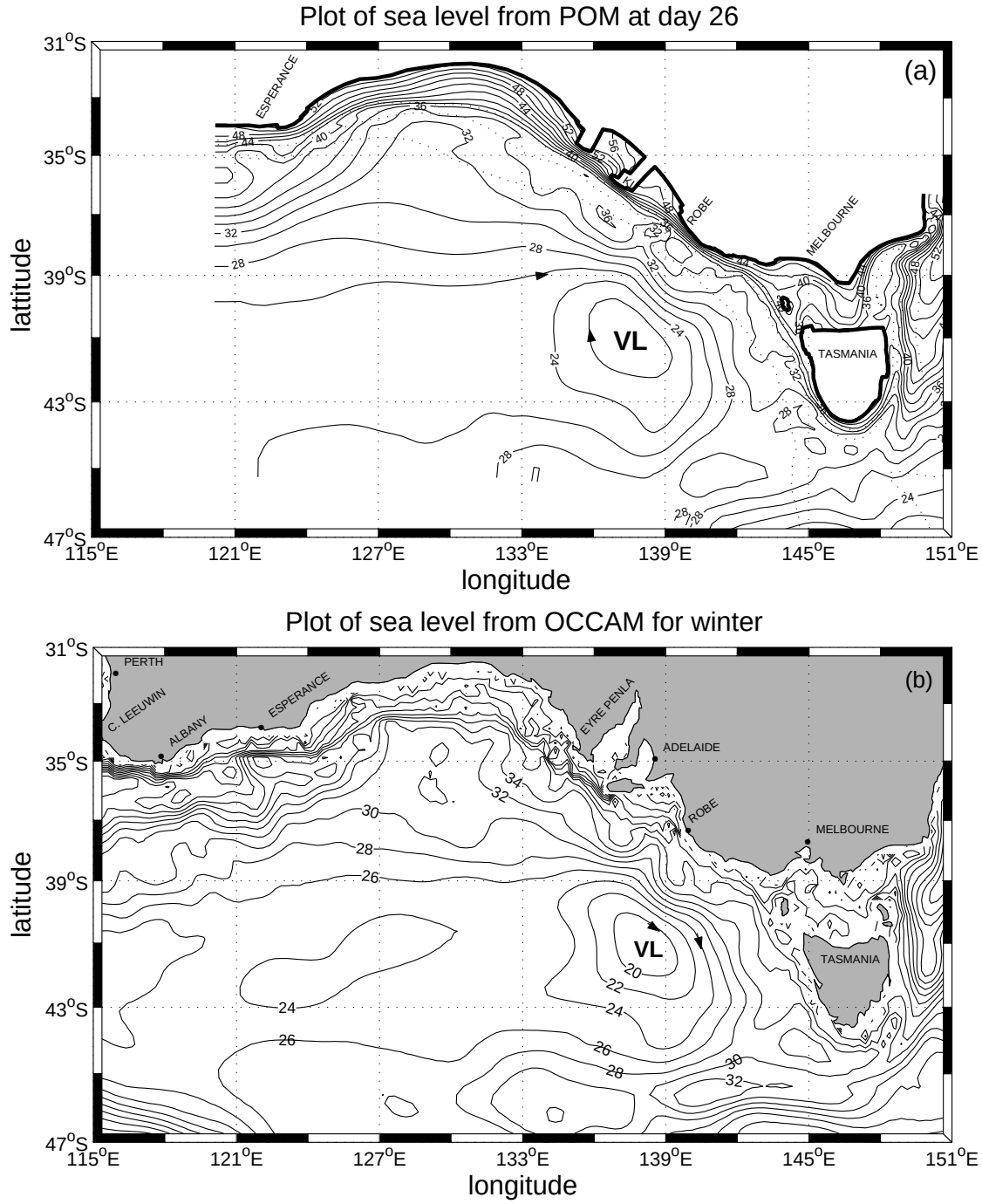

Figure 4.1: *Sea level from (a) POM and (b) OCCAM (Same as Fig. 2.20). The boundaries for POM can be seen in Fig. 3.1. The contour interval is 2 cm. The dotted lines are the 200, 1000 and 4000 m isobaths. The arrows represent the movement associated with the Victorian Low (VL).*

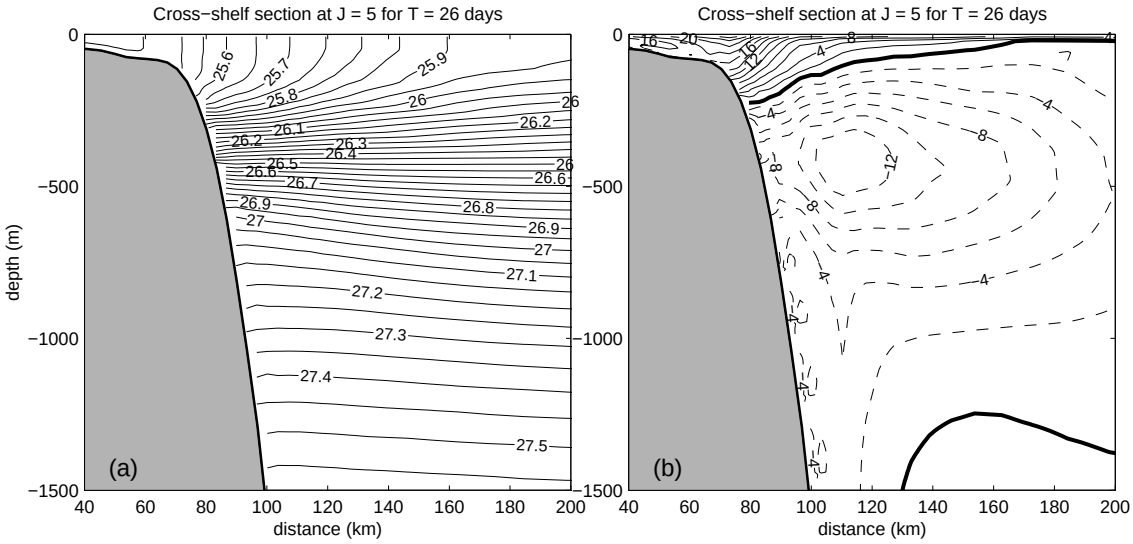

Figure 4.2: *Cross-shelf section at Esperance (J=5) for day 26. (a) The density field σ_θ (0.05 kg m^{-3} intervals). (b) The alongshore velocity (2 cm s^{-1} intervals).*

Off the southern tip of Tasmania (Fig. 4.3), the density field is similar to that in OCCAM (Fig. 2.10c,d), but the maximum value of the CC is again about twice as large (18 cm s^{-1}). The transports of the eastward flowing water (the CC) and westward flowing water (the Tasman Outflow) were determined and are presented in Fig. 4.4. Note that to be definite, the transport of the CC will be defined to be the waters between the coast and the 500 m isobath. With this definition, the results in Fig. 4.4 show the transport of the CC to be about 1 Sv at day 56.

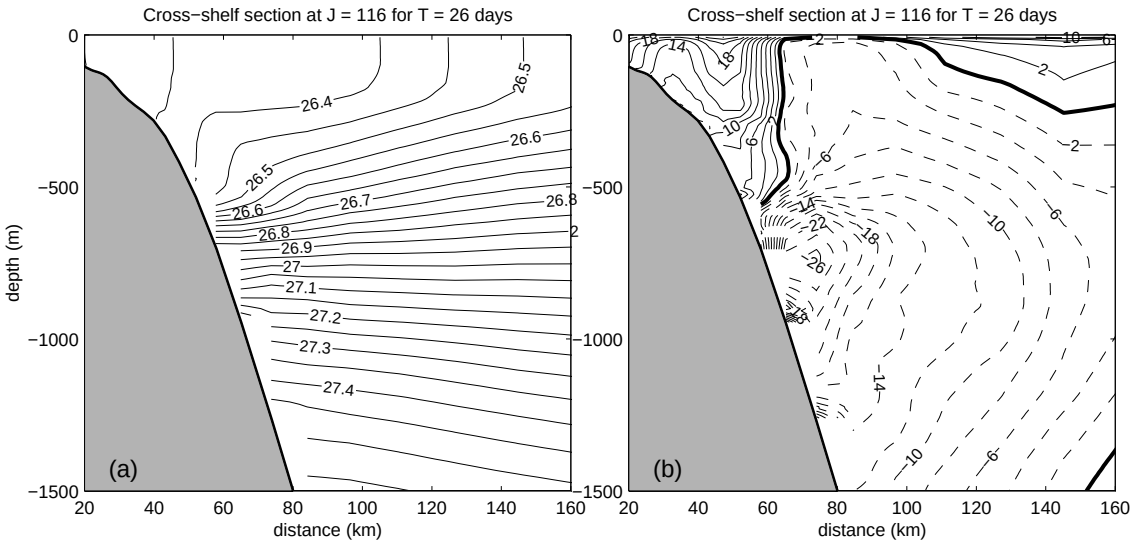

Figure 4.3: *Same as Fig. 4.2, but at the southern tip of Tasmania (J=116).*

The transport associated with the Tasman Outflow is about 16 Sv and in good agreement with the geostrophic calculations of Tomczak et al. (2000) and Rintoul and Sokolov (1999).

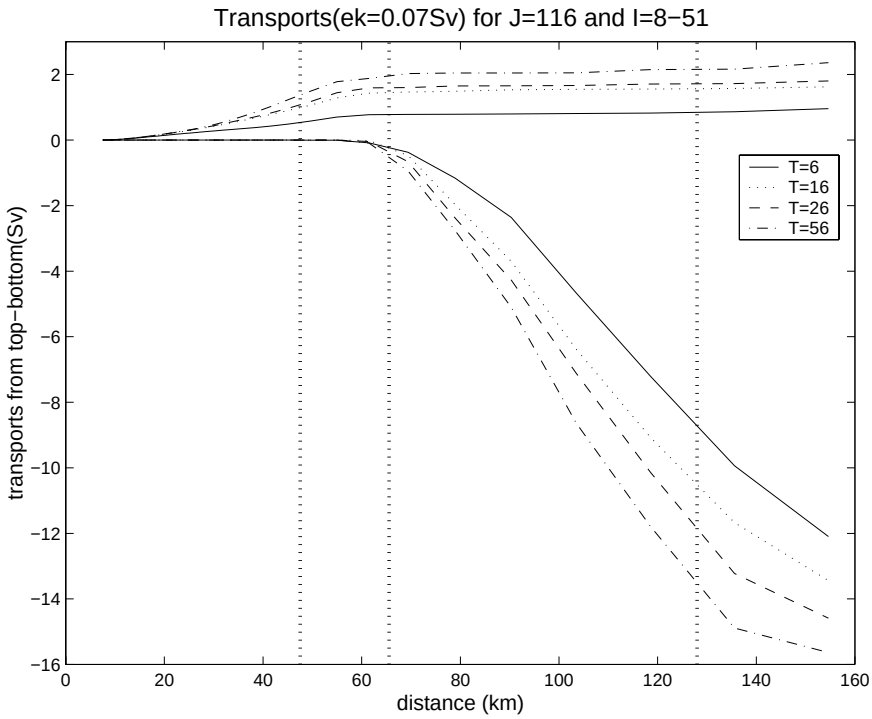

Figure 4.4: *Accumulated transports along the cross-shelf section at the southern tip of Tasmania (J=116 in Fig. 4.15). The different lines shown in the legend are for day 6, 16, 26 and 56. The dotted lines along the distance axes represent the position of the 500, 1000 and 2800 m isobaths.*

4.2 The Eastern SEIO

The results for sea level and depth-averaged velocities at day 6 and 26 are shown in Figs. 4.5 and 4.6. By day 6, the generally onshore Ekman flux (Fig. 4.7) results in a coastal rise in sea level of about 12 cm (relative to that over the 2000 m isobath) and over most of the domain. The rise in coastal sea level is consistent with observations for the region (see Fig. 6.12). The sea level field near the coast changes a little after day 6, since it is largely set-up by the first mode CTW which takes approximately 6 days to propagate from Cape Leeuwin to the west coast of Tasmania (*e.g.* Middleton and Cirano, 1999)(Appendix A). Results below show that the coastal waters (depth $<$ 100 m) are generally well mixed and thermal wind shear is negligible.

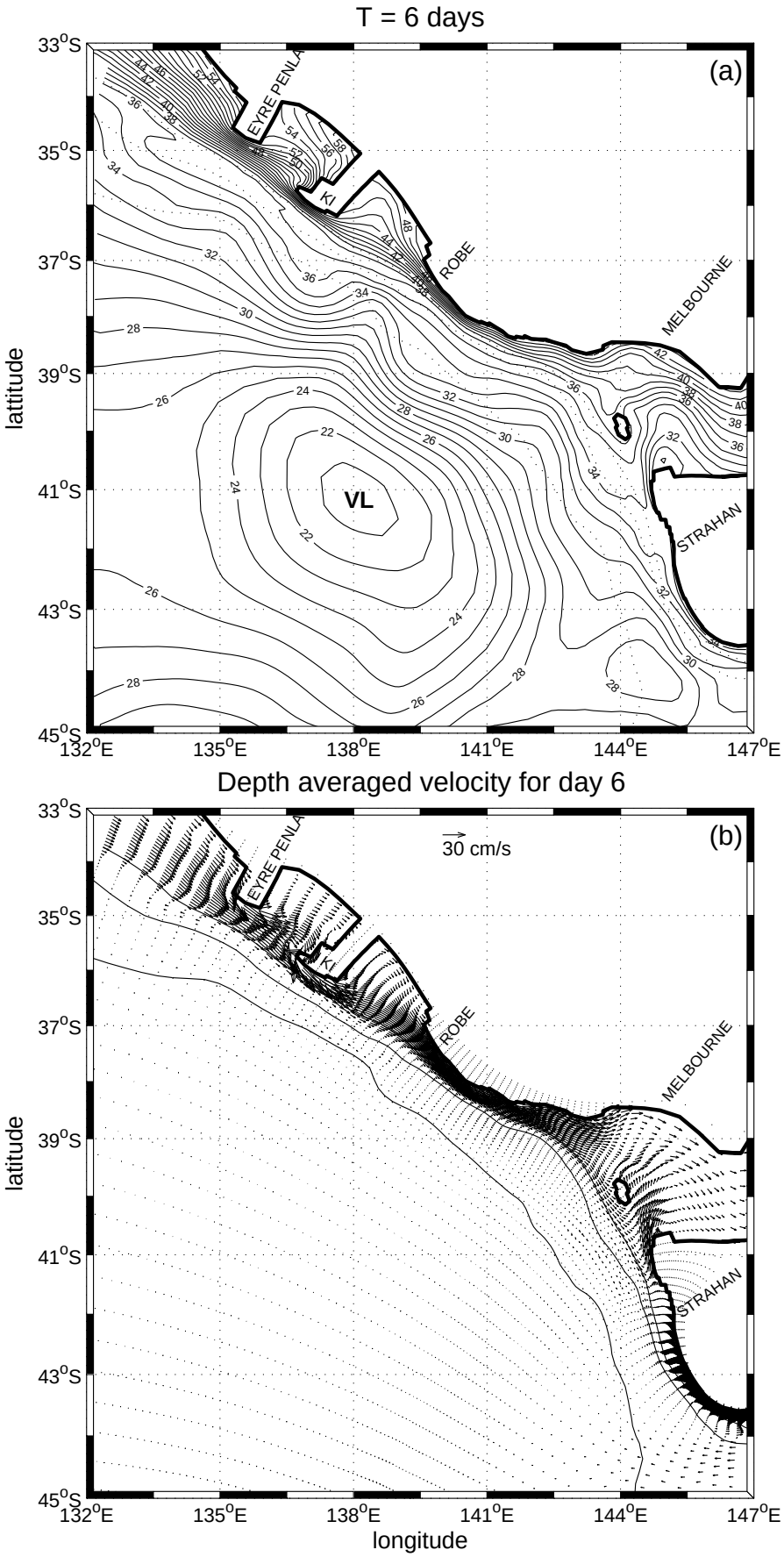

Figure 4.5: *(a) Sea level and (b) depth-averaged velocity for the eastern SEIO at day 6. The contour interval for (a) is 2 cm. Dotted (a) and solid lines (b) are the 200, 1000 and 4000 m isobaths.*

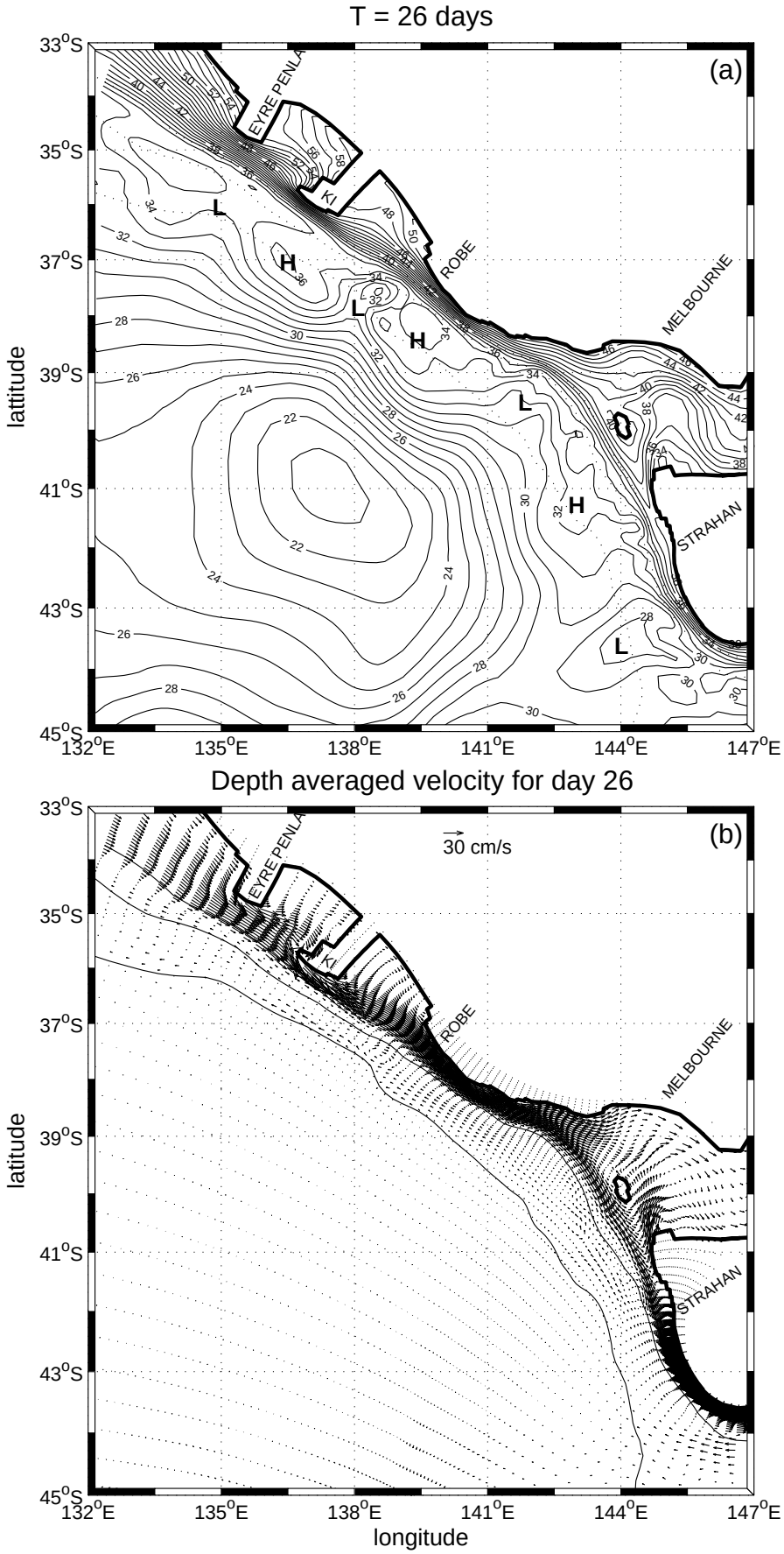

Figure 4.6: *Same as Fig. 4.5, but at day 26.*

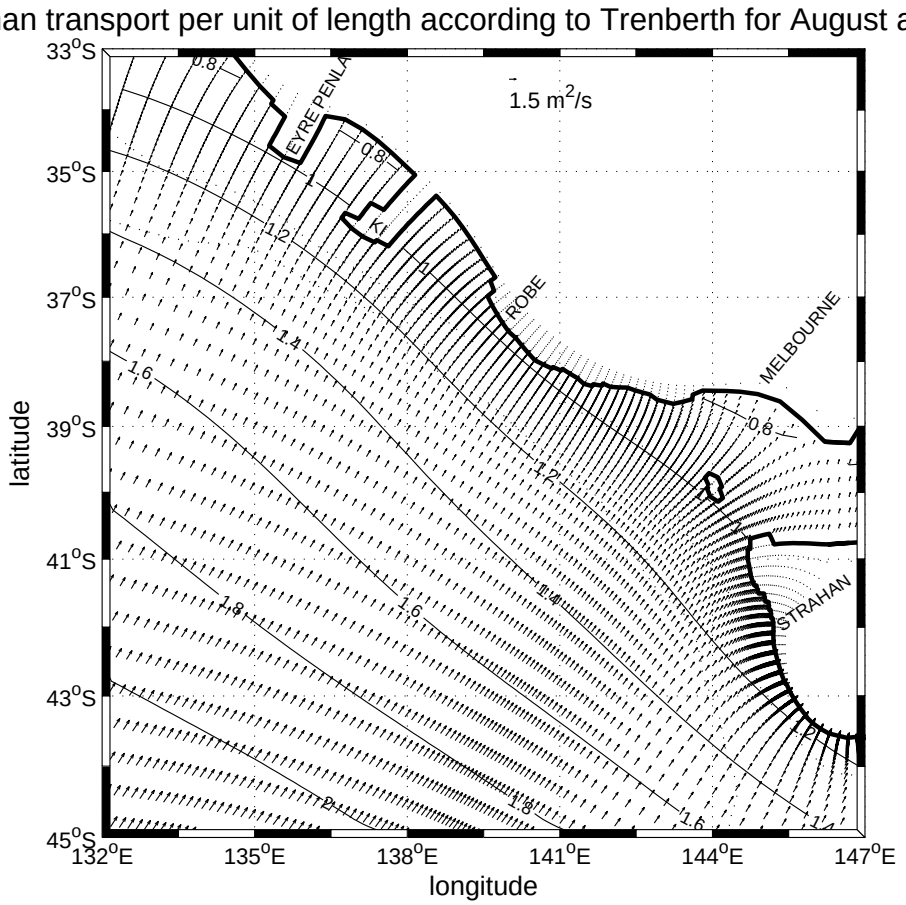

Figure 4.7: *Ekman transport per unit of length for the eastern SEIO according to the wind field in Fig. 3.10a. Dotted lines are the 1000 and 4000 m isobaths.*

The alongshore velocities associated with the near coastal set-up are also reasonably steady after about day 16, generally south-eastward, and largest ($\sim$ 40 cm s^{-1}) where the shelf narrows; the Eyre Peninsula, Kangaroo Is., Robe and the western coast of Tasmania (where the CC is poleward). For the Robe region, results may be compared with the wintertime means obtained from current meter data (Schahinger, 1987). The data, obtained over the 50 m and 143 m isobaths yield means of 25 cm s^{-1} and 27 cm s^{-1}, while the model results are somewhat larger, 35 cm s^{-1} and 37 cm s^{-1} respectively. Comparisons with the observations off the western coast of Tasmania will be discussed in Chapter 6.

A striking feature of the sea level results is the development of a succession of eddies over the shelf-slope, and poleward of Eyre Peninsula. The low pressure eddy off Robe, develops first, and by day 56 (Fig. 4.8) each of the eddies has a surface sea level signature of 3-4 cm and radial near surface currents of 2-3 cm s^{-1}. Off South Australia,

the alongshore wavelength of the high and low pressure eddies is about 250 km. The observations of SST shown in Fig. 2.9 would suggest eddy scales that are somewhat smaller than this.

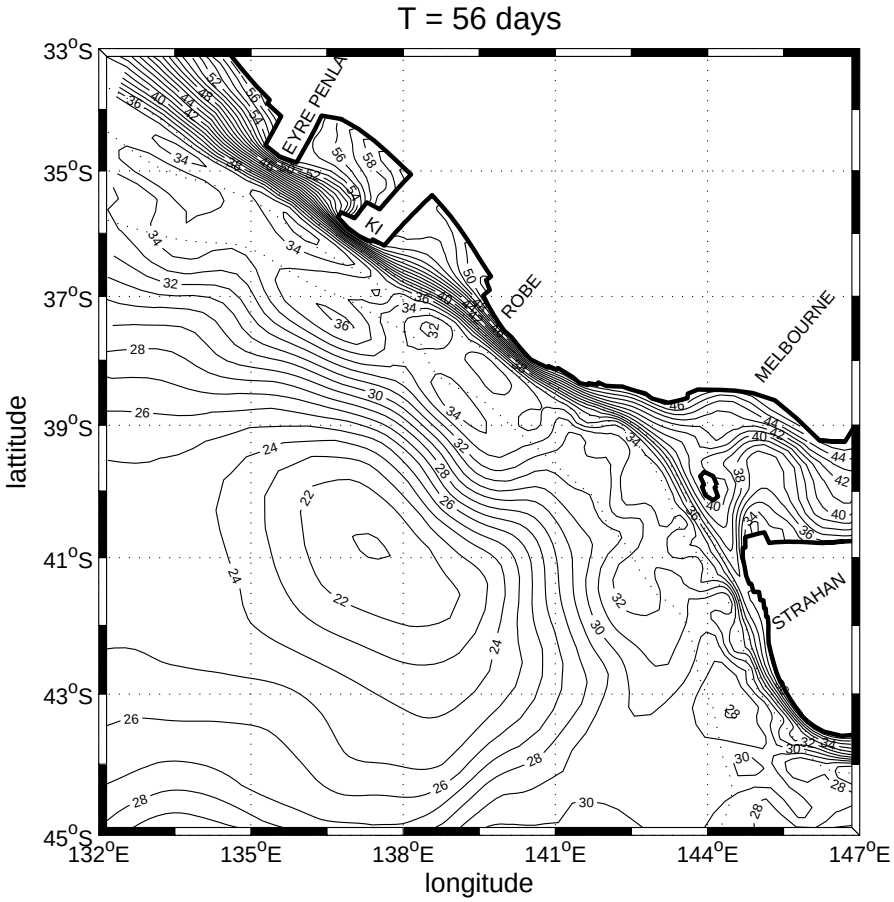

Figure 4.8: *Same as Fig. 4.5a, but at day 56.*

In the Appendix C, the idealised semi-analytical model of Gill et al. (1974) was used to show that conditions for baroclinic instability are satisfied and that unstable waves will occur at the 250 km scale and with a growth rate of 25 days: the latter is consistent with the model results found here. The fastest growing waves are however found to occur for a wavelength of 60 km. Such growing waves are not found in the model results due to the large horizontal diffusivity adopted and relatively coarse model resolution in the alongshore direction (10-20 km) (see Appendix C).

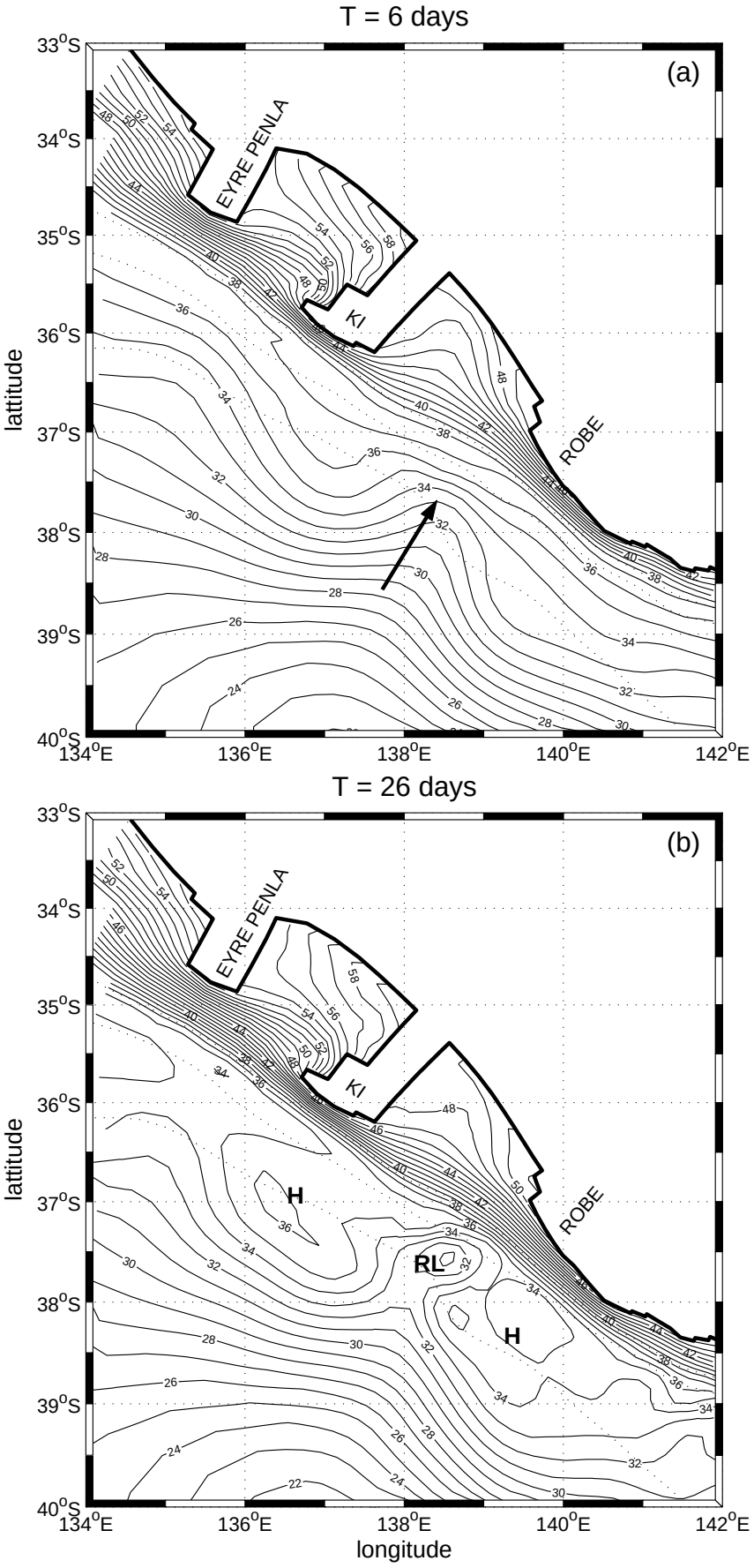

Figure 4.9: *Sea level at (a) day 6 and (b) at day 26 for the South Australian region. The contour interval is 2 cm. Dotted lines are the 200, 1000 and 4000 m isobaths.*

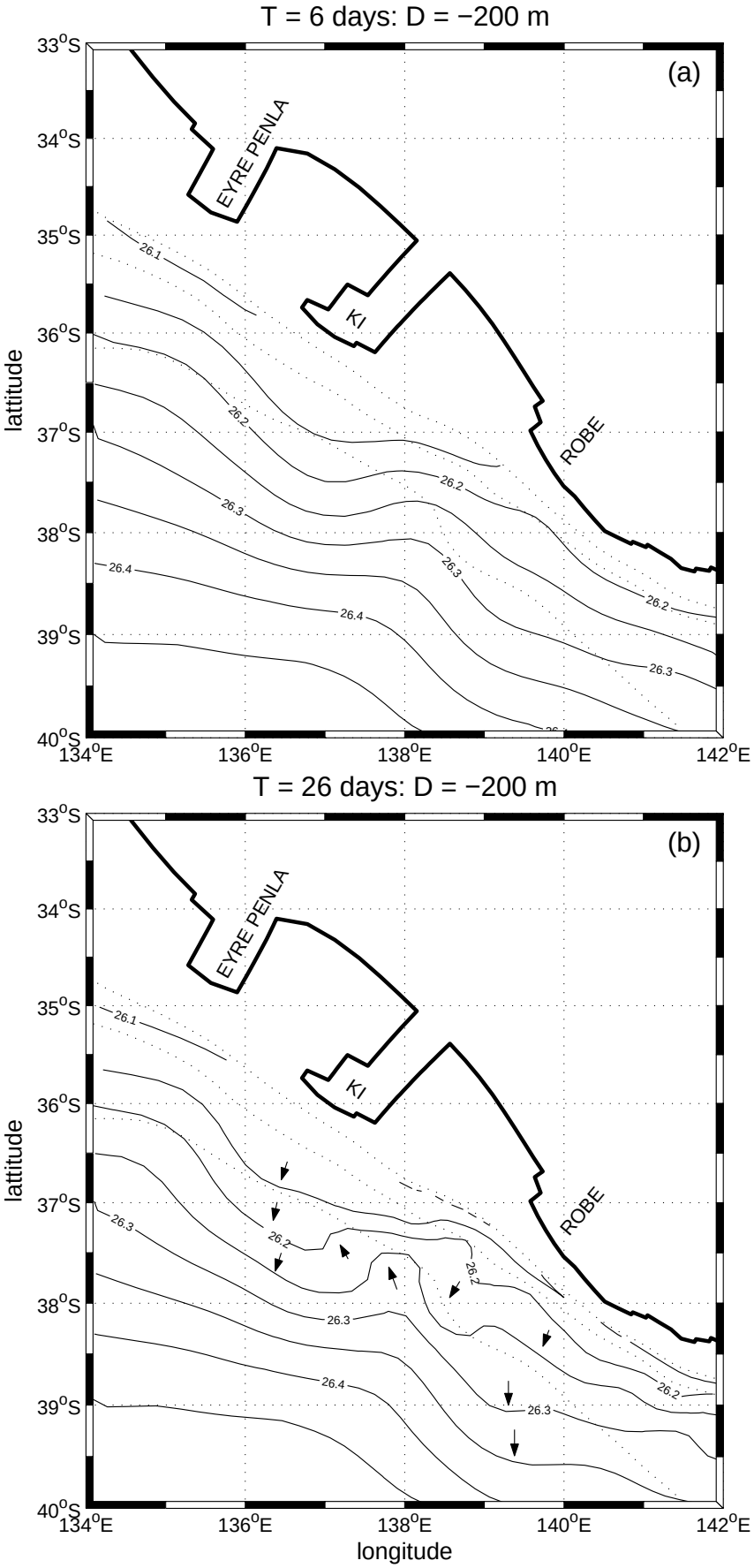

Figure 4.10: *As in Fig. 4.9 but for σ_θ at the depth of 200 m.*

4.2.1 South Australian Region

Details of the sea level and density (at 200 m) fields are presented in Figs. 4.9 and 4.10. At day 6, there is a notable offshore, and cross-isobath deflection of sea level contours south of Kangaroo Is. and Robe. Between these two sites, contours are deflected onshore, and notably near the point (indicated by the arrow in Fig. 4.9a) where the cross-shelf distance between 1000 m and 4000 m isobaths abruptly changes.

By day 26, these deflections have developed into high and low pressure eddies (Fig. 4.9b), and the cross-shelf circulation has advected the density field (depth 200 m) over some tens of kilometres (Fig. 4.10b): the arrows shown indicate the distance of advection between day 6 (Fig. 4.10a) and day 26 (Fig. 4.10b). Indeed, south of Kangaroo Is. and Robe, a southward flow is indicated.

Such offshore displacements at these sites (and depth) were inferred from wintertime observations of salinity by Godfrey et al. (1986). Their results shown here in Fig. 4.11 are remarkably similar in scale and pattern to those found for density in the model results (Fig. 4.10b). The mechanism for the offshore displacements was suggested by Godfrey et al. (1986) to result from the seaward crowding of the alongshore current by the narrowing shelf. Such crowding is evident in the model results off Kangaroo Is. and Robe, where the south-eastward CC reaches amplitudes of 40 cm s^{-1} (Fig. 4.12b).

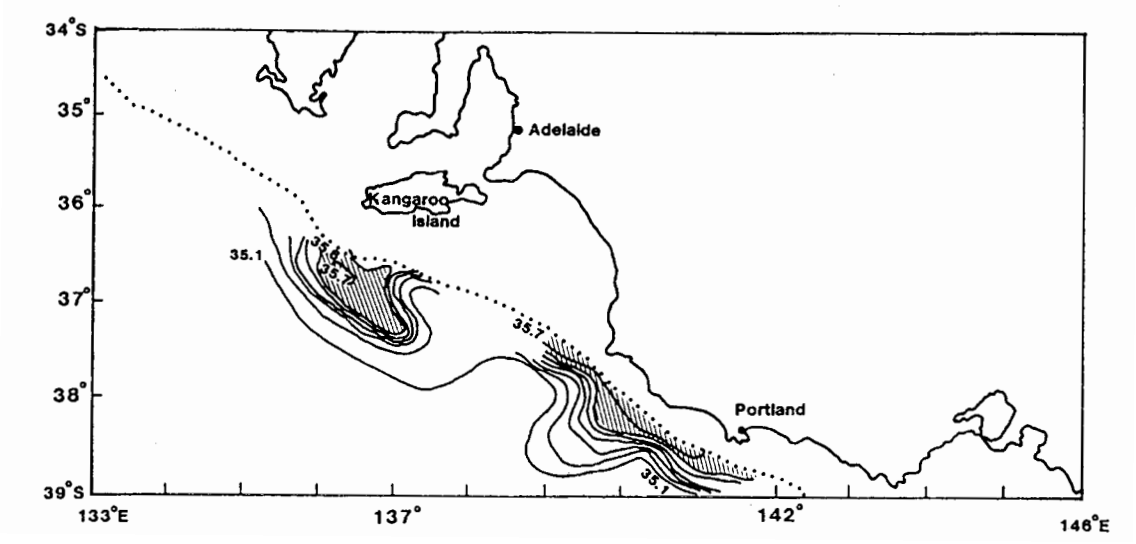

Figure 4.11: *Salinity contours at the depth of 200 m for a June-July 1982 cruise. Extracted from Godfrey et al. (1986). The dotted line is the 200 m isobath.*

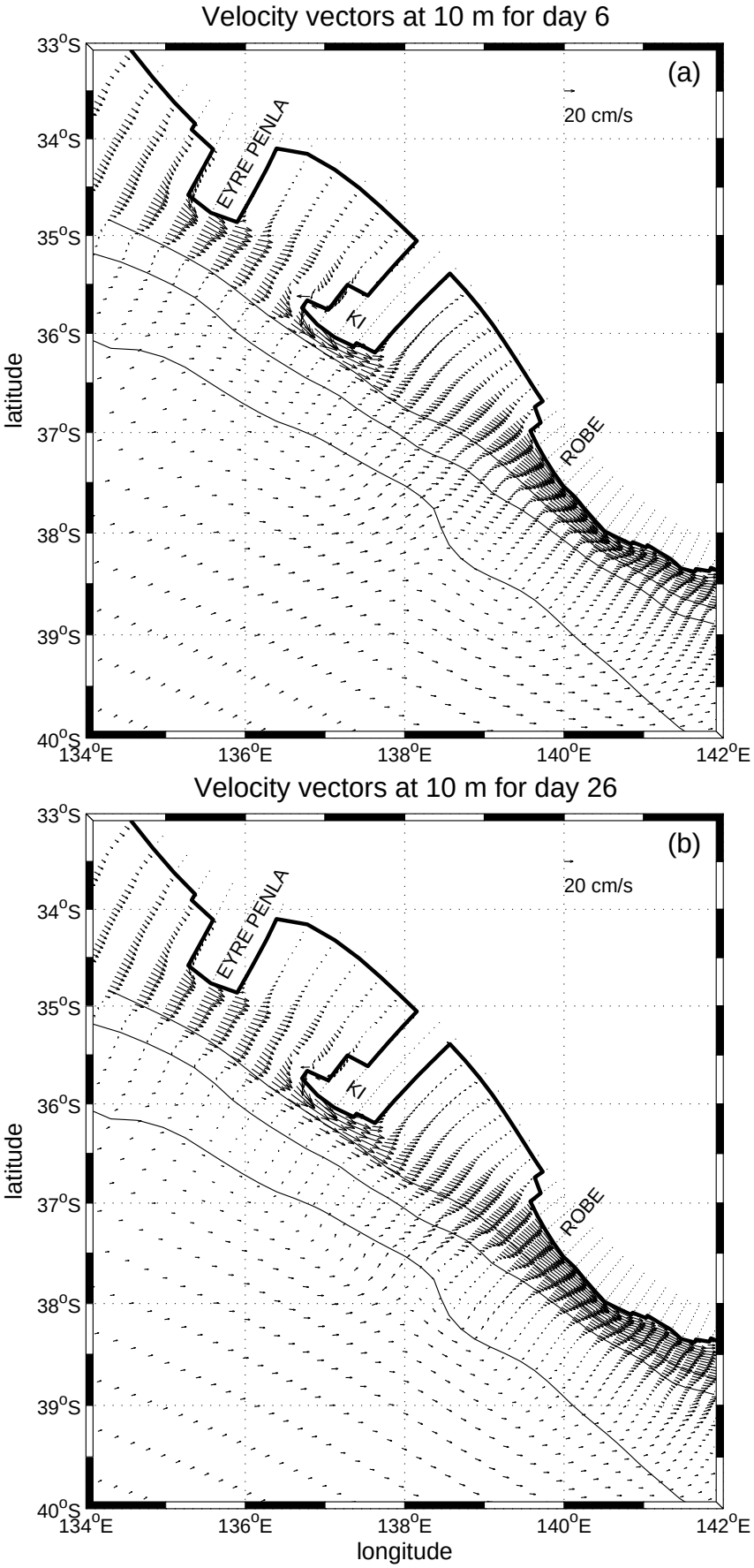

Figure 4.12: *As in Fig. 4.9 but for the velocity field at the depth of 10 m. Solid lines are the 200, 1000 and 4000 m isobaths.*

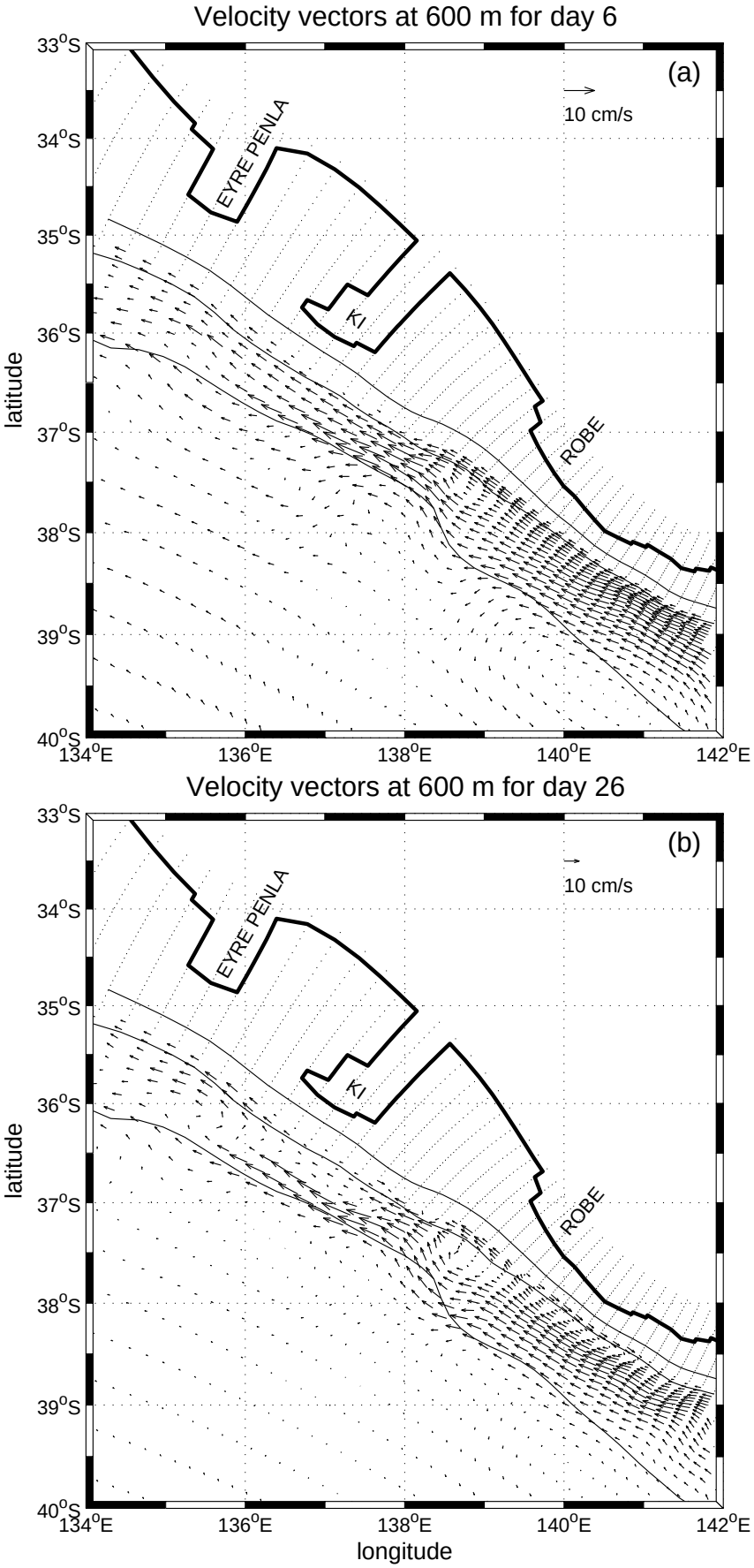

Figure 4.13: *Same as Fig. 4.12, but at the depth of 600 m.*

The onshore component of the near-surface flow associated with the "Robe Low" reaches magnitudes of up to 20 cm s^{-1} over the 1000 m isobath (Fig. 4.12b). The cause of this onshore deflection is thought to be related to changes in the shelf topography. Indeed, at the depth of 600 m, the slope currents have amplitudes of 10 cm s^{-1} and are generally north-westward (Fig. 4.13), forming part of the FC discussed earlier. However, below the Robe Low, the FC becomes directed into deeper water at the point where the shelf-slope narrows, and then turns back onshore and towards the slope. The overshoot into deeper water will result in vortex stretching and the production of cyclonic vorticity, and may explain the cyclonic deflection of the currents back onshore. Moreover, the production of cyclonic vorticity should act to amplify the growth of the Robe Low.

Now consider results for the cross-shelf section off Kangaroo Is. (J=40 in Fig. 4.15) shown in Fig. 4.14 for day 6 and 26. At day 6, the density field is similar to that interpolated from OCCAM, and the isopycnals slope down towards the shelf at depths less than 600 m. The alongshore velocity field is in close geostrophic balance with the sea level and density field. Currents are south-eastward in the top 400 m (Fig. 4.14c), with amplitudes up to 50 cm s^{-1} near the coast. The thermal wind shear associated with the downwelled isopycnals reverses this current below 400 m. The slight upwelling at depths below 400 m in turn reduces the magnitude of the FC.

Consistent with the results, the cross-shore flow below the Ekman layer and in the top 500 m is directed offshore (Fig. 4.14e). Moreover, the offshore flow here is directed towards isopycnal surfaces that slope up and converge away from the coast (Fig. 4.14a). There will thus be a tendency of vortex squashing, the production of anticyclonic vorticity and the growth of the high should be enhanced.

Indeed, such growth is evident in the cross-sectional results for day 26 (Fig. 4.14b). In the top 400 m, the isopycnal field has flattened out indicating that potential energy has been released. Below the high ($x \sim 260$ km), the cross-shelf currents converge (Fig. 4.14f), sea level is raised and the alongshore north-westward current doubles in magnitude to a maximum of 12 cm s^{-1} (Fig. 4.14d).

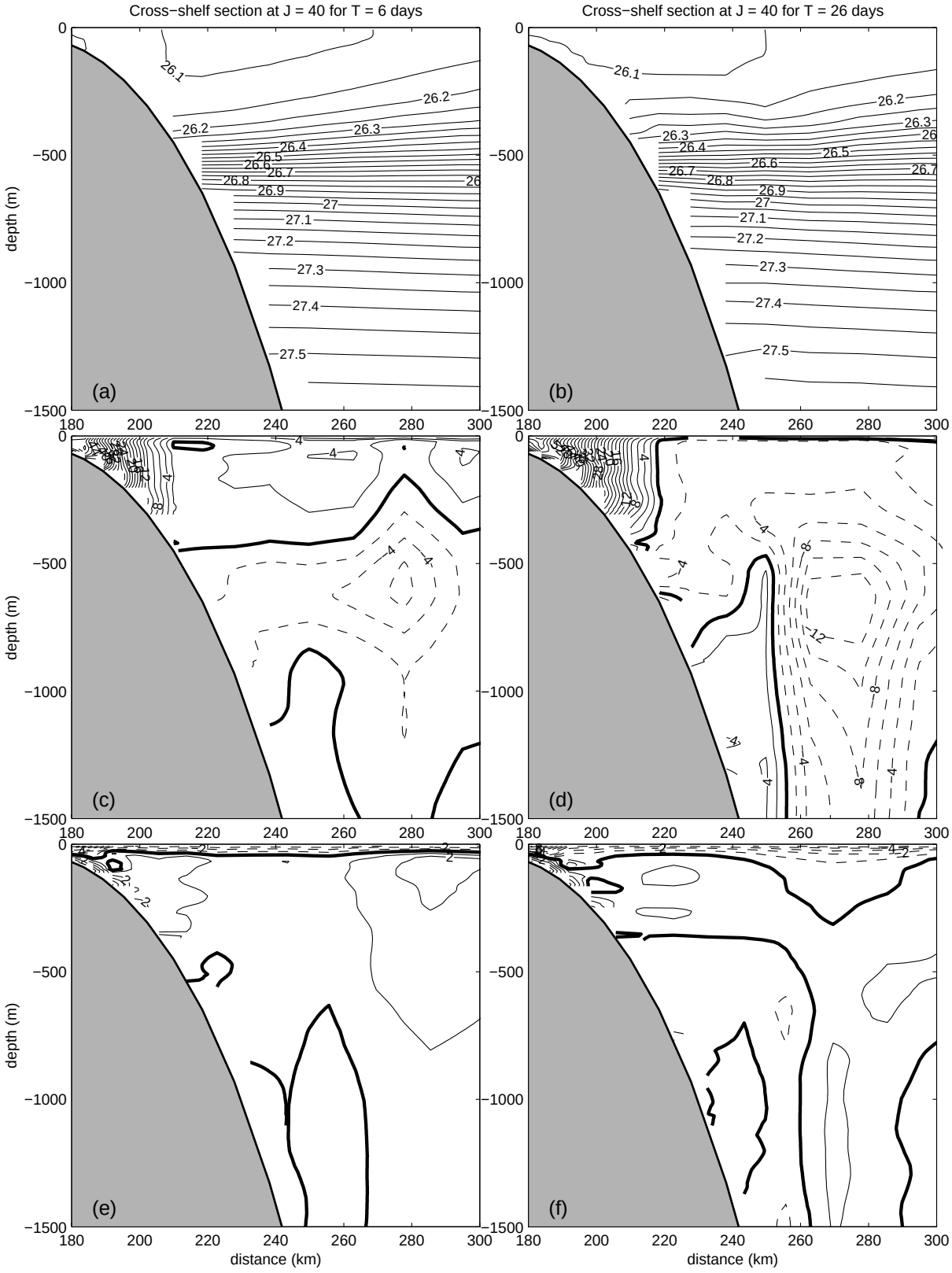

Figure 4.14: *Cross-shelf section off Kangaroo Is. (J=40 in Fig. 4.15) for day 6 and 26. (a) and (b) The density field σ_θ (0.05 kg m^{-3} intervals). (c) and (d) The alongshore velocity (2 cm s^{-1} intervals), where positive values represent south-eastward flow. (e) and (f) The cross-shore velocity (1 cm s^{-1} intervals), where positive values represent offshore flow.*

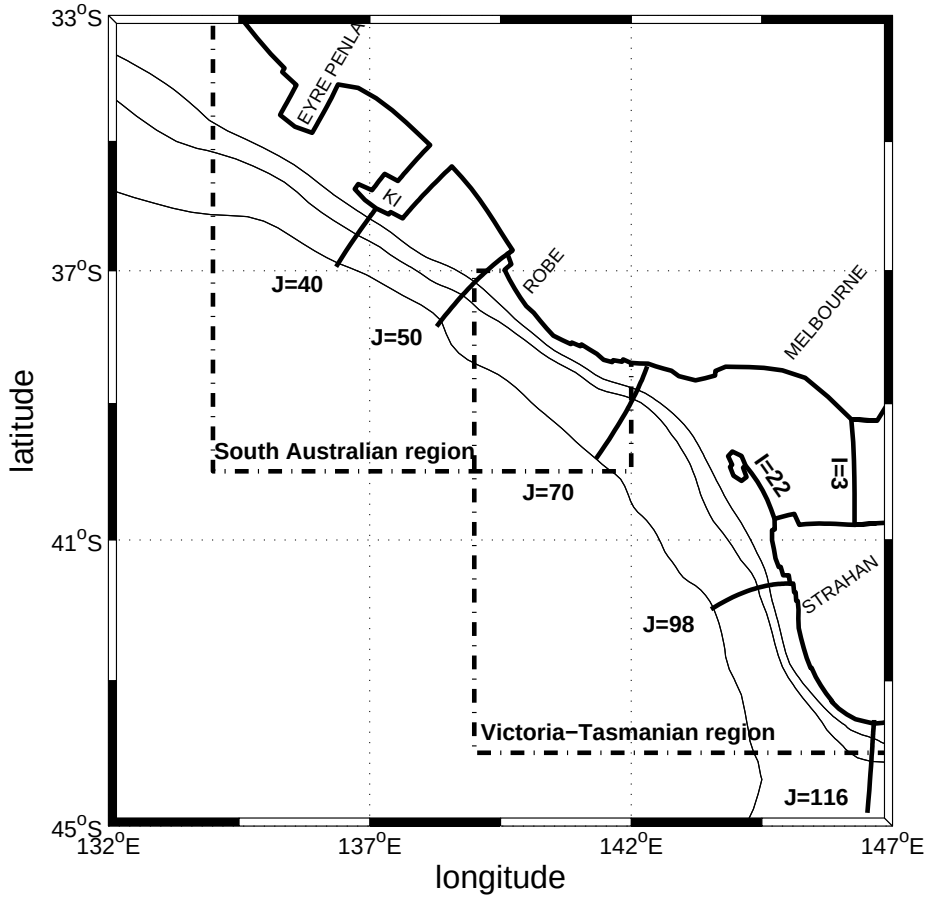

Figure 4.15: *Map illustrating the cross-shelf sections for the eastern SEIO. Solid lines are the 200, 1000 and 4000 m isobaths.*

Now let us consider cross-shelf results for the section through the Robe Low (J=50 in Fig. 4.9). At day 6, the density and alongshore current fields (Fig. 4.16a,c) are similar to that found of Kangaroo Is., although the cross-shelf current in the top 400 m is onshore (Fig. 4.16e), and directed towards isopycnal surfaces that diverge towards the coast. Vortex stretching and enhanced growth of the Robe Low should then result. Such stretching will be enhanced by that which results from the local overshoot of the FC into deeper water.

By day 26, the density field in the top 400 m and offshore of the 1000 m isobath has flattened somewhat (Fig. 4.16b), although the pattern of displacement and cross-shelf velocity (Fig. 4.16f) indicate a region of divergence below the Robe Low ($x \sim 160$ km). The alongshore current associated with the eddy is about 10 cm s^{-1} (Fig. 4.16d).

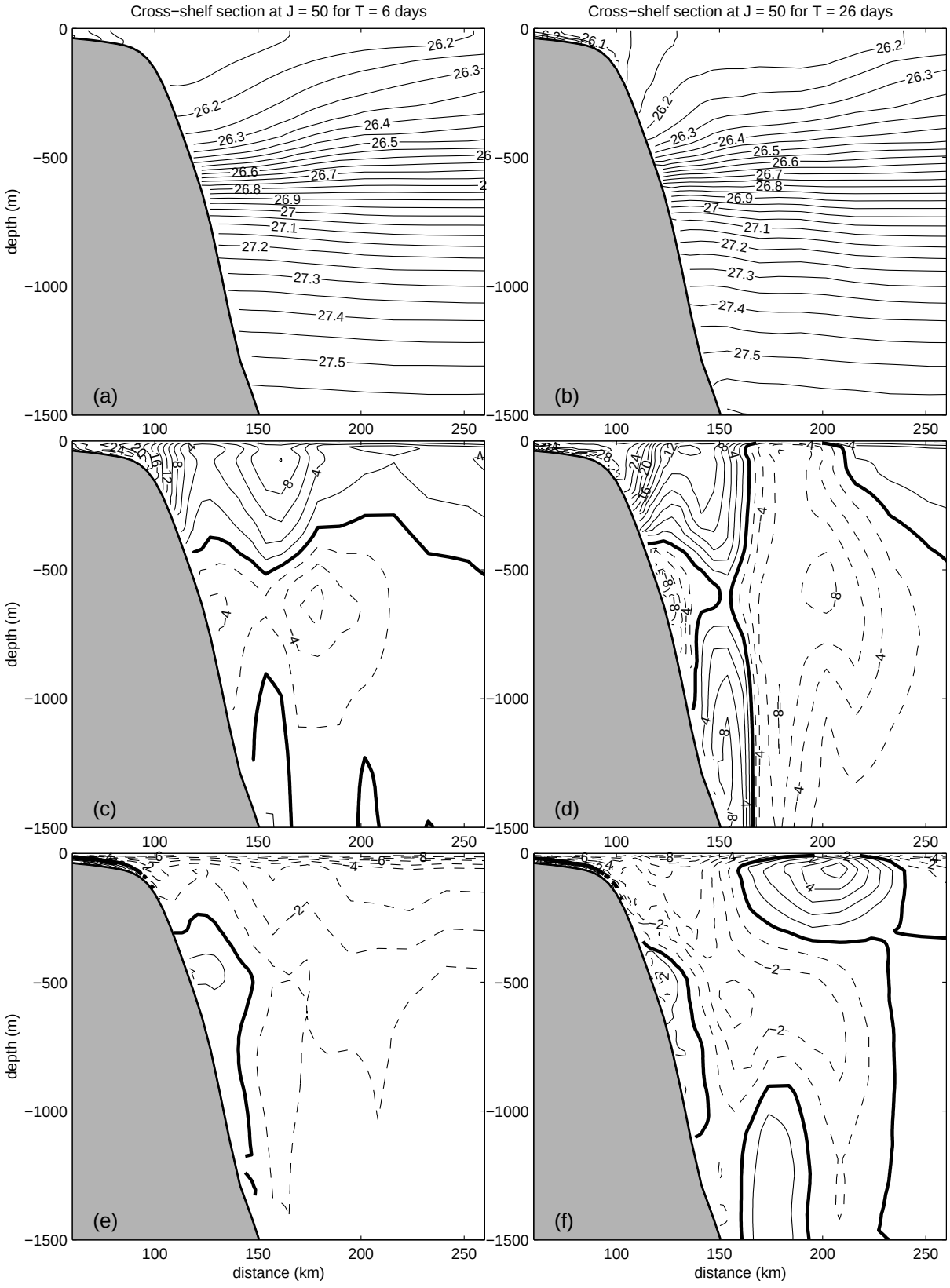

Figure 4.16: *Same as Fig. 4.14, but for the section off Robe (J=50 in Fig. 4.15).*

In summary, the results above (and Appendix C) suggest that the eddies are the result of baroclinic instability with a preferred wavelength of 250 km (growth rate of 25 days), that is set by the interactions of the shelf flow with changes in the shelf topography. Off Kangaroo Is. and Robe, the narrower shelf results in an offshore displacement, and vortex squashing and the production of anticyclonic vorticity (the highs). Between these two regions, the north-westward FC encounters a narrowing shelf-slope and the resultant vortex stretching leads to the production of cyclonic vorticity and the intense low.

Transport Analysis

An analysis of the depth-integrated transports for the region between Kangaroo Is. and Robe is presented, so as to ascertain the overall strength of the south-eastward and north-westward alongshore currents and how they change with time. The transports were calculated so as to encompass the Kangaroo Is. high and the Robe Low (Fig. 4.17). The alongshore section O1 transects these eddies, and approximately lies over the 4000 m isobath.

At day 6 (Fig. 4.17a), the south-eastward transport through sections C1 and C2 is 3.1 Sv: see the 2th column in Fig. 4.17a. The south-eastward transports farther offshore through sections C3 and C4 are about 0.8 Sv or 1/4 of that through C1 and C2. The reason for this is that most of the south-eastward transport is confined to lie inshore of the 500 m isobath (Fig. 4.16c).

The north-westward transports at day 6 (Fig. 4.17a, first column) are similar in magnitude through sections (C1 and C3) and (C2 and C4): a total of about 2.5 Sv is transported by the FC.

The strength of the initial meander in sea level shown in Fig. 4.17 is illustrated by the relatively large on/offshore transports through O1 of 3.3 Sv and 3.8 Sv respectively: note if the onshore Ekman transport of 0.4 is subtracted from the latter, the values on/offshore are nearly equal and about 3.4 Sv. Farther offshore, the transports through O2 are smaller reflecting the diminished offshore importance of the initial meander.

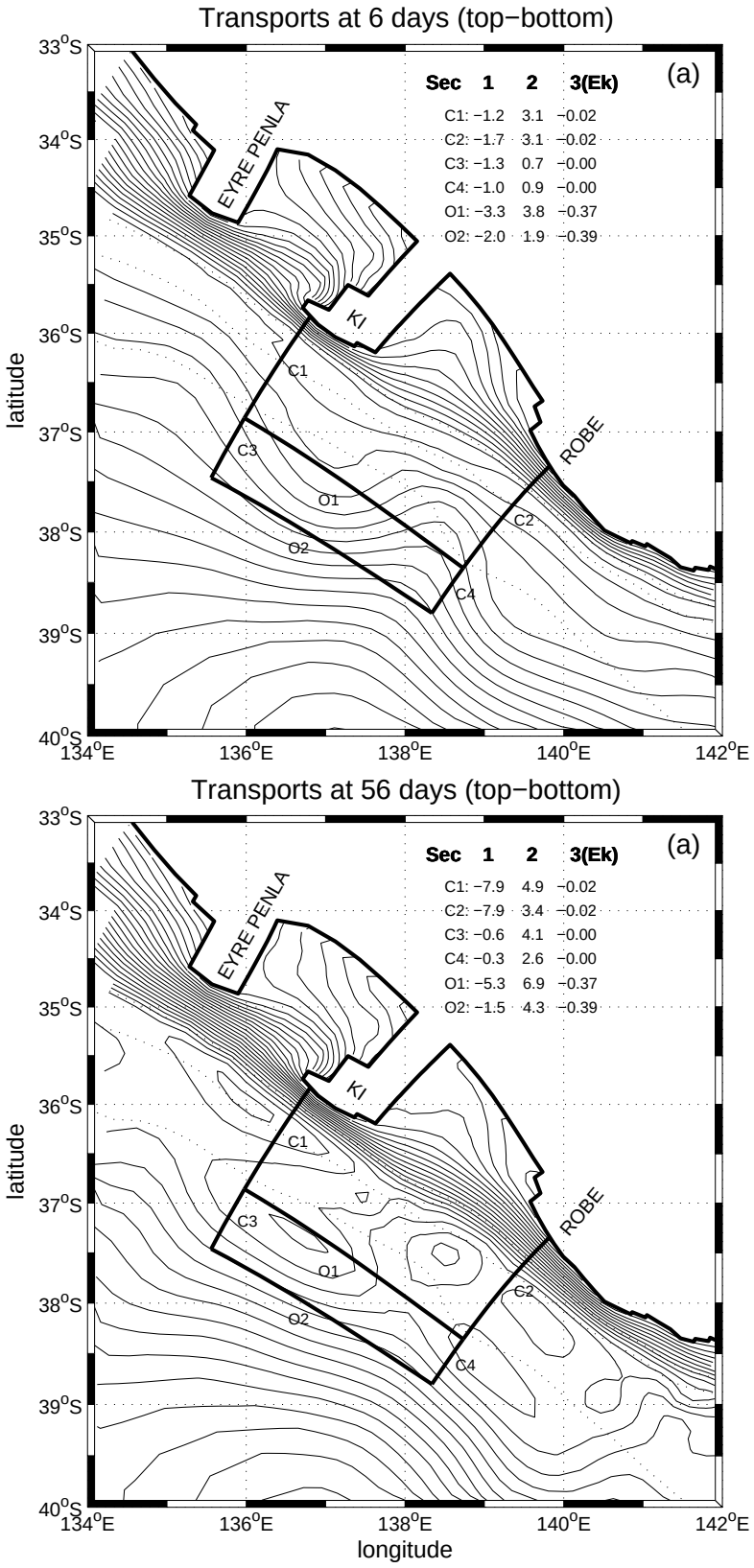

Figure 4.17: *Depth-integrated transport (Sv) for the South Australian region for the cross-shore and alongshore sections. The first column (positive values) represents south-eastward (C1-C4) and offshore (O1-O2) flows. The second column is the opposite flow. The third column is the associated Ekman transport for each section. (a) at day 6 and (b) at day 56. Dotted lines are the 200, 1000 and 4000 m isobaths.*

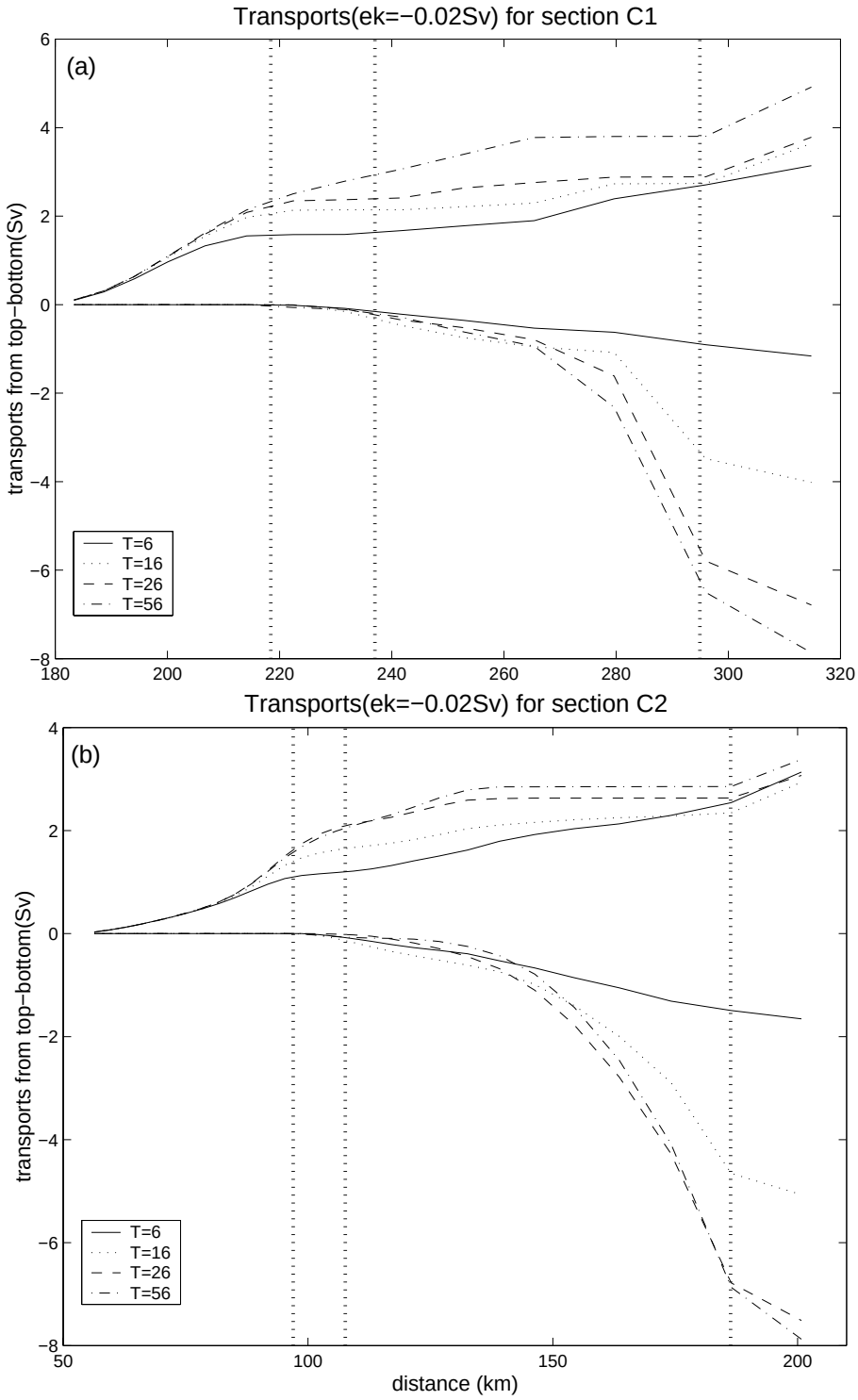

Figure 4.18: *Accumulated transports along cross-shore sections from Fig. 4.17. The different lines shown in the legend are for day 6, 16, 26 and 56. The dotted lines along the offshore x axis and from left to right, represent the position of the 500, 1000 and 4000 m isobaths. (a) Section C1 and (b) section C2. Positive (negative) values of transport represent south-eastward (north-westward) flow.*

The temporal evolution of the transports through C1 and C2 is illustrated in Fig. 4.18, where results for the alongshore transports are shown as an accumulating function of the offshore (x axis) distance.

Results for both sections are similar (Fig. 4.18). For the south-eastward transports (positive curves in Fig. 4.18), the net transport inshore of the 500 m isobath (first vertical dotted line), changes little from 2 Sv after day 16. To be definite, the south-eastward transport at inshore of the 500 m isobath will be taken to represent that associated with the CC. Farther offshore, and by day 56, an additional 2 Sv is found to flow south-eastward. This is probably due to the larger scale circulation of the Victorian Low that lies to the south.

The north-westward transport associated with the FC increases from 1 Sv at day 6 to nearly 8 Sv at day 56: most of the transport occurs offshore of the 1000 m isobath.

The increase in transport is reflected in the results shown in Fig. 4.17. By day 56, the south-eastward transports through sections C1 and C2 increase by 60% and 10% respectively, the former a result of the intensified Kangaroo Is. high. However farther offshore, the increase in south-eastward transports is larger, particularly through section C3. The increase here is ascribed to slight intensification and reorientation of the Victorian Low, which also results in a reduction and increase in the on/offshore transport through section O2 between day 6 and 56.

In summary, the south-eastward transport of the CC changes little after day 16 and is about 2 Sv or five times the onshore Ekman transport. The north-westward transport increases rapidly after day 6 to a near steady value of about 8 Sv by day 26. The south-eastward transport does increase farther offshore due to the combined effects of the growing eddies and reorientation of the Victorian Low. The eddies themselves drive transports on/offshore that increase from about 3 to 6 Sv between day 6 and 56.

4.2.2 A Comparison with Idealised Results

The above results may be compared with the idealised downwelling results obtained by Middleton and Cirano (1999)(Appendix A). These authors assumed an f-plane and a

constant (0.1 Pa) wind blowing along a 1500 km fetch and parallel to a uniform shelf. A flat, uniform summertime stratification was adopted so as to simulate the near surface stratification expected near the coast and within the GAB and South Australia (see Fig. 2.4).

After some 30-60 days a strong alongshore westward undercurrent (UC) was found ($\leq$ 10 cm s^{-1}; $\leq$ 1 Sv; see Fig. A.4) and shown to be accelerated by alongshore gradients of sea level set-up by the onshore Ekman flux. A necessary condition for the UC was the thermal wind shear that arose from the thick ($\leq$ 70 m) Bottom Boundary Layer (BBL) near the shelf-break. Within the UC, the isopycnal field was upwelled, but only within a relatively thin BBL (Fig. A.4e).

While somewhat similar with the results here, the dynamics are quite different. In the basic case above, the transports of the UC is much larger ($\sim$ 5-8 Sv) and is driven by the onshore Sverdrup transport from the deep ocean and deep upwelling results. Moreover, the transport of the UC in the idealised study was found to grow linearly with time (Fig. A.8b) along with the thickness of the BBL. In the basic case above, the transport of the UC remains approximately steady after 26 days (Fig. 4.18).

In addition, the transport of the CC in the idealised study was shown to increase downwind, directly by the amount of surface Ekman transport that was driven by the wind (Fig. A.9). In the basic case, the CC transport of Robe at day 56 is 1.5 Sv less than that of Kangaroo Is. (C1 compared to C2 in Fig. 4.17b) despite the additional 0.4 Sv supplied within the surface Ekman layer. The difference here and in other results related to cross-shelf currents is likely to be due to the effects of the eddies and non-uniform topography.

4.2.3 Victoria-Tasmanian Region

Southeast of Robe, the presence of Bass Strait strongly influences the set-up of sea level (Fig. 4.19) and the CC (Fig. 4.20) along the west coast of Tasmania. At day 6 (Fig. 4.19a) the coastal set-up of the sea level found northwest of Bass Strait induces a poleward coastal jet of up to 40 cm s^{-1}, while off the northwest coast of Tasmania such a jet is not present (Fig. 4.20a). Instead, a relatively strong northward jet enters the strait through the passage between King Is. and Tasmania, with maximum velocities of 30 cm s^{-1} (Fig. 4.20). A poleward jet is however found over the slope after day 16 and is steady by day 26 (Fig. 4.20b).

The circulation at a depth of 600 m is illustrated in Fig. 4.21. Over the slope, the FC is strong enough to oppose the poleward flow associated with sea level but does tend to follow the wave-like pathway set by the elevation. At regions where a high is present the flow meanders offshore, turning back to the coast where a low is present.

The Effect of Bass Strait

The explanation for the jet between King Is. and Tasmania follows from a study of CTW scattering for the region (Middleton, 1991), and indeed, the solutions for sea level near Bass Strait (Fig. 4.19) are remarkably similar to the amplitude of the CTW response found by Middleton and Black (1994).

In the absence of wind-forcing, the circulation in and around the strait is determined by the fact that (1) there is no equivalent set-up of sea level on the eastern coast of Tasmania and (2) the CTWs and Kelvin waves travel with the coast on the left in the southern hemisphere.

The effect on sea level is illustrated in the schematic description of the region shown in Fig. 4.22. Sea level is taken to be zero on the eastern Tasmanian shelf. Moreover, since the set-up of sea level is achieved by the propagation of CTWs and Kelvin waves, information cannot propagate down along the east Tasmanian coast. Assuming geostrophy, $fu = -g\eta_y$, and that $u = 0$ along the western Tasmanian coast, the above implies that sea level η_0 must vanish at the southeast corner of the strait. With a geostrophic balance within the strait, $fv = g\eta_x$, sea level must also vanish along the north Tasmanian coast, since here $v = 0$. Sea level is thus zero at the southwest corner of the strait.

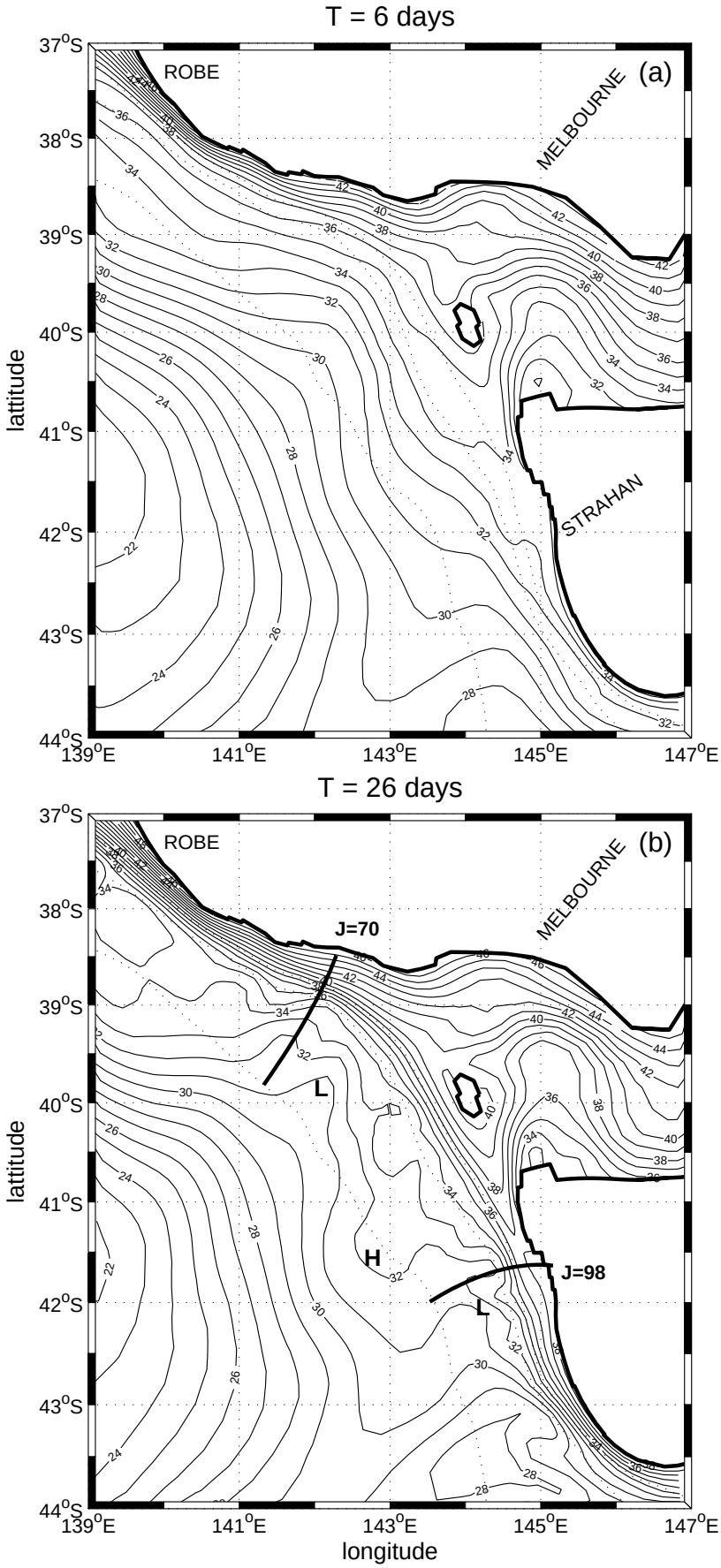

Figure 4.19: *Same as Fig. 4.9, but for the Victoria-Tasmanian region. Dotted lines are the 200, 1000 and 4000 m isobaths.*

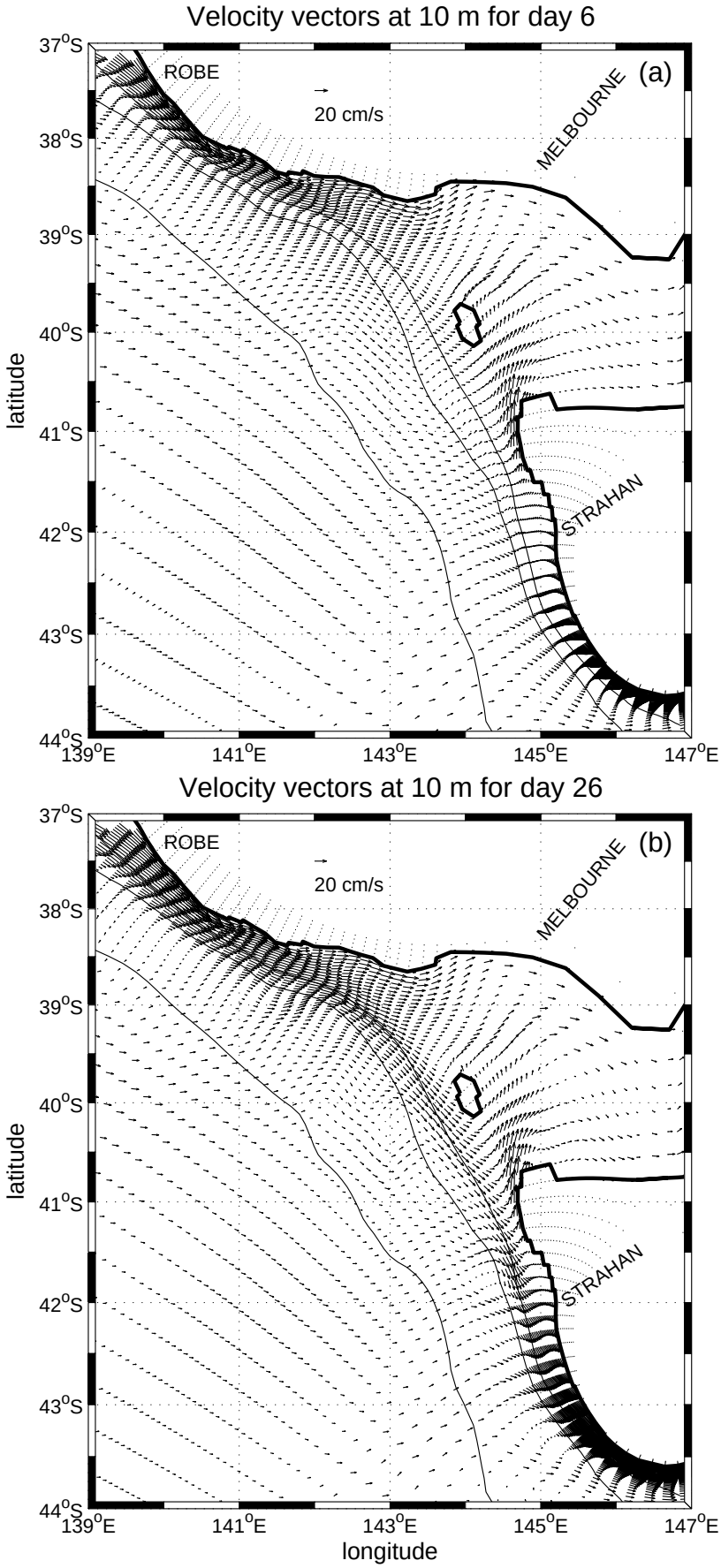

Figure 4.20: *Same as Fig. 4.12 but for the Victoria-Tasmanian region. Solid lines are the 200, 1000 and 4000 m isobaths.*

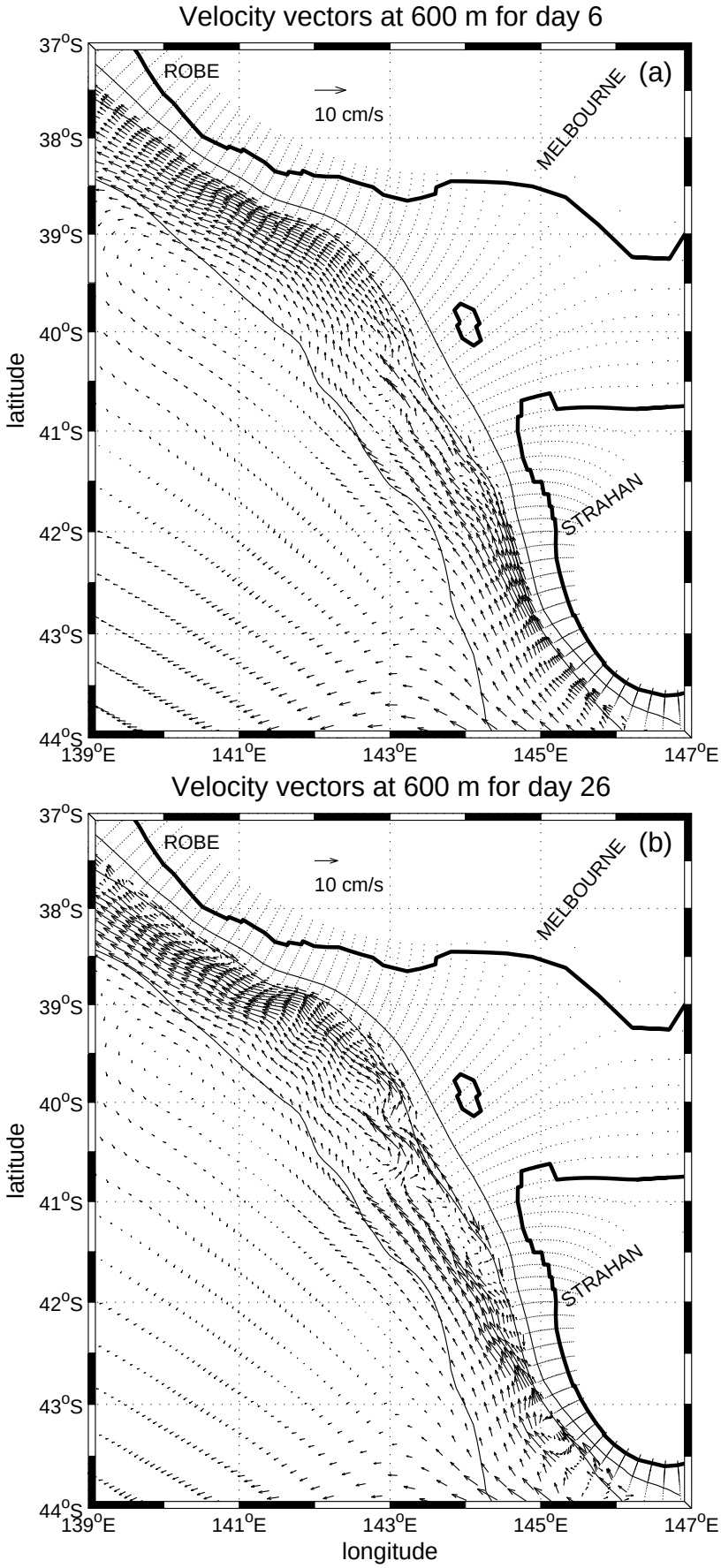

Figure 4.21: *Same as Fig. 4.20 but at 600 m.*

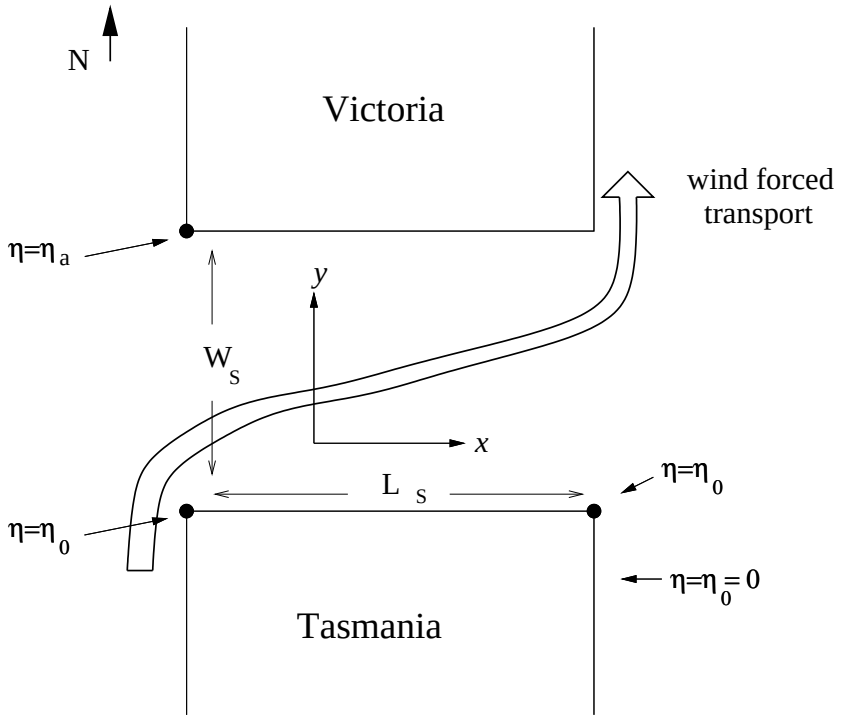

Figure 4.22: *Schematic description of the sea level adjustment at Bass Strait, where L_s and W_s are the length and width of the strait respectively.*

Part of the CC off Robe is then turned into the strait and indeed, the fraction of transport that does so is simply given by

$$H_s u W_s = -g H_s (\eta_a - \eta_0)/f \tag{4.1}$$

where $H_s \sim$ 70 m and $W_s \sim$ 200 km denote the depth and width of the strait. The dynamical process outlined above that leads to the transport estimate in Eq. (4.1) was originally examined by Garrett and Toulany (1982) and dubbed geostrophic control.

From Fig. 4.19, the sea level difference across the strait is about 14 cm, so that Eq. (4.1) above implies a transport of about 1 Sv. This estimate is almost exactly to that computed from the model solutions in Fig. 4.26.

Returning to the origin of the jet between King Is. and Tasmania, since only part of the CC flows into the strait, the remainder continues down along the western shelf. A reversal of the cross-shelf gradient of sea level must then occur between King Is. and Tasmania and this drives the jet into the strait.

Wind forcing within Bass Strait

An additional mechanism which will act to draw water into the southwest corner of the strait involves the local wind forcing within the strait. Following Middleton and Viera (1991), we consider barotropic motions without bottom drag (results are similar if bottom drag is included) and the steady equations of motion are:

$$-fv = -g\frac{\partial \eta}{\partial x} + \tau^{sx}/\rho_0 H \tag{4.2}$$

$$fu = -g\frac{\partial \eta}{\partial y} \tag{4.3}$$

Now we assume that there is no wind stress on either the west Victorian or east Tasmanian shelves, so that the level must vanish at the northwest and southeast corners of the strait. In addition, the response within the strait is assumed to be symmetric (*e.g. see* Middleton and Viera, 1991; Hannah, 1992) and $\eta(L_s, W_s) - \eta(0,0) > 0$. In this case, the net transport through the strait may be obtained from Eqs. (4.2)-(4.3) and written as

$$H_s W_s u = -\tau^{sx} L_s/(f\rho_0) \tag{4.4}$$

For the August climatology (Fig. 3.10a), $\tau^{sx} \sim 0.09$ Pa, L_s (length of the strait) $\sim$ 450 km so that the net transport is about 0.4 Sv or 40% of that estimated from the Eq. (4.4) above. The remaining 60% must come from the CC that flows along the west Victorian shelf.

Where does the wind forced transport come from? The answer again is dictated by the direction in which CTWs and information can propagate, which for the southern hemisphere is with the coast on the left. Thus, water is drawn into the strait from the shelf west of Tasmania and expelled onto the eastern shelf of Victoria as indicated by the arrow in Fig. 4.22. Thus a jet into the southwest corner of the strait results and acts in unison with that described above and which is produced by geostrophic control of the adjacent CC.

An important implication of the north-eastward jet is that frictional effects will act to slow the current so that water must be drawn from the deeper ocean farther offshore. Furthermore, the jet opposes the poleward CC and a region of divergence in the along-shore current field then occurs off the western Tasmanian shelf as illustrated by the detail of velocity field shown in Fig. 4.20b. Water drawn onshore by this process would seem to be a likely trigger for the formation of the high shown in Fig. 4.19b.

Sectional Analysis

Let us first examine a cross-shore section (J=70 in Fig. 4.15) off the northwestern region of Bass Strait, where isobaths change orientation and in the vicinity where the low in sea level is found (Fig. 4.19b). By day 6, the CC reaches velocities of 16 cm s^{-1}, while the FC is around 4 cm s^{-1} (Fig. 4.23c). Compared to the South Australian region the FC is weaker and broader (probably due to the wider slope). In the top 500 m the onshore flow (Fig. 4.23e) induces downwelling over the slope (Fig. 4.23a).

At day 26, the resulting velocity field reaches maximum poleward velocities of 26 cm s^{-1} and the FC is much broader (Fig. 4.23d). More interesting though is the increase in the onshore flow (Fig. 4.23f) below the Ekman layer. This increase is likely due to the formation of the cyclonic low (Fig. 4.19b) and can be seen in the velocity plot at the depth of 200 m (Fig. 4.25) where an offshoot of the flow is followed by an onshore flow in order to preserve potential vorticity.

The next section is off the west coast of Tasmania (J=98 in Fig. 4.15) and close to the small low shown in Fig. 4.19b. The offshore flow below 200 m and at day 6 (Fig. 4.24e) leads to the flattening of the isopycnals between day 6 (Fig. 4.24a) and day 26 (Fig. 4.24b). At day 6 a poleward CC is absent (Fig. 4.24c), since the propagation of CTWs has been slowed by the presence of the strait. However by day 26 it has grown in strength (Fig. 4.24d), with maximum poleward velocities of 20 cm s^{-1}. The presence of the eddy has generated a region of horizontal divergence at around $x \sim 120$ km where offshore currents can be up to 4 cm s^{-1} (Fig. 4.24f).

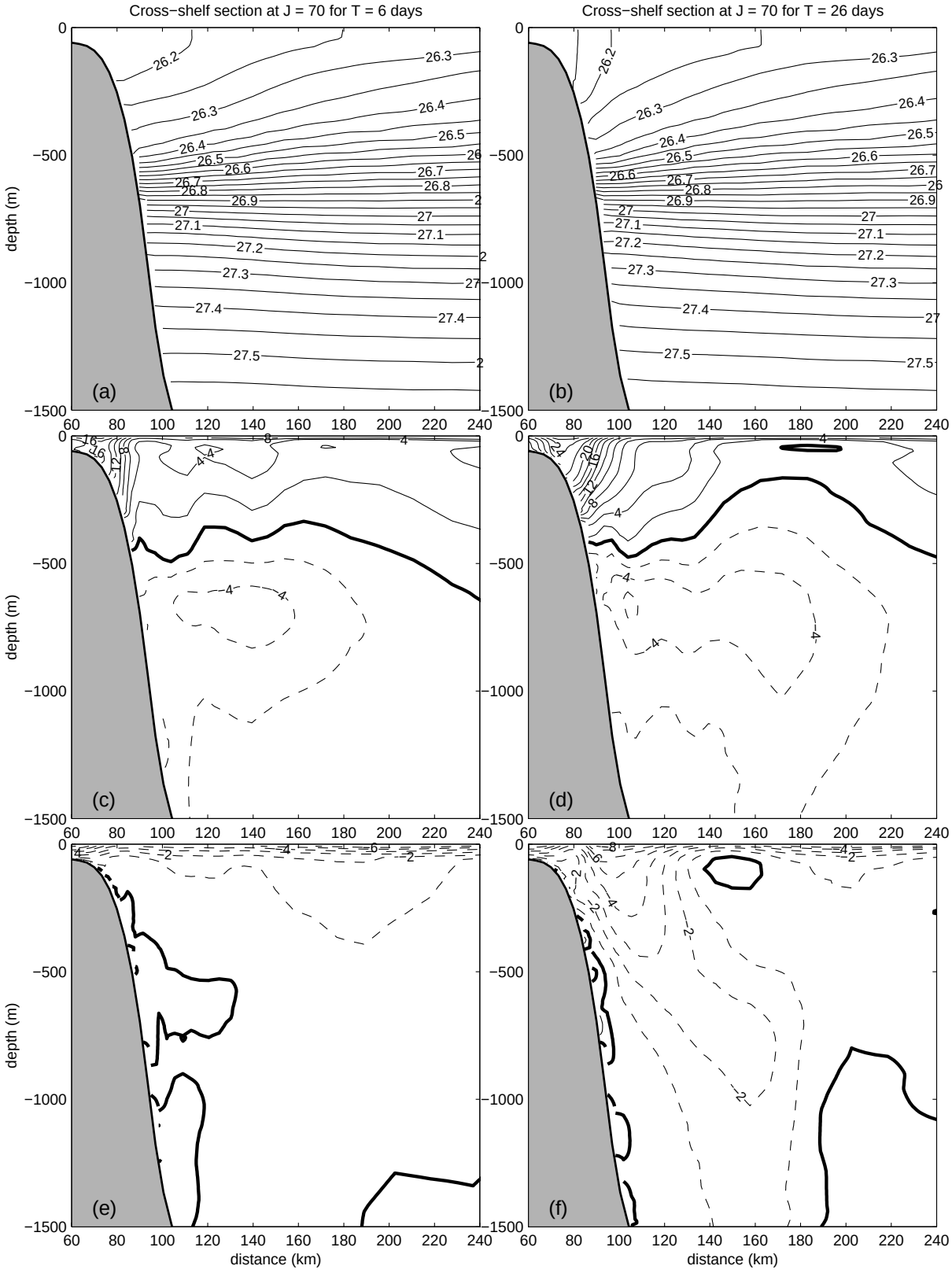

Figure 4.23: *Same as Fig. 4.14, but for the section off the Victorian coast (J=70 in Fig.4.15).*

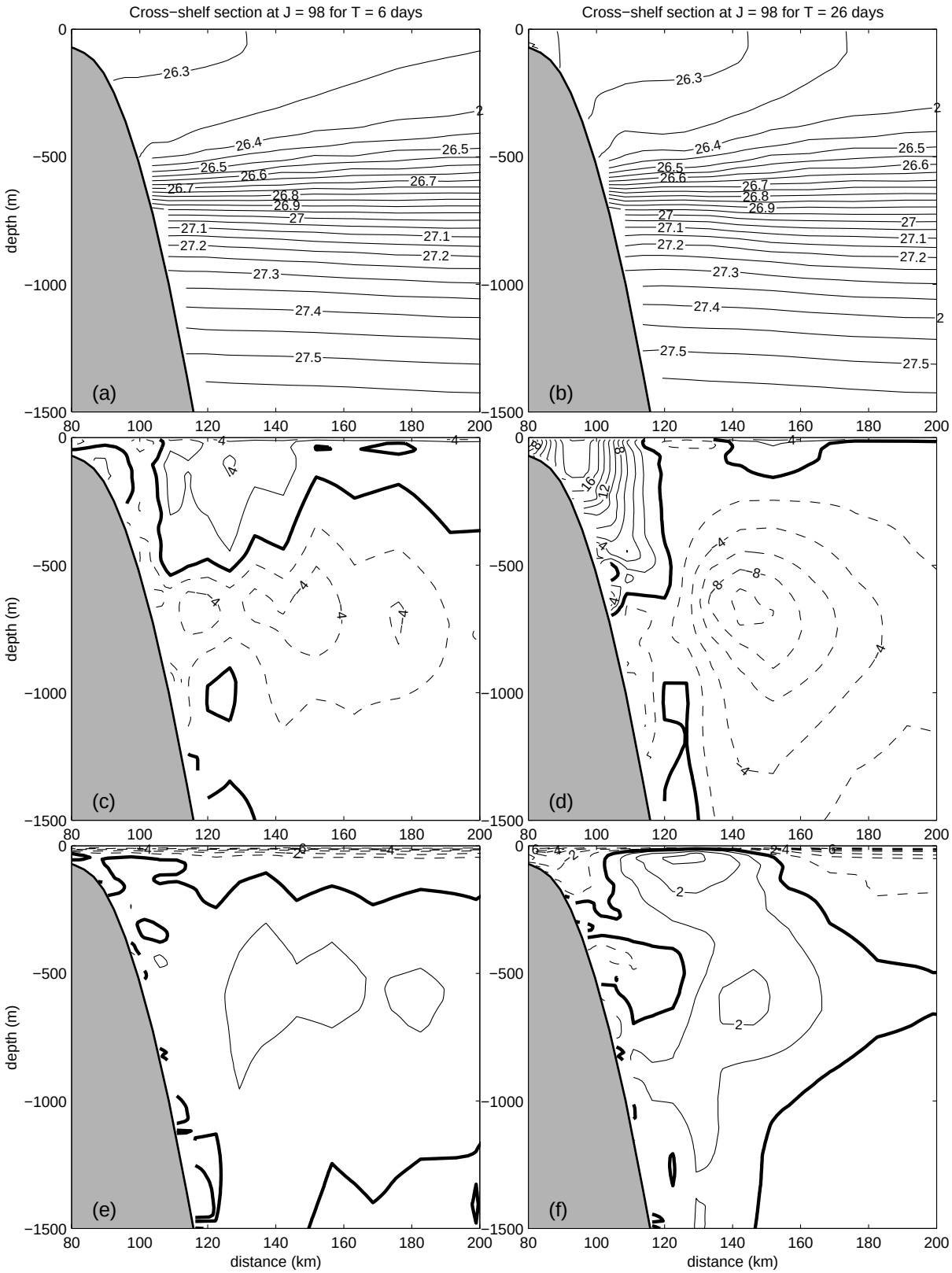

Figure 4.24: *Same as Fig. 4.14, but for the section off Strahan (J=98 in Fig. 4.15).*

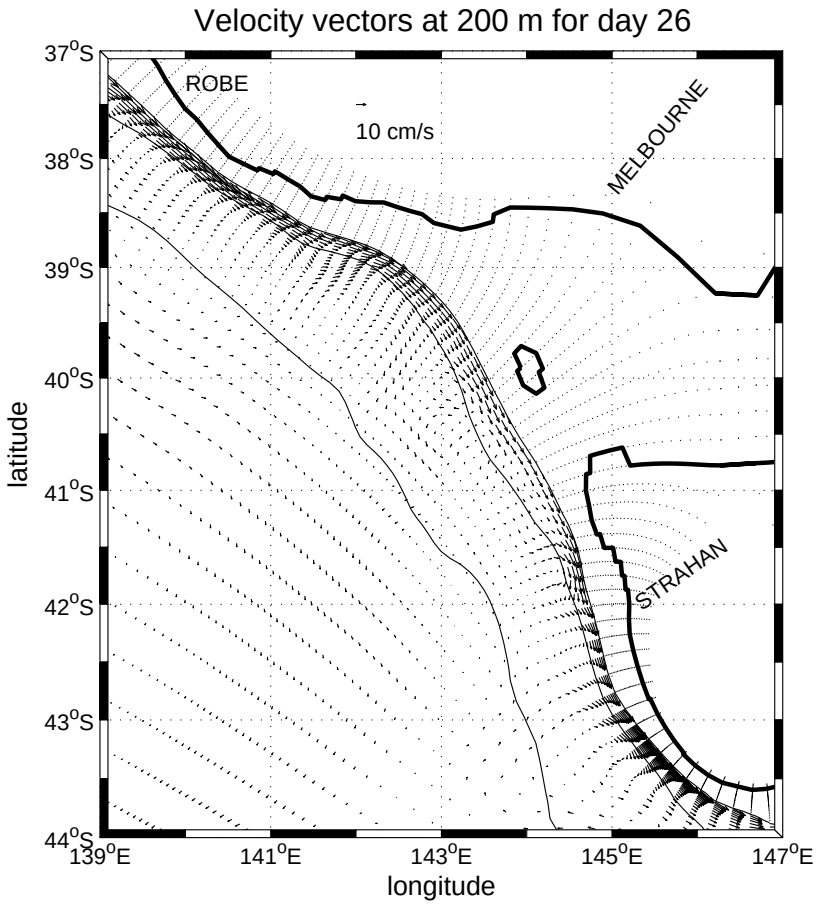

Figure 4.25: *Same as Fig. 4.20 but at 200 m and for day 26.*

Transport Analysis

Here again, the boxed region for analysis encompasses a high and a low (Fig. 4.27) and the integrated transports passing through it were determined.

For the northern section C1, the results (Fig. 4.28a) are similar to those found farther to the northwest (Fig. 4.18), although the poleward transports are less confined to shallower water due to the broader shelf.

For section C1, the transport of the CC (defined to be between 0 and 500 m) is from Fig. 4.28 at most 1 Sv, or half that found to the northwest at the South Australian region. From the transport results shown in Fig. 4.26, 1 Sv is found to pass through Bass Strait. However, since the depth of the strait is only 60 m, water is necessarily drawn up and towards the strait as shown by the cross-shelf velocities in Fig. 4.24e,f and horizontal vector plot in Fig. 4.20. Rather than lead to vortex squashing, the onshore flow to the northwest of King Is. leads to a lowering of sea level as shown in Fig. 4.19.

The onshore flow driven by the presence of the strait may well provide the trigger for the formation of the low in this region.

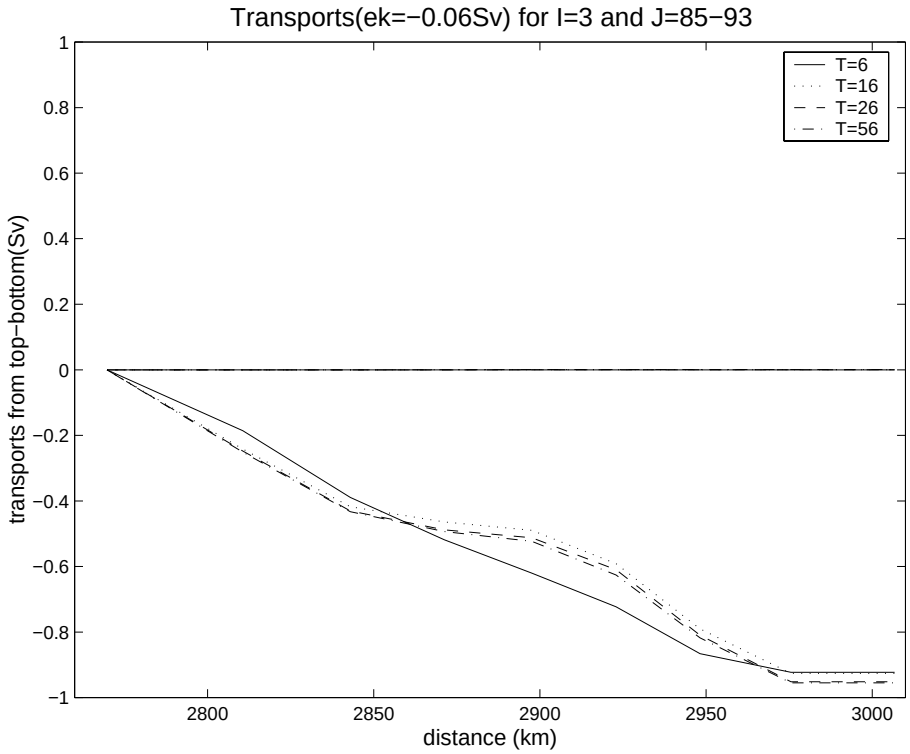

Figure 4.26: *Accumulated transports passing through Bass Strait at section I=3 in Fig. 4.15. Negatives values represent an eastward flow crossing the strait.*

Returning to the results shown in Fig. 4.28, the transport of the FC again increases markedly after day 6 reaching values of about 6 Sv inshore of the 4000 m isobath.

For the section C2 off the west Tasmanian coast, the transport of the CC is near zero at day 6 (Fig. 4.28b), but then rapidly adjusts towards a value of 0.5 Sv by day 16 or half of that through section C1. The smaller transport is of course due to the flow into the strait between King Is. and Tasmania. However, the net transport inshore of the 4000 m isobath is similar to that at C1 and about 2 Sv. The transport of the FC at C2 is also similar to that at C1 ($\sim$ 5 Sv).

Finally, a measure of the increase in eddy activity is illustrated by the large increase in the onshore and offshore transports through section O1 (Fig. 4.27). By day 56 the onshore and offshore transports are 7.4 Sv and 4.3 Sv respectively. Not all of this may be due to the eddies themselves since part could be due to the northward Sverdrup transport.

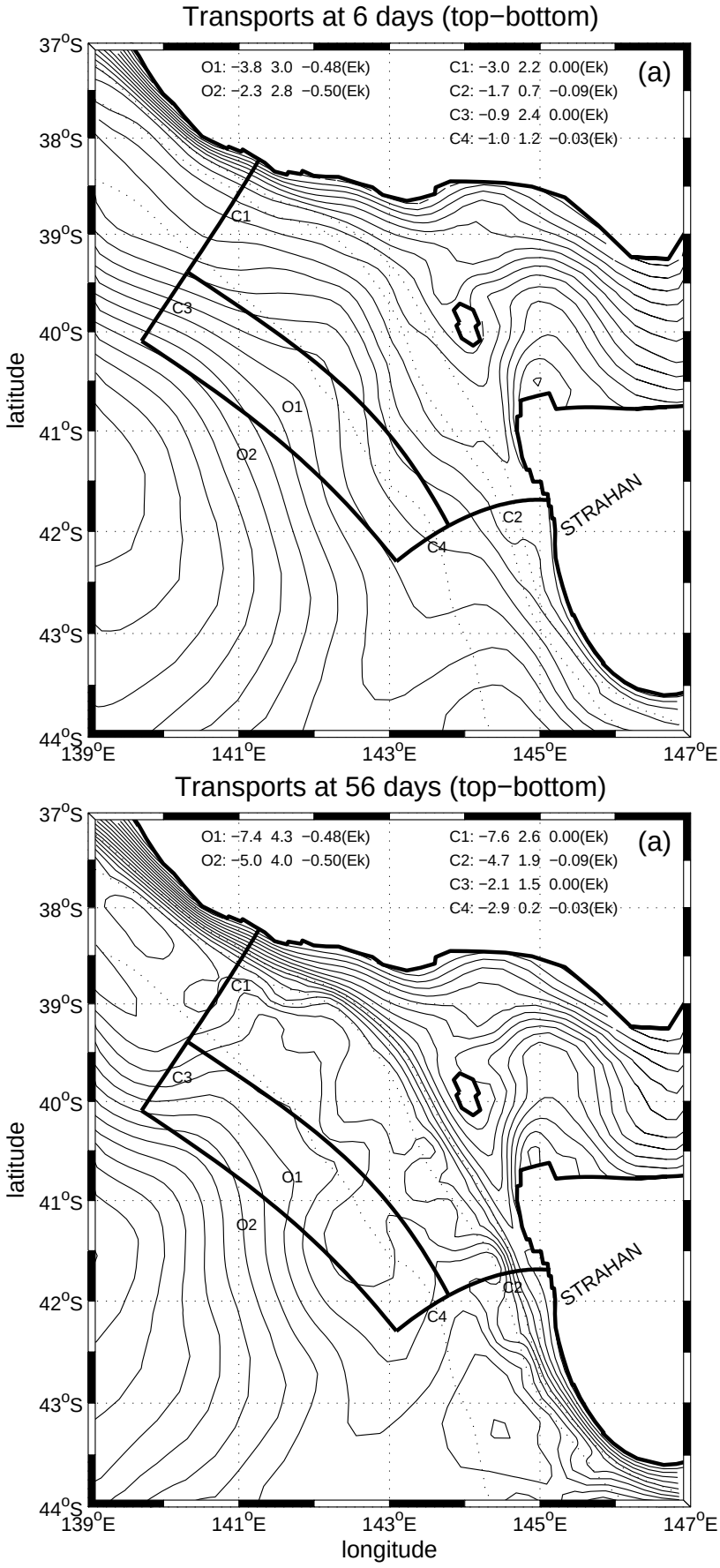

Figure 4.27: *As in Fig. 4.17, but for the Victoria-Tasmanian region. Dotted lines are the 200, 1000 and 4000 m isobaths.*

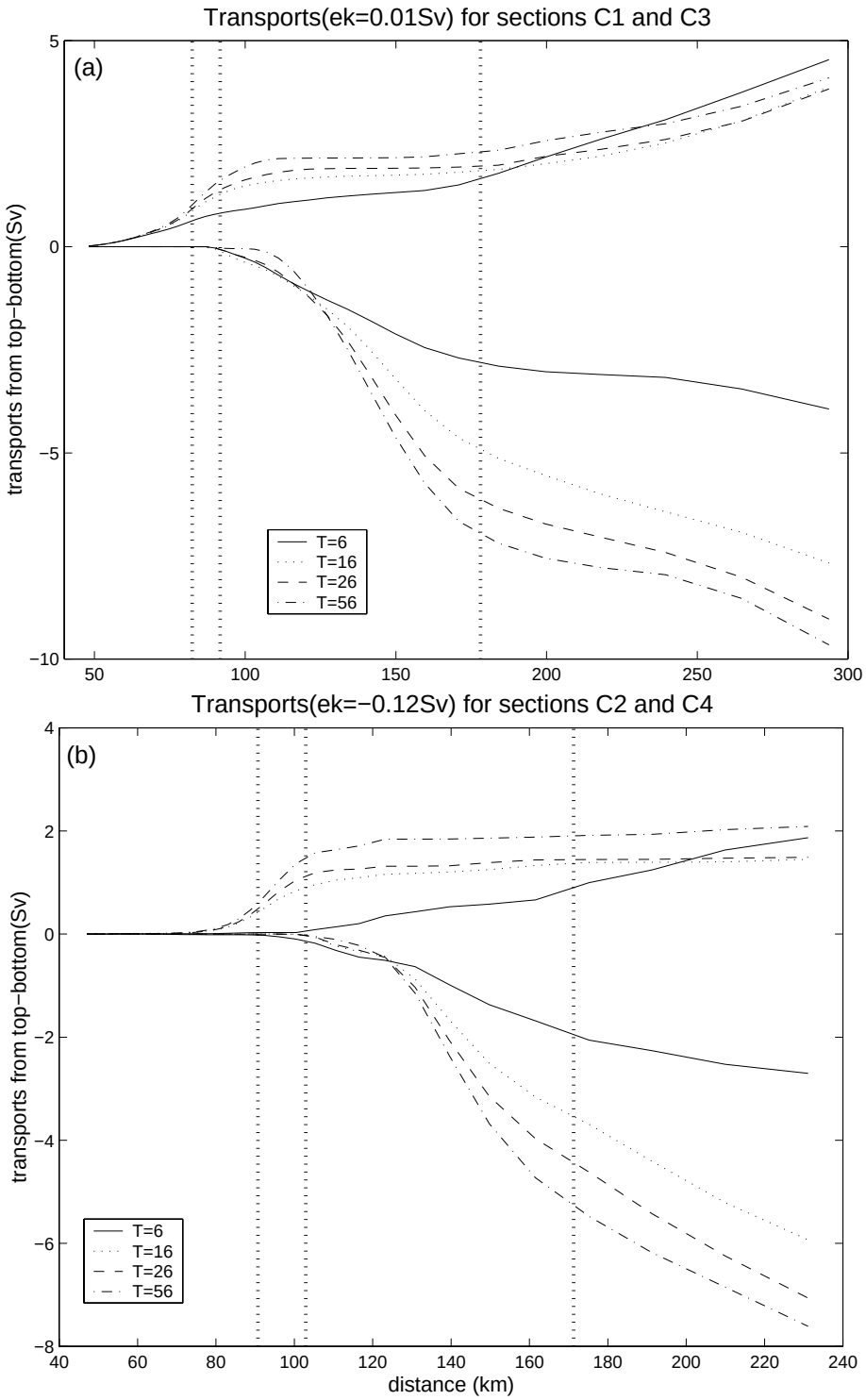

Figure 4.28: *Accumulated transports along cross-shore sections from Fig. 4.27. The different lines shown in the legend are for day 6, 16, 26 and 56. The dotted lines along the distance axes represent the position of the 500, 1000 and 4000 m isobaths. (a) Section C1 and C3 and (b) section C2 and C4.*

Chapter 5

The Effect of Varying Parameters

Here, numerical experiments are made to test a) the effects of globally estimated surface fluxes of heat and salt and b) increased bottom friction due to tides and CTWs. Some of the important results in case (a) are the changes that the imposed fluxes produce in the thickness of the Surface Mixed Layer (SML) and a better reproduction of the poleward density advection by the CC. In case (b), substantial increases in bottom stress are found to have little impact on alongshore currents since these are strongly geostrophic in nature. Increases in along-shelf component of bottom stress does however lead to corresponding increases in offshore transport in the Bottom Boundary Layer (BBL) inshore of 100 m but otherwise have little impact.

5.1 Effect of Heat and Salt Fluxes

In order to evaluate the effect of heat and salt fluxes, these surface forcings were included in the basic case run but without any other change. This experiment was named experiment 1 (Table 3.1). The density change that results from Fig. 2.3c shows the combined effect of the heat and salt fluxes (Fig. 2.3a-b) over 30 days and for top meter of water column.

Although the results show that there are regions where the imposed fluxes lead to better representation of the density field, there are also regions where they tend to deepen the SML to values greater than those observed. A discussion of this effect is provided below.

For example, the density field at 10 m obtained with the fluxes (Fig. 5.1a) shows a pattern of density advection by the CC, that is more in accordance with the satellite image in Fig. 2.11. For the basic case (Fig. 5.1b), the poleward advection and southward increase in density are not as prominent. The changes in density over 30 days due to fluxes can be determined by simply dividing the results in Fig. 2.3c by the depth of the

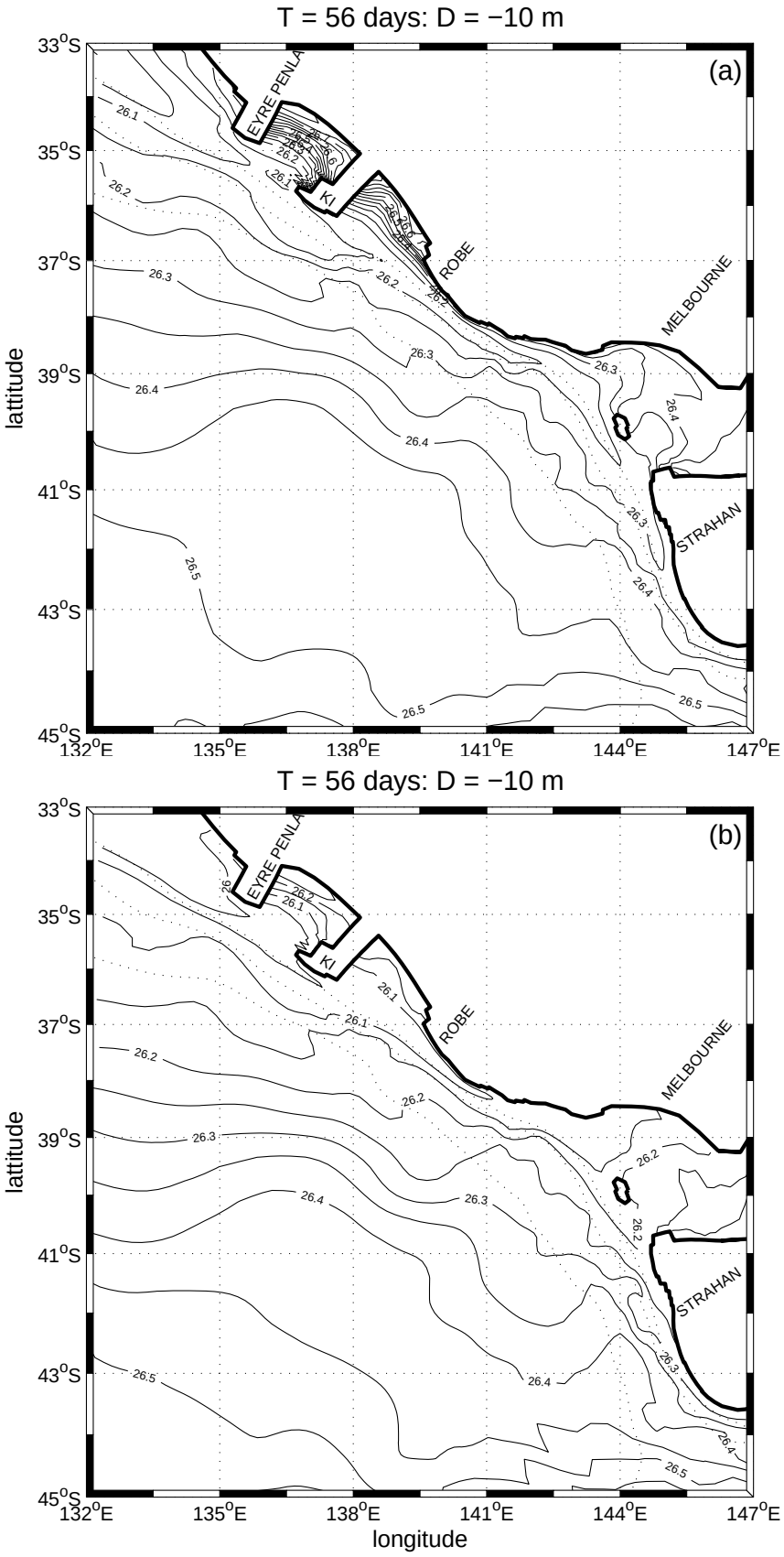

Figure 5.1: *σ_θ distribution at the depth of 10 m for eastern SEIO at day 56 with (a) heat and salt fluxes (exp 1) and (b) without the fluxes (basic case).*

SML. For Bass Strait, a SML depth of 70 m would imply an increase of ~ 0.24 kg m^{-3} (for day 56). This value is in good agreement with the difference in density between Fig. 5.1a and Fig. 5.1b and is probably part of the reason why this band of light water is observed along the 200 m isobath at the western Tasmanian shelf-break.

The application of the fluxes also lead to an increase in density off Robe (Fig. 5.1a) that is in better agreement with the hydrographic observations shown in the CARS atlas (Fig. 2.4c).

On the other hand, the imposed fluxes tend to generate a deeper SML. In less than 1 month of applied cooling the SML off Victoria is around 200 m (Fig. 5.2b) or twice that in the basic case (Fig. 5.2a). The SML depth of the basic case is in much better agreement with Levitus (see Appendix B). An analysis of the efficiency of the vertical scheme for diffusion was performed and the ~ 0.05 kg m^{-3} increase in the density of the SML is in agreement with the imposed density fluxes (Fig. 2.3), if a 200 m SML is considered. That probably rules out any concern regarding the proper representation of the physical mechanism involved in the convection process.

Application of the surface heat and salt fluxes however, only lead to minor changes in the CC, as can be seen from Figs. 5.2c and Fig. 5.2d. One change is the reduction in the onshore velocity in the top 50 m (Fig. 5.2f), when the cooling is applied. The likely reason for this is simply that the surface Ekman layer is deeper (and currents weaker when the surface cooling is applied).

A comparison of the transport values obtained for the basic case and for the South Australian region (Fig. 4.17) and Victoria-Tasmanian region (Fig. 4.27) shows that values are very similar. Generally the transports close to the coast appear to be reduced by at most 0.2 Sv, depending on the day and region.

The two possible explanations for why the use of surface fluxes generates a deeper SML when compared to observed values (Levitus et al., 1994; Levitus and Boyer, 1994) are that (1) the OCCAM initial thermohaline field, being a seasonal average, already contains most of the information necessary to generate SML similar to those observed in the hydrographic cruises. So, for seasonal scale simulations (2 months in this case), there is no need to impose surface fluxes and (2) the surface fluxes are too strong and

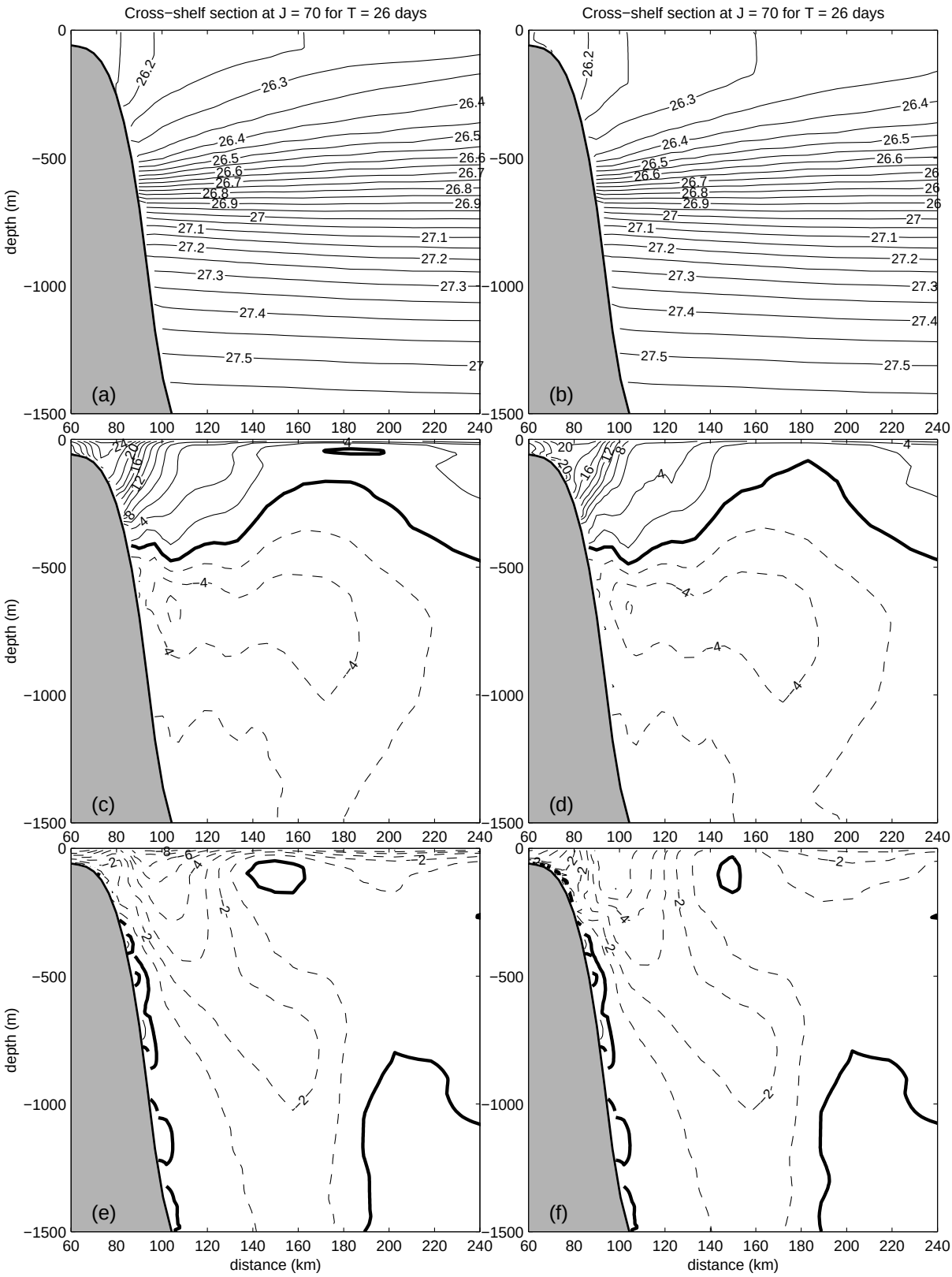

Figure 5.2: *Cross-shelf section off Victoria (J=70 in Fig. 4.15) for day 26 comparing the basic case (left panels) and the exp 1 (right panels) with heat and salt fluxes (Table 3.1). (a) and (b) The density field σ_θ (0.05 kg m^{-3} intervals). (c) and (d) The alongshore velocity (2 cm s^{-1} intervals). (e) and (f) The cross-shore velocity (1 cm s^{-1} intervals).*

As can be seen from Fig. 5.3, the largest rms bottom tidal currents were between King Is. and Tasmania ($\sim$ 60 cm s^{-1}) and within the gulfs ($\sim$ 30 cm s^{-1}). For the CTWs, the largest values ($\sim$ 20 cm s^{-1}) were found where the shelves are narrow, such as off Kangaroo Is., Robe and western Tasmania (Figs D.2b and D.3b).

In general, the results from the numerical simulation allowing for a larger friction show that, apart from the Bass Strait region, the velocity field is almost unaltered. For Bass Strait, the main effect is at the southern entrance, where the tangential velocity is reduced in values up to 50% (Fig. 5.4c,d). The enhanced friction also induces a reduction of 15% in the overall transport the passes through Bass Strait.

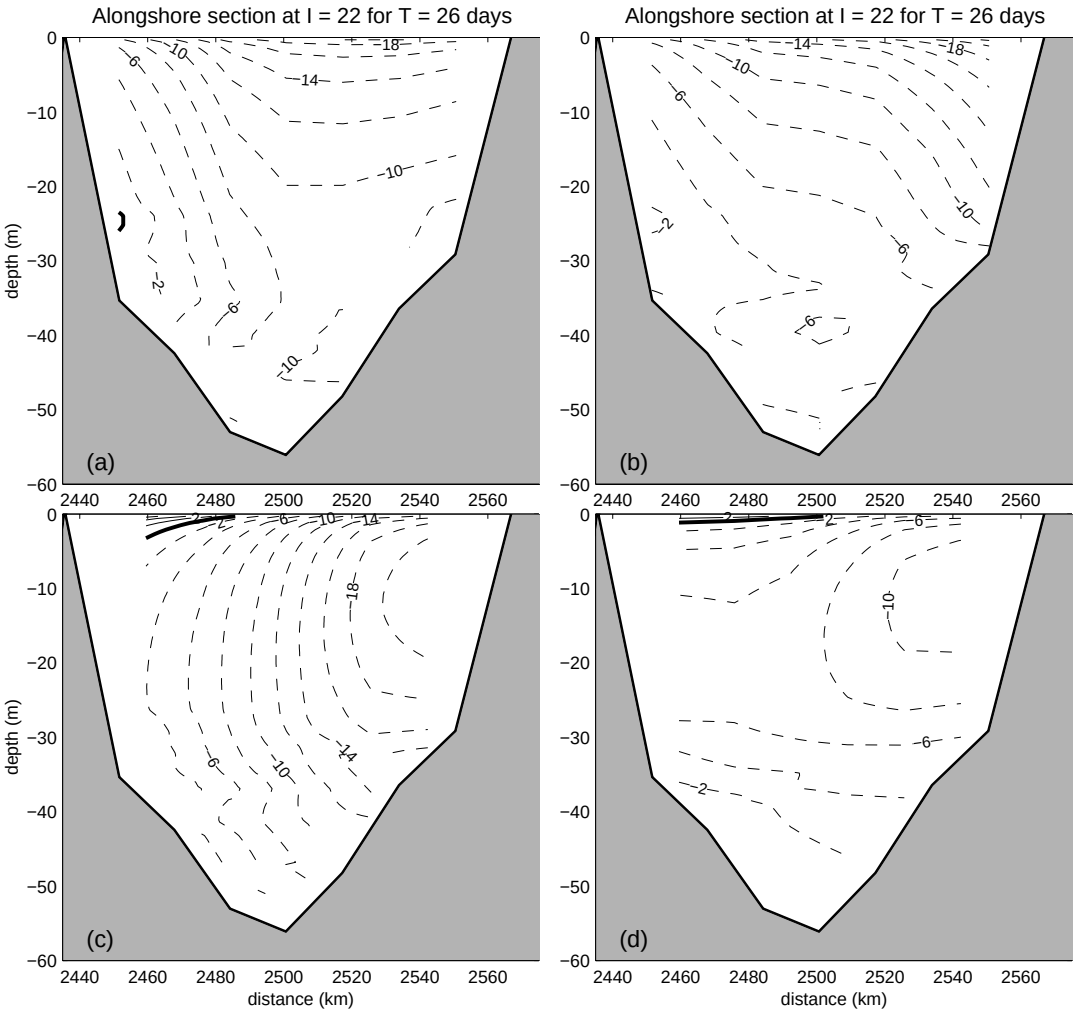

Figure 5.4: *Section between King Is. and Tasmania (I=22 in Fig. 4.15) comparing the basic case (left panels) and exp 2 with enhanced bottom (right panels) friction. (a) and (b) Normal velocity and (c) and (d) tangential velocity at day 26. Negative values (dashed lines) for the normal velocity indicate flow into the strait whereas negative values (dashed lines) for the tangential velocity indicate north-westward flow.*

The explanation for these results lies in the magnitude of the bottom stress relative to other terms in the equations of motion. For the depth-averaged cross-shore momentum balance off Robe and Kangaroo Is., the ratio of the bottom stress to Coriolis force may be written as

$$I_x = \frac{C_d u(|\mathbf{u}|^2 + \sigma^2)^{1/2}}{Hfv} \tag{5.1}$$

where $\sigma^2 = 2\sigma^2{}_{CTW} + 2\sigma^2{}_{TIDES}$

With $C_d = 2.5 \times 10^{-3}$, $H = 50$ m, $f = 10^{-4}$ s^{-1} and $u \sim 0.1v$ $I_x \sim 0.05(|\mathbf{u}|^2 + \sigma^2)^{1/2}$. Now for Robe and Kangaroo Is., the tidal and CTW results shown in Table 5.1 give average values of $(|\mathbf{u}|^2 + \sigma^2)^{1/2}$ that correspond to $I_x \sim 0.025$ and the bottom stress has negligible effect on the alongshore currents. Results show (not presented) that the Coriolis force is balanced by the cross-shelf gradients of pressure.

location	σ_{CTW}	σ_{TIDES}	σ^2	$\lvert\mathbf{u}\rvert^2$	$(\lvert\mathbf{u}\rvert^2 + \sigma^2)^{1/2}$	u/v
Robe	0.18	0.05	0.07	0.07	0.38	0.1
Kangaroo Is.	0.20	0.05	0.09	0.16	0.50	0.1
Bass Strait	0.15	0.60	0.77	0.02	0.89	1.0

Table 5.1: *Parameters used for the evaluation of the bottom stress term. Units for rms velocities are m s^{-1}.*

For the depth-averaged alongshore momentum balance

$$I_y = \frac{C_d v(|\mathbf{u}|^2 + \sigma^2)^{1/2}}{Hfu} \tag{5.2}$$

and the above scale estimates (Table 5.1) lead to a ratio $I_y \sim 2.5$ for the Coriolis to bottom stress terms. Without the effects of CTWs and tides, $I_y \sim 1.5$ so that their inclusion lead to a 67% increase in the importance of bottom friction. Results show that much of this increase is accounted for by an increase in the Coriolis term fu through an increase in the offshore transport within the BBL as shown in Fig. 5.5.

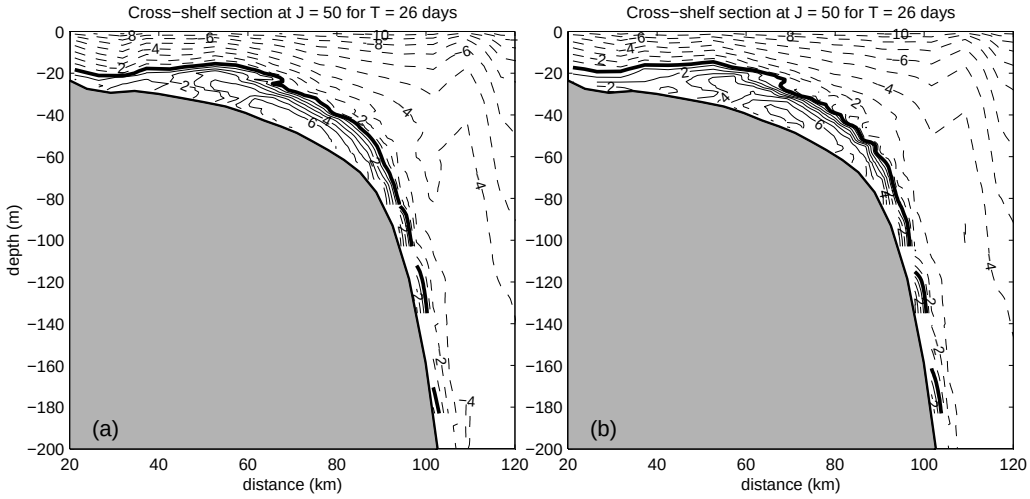

Figure 5.5: *Cross-shelf section off Robe (J=50 in Fig. 4.15) for day 26 comparing the cross-shore velocity for the (a) basic case and (b) exp 2 with enhanced bottom friction (Table 3.1). The contours interval is 1 cm* s^{-1}.

For the region between King Is. and Tasmania, the amplitude of the tides and CTWs are largest, the cross-shelf and along-shelf velocities have similar magnitudes and using the values in Table 5.1 in Eqs. (5.1)-(5.2) results in $I_x \sim I_y \sim 0.5$ so that the enhanced bottom friction due to tides and CTWs is important and leads to the marked reduction in currents shown in Fig. 5.4.

Chapter 6

The Zeehan Current

A description of the current meter data from the west Tasmanian shelf-slope is provided in the first section of this chapter. Since the data available covers different years, an investigation is also made of the presence and nature of the interannual signal in the mean current. In the second section, an investigation is made on the effect of local forcings due wind stress variability. In the third section, some of the possible mechanisms of remote forcing for the region are evaluated.

6.1 Description of the Zeehan Current

There exist two substantial data sets that provide a description of the ZC. The first was obtained between May and November of 1988 and is represented by an array of 9 current meters deployed across the west Tasmanian shelf at four different depths (see Fig. 6.1). The current meter data was obtained for use in a physical-biological model to examine the influence of passive larval drift on the distribution of *Macruronus novaezealandiae* (Lyne and Thresher, 1994) and the details of the deployments are presented in Table 6.1.

mooring		location		sampling		depth(m)	
		long. (°E)	lat. (°S)	start	end	local	instr.
S115	1	144° 44' 48"	42° 56' 48"	30/05/1988	18/11/1988	2040	167
	2			30/05/1988	18/11/1988		320
	3			30/05/1988	18/11/1988		995
S116	1	144° 51' 12"	42° 47' 36"	30/05/1988	19/11/1988	1000	125
	2			30/05/1988	19/11/1988		323
	3			30/05/1988	14/07/1988		936
S117	1	144° 54' 54"	42° 45'	30/05/1988	25/10/1988	200	125
	2			30/05/1988	13/10/1988		190
S118	1	145° 05' 54"	42° 38' 36"	30/05/1988	19/11/1988	93	72

Table 6.1: *Description of the current meter moorings for the year of 1988 as shown in Fig. 6.1.*

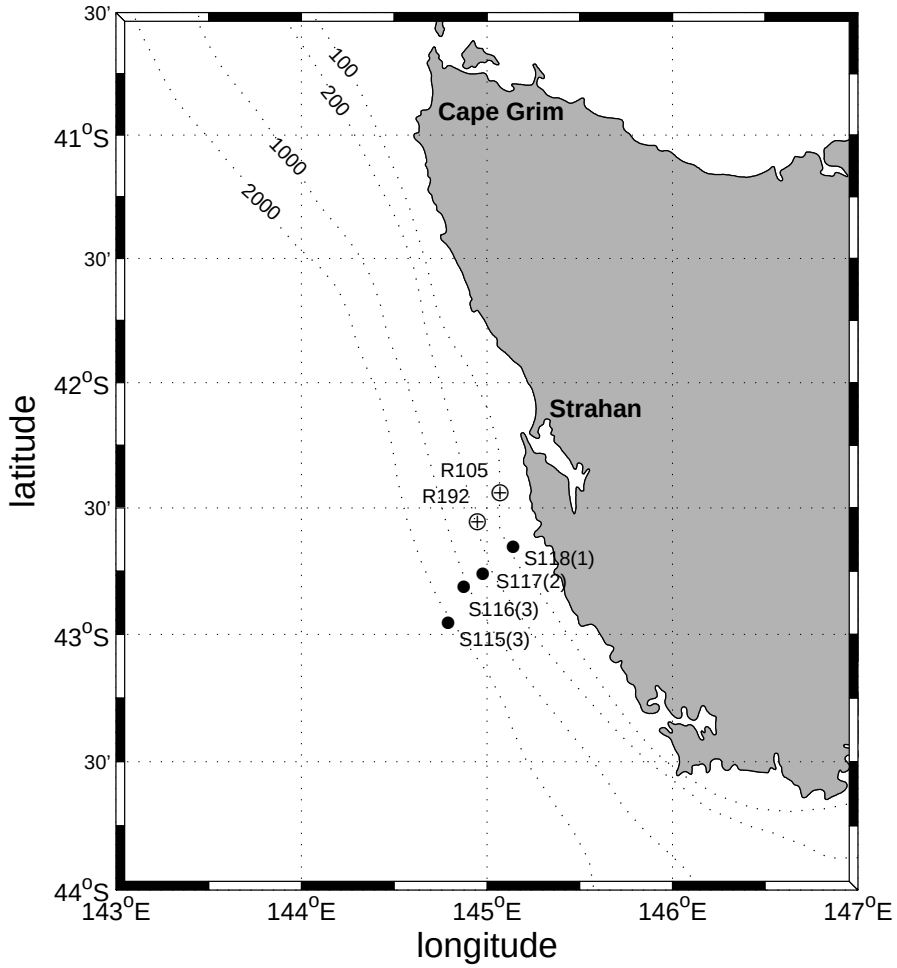

Figure 6.1: *Location map for the current meter moorings (•) for 1988 and the ADCPs moorings (⊕) for 1997-1998. The dotted lines are the 100, 200, 1000 and 2000 m isobaths.*

For the analysis here, the current meter results which showed the least current variability are examined first. These are the two current meters on the shelf-break mooring S117 (ocean depth 200 m) and the offshore mooring S115 (ocean depth 2040 m). The few gaps in the raw current meter data were interpolated using a cubic splines method (Ramp, 1997) and a low-pass spectral filter with 44 h cut-off was adopted to eliminate any tidal signal. The major axis was then estimated for each current meter and on average, was found to lie close to 10 degrees anti-clockwise from north, and tangential to the isobaths shown in Fig. 6.1.

The currents at both the upper and lower sites on the shelf-break mooring are shown in Figs. 6.2 and 6.3 and indicate a strong CTW signal (amplitude 30 cm s^{-1}) and are also

quite similar. Such similarity might be expected given the lack of thermal wind shear apparent from both the observed temperature field (Fig. B.12) and modelled density field (Fig. 4.24b). Monthly averaged currents were also obtained along the principal axes noted below. The negative values shown in Figs. 6.2c and 6.3c indicate poleward mean currents of 25-30 cm s^{-1}. The cross-shore currents shown in Figs. 6.2b and 6.3b indicate a flow of 2-4 cm s^{-1}, although these may not be reliable due to aliasing of the larger poleward currents.

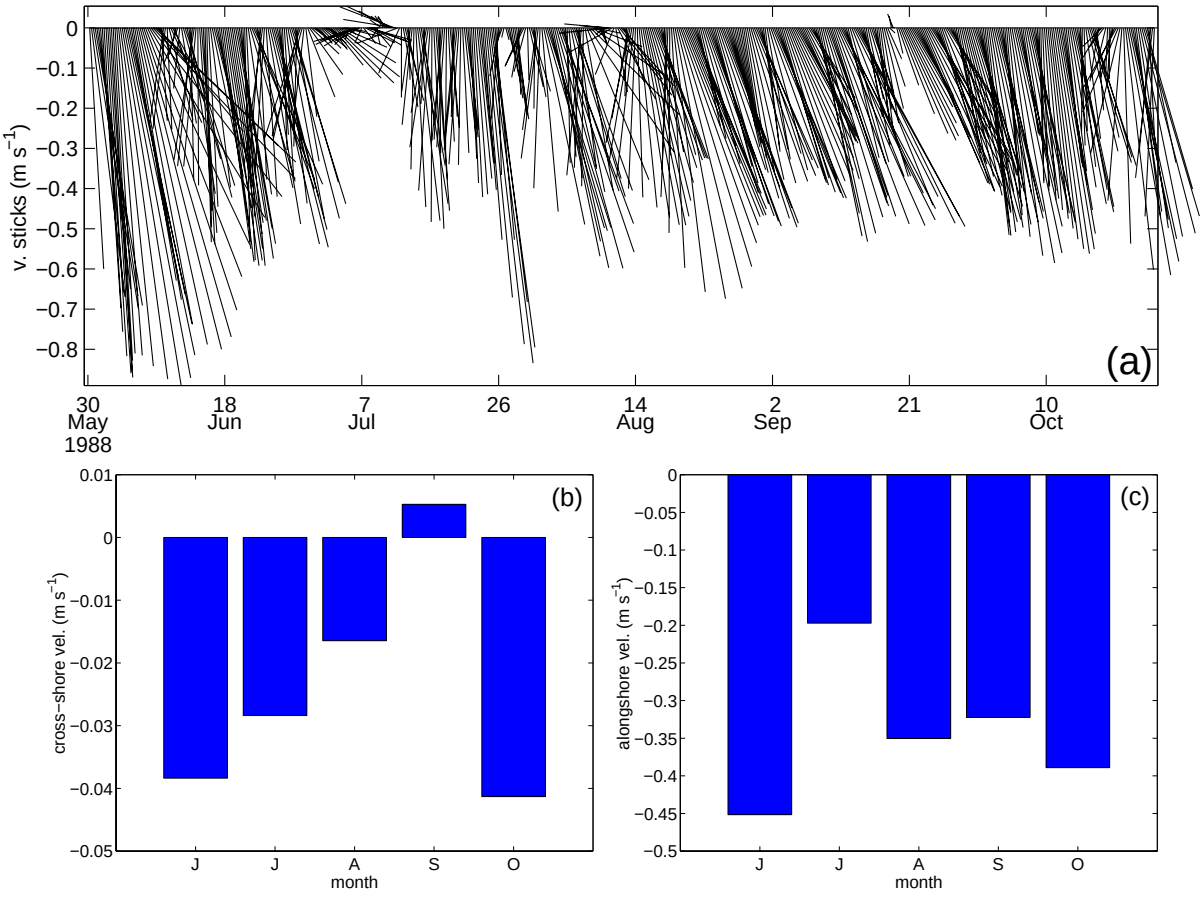

Figure 6.2: *(a) Time series for the upper shelf-break current meter S117-1 (depth 125 m, water depth 200 m). The stick vectors are north-south oriented. Monthly mean for (b) the cross-shore component of velocity (positive onshore) and (c) the alongshore component of the velocity (positive north-westwards) after rotation.*

Farther offshore, in the vicinity of the 2000 m isobath (mooring S115 in Fig. 6.1), the currents at a depth of 995 m again indicate substantial variability (Fig. 6.4a) although the alongshore component means (Fig. 6.4c) are now of order 3 cm s^{-1} and oriented equatorward and in the same direction as the FC.

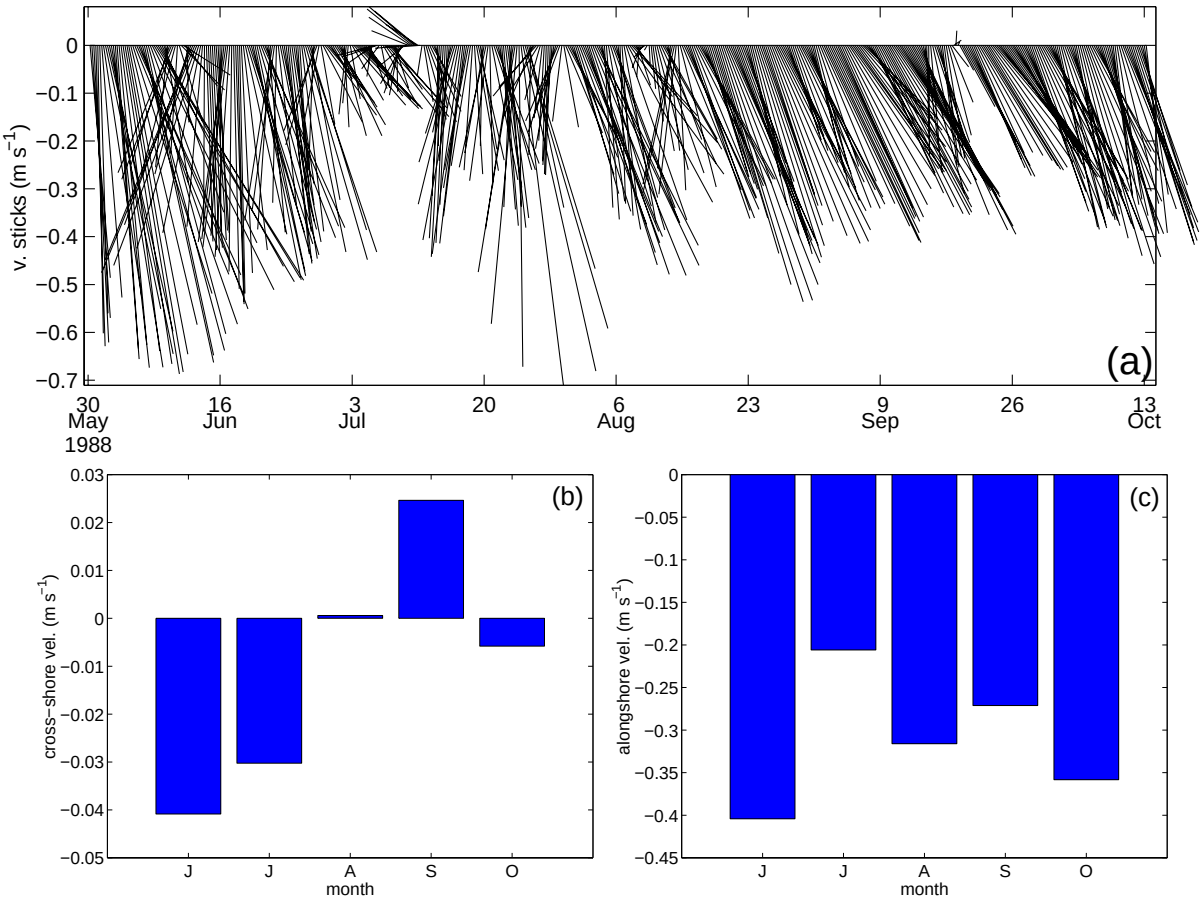

Figure 6.3: *Same as Fig. 6.2, but for the lower shelf-break current meter S117-2 (depth 190 m, water depth 200 m).*

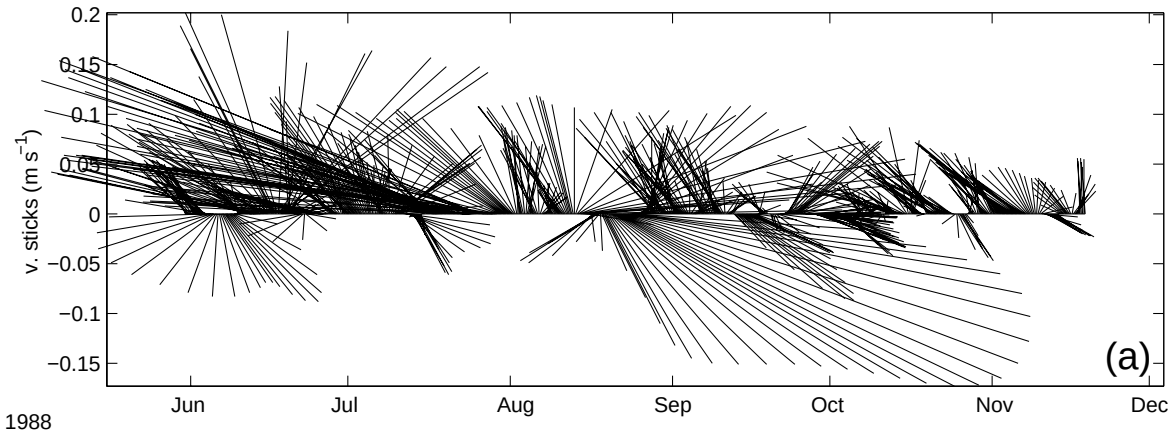

Figure 6.4: *Same as Fig. 6.2, but for the lower slope current meter S115-3 (depth 995 m, water depth 2040 m).*

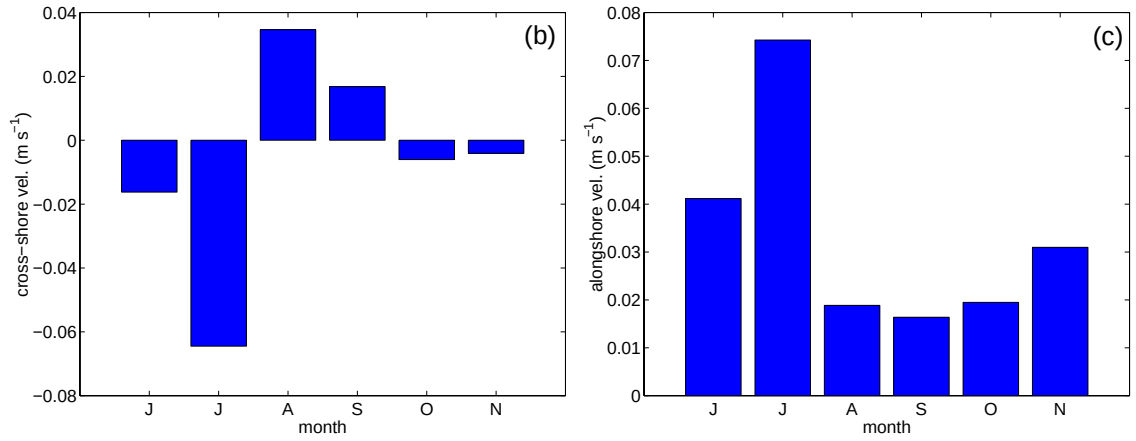

Figure 6.4: *(Continued)*

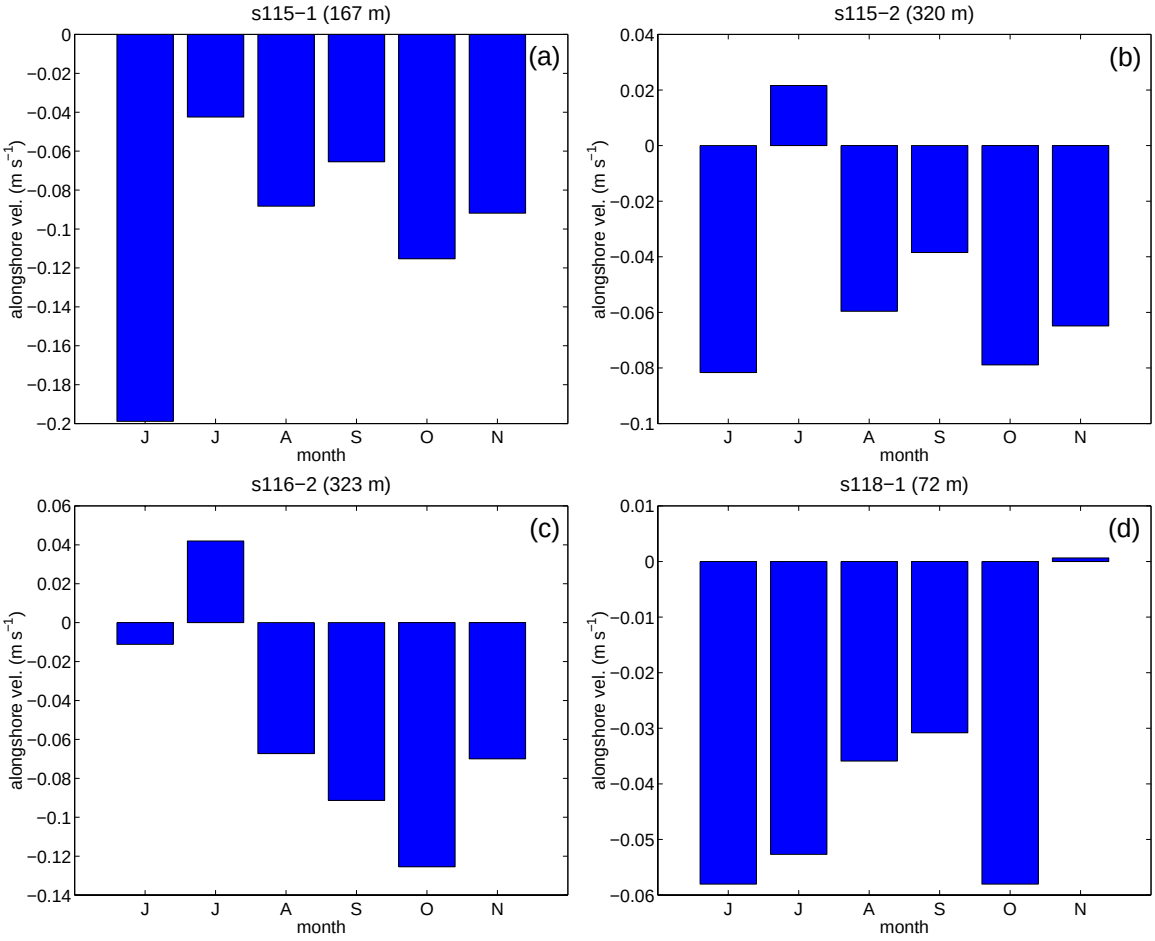

Figure 6.5: *Monthly mean for the alongshore component of the velocity (positive northwestwards) after rotation at (a) S115-1, (b) S115-3, (c) S116-2 and (d) S118-1 as described in Table 6.1.*

One notable feature of the results is that when the poleward mean currents are weakest (July in Figs. 6.2c and 6.3c), the equatorward means in deeper water are strongest (July in Fig. 6.4c). This feature will be discussed later.

Results for mean monthly currents were also obtained for all of the other currents meters and are presented in Fig. 6.5. The upper (S116-1 in Table 6.1) and lower (S116-3 in Table 6.1) instruments for the 1000 m isobath mooring were not included due to a failure in the recorded time series. In general, the alongshore mean currents for all analysed moorings are poleward and stronger for the outer locations, while the coastal mooring only registered mean velocities of the order of 5 cm s^{-1} (Fig. 6.5d).

The second set of current meter data consists of 11 months Acoustic Doppler Current Profiler (ADCP) records obtained by Cresswell (2000) during the period of March 1997 to February 1998, as an attempt to study the variability of the ZC. With this purpose, the data was obtained in a location very close to the 1988 current meters (S117 and S118 in Fig. 6.1) and in water depths of 100 m and 188 m (Table 6.2). The currents varied little with depth and those presented in Figs. 6.6 and 6.7 represent averages over the 40-90 m and 80-180 m depths. The principal axes were again determined and since they lie very close to the north-south axis no rotation was required.

Again the currents are poleward, although with the exception of June, the winter and spring mean currents at each site are about half that obtained from the 1988 data. For the shallower (Fig. 6.6c) and deeper (Fig. 6.7c) moorings, the means are of order of 3 cm s^{-1} and 15 cm s^{-1} respectively.

mooring	location		sampling		depth(m)
	long. (°E)	lat. (°S)	start	end	local
R105	145° 01' 05"	42° 26' 06"	21/03/1997	15/02/1998	100
R192	144° 53' 49"	42° 33' 09"	20/03/1997	15/02/1998	188

Table 6.2: *Description of the ADCP moorings for the years of 1997 to 1998 as shown in Fig. 6.1.*

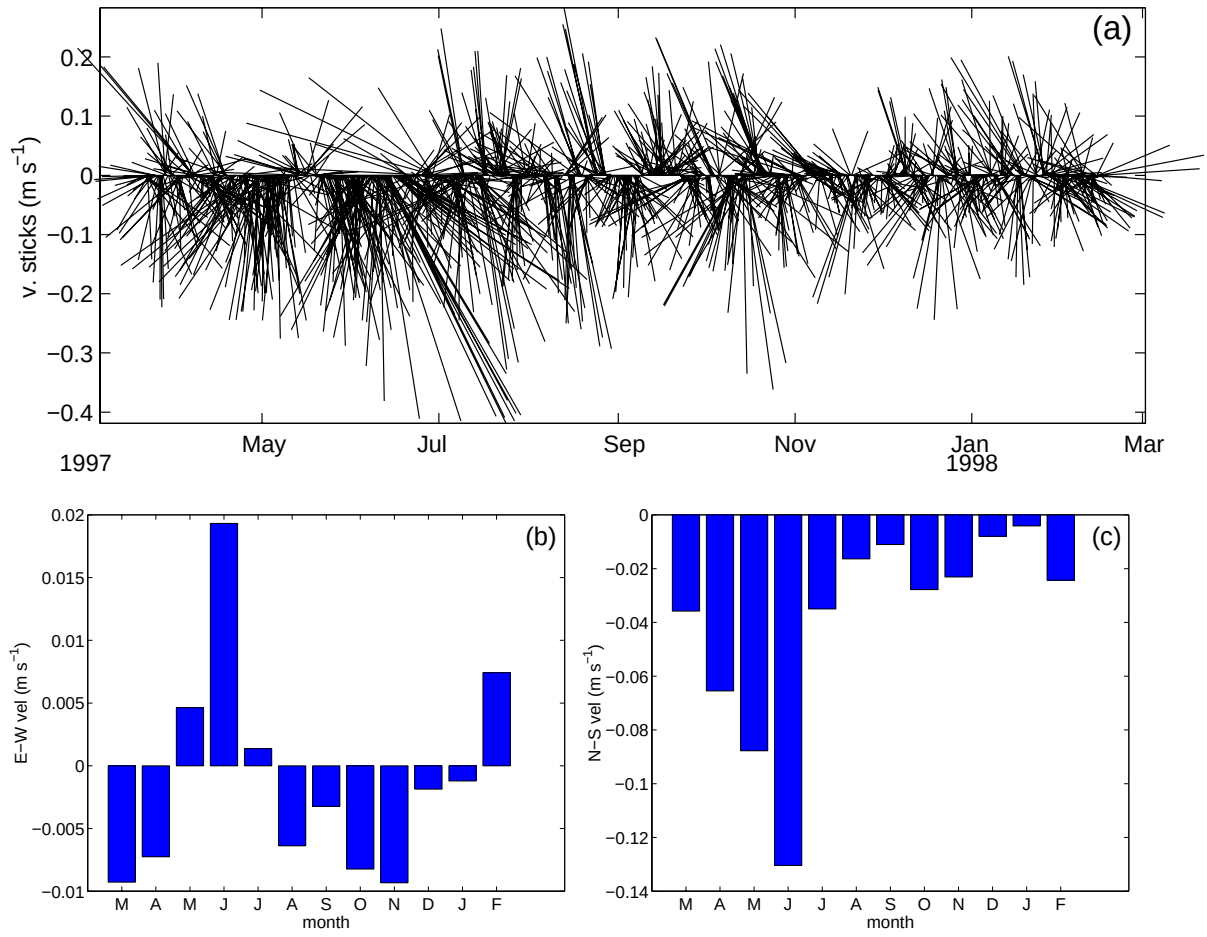

Figure 6.6: *(a) Time series for the shelf ADCP (water depth 100 m) averaged over the depths of 40-90 m. The stick vectors are north-south oriented. Monthly mean for (b) the E-W component of velocity (positive eastwards) and (c) the N-S component of the velocity (positive northwards).*

The wintertime (July-September) mean alongshore currents may be compared with those obtained from the basic case model simulation (as a result of an average over the last 30 days of model run) as well as with the other experiments (Table 3.1). Although all data sites were examined, the locations where variability was smaller, such as the shelf-break and the deep current meter at the 2000 m isobath were considered more comparable. Compared to the 1988 means and for the 200 m isobath (Table 6.3), the modelled currents (basic case) are about 35% smaller than that obtained from the S117-1 and S117-2 current meters. On the other hand, the 1997 ADCP wintertime average (water depth 188 m) is only 10 cm s^{-1} and much smaller than the 17-19 cm s^{-1} modelled currents. The possible causes for this variability, where the modelled current averages lie

just in between of the two data sources, will be addressed in sections 6.2 and 6.3. At the S115-3 current meter (depth 995 m), the model results are in a very good agreement and both present an equatorward mean of $\sim$ 4 cm s^{-1}.

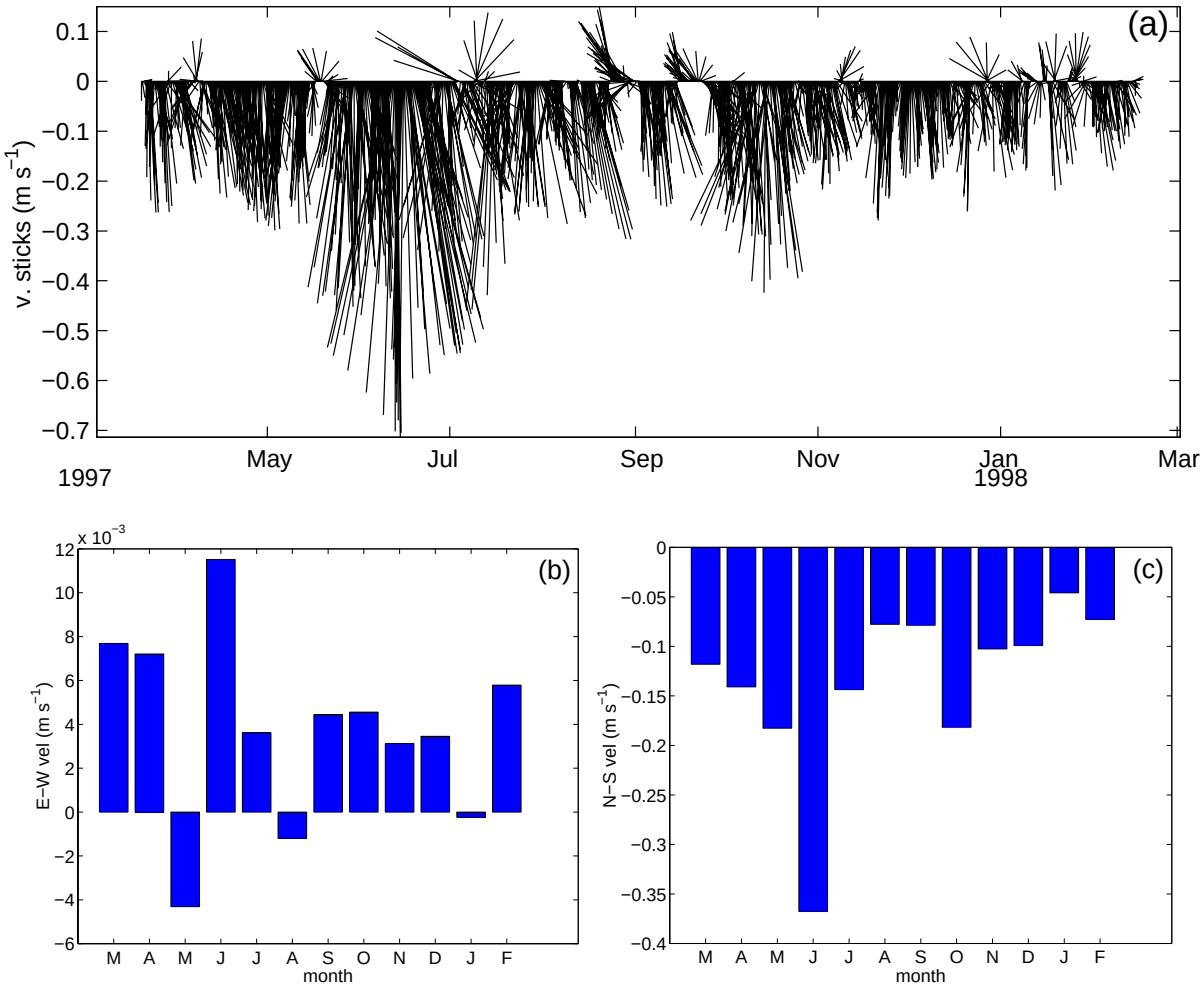

Figure 6.7: *Same as Fig. 6.6, but for the shelf-break ADCP (water depth 188 m) averaged over the depths of 80-180 m.*

As an overview, the wintertime current meter averages are also presented in Fig. 6.8b together with the modelled alongshore currents obtained at day 56 for all the proposed experiments (Figs. 6.8a,c-f). While the magnitudes differ from the observations, the model does reproduce a poleward current that extends 60 km from the shore and to depths of 300 m as well as the deep equatorward current. At shallower waters and in the observations, there is a clear horizontal shear in the velocity field (Fig. 6.8b), which constrains the core of the current at the shelf-break region. The same shear is found in the modelled currents, but here the location appears to be further north and that is the reason why the same gradient is not observed in Figs. 6.8a,c-f.

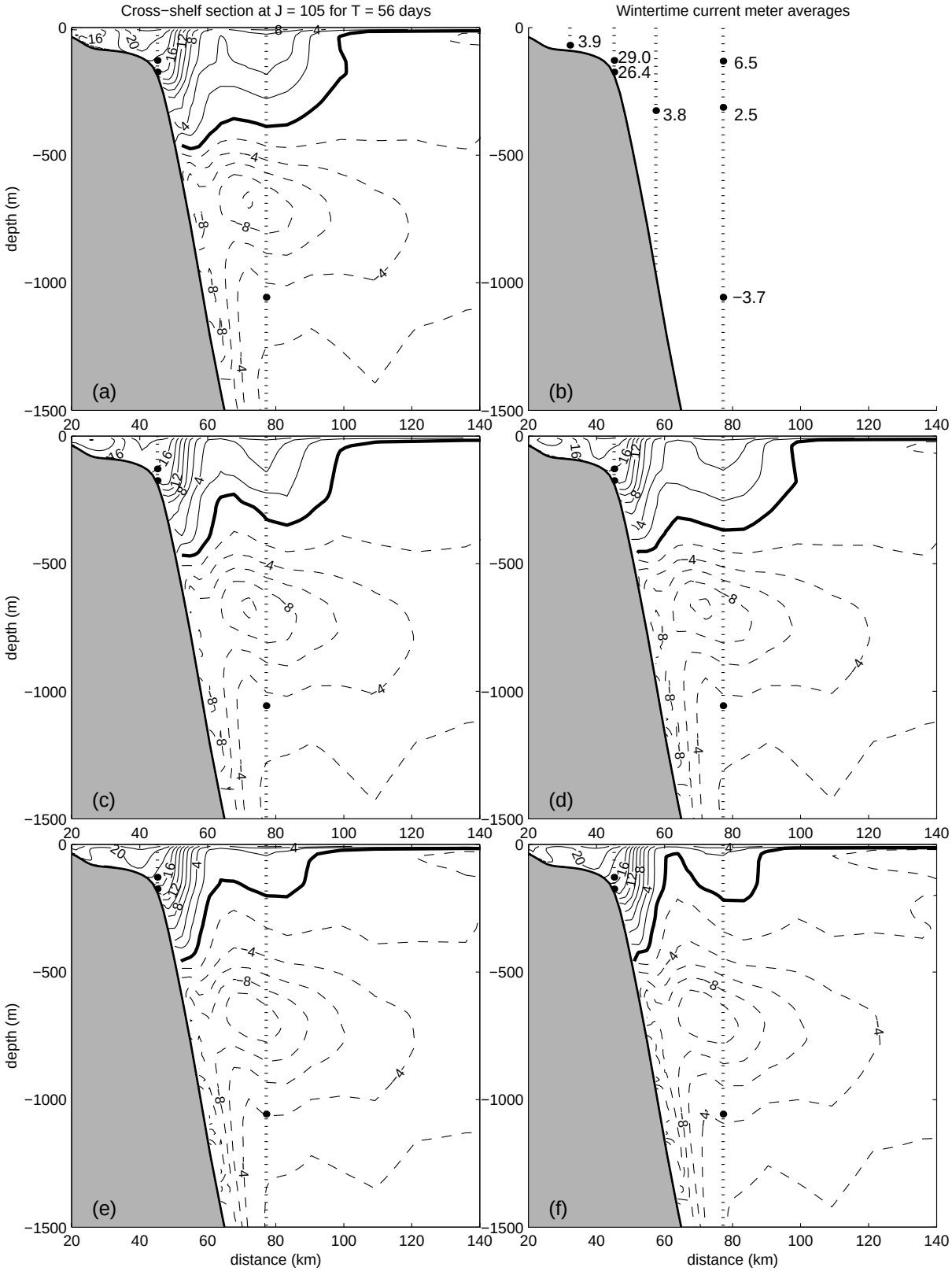

Figure 6.8: *(a) Cross-shore section of the alongshore velocity for day 56 at the current meter sites and for the basic case. (b) Wintertime averages for the current meters described in Table 6.1. Results for experiments with variant parameters as described in Table 3.1 are (c) exp 1, (d) exp 2, (e) exp 3 and (f) exp 4. Negative (positive) velocities are equatorward (poleward) according to the model axis.*

mooring		CM	basic	exp 1	exp 2	exp 3	exp 4
S115	3	3.7	4.4	4.1	4.3	5.1	5.1
S117	1	-29.0	-18.9	-16.3	-17.3	-18.0	-17.6
	2	-26.4	-16.7	-15.0	-15.5	-16.0	-15.8

Table 6.3: *Wintertime mean comparison between the current meters (Table 6.1) and the numerical results (Table 3.1). Positive (negative) values represent equatorward (poleward) flow. Units cm* s^{-1}.

6.2 Wind Stress Variability

Variations in the wind stress field can lead to changes in a) coastal sea level and magnitude of the coastal currents b) northward Sverdrup transport and magnitude of the equatorward FC and c) the transport through Bass Strait and magnitude of the currents on the western Tasmanian shelf.

In order to examine the wind stress variability, monthly mean wind stress for June 1988 (Fig. 6.9) was compared with the August climatological average (Fig. 3.10) used to force the basic model case. The first feature to note is that the alongshore component of the stress between Robe and Tasmania is up to 25% larger than that given by the August climatology. Linear dynamics would suggest that the poleward currents near the coast should be correspondingly larger.

On the other hand, the wind stress curl to the south west of Tasmania is 30-50% larger than the August climatology, suggesting a larger northward Sverdrup transport, FC and reduced poleward transport.

In order to examine these effects, the model was rerun using the June 1988 winds (this experiment was named experiment 3 and is described in Table 3.1), and the results found to be qualitatively similar to the basic case but with some notable quantitative differences. A cross-shelf section (at the mooring sites) obtained using the June winds is shown in Fig. 6.8e and compared to the basic case (Fig. 6.8a) the magnitude and extent of the FC is increased while the offshore extent of the ZC is reduced.

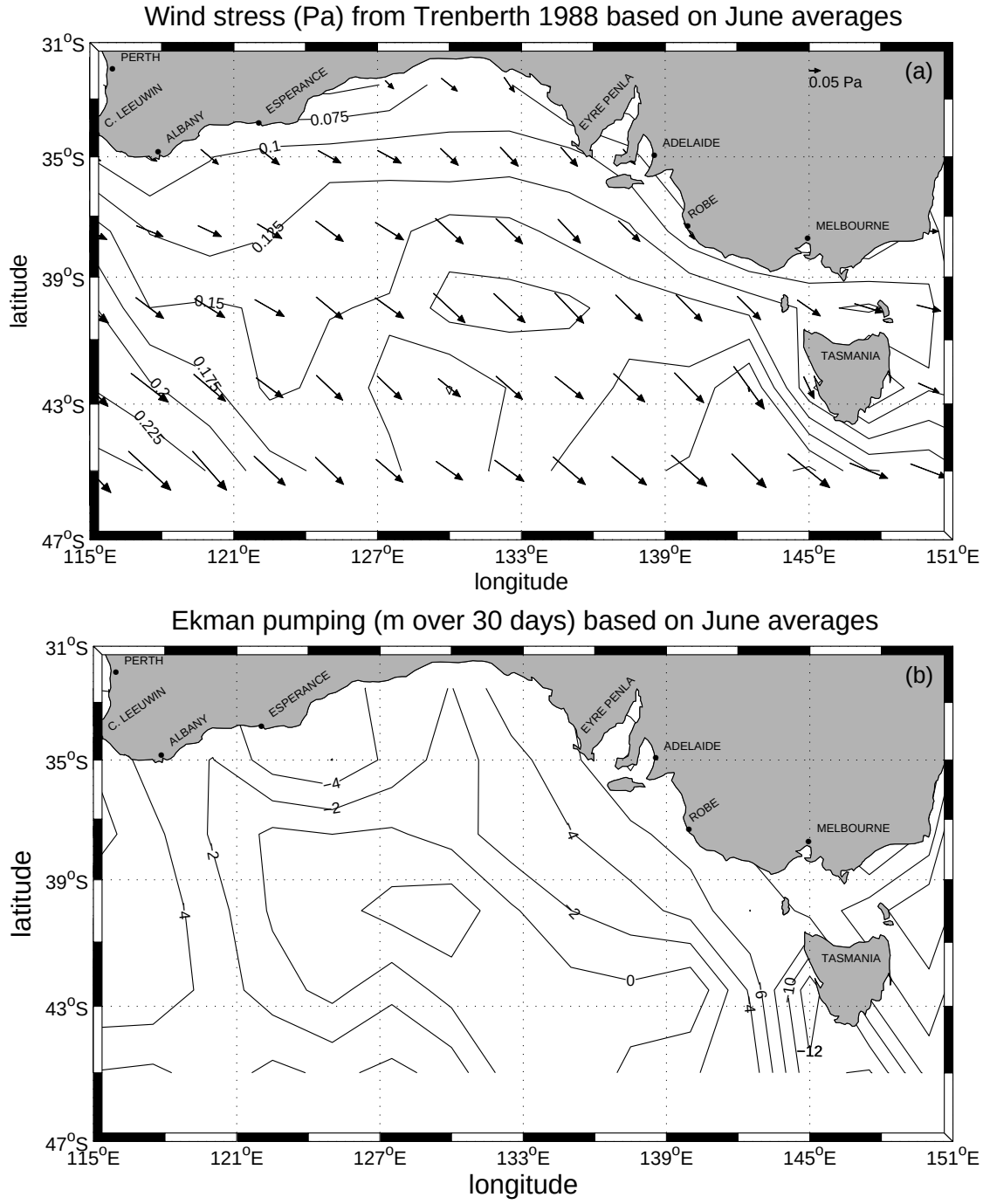

Figure 6.9: *Same as Fig. 3.10, but based on June averages for the year of 1988 only.*

Indeed, for the June wind case, the net equatorward transports through sections C1 and C2 and for both the South Australian and Victoria-Tasmanian region are increased by about 10% (see Table 6.4).

case	South Australian region						Victoria-Tasmanian region					
	C1			C2			C1			C2		
basic	4.9	-7.9	-3.0	3.4	-7.9	-4.5	2.6	-7.6	-5.0	1.9	-4.7	-2.8
exp 3	4.7	-8.2	-3.5	3.2	-8.4	-5.2	2.1	-7.7	-5.6	1.4	-4.9	-3.5
exp 4	4.4	-8.3	-3.9	3.1	-8.8	-5.7	2.1	-8.3	-6.2	1.3	-5.3	-4.0

Table 6.4: *Depth-integrated transports (Sv) at day 56 as an analogy of Fig. 4.17 (South Australian region) and Fig. 4.27 (Victoria-Tasmanian region). Positive (negative) values represent poleward (equatorward) flow.*

Now consider the July 1988 mean wind stress shown in Fig. 6.10. The alongshore component of wind stress between Robe and Tasmania is perhaps 25% larger than in June, while the wind stress curl is similar over most part of the domain and larger at the southern tip of Tasmania. This experiment was named experiment 4 (Table 3.1). Although the coastal winds are the strongest (relative to June and the basic case) when results are compared to the basic case, the transport of the CC decreases by 10-20%, presumably since the 25% increase in the alongshore winds is overwhelmed by the 30-50% increase in the curl and Sverdrup transport.

An additional mechanism that can affect the currents along the northwest shelf of Tasmania is the wind forced transport within Bass Strait. As shown in Chapter 4, this transport is given by $hW_s u = -\tau^{sx} L_s/(f\rho_0)$ and is drawn into the western strait mouth from the northwestern Tasmanian shelf. From Figs. 6.9a-6.10a, the zonal stress within the strait during June and July is about 0.1 Pa and 0.13 Pa respectively or 20% to 50% larger than that given by the August climatology (Fig. 3.10).

However, the numerical results obtained with June and July winds (Table 6.4), show that the transport through the strait increases by only 5% and 20%. The discrepancy here presumably arises from the smaller south-eastward currents and transport that flows past the western mouth of the strait and which also drive a transport into the strait. From Table 6.4, the transport through section C1 (near Robe), is reduced from 2.6 Sv for the basic case to 2.1 Sv for both June and July.

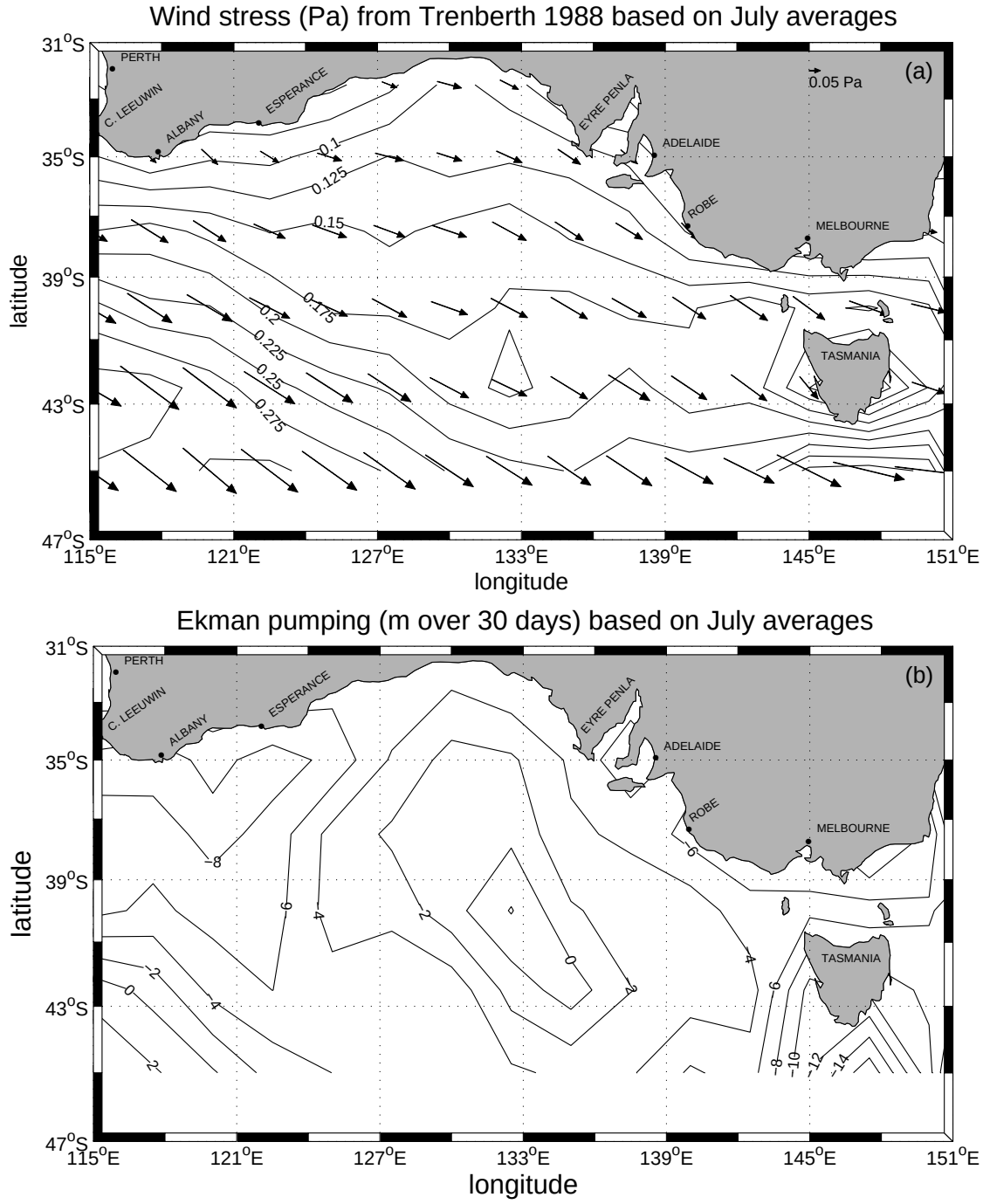

Figure 6.10: *Same as Fig. 3.10, but based on July averages for the year of 1988 only.*

The model results show (and the above arguments regarding the different wind fields suggest) that the poleward component of the ZC during June and July of 1988 is smaller rather than larger than that driven by the August climatology. Table 6.3 shows that the modelled ZC is around 40% weaker (exps 3 and 4) than that observed (compared to 35% for the basic case).

One possibility is that the Trenberth wind estimates (mainly for the year of 1988 alone) are simply unrepresentative of the true winds of the region. With this purpose, a comparison of the Trenberth June and July 1988 winds was made with wind stress estimates obtained from local observational sites from the Bureau of Meteorology in and around Bass Strait. The analysis here (Appendix E) suggests that the Trenberth zonal wind stress within the strait is about 15% too large during both June and July. In this case the transport drawn into the strait would be 15% too large and the poleward current on the west Tasmanian shelf at most 15% less than it should be. However, this is less than half of the 40% difference between the magnitude of the simulated ZC using the June or July winds and that observed.

The results above, using 1988 winds, do not appear to explain the stronger currents observed in 1988. But on the other hand, the results do show that changes in the curl of the wind as well as the wind stress (particularly within the strait) can effectively alter the strength of both the ZC and FC.

6.3 Interannual Variability

Finally, the possibility that interannual variability could play a role in affecting the overall circulation for the SEIO region is examined. Walker and Wilkin (1998) using 8 years of NOAA/NASA Pathfinder satellite SST data found a warming of some 2°C over the years 1987-1990 for the region south of the GAB. Within the interannual frequency, the El Ninõ Southern Oscillation (ENSO) is probably the most studied phenomenum and its wide range influence is still under investigation. Clarke (1991) and Clarke and Liu (1994) have suggested that the collapse in sea level in the western Pacific during an ENSO event radiates westward propagating Rossby waves that induce corresponding changes in sea level along the west Papua and New Guinea and Australian shelves.

Using sea level data from around Australia, such perturbations were examined by Pariwono et al. (1986) who found that positive (negative) interannual sea level anomalies of around 5 cm propagate coherently from Darwin to Bass Strait and are coherent with La Ninã (El Ninõ) events. Their plot of the interannual sea level anomaly between 1966 and 1980 is presented in Fig. 6.11 below and the El Ninõs events are starred. The analysis uses sea level data grouped for each region in an anti-clockwise manner: Northwest shelf (NW); West Australia (W); Southwest (Albany and Esperance) (SW); South Australia (S); Bass Strait (BS); New South Wales (NSW) and Queensland (QLD). A feature of the perturbations is that they do not seem to propagate east of Bass Strait.

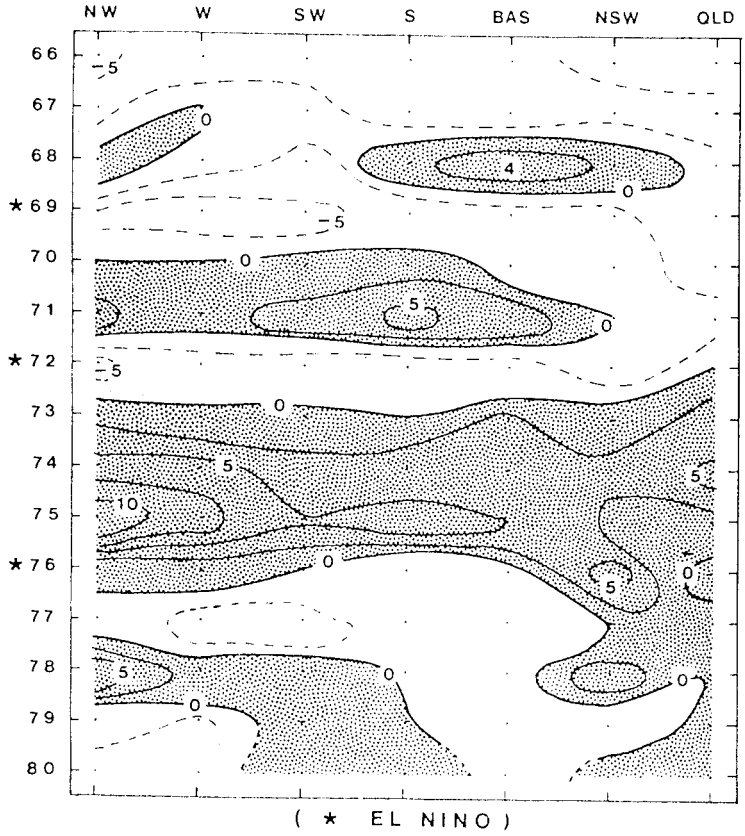

Figure 6.11: *Geographical distribution of interannual anomalies of sea level over a 15 year period. Units in cm. Extracted from Pariwono et al. (1986).*

A second plot of Pariwono et al. (1986) is shown in Fig. 6.12 and illustrates the (long-time) monthly sea level mean (dashed curves) and the monthly means for 1981-1983 (solid curves): 1982-83 was an El Ninõ period. As is evident, sea level stands higher than the long term mean during the La Ninã year of 1981 (the year before the ENSO year), and by up to 10-20 cm within the GAB. In the second half of 1982, mean sea level drops below the long term mean by a similar amount.

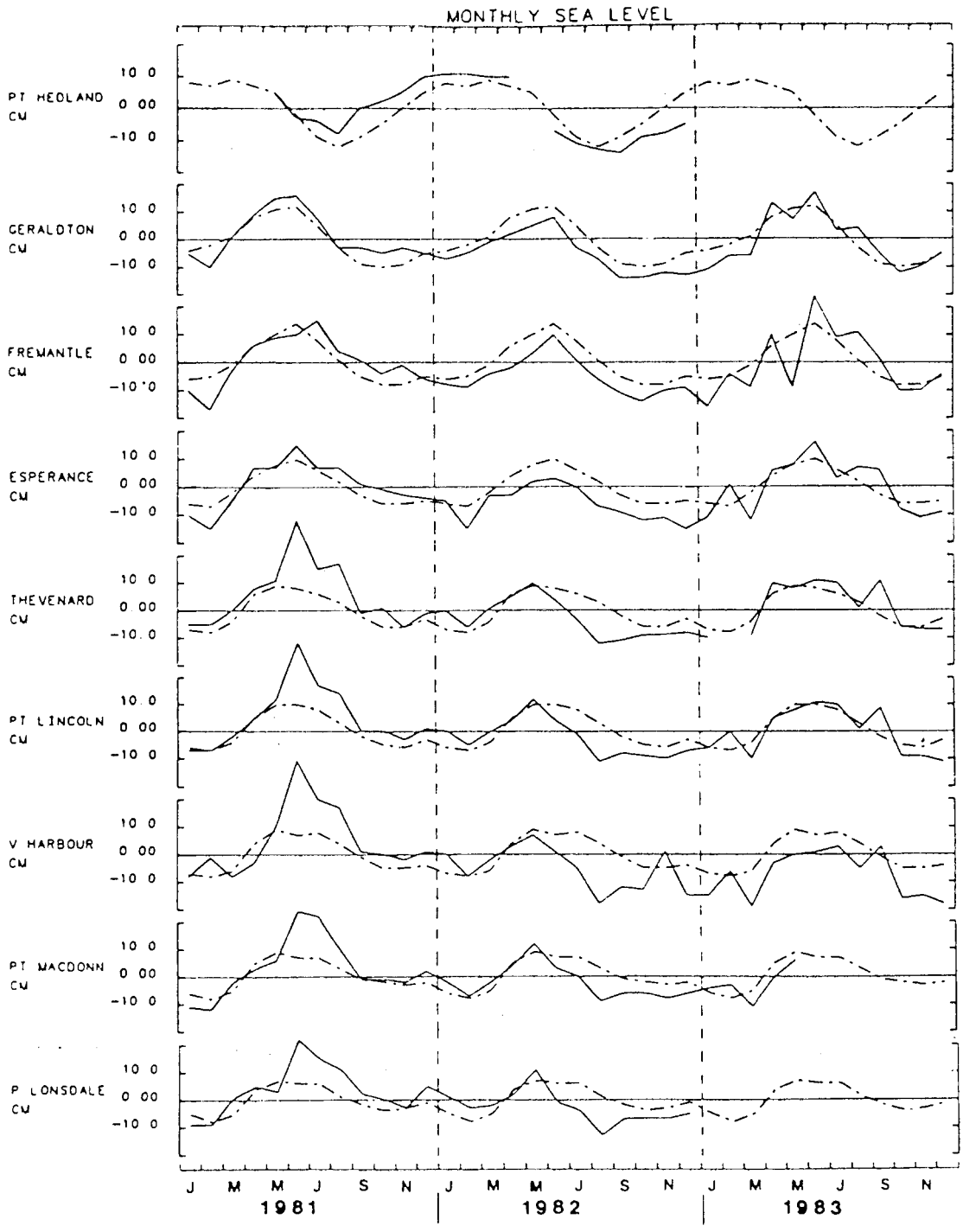

Figure 6.12: *A series of monthly mean sea levels for Port Headland on the northwest coast anti-clockwise to Point Lonsdale in Bass Strait for 1981, 1982 and 1983. The dashed line traces the long period mean. The continuous line traces the observed levels in the years indicated. Extracted from Pariwono et al. (1986).*

Clarke and Van Gorder (1994) have shown however that the ENSO currents close to the continental slope ($\sim$ 1300 m) are much larger ($\sim$ 10 cm s^{-1}) and are associated with the thermal wind shear of the first two Rossby waves modes and the distorting effects of bottom friction and topography. Moreover, the currents over the slope are around 180° out of phase with those near the surface. Such currents may well be important to the shelf-slope flow examined here since the strength of the FC can be enhanced or decreased during El Ninõ or La Ninã events.

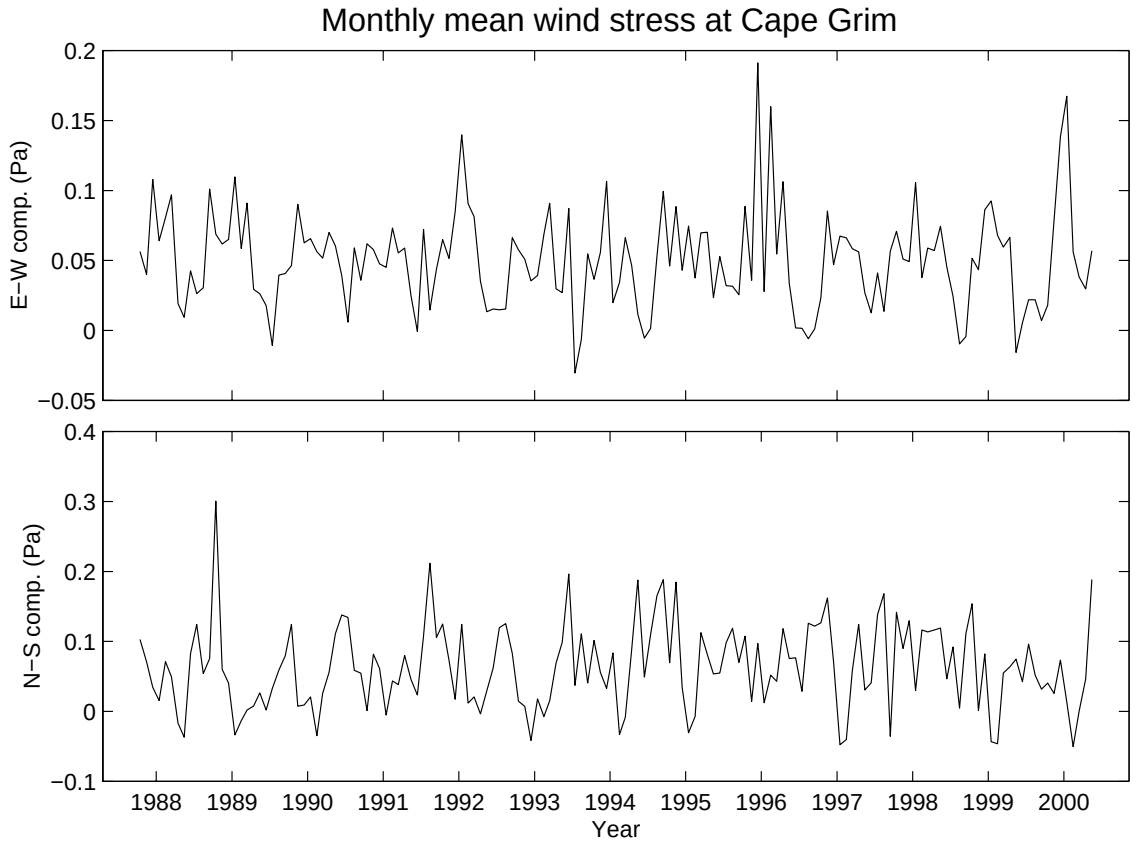

Figure 6.14: *Monthly wind stress averages at Cape Grim (Fig. E.1) between 1988 and 2000 based on the Bureau of Meteorology daily observations.*

Still in the context of remote forcing, since time series of local winds do not indicate a clear ENSO signal (Fig. 6.14), another issue that might be relevant within the SEIO circulation is the effect of both the Indonesian Throughflow (ITF) and LC transport within the SEIO region. Clarke and Liu (1994) found that the average interannual transport amplitude related to the ENSO is 2.5 Sv and has the tendency to be from the Indian to the Pacific Ocean when a warm ENSO event (El Ninõ) occurs and reverses for a cold ENSO event (La Ninã). Meyers (1996) using observations from 1983 to 1994

found similar results and for the 1988-1989 La Ninã the transport was 5 Sv larger than it was during the preceding and following ENSOs. Godfrey (1996) in his review of the ITF suggested that the ENSO events weakens the strength of the LC as well, where the El Ninõ acts to reduce the mean sea level along the Western Australian coast. The reverse occurs during a La Ninã event. Domingues et al. (1999) using 2 years of current meter data from 1994-1996 and for a transect at 22°S found that for the year of 1996 (La Ninã in Fig. 6.13) there was indeed a strengthening of the southward transport of the LC.

But the question is how variations in the ITF and LC can affect the circulation at the eastern region of the SEIO? Ribbe and Tomczak (1996), analysing the Fine Resolution Antarctic Model (FRAM) results, which does not include the ITF forcing found that its absence not only weakens the LC but results in a near coastal flow from the Tasman Sea to Cape Leeuwin. These results are also in agreement with the findings of Hirst and Godfrey (1993), who evaluated the influence of the ITF transport in their global model.

In summary, if there is a remotely forced interannual ENSO signal within the SEIO, it seems quite possible that it may influence the magnitude of the ZC during the La Ninã year of 1988 ($\sim$ 30 cm s^{-1}) as well as the El Ninõ years of 1997-1998 ($\sim$ 15 cm s^{-1}). Since the numerical results did not allow for such changes in the remote forcing field one would expect the results to be representative of a climatological situation only. In such a case, the modelled values would as found, lie in between the values estimated from the current meter data.

Chapter 7

Summary and Conclusions

The analysis of the OCCAM results together with the few observations available has allowed for the determination of a first order description of the wintertime circulation, summarised in Fig. 2.18. The downwelling favourable winds result in an alongshore eastward (poleward off the west coast of Tasmania) current near the coast, which extends uninterruptedly from Cape Leeuwin to the eastern coast of Tasmania, where it forms a confluence with the south branch of the East Australian Current (EAC). An additional forcing mechanism associated with the Coastal Current (CC) is the Leeuwin Current, which influences the western part of the domain as far east as 130°E (Herzfeld, 1997). Off the coast of Tasmania, the CC is named Zeehan Current (ZC). Below this surface current and with its core at the thermocline level, lies an westward (equatorward off the west coast of Tamania) current, which flows along the slope region with velocities up to 16 cm s^{-1} (Esperance).

The origin of the Flinders Current (FC) was shown to result from the northward Sverdrup transport associated with the positive wind stress curl. A comparison was made between the winter and summer seasons and the transport of the current found to vary from 5-10 Sv. This variation in transport is probably related to the change in the direction of the surface flow, which during summertime is in the same direction of the FC, as a result of the reversal of the coastal winds.

At the eastern side of the SEIO region an important feature in the overall circulation is the Victorian Low, a cyclonic gyre of around 200 km, which is induced by the combined effects of the poleward currents off Victoria and Tasmania and the westward currents south of Tasmania (the Tasman Outflow). This eddy is mainly seen in the top 300 m but it also influences the circulation at the thermocline level. The total transport associated with the low is around 5 Sv.

The net depth-integrated transport obtained from OCCAM compares well with the few observations available. At the southern tip of Tasmania and based on geostrophic cal-

culations, Tomczak and Pender (1998) found a westward flow of 16.4 Sv while Rintoul and Sokolov (1999) found 8 ± 13 Sv (Tasman Outflow). The OCCAM transport is 19.64 Sv. Using a global Sverdrup model Godfrey (1989) found a similar value of 20 Sv.

Compared to hydrographic data, the OCCAM model was able to reproduce features such as the deepening of the SML from 200 m in the western part of the domain (see Rochford, 1986) to 300-400 m around the coast of Tasmania (see Tomczak and Pender, 1998; Rintoul and Bullister, 1999) as well as the thermohaline structure of the surrounding currents (including the LC and the south branch of the EAC). In analogy to the results from Saunders et al. (1999), it appears that the model climatology is some 1°C warmer in the eastern SEIO.

The results noted above indicate that the OCCAM model is able to provide a suitable initial field (in terms of thermohaline structure and prescribed transports at the boundaries) for a high resolution nested model.

One result from the nested model is the change in the coastal circulation, where velocities are generally two times larger than those obtained from OCCAM. The regional model is also able to preserve the large-scale features, such as the Victorian Low, the overall distribution of the sea level and the transport of the Tasman Outflow.

For the eastern part of the SEIO region, the CC was generally found to be steady after 26 days of simulation. At regions where the shelf is very narrow, such as Kangaroo Is., velocities can be as large as 50 cm s^{-1}, while off the western coast of Tasmania typical values have are of order of 20 cm s^{-1}. The core of the current is generally constrained to the shelf-break region. At water depths less than 200 m, the current is in geostrophic balance with the sea level gradient and the thermal wind shear is negligible.

Off the South Australian region, the transport associated with the current (water depths less than 500 m) was found to be around 2 Sv while at the Victoria-Tasmanian region it did not reach values higher than 1 Sv. Close to 1 Sv passes through Bass Strait, where approximately 40% is related to local winds within the strait and 60% is due to the influence of the CC. If transports are estimated considering water depths of less than 1000 m instead of 500 m, values were found to be around 2 Sv at the Victoria-Tasmanian region and comparable with those found further west, where the current appears to be

more constrained to the coast.

Off the northwest coast of Tasmania, a northward coastal jet was found to enters the strait through the passage between Tasmania and King Is. The presence of this current was explained to result from geostrophic control of the CC and the effects of zonal winds within the strait. Notably, the jet also creates divergence in the alongshore currents and is why the poleward CC off the northwest coast of Tasmania, appears as a narrow core centered at the shelf-break region. Further south, the so called ZC is more uniformly spread over the shelf. Agreement with the current and drifter observations of Cresswell (2000) was also found in the confluence of the ZC with the southward EAC along the eastern side of Tasmania.

Below 300 m and over the shelf-slope, a FC is also found, steady after 26 days or so. The associated transport, between the 500 m and 4000 m isobaths varies between 5-7 Sv.

An important feature of the model results is the development of a succession of eddies over the shelf-slope, which have alongshore wavelengths of around 250 km and onshore an offshore flows of 3-4 Sv. The eddies were to result from baroclinic instability and in agreement with results obtained following Gill et al. (1974), have growth rates around 25 days for wavelengths of 250 km. The eddy activity found around Kangaroo Is. has also been observed by many authors and seems to be a permanent feature of the region (*e.g.* Bye, 1983b; Godfrey et al., 1986; Herzfeld, 1997).

The incorporation of heat and salt surface fluxes into the model led to a deepening of the SML (when compared to observed values), but resulted in more realistic coastal values of density. The effect of CTWs and tides, included in the model to enhance bottom friction, have little impact in the alongshore currents since these are strongly geostrophic. Increases in the along-shelf component of the bottom stress, for shallow water, can however lead to a increase in the offshore transport in the BBL. The enhanced bottom friction was effective in altering the velocity field within Bass Strait, where the transport through the Strait was reduced by approximately 15%. For this region, the tides are strongest and the bottom stress becomes an important term in the momentum balance.

At the western Tasmania shelf, analysis of two different data sets shown a poleward ZC with its core located at the shelf-break region (depth of 200 m). The current has an interannual variability and can vary from monthly averages of 15 cm s^{-1} to 30 cm s^{-1}. Below the ZC, results from one current meter at the 2040 m isobath (depth of 995 m) also shown the existence of a northward jet (the FC) of around 4 cm s^{-1}. Numerical results for the same depth compare very well with observations and suggest that a larger FC, with velocities around 10 cm s^{-1} and at depths of 500-1000 m may exist.

When numerical results are compared with the instruments at the core of the ZC (depth of 200 m), the wintertime monthly values (17-19 cm s^{-1}) lie between the 1988 (26-29 cm s^{-1}) and the 1997 (10 cm s^{-1}) observed values. Such a result might be expected since the numerical results are driven by a climatological average wind stress and transports along open boundaries. To evaluate the cause of the interannual variations in the observed currents, a study was made of possible local and remote forcings.

In terms of local forcing, the model was driven using 1988 winds. Despite the larger alongshore component of wind stress, the magnitude of the ZC was reduced compared with that driven by the climatological average. Local changes in wind stress do not appear to be the cause of the large ZC observed during 1988.

A review of the possible remote forcing mechanisms was also made and it appears that ENSO could be important in the strengthening of the ZC, through variations in the transports of both the Leeuwin Current and the Indonesian Throughflow. Possibly, during a La Ninã year (1988), the ZC is strengthened while during an El Ninõ year (1997-1998), the ZC is weakened. Probably, the reverse occurs for the FC, but this could not be verified due to the lack of data.

As a final remark, this study has contributed towards a better understanding of the complex system that exists at the eastern SEIO, its wintertime circulation and the possible causes for its interannual variation. Future areas of study might include the weather-band circulation and how the daily wind forcing and the associated passage of cold fronts and storms will influence the overall circulation. Detailed studies associated with the ENSO forcing, via changes in the coastal sea level and imposed interannual large-scale transports should also be addressed.

Appendices

Appendix A

Wind-Forced Downwelling Slope Currents: A Numerical Study (Middleton and Cirano, 1999)

abstract

A study is made of the dynamics of slope currents that arise from a steady, constant alongshore wind over a uniform shelf. Over the first 10-20 days, the evolution of the downwelled system on an f–plane is qualitatively described by linear coastal-trapped wave dynamics. After this time the thermal-wind shear associated with the bottom mixed layer becomes important in the evolution of the undercurrent (UC), which is shown to be driven by the alongshore pressure gradient due to sea level. As the UC over the slope evolves, the bottom Ekman transport becomes small and negative leading to the detachment of flow near the shelf-break, localised spreading of isopycnals and further intensification of the UC. In contrast to results obtained without bottom drag, bottom friction and boundary layer transport are shown to lead to a 2-3 fold increase in cross-shelf interior transport, downwelling and thermal-wind shear. By day 60, the resultant UC has speeds of up to $15\,\mathrm{cm\,s^{-1}}$ and a net transport of 0.7 Sv, or 2/3 of the surface Ekman transport. The alongshore transport associated with the UC is shown to be fed and drained by on- and offshore transports of comparable magnitude to the UC. The reduction in bottom stress over the shelf also leads to an alongshore current and density field that change little over many hundreds of kilometers. The sensitivity of results to the stratification, bathymetry and wind-stress curl is outlined and some suggestions made regarding the shelf circulation forced by winds within the Great Australian Bight.

A.1 Introduction

During the Austral winter, the mean winds within the Great Australian Bight are directed towards the east and drive an onshore Ekman transport that leads to downwelling and an

eastward current near the coast. While the shelf circulation in the far west is dominated by the inflow from the Leeuwin Current (Church et al., 1989), wind forced downwelling may be important over much of the eastern region. Indeed, Lyne and Thresher (1994) present observations which show that the poleward Zeehan Current off the west Tasmanian Coast averages speeds of about $50\,\mathrm{cm\,s^{-1}}$ over the winter months. An equatorward Undercurrent (UC) is also found (Vince Lyne, *pers. comm.*). However, while the Bight as a whole extends over more than 3000 km, few current meter observations have been made and the nature of the circulation remains to be determined.

Elsewhere, few investigations have been made into the slope circulation driven by seasonally downwelling favourable winds. The likely reason for this is simply that there are few regions explored to date where both downwelling favourable winds exist and the associated circulation is dominant. For example, along most eastern ocean boundaries, the winds are generally upwelling favourable (Neshyba et al., 1989), while along the western ocean boundaries, intense currents (driven by basin scale wind fields), dominate the slope circulation.

One exception appears to be the slope circulation over the Oregon and Washington shelves. Observations show (Hickey, 1989), that the alongshelf wind, coastal current (CC) and UC all reverse direction during winter. That is, the CC is poleward and in the direction of the wind while over the slope, an equatorward UC is found. A second example that highlights the importance of downwelling is the Leeuwin Current off the west coast of Australia where a poleward CC and equatorward UC are both found to have speeds of $20\,\mathrm{cm\,s^{-1}}$ or so, (Church et al., 1989). The downwelling here is caused by the meridional gradient of density in the Indian Ocean which, in analogy with wind forcing, drives an onshore flow within the surface mixed layer.

The motivation for the study below is to understand the dynamics of wind forced downwelling with particular regard to the circulation within the Great Australian Bight. As a first step we consider the response to a steady downwelling favourable wind with a finite alongshore fetch. Alongshelf bathymetric variations will not be considered. The problem is quite idealised but we have found no comparable study in the literature. Certainly, the problem of upwelling has received attention.

In an idealised study, McCreary (1981) adopted a vertical coastal wall and using a modal analysis, developed an analytical model for upwelling. A key result was that an alongshore pressure gradient and internal friction were necessary for the existence of a realistic UC. McCreary and Chao (1985), extended these results to obtain steady solutions over a shelf and found that unlike the flat ocean model, the UC was confined to the region of wind forcing. Within the UC, the cross-shelf flow was found to be downwelling favourable, while above it, an (Ekman) upwelling response was found. The strength of the UC was found to depend upon the following. First, the UC weakened and even disappeared as the depth of the shelf at the coast decreased to realistic values. In this case, the effective strength of the stratification was reduced. Second, on a β–plane, Rossby wave propagation was found to leak energy offshore, leading to a strengthening of the UC. Finally, an offshore increase in wind stress was shown to lead to a Sverdrup transport that enhanced the strength of the UC.

These results were complemented by the primitive equation studies of Suginohara (1982) and Suginohara and Kitamura (1984). Suginohara (1982) examined the short term (0–14 days) evolution of an upwelling favourable current system and found that a weak UC developed below the equatorward CC. The set-up of the current system was found to be qualitatively described by the passage of the first two coastal-trapped wave (CTW) modes.

Suginohara and Kitamura (1984) considered the long time (0–160 days) evolution of the current system and for an f–plane, found that the weak UC ultimately disappeared. Surprisingly, the inclusion of bottom friction did not lead to any substantial change in the results, suggesting that the bottom boundary layer plays only a minor role in the overall dynamics. Indeed, Suginohara and Kitamura (1984) claimed "the whole stage response is accounted for by CTW dynamics". In accordance with the results of McCreary and Chao (1985), these authors also found that the inclusion of the beta effect led to a strengthening of the UC, although again the magnitude was weak ($1.5\,\mathrm{cm\,s^{-1}}$) compared to the CC ($20\,\mathrm{cm\,s^{-1}}$). The UC was not found to extend far beyond the region of forcing and the marginal intensification of the UC was attributed to the leakage of barotropic energy by westward Rossby wave dispersion.

The above results raise some interesting points within the context of wind-driven down-

welling slope currents. First, since the analysis of McCreary and Chao (1985) is based upon linear equations, with a change of sign, all of their results are applicable to downwelling current systems. Moreover, since Suginohara and Kitamura (1984) find the long term f–plane response to be independent of bottom friction and explained by CTW dynamics, we might expect their results to also pertain to downwelling systems. That is, for a realistic shelf geometry with a shallow coastal region, we expect a weak UC to ultimately disappear, the long-term response to be independent of bottom friction and qualitatively described by inviscid CTW dynamics. As we will show, none of these expectations will be realised because of the thermal-wind shear that arises within the bottom mixed layer.

One dimensional models have shown that within downwelling boundary layers, the thermal-wind shear can be large enough to completely eliminate or "shutdown" bottom stress (MacCready and Rhines, 1993). In this case we might expect the results here to be independent of bottom friction as Suginohara and Kitamura (1984) found for the upwelling case. However, the shutdown of bottom stress leads to the arrest of the cross-slope Ekman transport. Since the slope and stratification typically vary across a shelf, variations in the Ekman transport can lead to the formation of fronts and profoundly effect the interior flow (Gawarkiewicz and Chapman, 1991). Most recently, Chapman and Lentz (1997) have shown that the downstream evolution of an alongshore current may involve a state of complete shutdown, so that the slope current may persist indefinitely! None of these studies included wind forcing, although the concepts developed will provide a framework for the analysis of the downwelled circulation.

With the wintertime circulation along the Great Australian Bight in mind, we will examine in detail wind-forced downwelling on an f–plane. A summertime stratification will be used for most of the study. There are two reasons for this. First, while wintertime cooling leads to a 100 m deep surface mixed layer within the Bight, over the shelf and slope, warm light water is driven eastwards over many hundreds of kilometres by the Leeuwin Current. During winter this water, and warm, saline water formed at the head of the Bight, form various tongues and meanders near the edge of the shelf and can be downwelled by 50–100 m (Legeckis and Cresswell, 1981; Rochford, 1986; Godfrey et al., 1986). Thus, even while the mixed layer is deep offshore, light water over the

shelf should act to locally replace the summertime thermocline that is otherwise found between depths of 25 m and 100 m (Levitus et al., 1994; Levitus and Boyer, 1994). A second reason for using the "summertime" stratification is simply that the UC is largest in this case and the dynamics of the current system most easily identified.

In section A.2, an outline is given of the boundary conditions and configuration of the Princeton Ocean Model (Blumberg and Mellor, 1987). In section A.3, an overview of the circulation is presented together with an examination of the role of CTWs in determining the initial circulation. The subsequent circulation and UC are examined in section A.4 in terms of the dynamics associated with alongshore pressure gradients, friction and thermal-wind shear within the bottom mixed layer. In section A.5, we examine the effects that arise from a β–plane, wind-stress curl and variations in bathymetry and stratification. In the summary (section A.6), some tentative suggestions are made regarding the circulation forced by wintertime winds within the Great Australian Bight.

A.2 Model Configuration

The numerical model used is the Princeton Ocean Model configured for the domain shown in Fig. A.1. We take x to be the offshore coordinate and y to be the alongshore coordinate. The shelf will be taken to extend from west to east as indicated since we are interested in downwelling over zonal shelves.

The shelf depth $h(x)$ is uniform in the alongshore direction and the top 280 m is illustrated in Fig. A.2. The shelf intercepts the deep ocean at (x, h) =(60 km,1000 m). As shown along the edge of Fig. A.1, the $x-$ grid size varies from about 2 km over the slope to 8 km at the edge of the shelf and then increases linearly by 20% to a maximum of 82 km at the southern end of the ocean basin (x=1017 km). The $y-$ grid size decreases from 40 km at the western end of the domain to 20 km at y= 500 km. For $y\epsilon$[500, 2500] km, the grid size is fixed at 20 km while further to the east, the grid size increases linearly to 60 km yielding an alongshore extent of 4000 km. A total of 45 and 145 cells are used in the $x-$ and $y-$ directions, while in the vertical 40 sigma levels are adopted with greatest resolution near the surface and bottom (Fig. A.2). To

satisfy the CFL criteria, the internal and external time steps are chosen to be 400 and 10 seconds respectively.

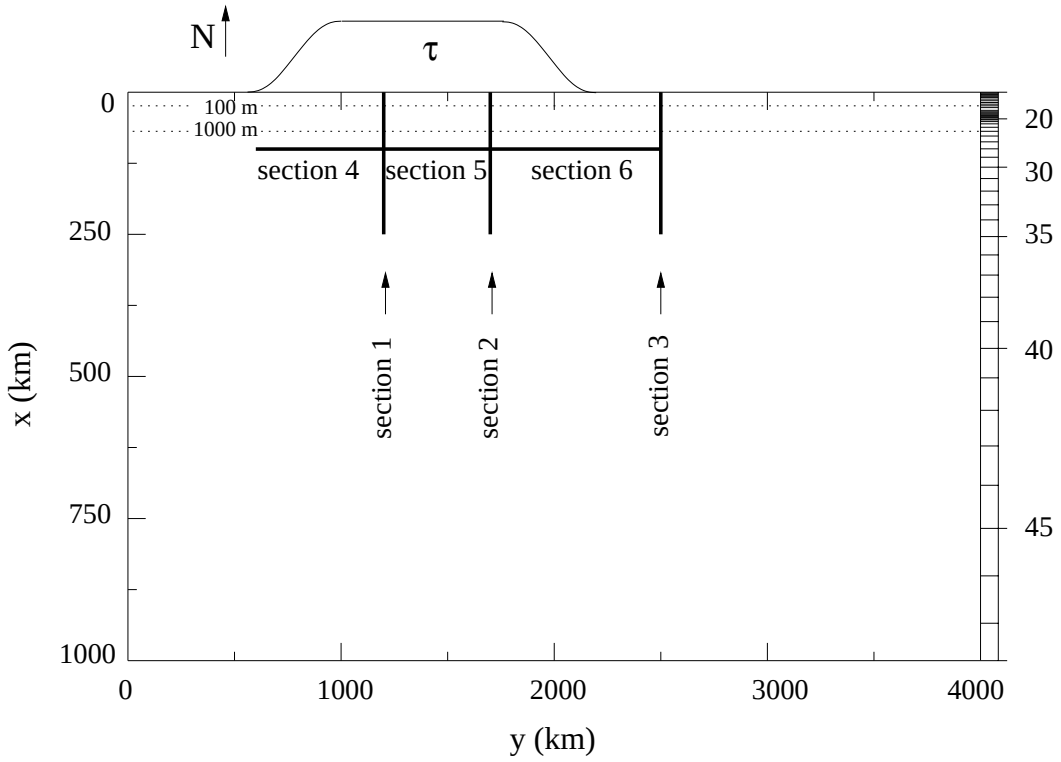

Figure A.1: *The model domain including the sections for analysis and the 100 m and 1000 m depth contours (.....) of the zonal shelf. The direction north (N) and region of wind forcing are indicated above the panel. The seaward ocean has a uniform depth of 1000 m and the cell width in the $x-$ direction is indicated on the right edge of the panel.*

The horizontal eddy viscosity (and diffusivity) and the bottom drag coefficient are taken to be 50 $m^2\,s^{-1}$ and $C_D = 2.5 \times 10^{-3}$ respectively and a Coriolis parameter for the southern hemisphere is chosen as $f = -10^{-4}$ s^{-1}. The vertical diffusivities of momentum, salt and heat are determined from the Mellor-Yamada turbulence closure scheme and are thus generally zero in the interior where the velocity shear is small. The surface and bottom fluxes of heat and salt are set to zero.

The initial density field (Fig. A.2) varies only with depth and is calculated from the summertime (January-March) seasonal climatology of Levitus et al. (1994) and Levitus and Boyer (1994) and for the South Australian region. From this initial field, the Buoyancy frequency N and Burger number $S = (Nh_x/f)^2$ were calculated and as shown in Fig.

A.2, the effective stratification indicated by S, is largest over the inner and outer shelf and small near the shelf-break ($h \approx 140$ m).

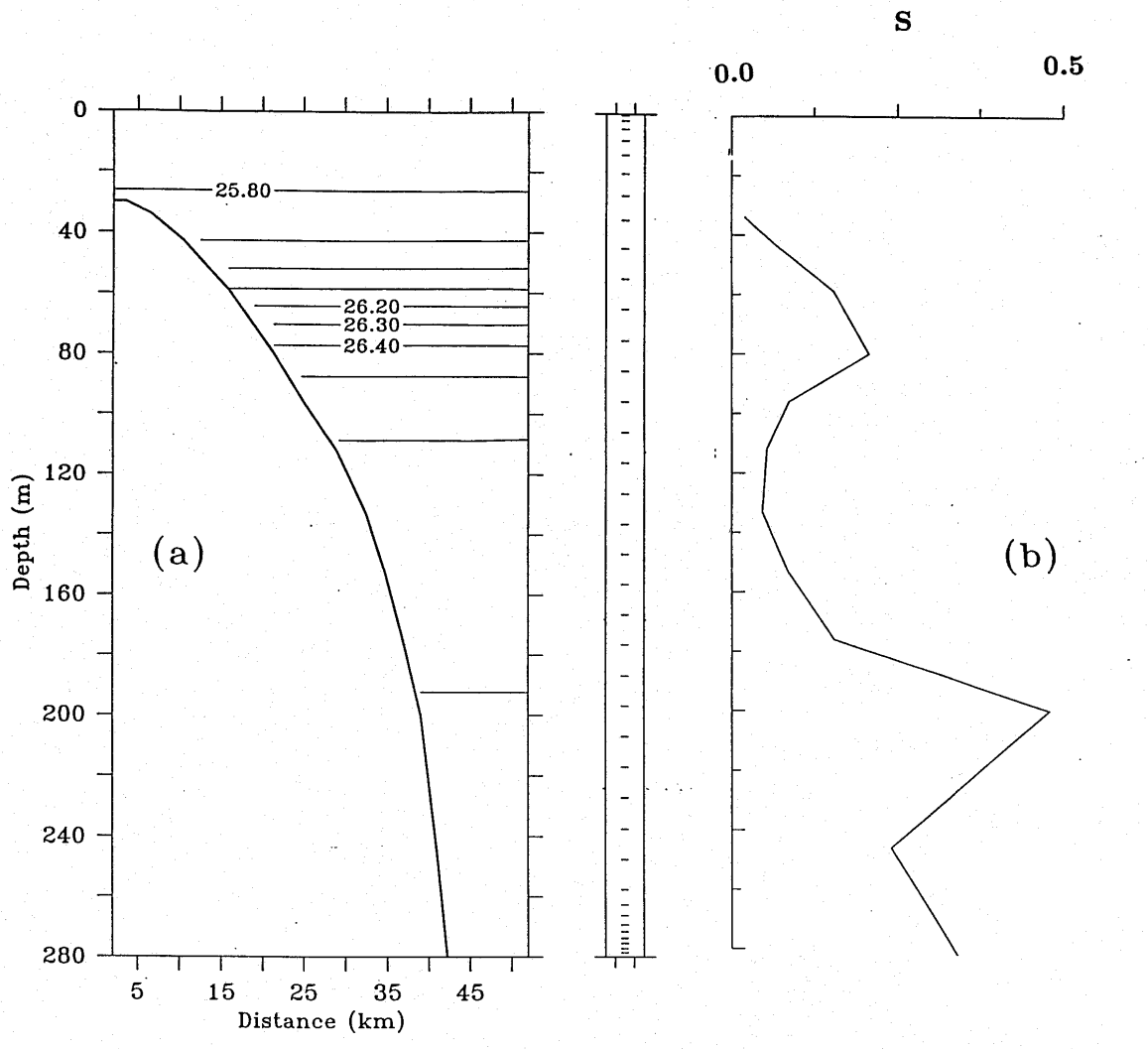

Figure A.2: *a) The shelf bathymetry to a depth of 280 m and the initial density field σ_t. Units kg m^{-3}. b) The Burger number $S = (Nh_x/f)^2$ based on the initial stratification. The vertical distribution of the 40 sigma coordinates is illustrated by the middle panel.*

The Burger number is important in the context of downwelling favourable flows since the time scale T_S for the shutdown of bottom stress and arrest of the cross-shelf Ekman transport is proportional to $S^{-3/2}$ (Garrett et al., 1993). For the case here (Fig. A.2), we might therefore expect the arrest of the bottom mixed layer (BML) transport over the slope to occur before it does near the shelf-break. As will be found, the resultant divergence in cross-shelf transport, in turn leads to the detachment of water from the BML into the interior and enhancement of the thermal-wind shear and magnitude of the UC.

The boundary conditions are similar to those adopted by McCreary et al. (1991). No energy should be present at the western boundary since in the southern hemisphere, CTWs can only propagate with the coast on the left. However, model results show that some energy does propagate to the west (along the southern open boundary) and so an Orlanski radiation condition was adopted for the western boundary. To absorb any residual energy near the western boundary, a Rayleigh sponge was adopted for sea-level η, the depth-averaged velocities (U, V) and the depth dependent velocities (u, v). For the sponge, the damping coefficient increases linearly from zero at y=433 km, to a value of 1/(2400 seconds) at the western boundary ($y = 0$).

A modified Orlanski condition was applied to all variables at the southern open boundary since use of an Orlanski condition led to large numerical instabilities after a few days of model evolution (McCreary et al., 1991). At the eastern boundary a zero gradient condition was applied so as to allow for the transmission of the wind-driven coastal current .

Forcing of the model was accomplished by an alongshore wind stress tapered in the alongshore direction from zero to a constant value of $\tau^w = 0.1$ Pa between $y = 1000$ km and $y = 1800$ km (Fig. A.1). The net surface Ekman flux is 1.2 Sv indicating an effective fetch of $L_w = 1200$ km.

The model solutions were found to be subject to weak 2-grid point instabilities that were most evident in the alongshore direction. Since the alongshore scale of the uncontaminated solutions should exceed the $3\Delta y$ scale of 60 km, the instabilities were kept under reasonable control by applying a Shapiro filter in the alongshore direction and to all time-dependent variables. For sea level the filter may be written as

$$\eta_{i,j} = (1 - \gamma)\eta_{i,j} + 0.5\gamma[\eta_{i,j-1} + \eta_{i,j+1}],$$

where once a model run day, γ was fixed at 0.5 so as to provide a severe filter. At all other time steps γ was fixed at 0.1.

As a check on artificial pressure gradients that arise from the sigma coordinate system, the model was run for 30 days without any wind forcing. As desired, the velocity field

was essentially zero and less than the maximum of 0.5 cm s^{-1} found over the outer shelf (depth 300 m).

In order to test the influence of the seaward (southern) boundary condition, results were compared with those obtained from a larger domain model. For this model, the domain was doubled in the offshore direction by forming a mirror image of the bathymetry about the $x = 1017$ km axis. The seaward boundary condition is thus replaced by a shelf and coast (at $x = 2034$ km) which serve to trap disturbances that there arise from upwelling. Moreover, to allow for the outflow of the westward CC along this shelf, zero gradient conditions were imposed along $y = 0$ and within 200 km of the new coast. The Rayleigh sponge at the western open boundary was relaxed to zero over $x\epsilon[1400, 1800]$ km and the drag coefficient increased from 2.5×10^{-3} to 2.0×10^{-2} over $x\epsilon[1400, 2034]$ km so as to damp the flow. Computational limitations meant it was necessary to halve the vertical resolution.

In summary, the solutions were found to be almost identical to those presented below using the smaller domain indicating that results are insensitive to both the seaward open boundary condition and vertical resolution. Again, problems associated with artificial pressure gradients do not appear to be significant.

A.3 An Overview and the Role of Coastal-Trapped Waves

Here we present an overview of the circulation over 60 model days. In agreement with the upwelling study of Suginohara (1981), the analysis below shows that the initial set-up and character of the circulation over the first 10–20 days is qualitatively described by linear, inviscid CTW dynamics. After this time, and in contrast to the upwelling case (Suginohara and Kitamura, 1984), CTW dynamics do not provide a definitive explanation of the circulation associated with the UC. Rather, the important dynamics here are related to alongshore pressure gradients and the evolution of the BML. These will be examined in the following section.

To begin, consider the results at day 10 (Fig. A.3a), which show that the onshore surface Ekman flux acts to raise sea level by about 12 cm near the coast. By day 30 (Fig. A.3b),

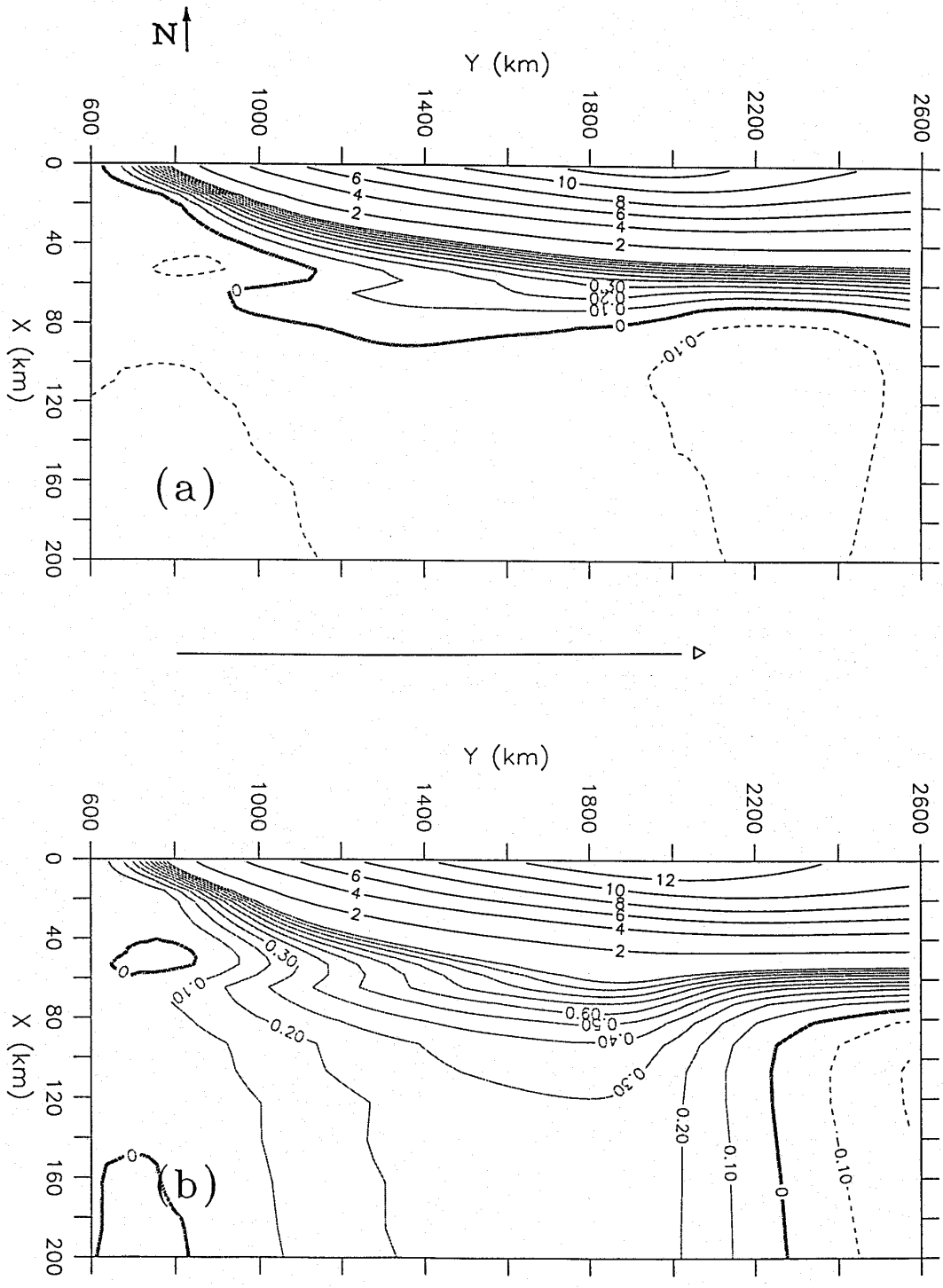

Figure A.3: *a) The sea level field at day 10. The contour interval is* 2 *cm for* $\eta \geq 1$ *cm and* 0.1 *cm for* $\eta \leq 1$ *cm. Dashed contours indicate negative sea level displacement. The direction north (N) is indicated above the panel. The region of wind forcing is indicated below the panel by the arrow and the edge of the shelf is located at* $x = 60$ *km. b) As in (a) but for day 30.*

the sea level pattern within 20 km of the coast has changed little although farther offshore, an alongshore pressure gradient (and cross-shelf flow) has been established which is shown below to be important to the circulation of the UC.

Below the surface and at section 2, a CC of up to $30\,\mathrm{cm\,s^{-1}}$ is found near the coast that also changes little between days 10 and 30 (Fig. A.4). At day 10 a weak UC is found but only at depths greater than 400 m or so. By day 30, the strength of the UC has increased to about $5\,\mathrm{cm\,s^{-1}}$ (maximum $8\,\mathrm{cm\,s^{-1}}$), is now found over the shelf-slope and extends to both sections 1 and 3 (Fig. A.5). At day 60, the magnitude of the UC doubles to about $10\,\mathrm{cm\,s^{-1}}$ (maximum $15\,\mathrm{cm\,s^{-1}}$). The continual downwelling also results in an increase in the depth of the BML from about 25 m at day 10, to 50 m at day 30 and 70 m at day 60. Over these times and over the outer slope, there is a steady increase in the downward tilt of the isopycnals. This tilt, in conjunction with the thermal-wind shear within the BML supports the strengthening of the UC shown in Fig. A.4.

Results for the cross-shelf circulation at day 30 are presented in Fig. A.6. The results at day 10 are similar. For clarity, the surface mixed layer is excluded from the plot and as shown, the return flow that is driven by the onshore Ekman flux is downwelling favourable at depths of 150 m or less. Near to the shelf and at depths greater than 200 m, the cross-shelf velocities are upwelling favourable. Part of this upwelling is associated with the Ekman transport within the bottom boundary layer, and as shown next, part with the larger scale circulation that is set up by the second mode CTW.

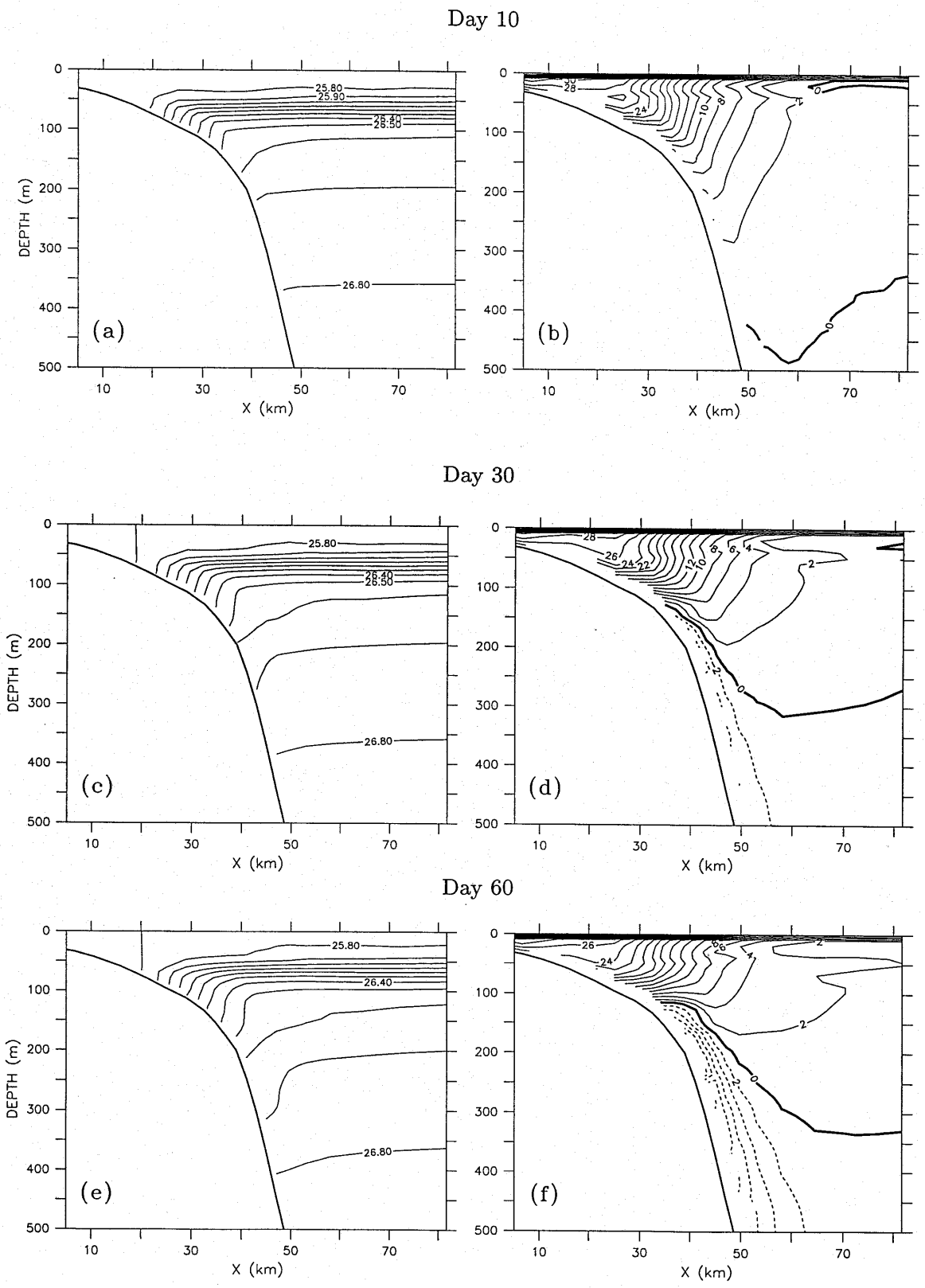

Figure A.4: *a) The density field σ_t at section 2 and at day 10. Units kg m^{-3}, interval 0.1 kg m^{-3}. b) The alongshore velocity field v at section 2 and day 10. The solid (dashed) contours indicate flow to the east (west). Units cm s^{-1}, interval 2 cm s^{-1}. c) and d) As in a) and b) but at day 30. e) and f) As in a) and b) but at day 60.*

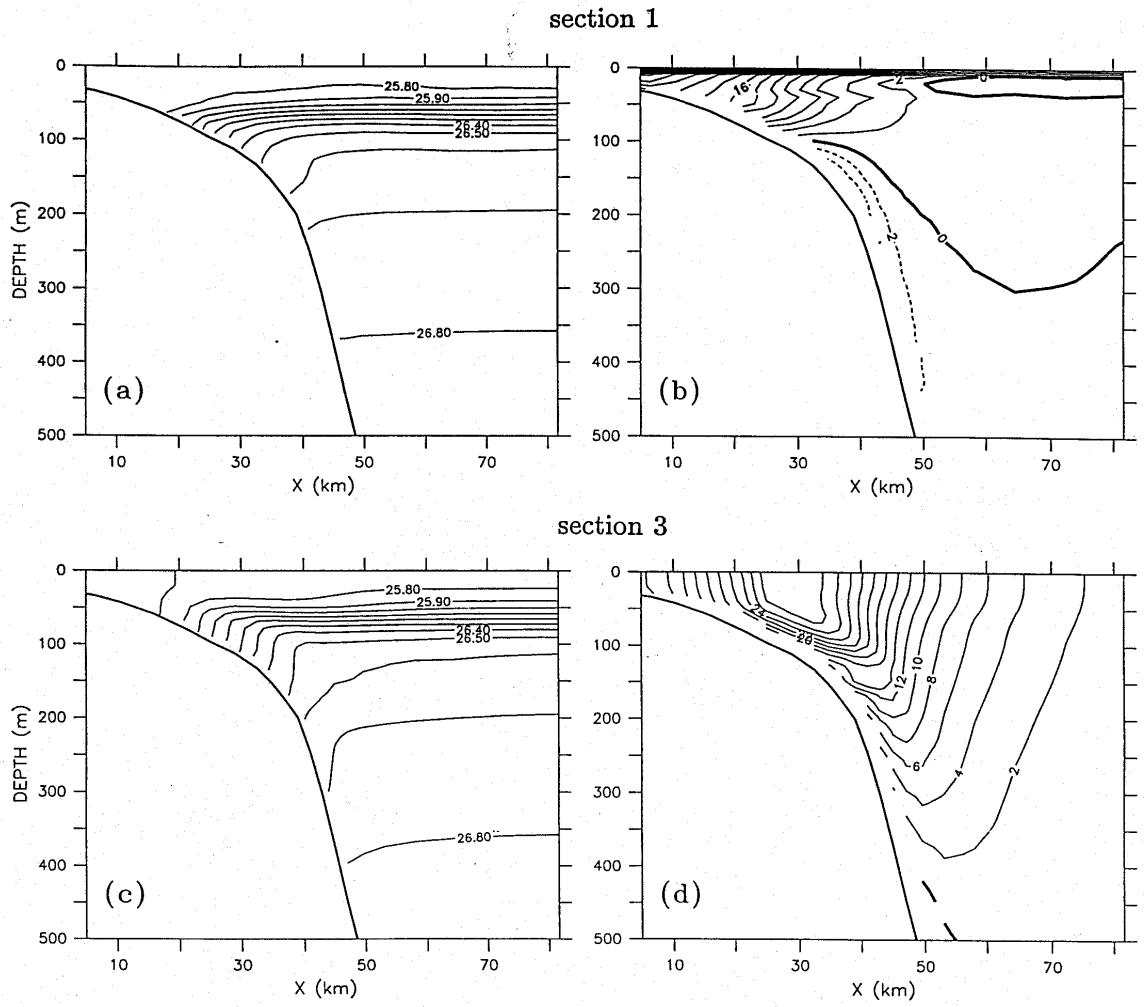

Figure A.5: *a) The density field σ_t at section 1 and at day 30. Units kg m^{-3}, interval 0.1 kg m^{-3}. b) The alongshore velocity field v at section 1 and day 30. The solid (dashed) contours indicate flow to the east (west). Units cm s^{-1}, interval 2 cm s^{-1}. c) and d) As in a) and b) but at section 3.*

a. A CTW model

A linear, inviscid coastal-trapped wave model for downwelling may be obtained by expanding the pressure field as a sum of orthonormal CTW modes $F_n(x,z)$ such that

$$p = \Sigma\phi_n(y,t)F_n(x,z) \tag{A.1}$$

where $v = (\rho_0 f)^{-1}\partial p/\partial x$, ρ_0 is the average density of the ocean and the ϕ_n satisfy the

forced wave equation,

$$\frac{1}{c_n}\partial\phi_n/\partial t + \partial\phi_n/\partial y = b_n\tau^w(y,t) \tag{A.2}$$

with c_n the phase speed of the nth mode and $b_n \approx F_n(0,0) \geq 0$ a coupling coefficient (Clarke, 1977). In accordance with the numerical model, we consider a top hat distribution of wind stress

$$\tau^w = \tau_0 \begin{cases} 1 & 0 \leq y^* \leq L_w \\ 0 & \text{otherwise} \end{cases} \tag{A.3}$$

where the transformation $y^* = y - 800$ km shifts the region of wind forcing to lie in the interval $y^*\epsilon[0, L_w]$. The fetch of the wind-forced region is denoted by $L_w = 1200$ km.

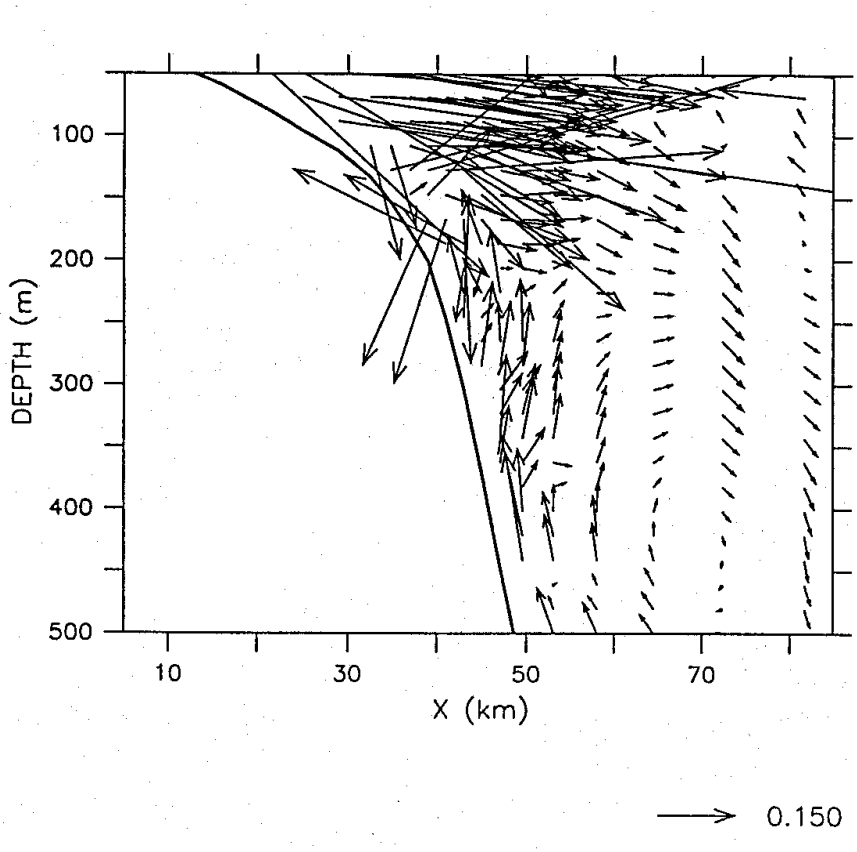

Figure A.6: *The* $(u, 100w)$ *vector field at section 2 and day 30. A vector of length* $0.15\,cm\,s^{-1}$ *vector is indicated.*

Within the wind forced region, the solution to (A.2) can be shown to consist of a CTW mode that grows linearly with time and is independent of y^*

$$\phi_n = c_n t b_n \tau_0, \tag{A.4}$$

until at a time $t = y^*/c_n$, a wave crest arrives from the western end of the forced region. A schematic of the solution is shown in Fig. A.7a. After the crest passes, the amplitude is steady and the alongshore pressure gradient that is established $\partial\phi_n/\partial y^* = b_n\tau_0$, partially balances the force of the wind. At the eastern end of the forcing region the amplitude of each mode is

$$\phi_n(L_w, t) = L_w b_n \tau_0 \tag{A.4b}$$

for $c_n t \geq L_w$. Thus, at times before the arrival of the first mode, both η and v are independent of y and grow linearly with time due to the contribution of all modes. Since $u_x + w_z = 0$ at these times, the onshore Ekman flux is largely balanced by a transport away from the coast and the downwelling is two-dimensional in character. After the passage of mode 1, an alongshore gradient v_y is established, but η and v also grow with time because of the higher modes. To the east of the forcing region $\tau^w = 0$, and as shown by the schematic solution (Fig. A.7a), the circulation is set up by the arrival of CTWs generated at both the eastern and western ends of the forced region.

To compare these predictions with the numerical results, the first two CTW modal eigenfunctions $F_n(x, z)$ were calculated using the programs of (Brink and Chapman, 1985). The phase speeds were determined to be $c_1 = 270\,\mathrm{km\,day^{-1}}$ ($3.12\,\mathrm{m\,s^{-1}}$) and $c_2 = 80\,\mathrm{km\,day^{-1}}$ ($0.93\,\mathrm{m\,s^{-1}}$) and the coupling coefficients were $b_1 = 0.13\ \mathrm{m^{-1/2}}$ and $b_2 = 0.068\ \mathrm{m^{-1/2}}$.

Now after the passage of the first two modes, coastal sea-level at the eastern end of the forced region must satisfy the inequality

$$\eta(0, L_w, t) \geq (L_w\tau_0/\rho_0 g)[b_1^2 + b_2^2] \tag{A.5}$$

since the growing contribution (A.4) made by the higher modes is positive. A similar result pertains to the alongshore velocity v and using values calculated for the first two

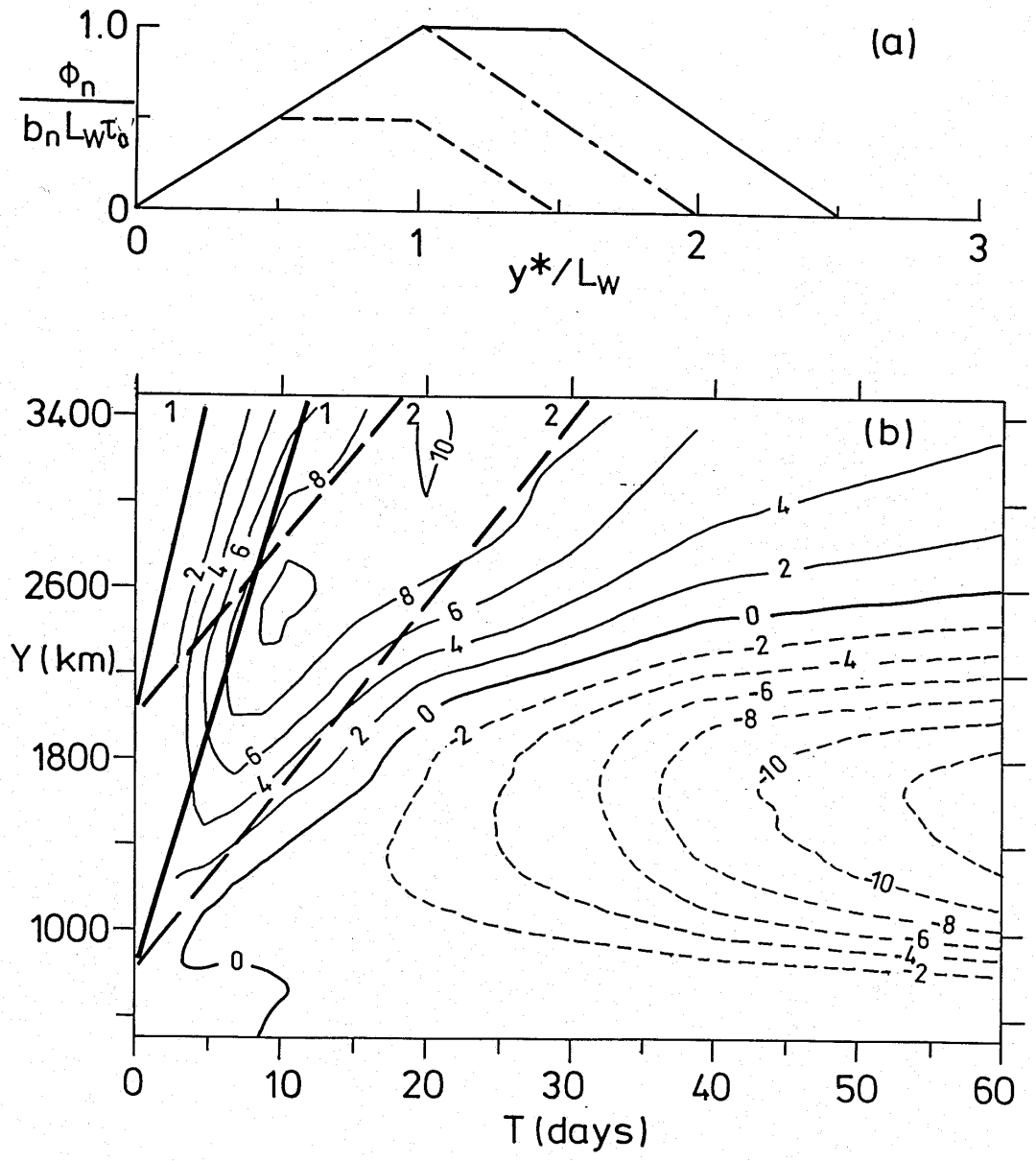

Figure A.7: *a) The CTW model solutions (A.4) for ϕ_n as a function of the alongshore distance y^* from the western end of the forcing region, and at times given by $c_n t = L_w/2$ (- - - -), $c_n t = L_w$ (— — —) and $c_n t = 3L_w/2$ (———). b) A phase plot of the alongshore velocity obtained from the numerical model and over the slope at (x, z) =(44 km,245 m). The solid (dashed) contours indicate flow to the east (west). Units cm s^{-1}, interval 2 cm s^{-1}. The straight lines labelled 1 (———) and 2 (- - - -) denote the lines of constant phase for the mode 1 and 2 CTWs that emanate from the western and eastern ends of the forcing region.*

CTW modes, the values of η and v at $(x, y^*) = (0, L_w)$ should exceed 27 cm s^{-1} and 120 cm s^{-1} respectively.

The values from the numerical model are much less, with η and v being about 13 cm and 30 cm s^{-1} over days 10–30. The discrepancy here is due partly to bottom drag which at the coast accounts for about half of the alongshore force needed to balance the wind stress (see Fig. A.10a below). Results obtained with bottom drag set to zero show that the alongshore gradient of sea level at the coast increases by a factor of two, leading to increases in coastal sea level and velocity (see Fig. A.11 below). The values obtained, $\eta \approx 20$ cm s^{-1} and $v \approx 100$ cm s^{-1} at $(x, y^*) = (0, L_w)$ and over days 10–30 were again smaller than those predicted by the CTW model.

Despite these discrepancies, the linear CTW model does reproduce some qualitative features of flow evolution. Presented in Fig. A.7b is a phase plot of the velocity v obtained near the slope and from the numerical model with bottom drag. Also shown are lines of constant phase for the first two CTW modes. Within the forcing region, and at times before the arrival of the first mode, the results are in accord with the CTW result (A.4): v increases with time and the alongshore gradients are small. After the passage of the mode 1 wave, an alongshore gradient in v is established in agreement with (A.4b). The amplitude of the slope velocity v then decreases with time. Part of this decrease may be attributed to the (locally negative) contribution made by the second mode although the arrival of this CTW has little impact on the shelf-slope results for v shown in Fig. A.7b. However, an additional feature of the second CTW is that the cross-shelf circulation changes sign near the shelf-break and such a result is found both at day 10 and day 30 in the numerical results (Fig. A.6).

Beyond day 20 there is no strong evidence of higher mode propagation and as will be shown, the continued evolution of the UC is due largely to the thermal-wind shear that arises from the BML.

b. Net transports

The role of the first mode CTW and evolution of the flow may be further examined by consideration of the net transports through the sections shown in Figs. A.1 and A.9a below. Reference will be made to the schematic of transport and the time line of events

shown in Fig. A.9b.

Consider first the depth integrated transport of water hV through section 2 (Fig. A.8a). At days 5 and 10, the transport is everywhere to the east and changes little with time within 20 km of the coast, indicating that here, it is set-up largely by the passage of the first CTW mode. Over the slope however, the growth in the UC leads to a net westward transport by day 30. By day 60, the transport directly associated with the UC is as large as the CC farther inshore.

Now consider results for the net transport $[V] = \int hV dx$, (integrated from the coast to $x = 100$ km). Consistent with the model solution shown in Fig. A.7a, the arrival of the first mode at section 3 leads to an increase in the transport over the first few days (Fig. A.8b). By day 10, the crest generated at the western end of the forcing region has arrived so that $v_y \approx 0$. The growth in the net transport $[V]$ is then substantially reduced, and the net alongshore transport remains close to 1.2 Sv. In the absence of higher modes, non-linear and viscous effects, all of the transport supplied by the wind must be carried by the first CTW mode.

Further evidence of the importance of the first mode is given by the transports through sections 1 and 2 which peak at times that correspond to the arrival of the mode 1 crest (day 3 and day 5). At these sections, v_y becomes positive (Fig. A.7a), and the net alongshore transports of 0.4 Sv and 0.9 Sv shown in Fig. A.8b closely reflect the onshore transport of water that is supplied by the wind (see Fig. A.9b).

After day 10, the transport through sections 1 and 2 decreases with time. The decrease here is due to the linear growth of the westward transport associated with the UC (Fig. A.8b) which by day 60 amounts to about 0.5 Sv and 0.7 Sv at sections 1 and 2. The corresponding transports of the CC are therefore 0.4 Sv and 0.9 Sv respectively and essentially unchanged from the values at around day 10. That is, the alongshore divergence of the CC accounts for nearly all of the mass flux that is driven onshore by the wind. These estimates are presented in the schematic shown in Fig. A.9a.

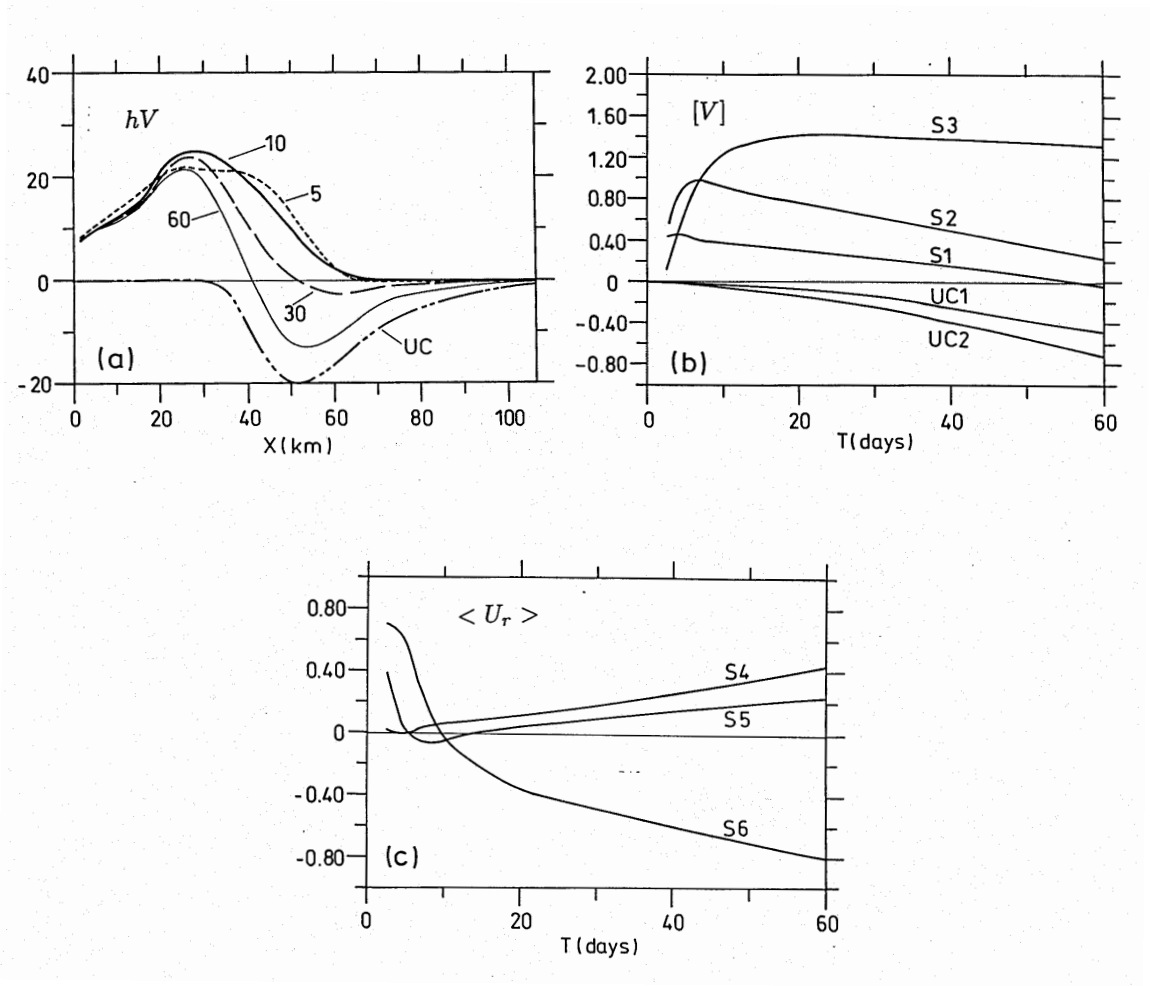

Figure A.8: *a) The net transport hV at section 2 and at the days indicated. The net transport associated with westward moving water (the Undercurrent) at section 2 and day 60 is labelled UC. Units $m^2\,s^{-1}$. b) Results for $[V] = \int hV dx$, integrated from the coast to $x =$ 100 km and at sections 1 (S1), 2 (S2) and 3 (S3). The integrated transport for the UC at sections 1 and 2 are labelled UC1 and UC2 respectively. Units Sv. c) The cross-shelf transport $< U_r >= \int hU_r dy$ through sections 4 (S4), 5 (S5) and 6 (S6). Note that the surface Ekman transport has been removed. Units Sv.*

Next consider cross-shelf transports through sections 4, 5 and 6. To facilitate the analysis, we define a cross-shelf residual transport hU_r to be the total transport, less the onshore surface Ekman transport (hU_E). Results for the *net* transport $< U_r >= \int hU_r dy$ through sections 4, 5 and 6, are presented in Fig. A.8c. At section 4, the residual cross-shelf transport is near zero over the first 10 days since the early passage of the first CTW crest sets up a divergence $v_y \geq 0$ which absorbs the onshore surface Ekman transport.

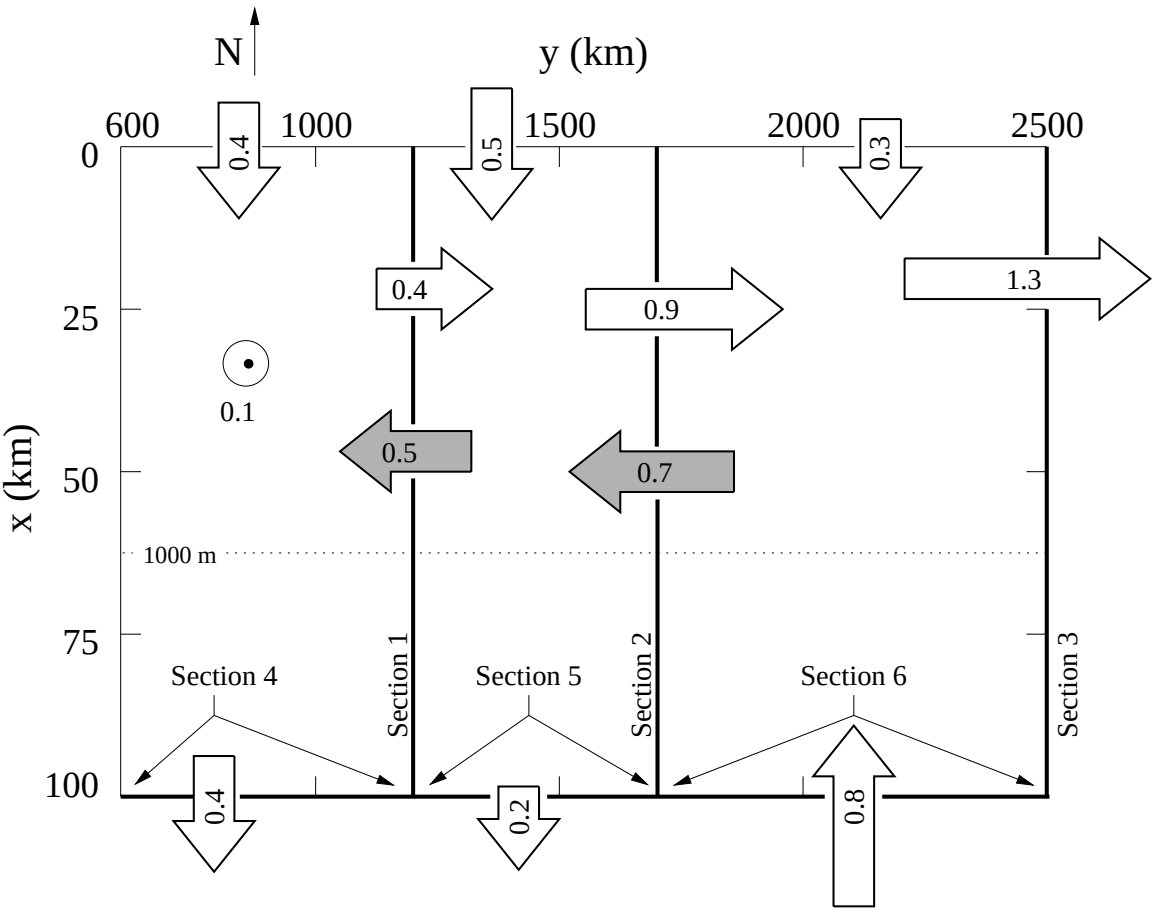

Figure A.9: *a) A schematic of the net transports (units Sv) through sections 1 to 6 at day 60. The direction north (N) is indicated above the panel. The eastward and westward directed arrows indicate the transport associated with the Coastal Current and Undercurrent (shaded). The offshore transports are indicated at the bottom of the panel. The transports indicated at the coast (top of the panel) correspond to the return flow driven by the wind-forced Ekman transport. The vertical transport to the west of section 2 and at a depth of 300 m is estimated to be about* 0.1 *Sv.*

At section 5, the CTW arrives later so that from the model solution (A.4), initially $v_y \approx 0$, and the offshore residual transport of about 0.4 Sv simply reflects the 0.5 Sv that is supplied by the wind. With $hU_r \approx -hU_E$ and $v_y \approx 0$, the downwelling over this initial period is two-dimensional in nature as indicated by the time line (Fig. A.9b). By day 10, and again following the arrival of the first CTW, the surface Ekman transport is again absorbed by the alongshore CC and the residual offshore transport drops to near zero.

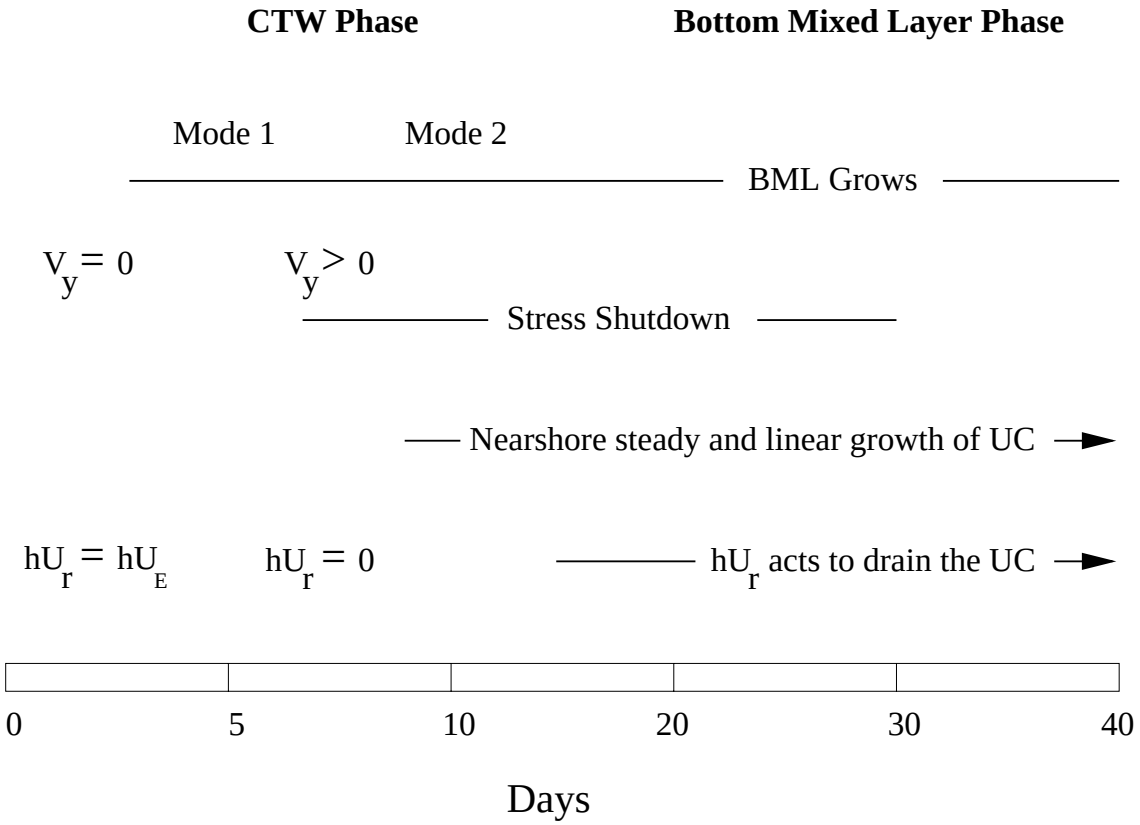

Figure A.9: *(continued) b) A time line illustrating the events in the circulation at section 2. (The time scale is not linear.) Before the arrival of the first CTW at day 5, the downwelling is essentially two dimensional and the onshore Ekman transport hU_E is mostly directed offshore into hU_r. After day 5, hU_E is redirected into the now divergent alongshore coastal current. The nearshore zone becomes quasi-steady upon arrival of the second mode CTW at around day 10. This mode also sets up a weak UC which then grows due to the increasing thermal wind shear associated with the BML and interior isopycnal tilt. The alongshore divergence of the UC drives an offshore transport hU_r through section 5 and onshore transport through section 6.*

Section 6 encompasses part of the region of wind forcing so that the offshore transport is driven by the surface flux and by the alongshore divergence of the CC in the unforced region. Again, the transport falls to near zero upon arrival of the first mode CTW that is generated at the western end of the forcing region.

While the initial transports are consistent with first mode dynamics, at later times they are dominated by the linear growth of the UC. By day 60 for example, the transports through sections 4 and 5, and through section 6 are respectively directed away and

towards the shelf (Fig. A.9a) and the values are consistent with the alongshore divergence of the UC. The onshore transport of 0.8 Sv through section 6 is largely redirected into the westward UC, and in turn drained offshore through sections 4 and 5. These cross-shelf transports are geostrophically supported by the alongshore gradients of sea level illustrated in Fig. A.3b.

These results suggest there to be little exchange between the CC and UC and estimates of upwelling based on the vertical velocity (300 m depth) indicate transports of only 0.03 Sv and 0.06 Sv through the horizontal sections $(x, y)\epsilon([0, 100], [600, 1200])$ and $(x, y)\epsilon([0, 100], [1200, 1700])$. Thus at zeroth order, the alongshore divergence of the CC can be accounted for by the supply of water from the surface Ekman flux, while within the forced region, the alongshore divergence of the UC leads to a cross-shelf circulation.

Finally, we return to the results for the cross-shelf velocity (Fig. A.6) which over the shelf-slope and within the BML, are notably chaotic in appearance. Results (not presented) show that the fluid is rising and falling along isopycnal surfaces within the BML and the circulation here has the characteristics of a slantwise convective instability (Emanuel, 1994). Such an instability was found by Allen and Newberger (1996) in a simulation of two-dimensional downwelling. Here the conditions for the instability are met including a change in the sign of the potential vorticity. The cross-shelf scale of the instability is of order v/f (Emanuel, 1994), or 1 km assuming $v = 10\,\mathrm{cm\,s^{-1}}$ for the shelf-break region. The instabilities are not well resolved since the model grid size $\Delta x \approx 2$ km is larger than the scale of the instability. In light of this, and the fact that the instabilities do not seem to have any impact on the larger scale circulation, no further discussion is made.

A.4 Dynamics: the Role of the Bottom Mixed Layer

Here the role of the BML and bottom friction in determining the circulation is examined. In particular, it is shown that the thermal-wind shear associated with the BML is important to the UC, while variations in the rapidity of shutdown of bottom stress and arrest of BML transport, can lead to the detachment of flow into the interior and

a further downwelling of isotherms. While bottom friction does become small over the slope, it is nonetheless shown to be important nearer the coast in determining the overall cross-shelf transport, degree of downwelling, thermal-wind shear and magnitude of the UC. An explanation for the cause of the UC is given and the evolution of the flow far from the forcing region examined.

To facilitate the analysis, terms in the depth-integrated momentum equations will be presented for section 2 and at day 30. In particular with g the acceleration due to gravity, and the pressure due to density (σ) denoted by,

$$p^{'} = g \int_{z}^{0} \sigma \, dz \tag{A.6}$$

the depth-integrated momentum equations may be approximated by

$$\rho_0 h \partial U/\partial t = \rho_0 f h V - \rho_0 g h \eta_x - h P_x \tag{A.7}$$
$$CFX \qquad SGX \quad DGX$$

and

$$\rho_0 h \partial V/\partial t = -\rho_0 f h U_r - \rho_0 g h \eta_y - \quad h P_y \; - \; \tau^b \tag{A.7b}$$
$$CFY \qquad SLY \qquad DGY \quad BSY$$

where the depth-average of (u, v) and $(p_x^{'}, p_y^{'})$ are denoted by (U, V) and (P_x, P_y). The (negligible) bottom friction term in (A.7) has been deleted, but retained in (A.7b). Non-linear and horizontal diffusion terms are neglected. The sum of the right-side terms while generally small, is presented below. In (A.7b), the alongshore wind stress τ^w has been subtracted from the Coriolis term and results for the (residual) Coriolis force $CFY = -\rho_0 f h U_r$ are presented.

The labels used for each term in the plots are indicated above and with a change of sign, the forces $SGX = -\rho_0 g h \eta_x$ and $DGX = -h P_x$ are also measures of the gradients of sea level and density. In the following, the sign change is taken to be understood when both these and the alongshelf forces SGY and DGY are referred to as gradients.

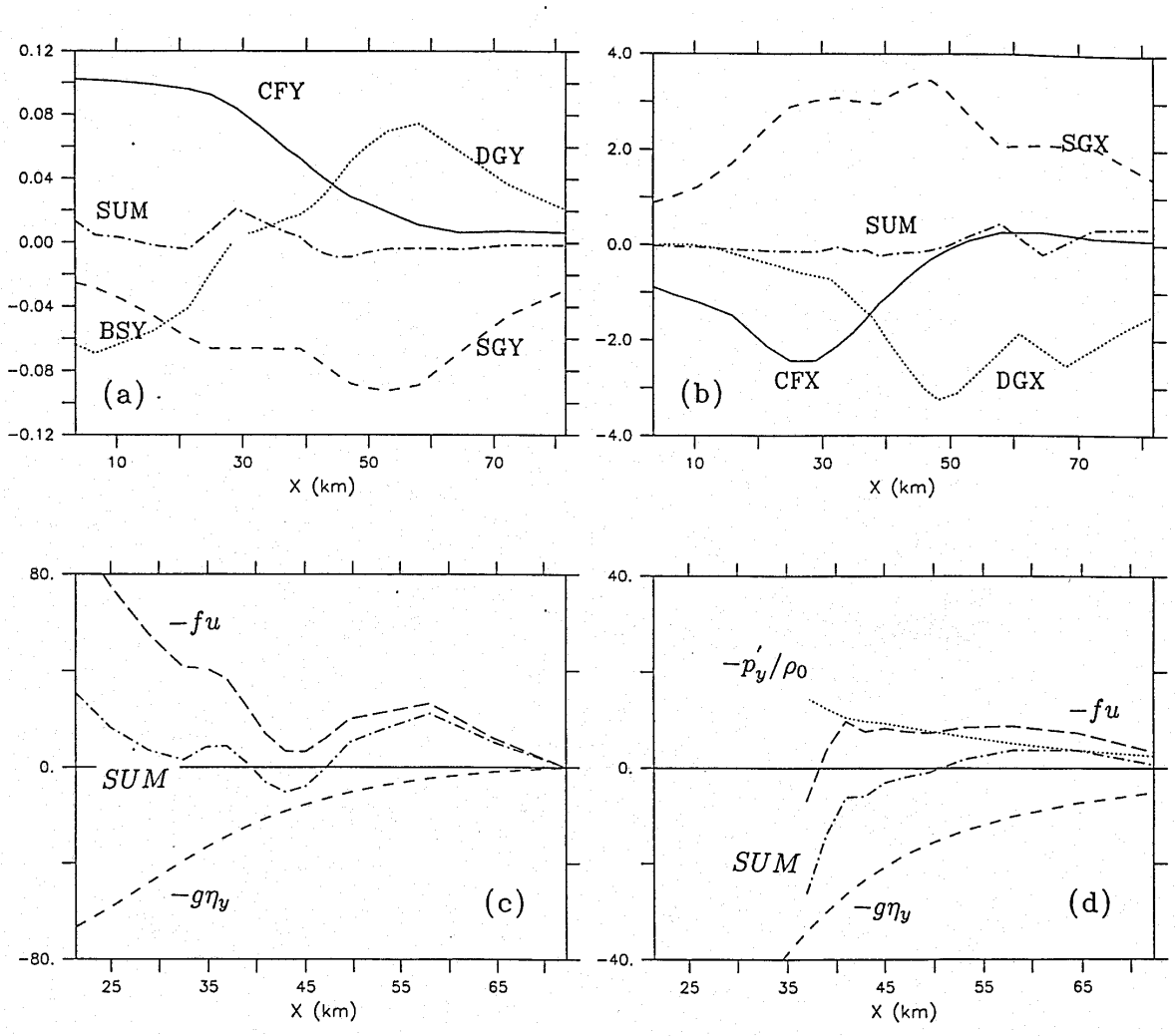

Figure A.10: *a) Results for the integrated alongshore momentum equation at day 30 and for section 2, (units, Pa). Indicated are the Coriolis force (CFY) associated with the residual cross-shelf transport U_r, the force (SGY) due to the alongshelf gradient of sea level, the force (DGY) due to the alongshore density gradient, the alongshore bottom stress (BSY) and the sum (SUM). Note that DGY is near zero for $x \leq$ 30 km while BSY is near zero for $x \geq$ 30 km. b) Results for the integrated cross-shelf momentum equation at day 30 and for section 2, (units, Pa). Indicated are the Coriolis force (CFX), the force (SGX) due to the cross-shelf gradient of sea level, the force (DGX) due to the cross-shelf density gradient and the sum (SUM). c) Day 10 results for the alongshore momentum terms $-fu$, $-g\eta_y$ and their sum at a depth of 50 m and for $y =$ 1500 km, (units, $10^{-8} \times ms^{-2}$). d) Day 30 results for the alongshore momentum terms $-fu$, $-g\eta_y$, $-p_y'/\rho_0$ and their sum at a depth of 150 m and for $y =$ 1500 km, (units, $10^{-8} \times ms^{-2}$).*

Now consider the nearshore region $x \leq 20$ km, where the water is well mixed (Fig. A.4). From Fig. A.10b, $CFX + SGX \approx 0$ so that the cross-shelf balance is strongly barotropic and geostrophic

$$fV = g\eta_x, \tag{A.8}$$

while the results in Fig. A.10a show that $CFY + SGY + BSY \approx 0$ and the alongshore wind stress is approximately balanced by the retarding forces that arise from friction and the gradient of sea level,

$$\rho_0 fhU \approx 0 \approx -\rho_0 hg\eta_y + \tau^w - \tau^b \tag{A.8b}$$

a. The Role of the Bottom Mixed Layer

Over the shelf-slope ($x \geq 40$ km), downwelling leads to cross-shelf density gradients (DGX) that are of similar magnitude to the large opposing sea-level gradients (SGX) and an UC is present. The maximum in the depth-integrated density gradient (DGX) occurs at ($x \approx 48$ km) while the maximum of the *depth-average* (not shown) occurs further inshore at ($x \approx 36$ km) and near the top of the UC. The density gradients here arise from the downwelled isopycnals within the BML and the inviscid interior. The contribution made by the shear within the BML to the depth-integrated density gradient is large and can be estimated from

$$DGX_B = -\frac{gh_B^2}{2}\partial\sigma_t/\partial x \tag{A.9}$$

if $\partial\sigma_t/\partial x$ is constant over the BML, height h_B. For section 2 and at $x = 36$ km, the numerical results show that $\partial\sigma_t/\partial x$ is about 3.5×10^{-5} kg m^{-4}, while the results in Fig. A.4d indicate the BML height to be about 70 m. The gradient DGX_B is then about -0.9 Pa or 75% of the total -1.2 Pa shown in Fig. A.10

Farther offshore, the density gradient is larger due to the increased tilt of isopycnals over the slope and spreading of isopycnals near the shelf-break (Fig. A.4). The spreading results from the convergence and detachment of the cross-isobath flow near the shelf-break (Fig. A.6) and is similar in appearance to that found by Gawarkiewicz and

Chapman (1991). They considered the evolution of a vertically uniform inflow along a linearly stratified shelf and found the bottom Ekman transport over the shelf to be blocked at the shelf-break and redirected into the interior. In their case, the blocking occurs because the bottom Ekman transport over the steep slope is effectively arrested due to thermal-wind shutdown within the BML. In terms of scales for shutdown, the Burger number S and effective stratification are larger over the steeper slope so that the time scale for shutdown $T_S = (S+1)/(C_D N S^{3/2})$ is smaller (Garrett et al., 1993; Middleton and Ramsden, 1996). The arrest of the Ekman transport over the steep slope occurs well before the arrest over the inner shelf and the flow within the BML is driven into the interior.

Here, the detachment of the cross-isobath flow near the shelf-break arises from the convergence of the offshore and upwelled circulation shown in Fig. A.6 and from the near arrest of the Ekman transport over the slope. The latter is illustrated in Fig. A.11 by the results for $hU_b = -\tau^b/\rho_0 f$, the offshore transport within the BML. Note that at day 30, the surface and bottom boundary layers merge within 25 km of the coast so that hU_b is only a useful measure of transport farther offshore. Over these distances the transport does change sign indicating a convergence and detachment of flow near the shelf-break.

The results in Fig. A.11 also show that the bottom transport and stress are more rapidly shutdown over the slope ($x \geq 30$ km) where the Burger number becomes large (Fig. A.2). The shutdown of bottom stress by the BML is also enhanced by the thermal-wind shear of the overlying isopycnals as shown by the calculation based on (A.9) above. About 25% of the integrated thermal-wind shear at $x = 36$ km was found to arise from the tilt of isopycnals above the BML.

Models for the downwelled BML have been developed assuming a constant slope, stratification and interior along-slope current. For example, Garrett et al. (1993) have shown that over several shutdown scales T_S, the BML height should grow towards a value of $h_D = v_i/NS^{1/2}$, where v_i is the alongslope velocity above the boundary layer. Such models are only of qualitative use in describing the BML here since the slope, stratification and alongshore current are not uniform and the latter evolve with time. For example, the $26.4\sigma_t$ curve shown in Fig. A.4e is advected and downwelled by 10 km and

70 m from the initial state.

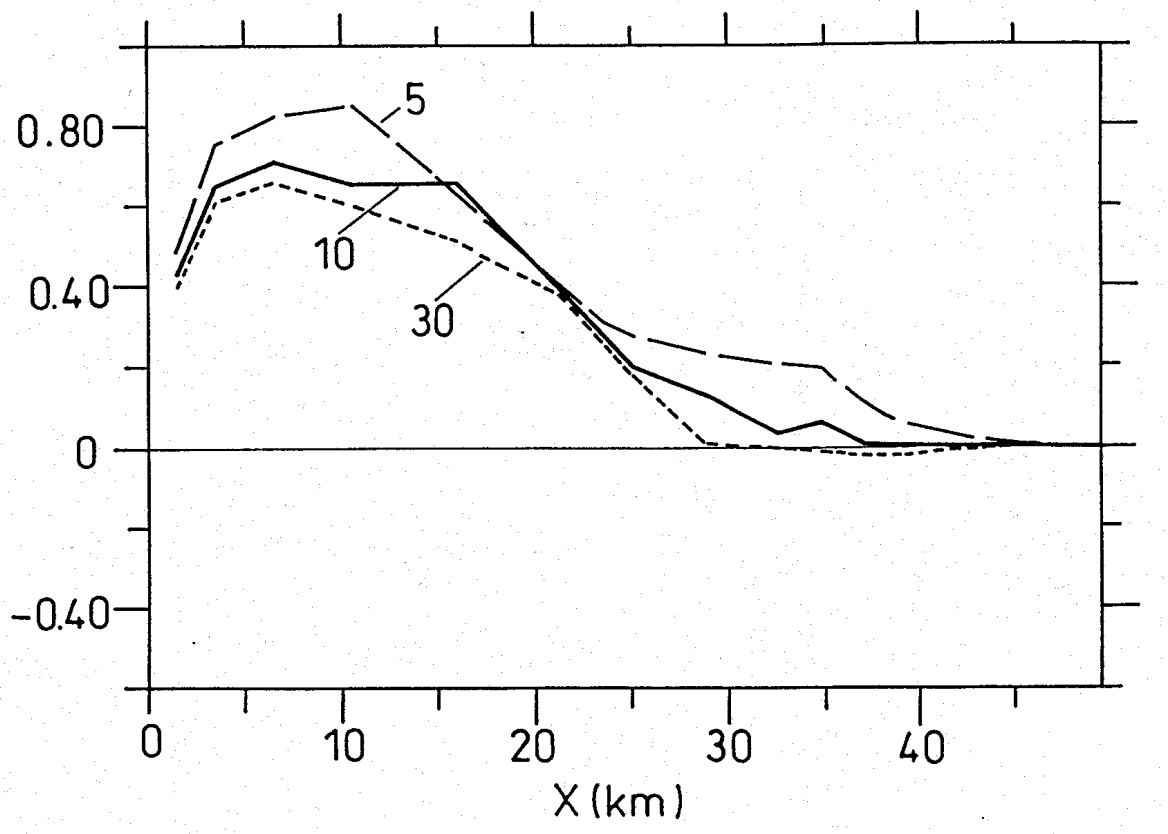

Figure A.11: *The offshore transport $hU_b = -\tau^b/(\rho_0 f)$ as indicated by the alongshore bottom stress τ^b at section 2 and at the days indicated. Units $m^2\,s^{-1}$.*

Nonetheless, let us estimate these BML scales for the $26.4\sigma_t$ isopycnal which lies initially at a depth of 80 m and intercepts the shelf at $x = 20$ km. Using the values of $S = 0.2$ and $N = 0.01$ at this point, we obtain $T_S \approx 6$ days and $h_D \approx 38$ m. A value of $v_i = 17\,\mathrm{cm\,s^{-1}}$ is taken from the numerical results at section 2. The shutdown scale is perhaps consistent with the reduction in bottom stress shown in Fig. A.11, although the predicted height is about half the 70 m found from the numerical model. These predictions can be improved if estimates of the stratification within the BML at day 30 are used. Assuming the scaling $\sigma_x = \sigma_z h_x$ and the value for σ_x noted above for the BML at $x = 36$ km, we obtain values of $N = 0.006$, $S = 0.34$, $T_S \approx 5$ days and $h_D \approx 50$ m. The choice of stratification and slope is somewhat arbitrary.

The events above are summarised in the time line (Fig. A.9b). Over the first 10 days, the dynamics are dominated by a CTW phase and a quasi-steady circulation is set up

near the coast. The shutdown of bottom stress begins soon after day 5 and is complete by day 30 leading to the detachment of BML water into the interior and spreading of isopycnals. Indeed, after day 10, the slope dynamics are characterised by a BML phase: the thermal-wind shear and UC over the slope increase linearly with time due to the growth of the BML and to a lesser extent, due to the increasing tilt of isopycnals in the interior.

To further examine the role of the bottom friction and the BML, results were obtained with the bottom drag coefficient C_D set to zero (Fig. A.12). In this case, the downwelling over the slope and magnitude of the UC are much weaker than where the BML was present (Fig. A.4c), while near the coast, the CC and cross-shelf gradient of sea level are much larger. The explanation for these results may be gleaned from the momentum balances shown in Figs. A.10 and A.12. In the absence of bottom drag, the current v accelerates so as to balance wind stress. This leads to a larger alongshore velocity and divergence v_y which is fed primarily by water supplied by the offshore transport hU_r. The reduction in the transport across the shelf is illustrated in Fig. A.12c where at $x = 25$ km, $\rho_0 f h U_r = CFY$ is about half that obtained where friction is present (Fig. A.10a).

Downwelling over the shelf is thus larger in the case where bottom drag is *non-zero*, and leads to a density gradient over the slope that is 2–3 times larger than that obtained with zero bottom drag. The sea-level gradient is also 2–3 times larger when bottom drag is present since more of the CC lies over the slope. Through geostrophy, the larger cross-shelf gradients of sea level and density support a larger UC.

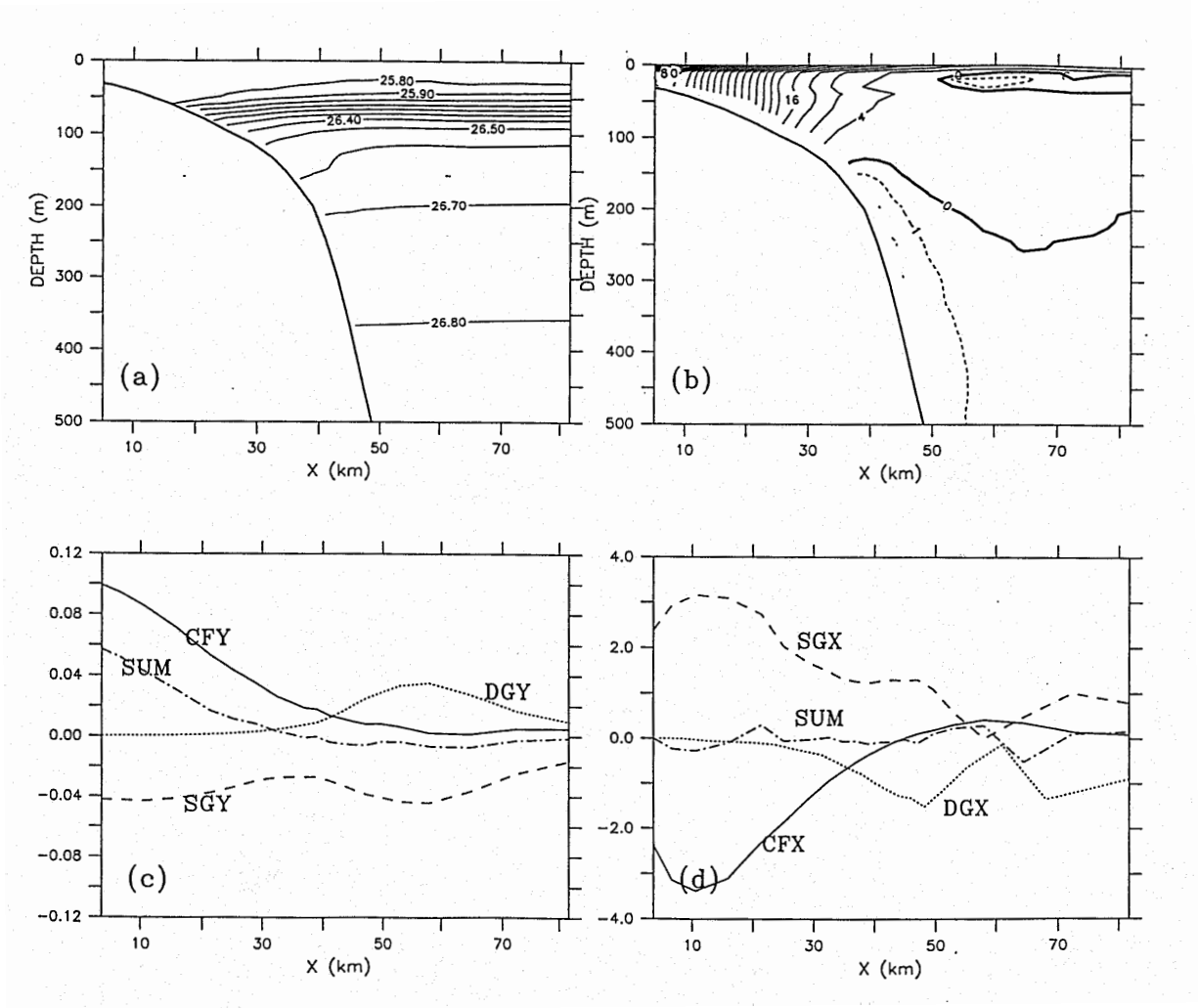

Figure A.12: *Results obtained at day 30 and for section 2 but with bottom drag set to zero. a) The density field σ_t at section 2 and at day 30. Units kg m^{-3}, interval 0.1 kg m^{-3}. b) The alongshore velocity field v at section 2 and day 30. The solid (dashed) contours indicate flow to the east (west). Units cm s^{-1}. Note that the contour interval is 4 cm s^{-1} (1 cm s^{-1}) for flow to the east (west). c) and d) Results for the alongshelf and cross-shelf integrated momentum equations at section 2. The labels are described in Fig. A.10 and in the text.*

b. The cause of the undercurrent

The presence of an UC in the results above may be contrasted with the two-dimensional circulation obtained when alongshore variations are precluded. The results of Mellor (1986) and Allen and Newberger (1996) show that under these conditions, an UC does not develop for downwelling (or upwelling) favourable flows and v is everywhere in the direction of the wind. The reason given here is that since $v_y = 0$, the onshore surface

Ekman transport leads to an offshore transport everywhere within the interior. The alongshore momentum equation reduces to $d[v+fX]/dt = 0$ in the inviscid interior and since the fluid parcel displacements X are positive, $-v/f$ and v must be positive and the latter in the direction of the wind. [Recall that f is negative.] Moreover, since v is positive and nearly geostrophic, the pressure gradient due to sea level must be greater than that due to density;

$$-\rho_0 g\eta_x \geq p_x^{'} \tag{A.10}$$

In the fully three dimensional results above, alongshore gradients exist so that the constraint (A.10) is relaxed, the pressure gradient due to density can exceed that due to sea level and an UC can exist. Thus, a necessary condition for an UC is that the wind act over a finite or semi-infinite fetch so that alongshore pressure gradients can exist.

The pressure gradient necessary to drive the UC can be gleaned from the alongshore momentum terms presented in Figs. A.10c,d. At day 10, and at a depth of 50 m, the Coriolis force $(-fu)$ due to the downwelling exceeds that due to sea level $(-g\eta_y)$, and thus acts to accelerate the CC (Fig. A.10c). The alongshore pressure gradient due to density is negligible at this depth. After day 10, the downwelling and acceleration become smaller and as noted above, the CC becomes quasi-steady.

Now consider the results in Fig. A.10d obtained at a depth of 150 m. Results are presented for day 30, since at this time the alongshore gradient due to density is significant and bottom stress and frictional effects are negligible. As shown, the alongshore gradient of sea level over the slope, $x\epsilon(35, 50)$ km, is larger than the sum of the Coriolis force $(-fu)$ and density gradient $(-p_y^{'}/\rho_0)$, since the downwelling and u diminish with depth. The alongshore gradient of sea level thus drives the UC, although through geostrophy, the magnitude is also determined by the degree of thermal-wind shear. Indeed, without thermal-wind shear, no UC could arise and the momentum balance would be just that given by (A.8): the alongshore current would be everywhere in the direction of the wind, while the alongshore gradient in sea level would be balanced by frictional stresses.

c. The far field

The behaviour of the velocity field far from the forcing region is also of interest. Results at $y = 3000$ km (not presented) show the solutions for both σ_t and v to be very similar to those for section 3 although friction does act to spread the maximum in the alongshore velocity a little more across the shelf. The amplitudes of the alongshore pressure gradients, bottom friction and cross-shelf transport ($CFY = \rho_0 f h U_r$) are similar and small at these sections being within 0.2 Pa or a $1/4$ of that found within the forcing region.

Similar results were reported by Chapman and Lentz (1997) who found that an initially narrow along-isobath current will spread across the shelf due to transport within the bottom boundary layer. As this layer grows in height, the associated thermal-wind shear reduces bottom stress and cross-shelf Ekman transport, until an equilibrium state is reached where bottom stress is completely shutdown and the boundary layer transport is arrested. For the results here, the shutdown of bottom stress and cross-shelf transport is not complete, although the conclusion is the same. A quasi-equilibrium state results in which the effects of bottom friction are small and the alongshore current can flow unimpeded over many hundreds of kilometres.

While these comments relate to the circulation outside of the forcing region, a striking feature of the solutions is that the details of the density field within the BML at section 3 (Fig. A.5c) are almost identical to those at section 2, (Fig. A.4c). Section 2 lies 800 km to the east of section 3 and 300 km inside of the forcing region. The alongshore velocity field at the two sections is quite different, so that the sea level fields must also be different.

The explanation for the similarity of the density field may involve the downwelling and mixing that should result from the adjustment of any along-isobath variations in density. For example, suppose that within the wind-forced region, the isopycnals are downwelled to form a BML and are in geostrophic balance with an along-isobath current. Assume also that the isopycnals are flat to the east of the forced region. Now in the absence of an opposing sea level gradient, the relatively dense fluid in the east will accelerate towards the BML, be deflected into deeper water by the Coriolis force and then mix vertically until the along-isobath density gradient is eliminated. The downwelling then ceases and once the water is mixed, it does not restratify immediately. Rather, it remains locked

in a state of thermal-wind balance even if the overlying alongshore current changes in time (Middleton and Ramsden, 1996). Through this process, the BML will tend to replicate itself along the shelf and in the direction of CTW propagation. Note that this adjustment process cannot occur to the west of the forced region since dense water would be deflected into shallower and not deeper water.

The adjustment of alongshore variations in sea-level will also give rise to a cross-isobath velocity, although unlike density, there is no process of advection and mixing to eliminate the along-isobath gradient. Rather, such an along-isobath gradient can be maintained through a geostrophic balance with the Coriolis force that is associated with the cross-isobath velocity.

A.5 The Effect of Varying Parameters

Here we consider the effects of spatial variations in the Coriolis parameter and wind stress and the sensitivity of results to the stratification and bathymetry. Our first goal is to examine the dynamical consequences of such variations relative to the basic downwelling case above and the upwelling results of Suginohara and Kitamura (1984). We also wish to examine these effects in the context of the wind-forced shelf circulation of the Great Australian Bight. However, since the stratification, bathymetry and wind stress vary considerably within the Bight, our aim here is to ascertain the qualitative nature of these effects rather than to provide an exact diagnosis of the shelf circulation.

a. Positive wind stress curl

Alongshore winds within the Bight (and in many other regions) increase in strength with distance from the coast. To investigate the effects of a positive wind-stress curl, we follow McCreary and Chao (1985) and let the stress distribution shown in Fig. A.1 increase linearly with distance from the coast

$$\tau^w = \tau_0 \begin{cases} 0.5\,[1 + x/L_s] & 0 \le x \le L_s \\ 1.0 & x > L_s \end{cases} \tag{A.11}$$

where $\tau_0 = 0.1$ Pa and $L_s = 60$ km denotes the width of the shelf. The stress distribution will lead to a 50% reduction in the nearshore surface Ekman transport and the numerical results (not presented) show a 30% reduction in coastal sea level relative to the basic curl-free case (Fig. A.3). The amplitude of the nearshore CC is also reduced by a similar amount (Fig. A.13b) and the net reduction in the offshore transport below the surface mixed layer leads to a reduction in the downwelling of isopycnals (Fig. A.13a).

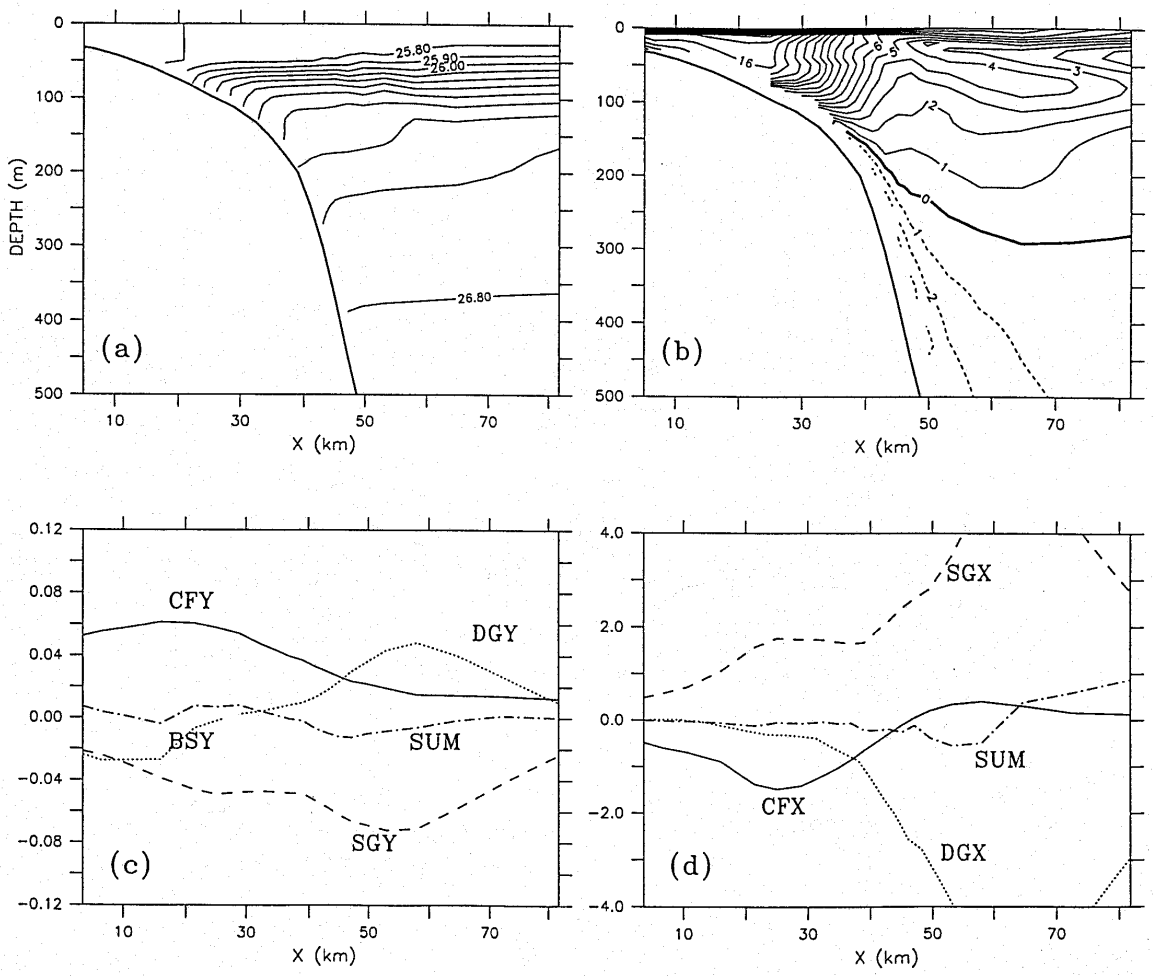

Figure A.13: *Results obtained at section 2 and day 30 with the positive wind stress curl (A.11). a) The density field σ_t. Units kg m^{-3}, interval 0.1 kg m^{-3}. b) The alongshore velocity field v. The solid (dashed) contours indicate flow to the east (west). Units cm s^{-1}, interval 1 cm s^{-1}. c) and d) Results for the alongshelf and cross-shelf integrated momentum equations. The labels are described in Fig. A.10.*

The reduction in downwelling is offset by the Ekman pumping associated with the curl of the wind stress. Over the shelf-slope ($x \geq 40$ km), the pumping acts to tilt the isopycnals down, raise sea-level and the cross-shelf gradients of sea level and density are

much larger than those found in the curl-free case (Fig. A.10b). Through geostrophy, these larger gradients support an intensification and spreading of the CC near the surface (Fig. A.12b) and an UC that is similar to that found in the curl-free case (Fig. A.4d).

By day 60, the CC and UC are similar to that shown in Fig. A.4f, but spread farther across the shelf since the Ekman pumping leads to a general tilt in both sea level and isopycnals. In the curl-free case the UC is narrower since the thermal-wind shear near the shelf is larger due to the thicker BML and spreading of isopycnals.

b. Wintertime stratification

As noted in the introduction, a feature of the wintertime stratification within the Bight is the presence of relatively light water over much of the shelf, while farther offshore, a 100 m deep, surface mixed layer results from mixing and cooling. Possibly, the results obtained using using the "summertime" stratification may be more indicative of the wind-forced currents during winter. In any case, it is worth determining the sensitivity of the results to the density field and solutions were obtained using a wintertime stratification (Levitus et al., 1994; Levitus and Boyer, 1994) and for the South Australian region (Fig. A.14a).

With no other changes to the basic case, the results at day 30 show that the presence of the deep surface mixed layer leads to a reduction in downwelling and in the magnitude of the UC. The latter is reduced to speeds of $1\,\mathrm{cm\,s^{-1}}$ and is only found at depths of more than 400 m. The near elimination of the UC results from the absence of the summertime thermocline and associated thermal-wind shear within and above the BML. From Fig. A.14d, the cross-shelf density gradient DGX is about $-0.2\,\mathrm{Pa}$ at $x = 36$ km and much smaller than the summertime value of $-1.2\,\mathrm{Pa}$ (Fig. A.10b).

The results in Fig. A.14 also show that the CC and gradients of sea level and density are generally smaller than found in the original summertime case. The simplest explanation for the weaker CC is that in the absence of the summertime thermocline, shutdown over the shelf is precluded and more energy is dissipated by the increased bottom drag. In the basic summertime case, thermal-wind shear led to a bottom stress BSY that was zero at $x = 30$ km. Here, the stress at $x = 30$ km is non-zero and leads to a decrease in the alongshore gradient of sea level since both must approximately balance the Coriolis

force CFY. The reduction in the alongshore gradient of sea level in turn leads to a reduction in the cross-shelf gradient SGX and velocity v.

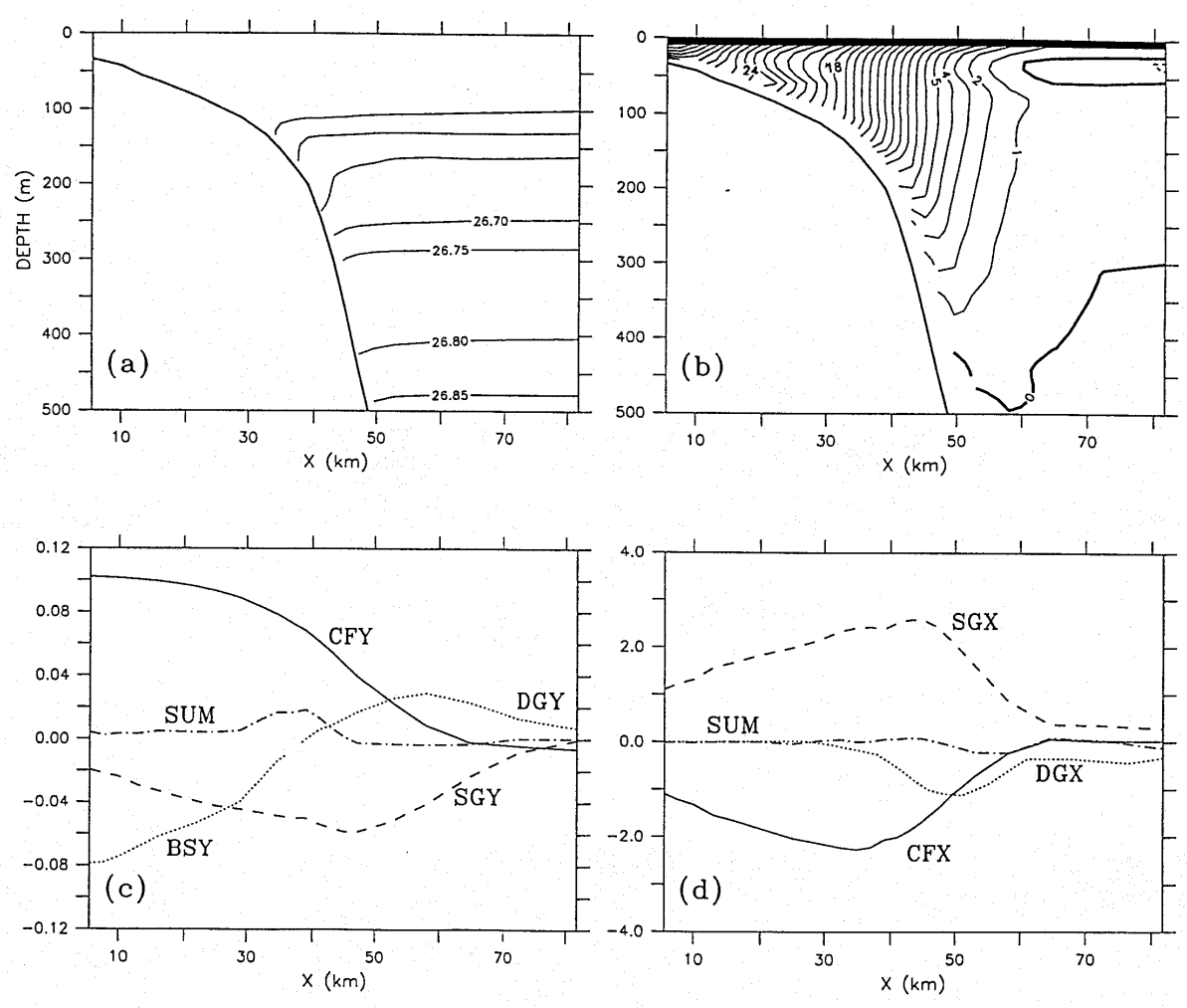

Figure A.14: *Results obtained at section 2 and day 30 with a wintertime stratification. a) The density field σ_t. Units kg m^{-3}, interval 0.05 kg m^{-3}. b) The alongshore velocity field v. The solid (dashed) contours indicate flow to the east (west). Units cm s^{-1}, interval 1 cm s^{-1}. c) and d) Results for the alongshelf and cross-shelf integrated momentum equations. The labels are described in Fig. A.10.*

c. Bathymetry

Within the Bight, the width of the shelf can vary from 40 km to more than 200 km. To illustrate the effect of a wider shelf, an extra 25 km of linearly sloping shelf was added to that above and between the depths of 50 m and 100 m. Using the summertime stratification, the results obtained (Fig. A.15) show that the nearshore velocity v is similar to that found in the original case. Farther offshore, the circulation is generally

weaker and near the shelf-break ($x \approx 65$ km), the near surface CC and gradient SGX are about 7 cm s^{-1} and 1.4 Pa or 40% smaller than found in the original case. The UC is also reduced in magnitude.

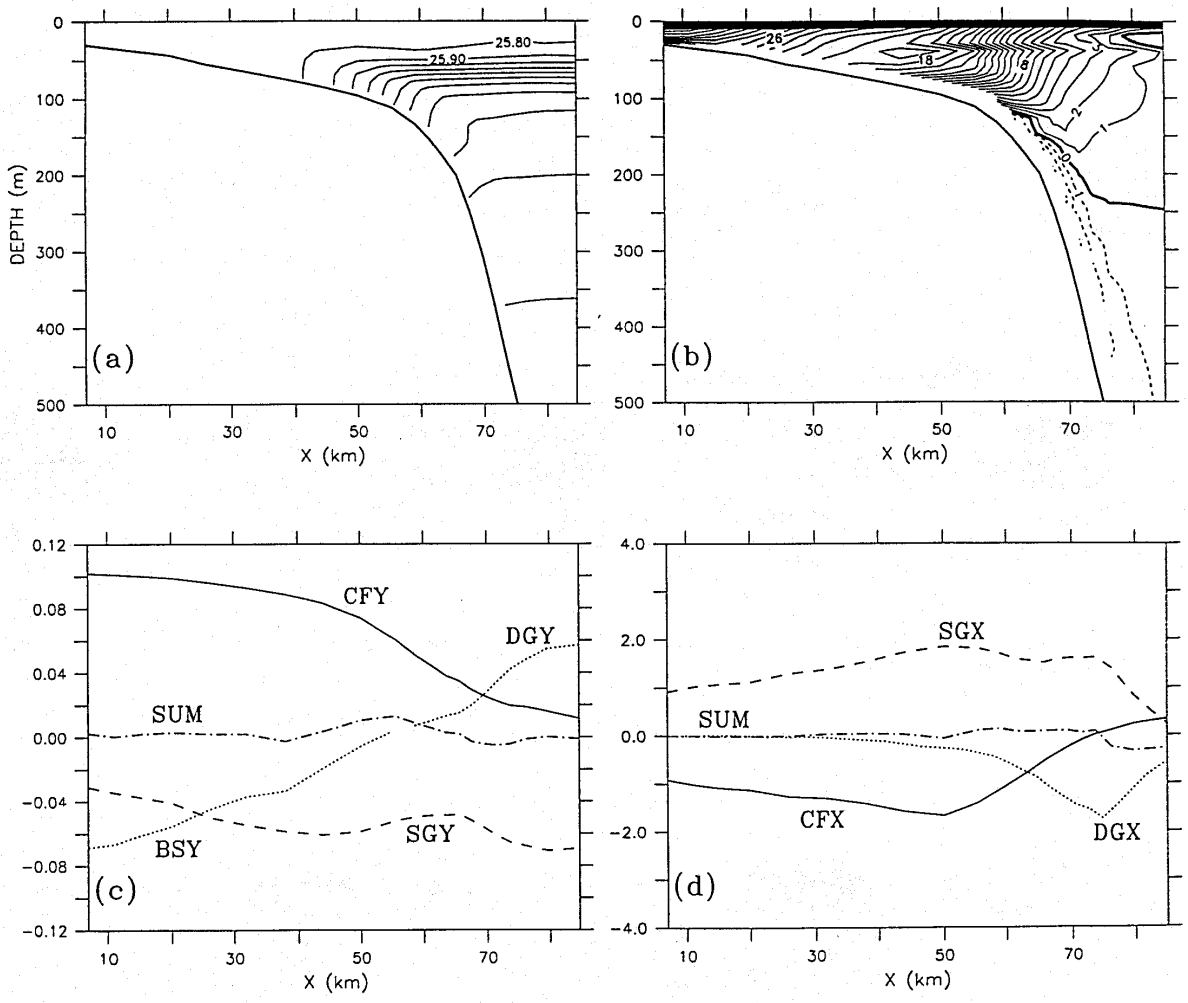

Figure A.15: *Results obtained at section 2 and day 30 with a 25 km wider shelf and the original summertime stratification. a) The density field σ_t. Units kg m^{-3}, interval 0.1 kg m^{-3}. b) The alongshore velocity field v. The solid (dashed) contours indicate flow to the east (west). Units cm s^{-1}, interval 1 cm s^{-1}. c) and d) Results for the alongshelf and cross-shelf integrated momentum equations. The labels are described in Fig. A.10.*

The explanation for these results involves the wider shelf which effects the circulation in two ways. First, vertical mixing within 40 km of the coast eliminates thermal-wind shear and leads to an increase in drag over more of the shelf (Fig. A.15c). The circulation is weakened. Second, since the (divergent) alongshore transport of the CC is spread over a shelf of greater width, the associated sea-level gradient SGX and cross-shelf transport

near the shelf-break are reduced. For example, the results for CFY in Fig. A.15 ($x = 65$ km) indicate a 30% reduction in hU_r relative to that shown in Fig. A.10 ($x = 40$ km). Downwelling and the cross-shelf density gradient are reduced by a similar amount but an UC results that is similar to that found in the basic case since the opposing contribution made by the sea-level gradient SGX is also reduced.

These results may be extrapolated to a very wide shelf such as that found in the central region of the Bight. For such a shelf, the cross-shelf transport that is driven by the wind may be spent over the shelf in supplying water to the divergent CC. Near the shelf-break the offshore transport may be near zero and a wind-forced UC may not exist.

d. The Beta effect

While the Bight is predominantly zonal, the shelf veers some 900 km to the south at the eastern end so that Rossby wave dispersion of energy may be significant. In an upwelling study, Suginohara and Kitamura (1984) found that such dispersion led to a strengthening of the UC. They chose a β–plane centered on the Coriolis parameter $f_0 = 0.5 \times 10^{-4}$ s^{-1} so as to approximate the latitude of the southern Californian Shelf. Here we adopt the β–plane approximation $f = f_0 - \beta[y - L_c]$, where $\beta = 1.6 \times 10^{-11}$ m^{-1} s^{-1}, $L_c = 2000$ km and the value $f_0 = -10^{-4}$ s^{-1} is chosen to reflect the higher latitude of the eastern Bight.

With all other parameters unchanged, the model was run for 60 days and the circulation over the shelf was found to be almost identical to that obtained for the basic f–plane case. The reason for this would appear to involve the slow phase speed of the internal Rossby waves that are important for the adjustment of the circulation. Anderson and Gill (1975) derived a time scale for this adjustment to be

$$T_\beta = 4r_i/c_R = 4/\beta r_i, \tag{A.12}$$

where r_i and $c_R = \beta r_i^2$ are the internal deformation radius and Rossby wave speed. The scale (A.12) gives the time it takes for an internal Rossby wave to travel 4 internal deformation radii away from the shelf. Here, r_i is in the range (5-10) km so that $c_R = (0.4 - 1.6) \times 10^{-3}$ m s^{-1}. The scale $T_\beta = (290 - 580)$ days is larger than the

integration time of 60 days, and much larger than the 180 day seasonal scale of winds within the Bight. Rossby wave dispersion may not be important for this region.

Suginohara and Kitamura (1984) on the other hand considered upwelling closer to the equator and chose $f_0 = 0.5 \times 10^{-4}$ s^{-1} and $\beta = 2 \times 10^{-11}$ m^{-1} s^{-1} leading to a larger deformation radius $r_i = 24$ km, faster phase speed $c_R = 1.2 \times 10^{-2}$ m s^{-1}, and shorter adjustment time, $T_\beta = 96$ days. Certainly their results (Figs. 6 and 10) indicate phase speeds of order 10^{-2} m s^{-1} and that dispersion is important after a 100 days or so.

A.6 Summary and Discussion

Using the Princeton Ocean Model, a study has been made of wind-forced downwelling slope currents on a zonal shelf and f–plane. In agreement with the upwelling study of Suginohara (1982), the evolution of the current system over the first 10-20 days was characterised by a linear CTW phase and notably by the propagation of the first mode. In particular, before the arrival of this mode, the downwelling was two-dimensional in nature, and almost all of the wind-driven Ekman flux was redirected offshore at depth. After the arrival of the first mode, a divergence of the alongshore transport was set up, and fed largely by the onshore Ekman transport due to the wind.

After this initial CTW phase, the dynamics of downwelling and upwelling systems appear to be quite different. Suginohara and Kitamura (1984) report that the upwelling system is insensitive to the presence or absence of bottom drag. They also claim that the long time (0–160day) evolution of the upwelled system is accounted for by CTW dynamics and find that the UC ultimately disappears on an f–plane.

None of these conclusions appear valid for the downwelling case here since the dynamics after 10 days or so are primarily governed by a BML phase. During this phase the depth of the downwelled BML grows and thermal-wind shutdown occurs. Indeed, within the forcing region, the thermal-wind shear associated with the BML was shown to account for up to 75% of the depth-integrated total and to be important in determining the magnitude of the UC. The shutdown of bottom stress over the slope was also shown to be important for the detachment of flow and spreading of isopycnals near the shelf-break.

Such spreading leads to an increase in the thermal wind and magnitude of the UC.

Thus, rather than disappearing, the UC grew in amplitude, reaching speeds of more than $10\,\mathrm{cm\,s^{-1}}$ or about one third of the CC. For the basic case considered, the alongshore transport associated with the UC was found to grow linearly with time to a value of about 0.7 Sv at day 60. A simple mass budget showed the UC to be largely fed and drained by on- and offshore transports of similar magnitude at the eastern and western ends of the forcing region. The transport of water upwelled into the overlying CC was found to be relatively small indicating only a weak connection between the water masses that are advected by the UC and CC.

While bottom stress is shutdown over the slope, we do not find the results to be insensitive to the presence or absence of bottom drag. Results obtained without bottom drag showed an increase in the magnitude and divergence of the CC. The larger divergence in turn leads to a reduction in the interior cross-shelf transport, downwelling and UC.

The downwelling solutions thus differ markedly from the upwelling results obtained by Suginohara and Kitamura (1984) and by simply reversing the sign of the wind stress, we obtain results that are similar to these authors: downwelling, rather than upwelling is found within the thermocline and over the slope, and the UC is weak or non-existent over the first 30 days or so. Thermal-wind shear within the thin upwelled BML plays only a minor role in the formation of the UC and we plan to report on these results in the near future (Middleton, 2000).

For the downwelling solutions obtained here, two conditions were found to be necessary for the existence of the UC. The first is that since the UC is essentially geostrophic, the thermal-wind shear must be large enough to overcome the opposing cross-shelf gradient in sea level. The second condition is that there must exist an an alongshore pressure gradient in sea level. The alongshore pressure gradient due to density $-p_y^{'}/\rho_0$ and the Coriolis force $-fu$, generally act to decellerate the UC.

These results are perhaps not new, although the proof of the second condition is novel and the results differ somewhat from those given by McCreary (1981) who obtained steady solutions adjacent to a vertical coastal wall. For these steady solutions, an UC was obtained, although vertical mixing of momentum was needed to balance the alongshore

pressure gradient at the wall. For the solutions here, a steady state is not obtained (even after 60 days) and frictional effects and the vertical diffusivity is are generally zero in the interior and within the BML (following shutdown).

The effects of a β–plane and of varying the stratification, shelf width and wind stress were also investigated with the wintertime slope circulation of the Great Australian Bight in mind. Results suggest that Rossby wave dispersion may be unimportant in determining the slope circulation for the region since the adjustment time scale for the Bight region (290-580 days) is larger than the seasonal scale of the winds (180 days).

Analyses by Trenberth et al. (1989) indicate a mean eastward stress within the Bight of about 0.1 Pa. The stress increases to the south and the associated curl, $1.5 \times 10^{-7}\,\mathrm{Pa\,m^{-1}}$, is an order of magnitude smaller than that used in the numerical solutions ($10^{-6}\,\mathrm{Pa\,m^{-1}}$). The net Ekman displacement after 180 days would only be about 15 m suggesting that the wind-stress curl over the shelf may not be important.

The effects of a wind-stress curl are of interest since the dynamics are different to the basic case above. Over the shelf-slope, the Ekman pumping leads to a general upward and downward tilt of sea-level and isopycnals leading to a broader CC and UC. In the basic (curl-free) case, the UC was narrower since the thermal-wind shear was larger near the shelf due to the BML and spreading of isopycnals.

During the autumn and winter months, the shelf stratification within the Bight varies considerably and will act to modify the idealised slope circulation modelled here. In the western, central, and South Australian regions, the influx and formation of light water should act to provide a local thermocline over the shelf. In the far west however, the wind-forced circulation is likely to be dominated by the Leeuwin Current (Church et al., 1989), while in the central region, where the shelf width exceeds 200 km, the results above suggest that the wind-forced circulation may lie shoreward of the shelf-break.

Off the narrow South Australian shelf, light water is present during the winter months (Godfrey et al., 1986) and zonal wind forcing may lead to an UC that is similar to that modelled here for the basic "summertime" case. Downwelling is found during May and over the shelf, the currents are poleward ($25\,\mathrm{cm\,s^{-1}}$) during winter (Schahinger, 1987).

As noted in the introduction, the poleward Zeehan Current also exists during the winter months off the west Tasmanian shelf. Measurements by Lyne and Thresher (1994) indicate that it is largely subsurface, confined to the outer slope and has average speeds of about 50 cm s^{-1}. Within the top 500 m of the water column, isotherms are downwelled by around 100 m and the thermal-wind shear is sufficient to drive an UC over the slope.

The cause of the Zeehan Current is unknown. The local mean winds while zonal, are directed predominantly across isobaths due to the meridional orientation of the shelf. Possibly the forcing region for the current lies farther to the north-west and off the South Australian shelf. The deeply downwelled isotherms off Tasmania may represent the poleward extension of the hydrography within the forcing region. Such a result was found here (Figs. A.4c and A.5c) and suggested to arise from the adjustment and mixing of along-isobath variations in density within the BML.

In summary, the wind-forced shelf circulation within the Bight will be influenced by the significant variations that occur in stratification and shelf width. While idealised, the results here do illustrate some of the fundamental dynamics of downwelling slope currents and should be of use in comparative studies of upwelling and in future analyses of the slope circulation of the Great Australian Bight.

Appendix B

The OCCAM Temperature and Salinity Fields: a Critical Comparison

The OCCAM wintertime TS climatology discussed here is also used as the initial field for the regional model described in Chapter 3. The reason for that is based on the fact that the climatological data available for the region are obtained at very few and generally localised hydrographic stations (Ridgway and Loch, 1987).

The two atlas available for the region are the Levitus climatology (Levitus et al., 1994; Levitus and Boyer, 1994), with a horizontal resolution of 1 degree and the Climatology of Australasian Regional Seas (CARS) (Dunn et al., 2000), with a horizontal resolution of 0.5 degree. In terms of vertical resolution, both are the same and use 32 layers.

The CARS atlas, with a higher resolution contains more observations than Levitus and shows more realistic features. However, both do not seem to be reliable near coastal regions. In some cases, a profile is presented where a shelf exists and in others, the first profile only occurs offshore of the 2000 m isobath. Moreover, the averaging used, more pronounced in the case of Levitus, has undoubtedly smeared out some important details and led to some regions of hydrostatic instability.

As a way of providing a critical comparison, 5 selected cross-shore sections (Fig. B.1) for the top 1000 m and 1 horizontal profile was chosen from CARS (Fig. 2.4) and OCCAM (Fig. 2.5) climatology. Whenever possible, comparison was also made with synoptic hydrographic cruises for the same season. It is important to point out that since the land masking from CARS was found to be incorrect, the OCCAM land masking was adopted instead.

The results for the five sections of CARS and OCCAM hydrography are presented in Figs. B.3-B.14 and are in reasonable agreement. In summary, isopycnals slope down towards the coast within the Surface Mixed Layer (SML), while at greater depths there is a general upward tilt of the density surfaces towards the shelf-slope. The first is basically

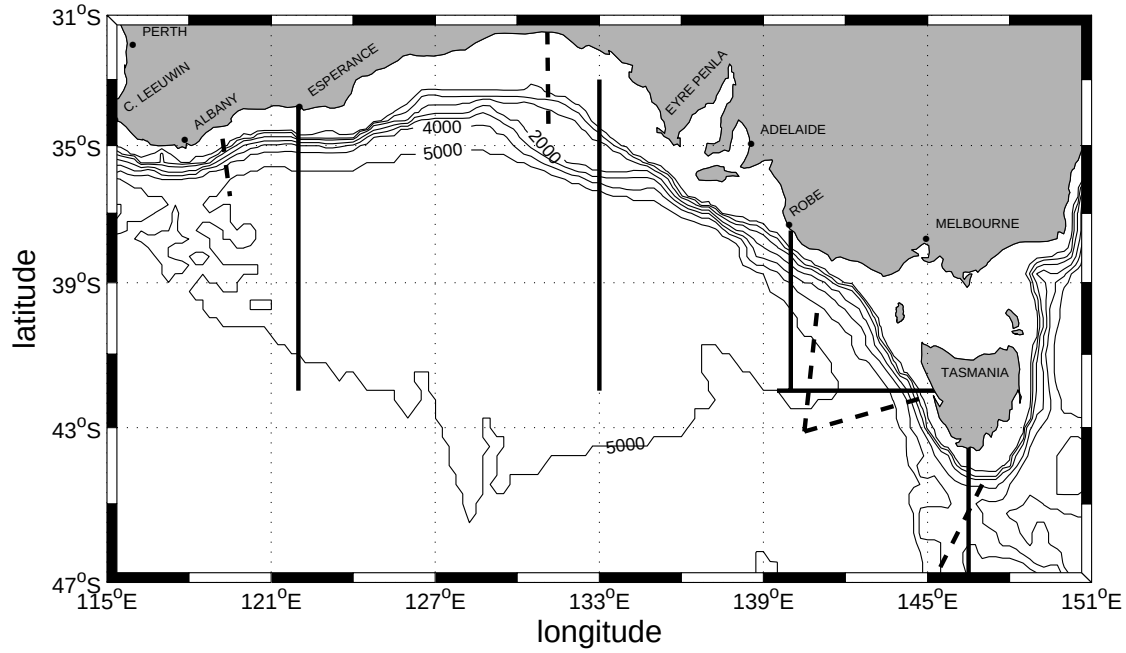

Figure B.1: *Map illustrating the sections for OCCAM and CARS (solid lines) and the CTD cruises sections (dashed lines). Thin solid contours (200, 500, 1000, 2000, 3000, 4000 and 5000 m) represent OCCAM bathymetry.*

a composition of two factors: (1) the cooler water found towards Antarctica and (2) the downwelling induced alongshore winds (*e.g.* Trenberth et al., 1989; Siefridt and Barnier, 1993) close to the coastal regions. As a result, the tilt of isopycnals is seen for some hundreds of kilometres away from the coast. On the other hand, the upward tilt, as was explained before, appears to be a more localised feature, only occurring close to the slope regions. In addition the SML also deepens from west to east, and at 140°E it can be as thick as 400 m (Fig. B.8).

At 122°E and below the 700 m, the TS structure (Figs. B.3 and B.2) is basically the same, apart from the fact that the minimum salinity in OCCAM is around 34.48 (Fig. B.3b) instead of 34.4 (Fig. B.2b) as shown in CARS. The OCCAM climatology also presents a more pronounced region of upwelling close to the slope (Fig. B.3a). Above the 700 m level, what is observed is that OCCAM can be up to 2°C warmer, which could lead to a reduction of up to 0.4 kg m^{-3} (Fig. B.3c compared to Fig. B.2c). Not only that, the thick region that encloses the 9°C isotherm, probably related to the presence of Subantartic Mode Water (McCartney, 1977, 1982), is not evident in the OCCAM results. This discrepancy is probably related to the deepening of the thermocline, as noted by

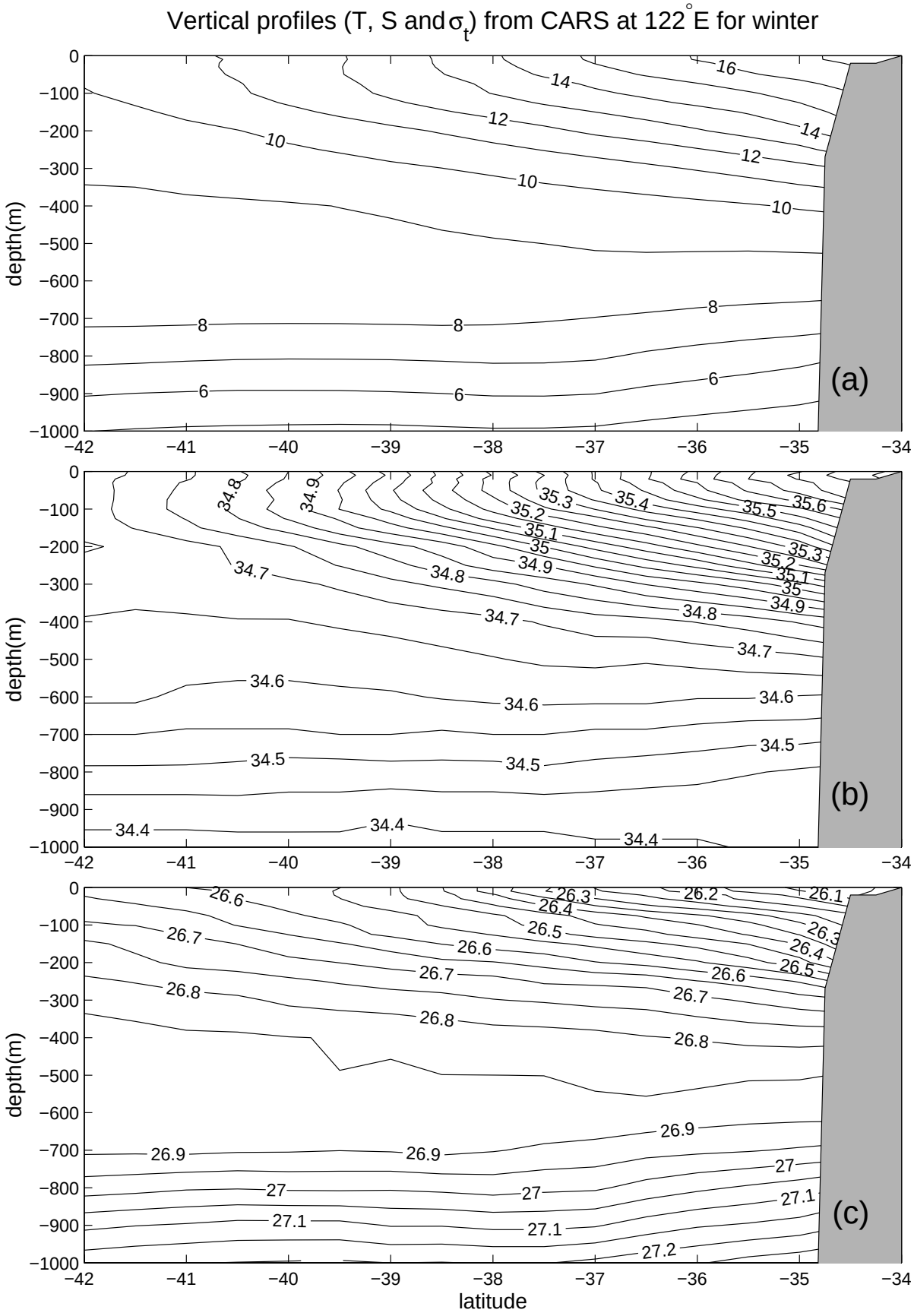

Figure B.2: *Vertical sections of (a) temperature, (b) salinity and (c) σ_t from CARS at 122°E as shown in Fig. B.1.*

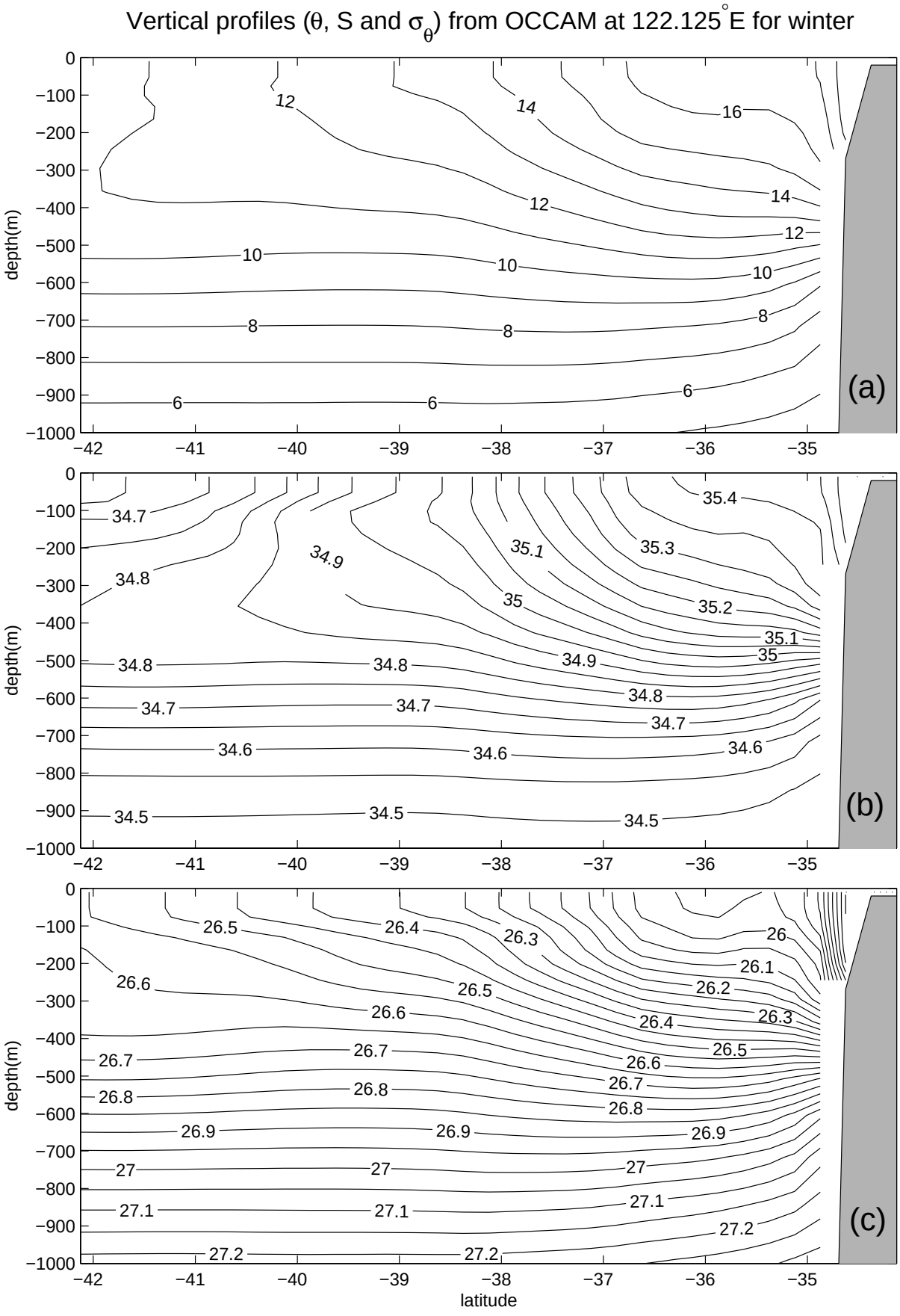

Figure B.3: *Vertical sections of (a) potential temperature, (b) salinity and (c) σ_θ from OCCAM at 122°E as shown in Fig. B.1.*

Saunders et al. (1999), in their analysis of the OCCAM results for the Pacific Ocean. Even considering those differences, the horizontal gradients of both temperature and salinity in the top 300 m are generally similar. The OCCAM climatology (Fig. B.3) near the shelf is also in good agreement with the synoptic CTD section (Fig 2.8a) obtained by Rochford (1986), where close to the shelf-break and slope region, the downwelling system can mix water down to 250 m. These feature, is not evident in the CARS atlas (Fig. B.2).

The section close to the head of the GAB, at 133°E, in general presents the same characteristics mentioned above. However, a pool of of light water centered at 38°S is evident in the top 100 m of CARS (Fig. B.4c) but not OCCAM (Fig. B.5c). Light surface water some 300 km from the coast does not seem realistic and is not evident in Levitus. That is just one of the examples where the climatology seems to fail when compared to OCCAM (Fig. B.5). In terms of vertical structure, a common feature of both atlas is the vertical orientation of the isohalines in the top 200 m or so (Figs. B.5b and B.4b). The horizontal variation of salinity is greater than 1 in both atlas, reaching coastal values of $\sim$ 36 (CARS) and $\sim$ 35.9 (OCCAM). Compared to the CTD section available (Fig. 2.8b), the OCCAM dataset is again in better agreement, where both isotherms and isohalines sink down to around 200 m close to the shelf-slope region. The density structure of the shelf region is completely well mixed (Fig. B.5c).

At the eastern end of the SEIO region, the SML is generally much deeper. At 140°E section, the CARS atlas (Fig. B.6c) shows that the SML at offshore regions can be as deep as 300 m. However, in analogy with the 133.5°E section (Fig. B.4c), an anomalous surface pool of light water is found centered at 39°S (Fig. B.6c). For this particular section, Levitus shows (Fig. B.7c) regions of hydrostatic instability in the first 200 m and a SML as thick as 500 m. On the other hand, the OCCAM climatology (Fig. B.8c) shows the SML to deepen towards the coast and is consistent with the synoptic CTD section shown in Fig. B.9. This section, taken during winter, lies approximately at 141°E and between 42.5°S and 39.5°S. The SML deepens from 200 m farthest offshore to almost 300 m nearest the coast.

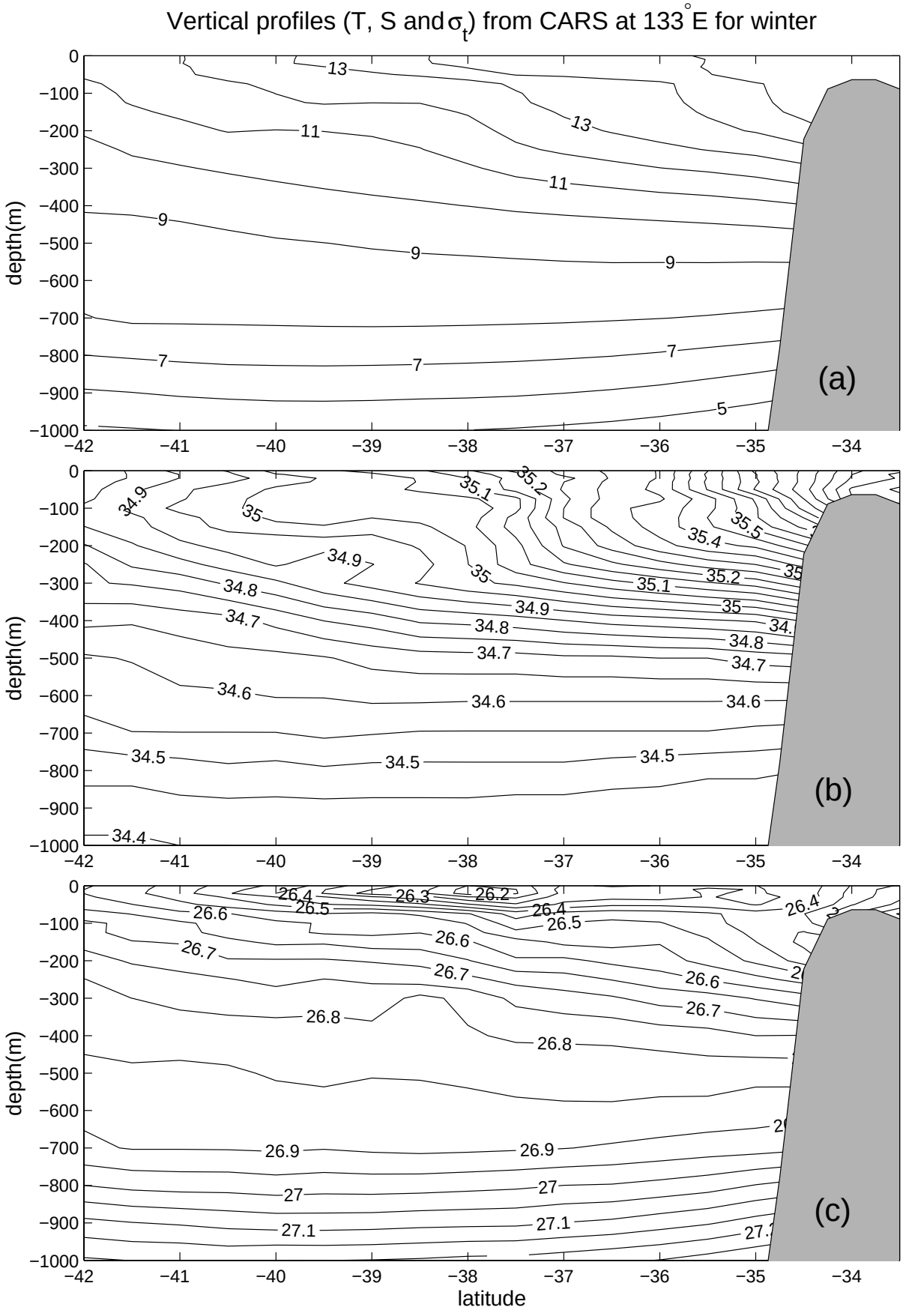

Figure B.4: *Same as Fig. B.2, but at 133°E.*

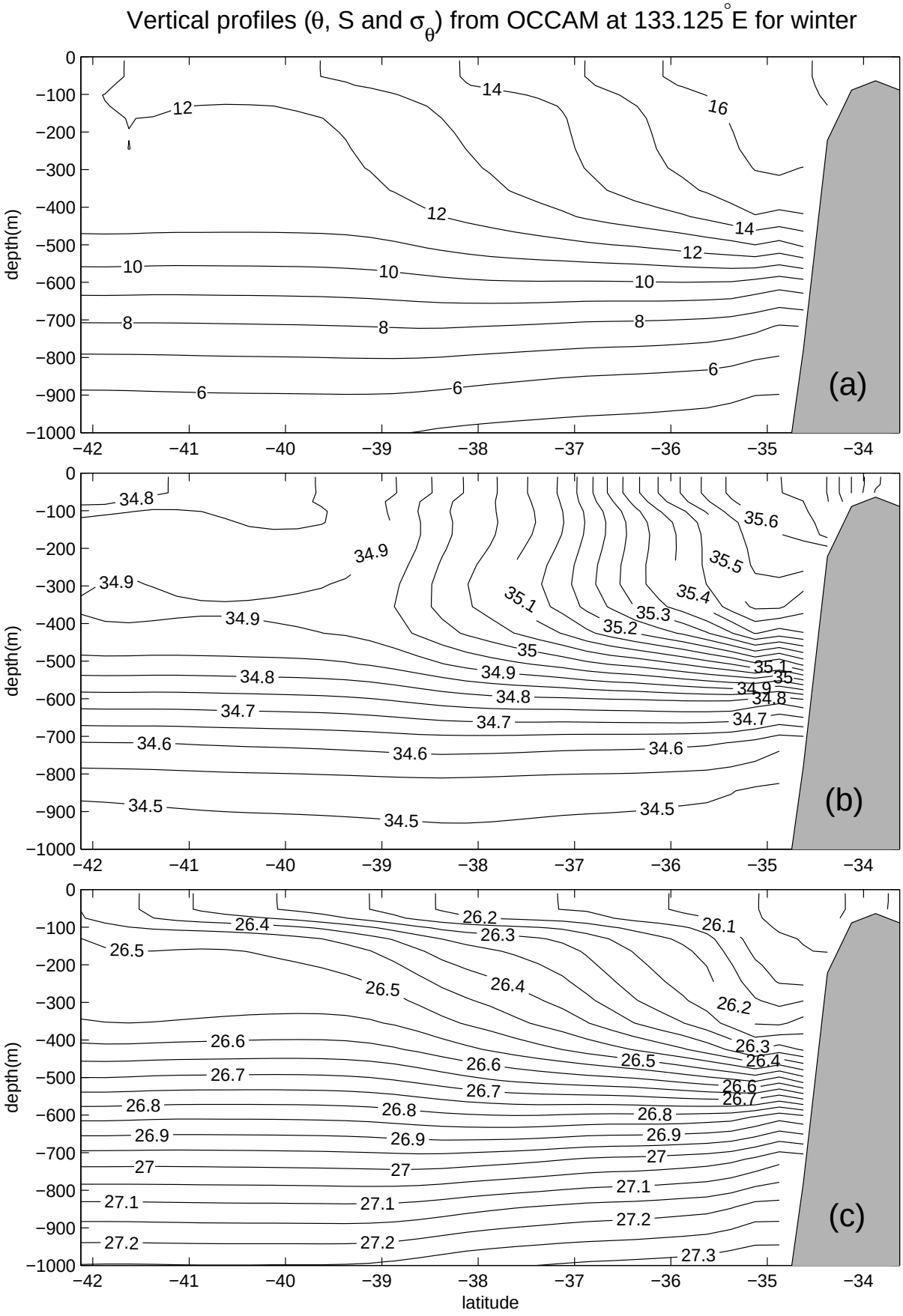

Figure B.5: *Same as Fig. B.3, but at 133°E.*

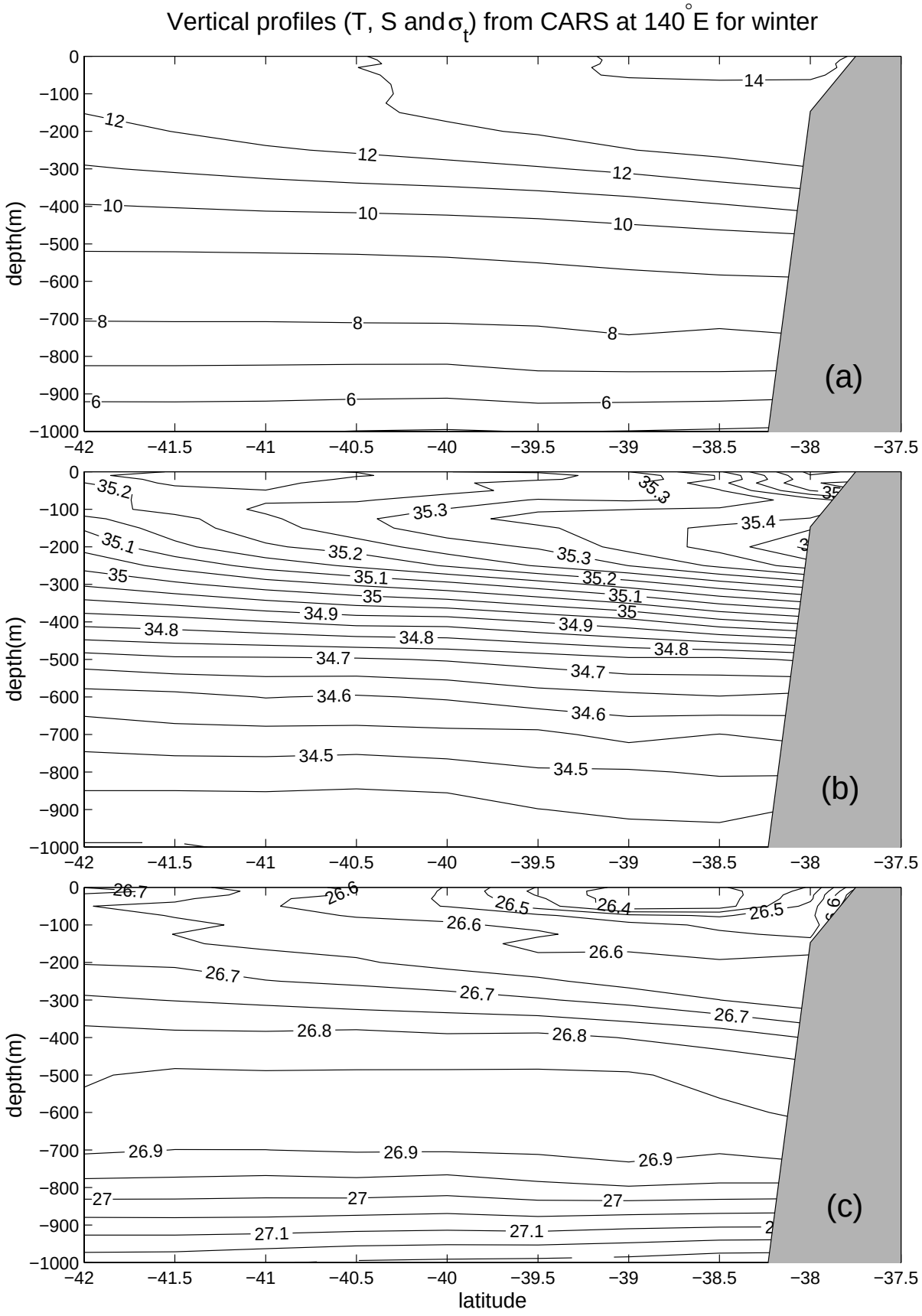

Figure B.6: *Same as Fig. B.2, but at 140°E.*

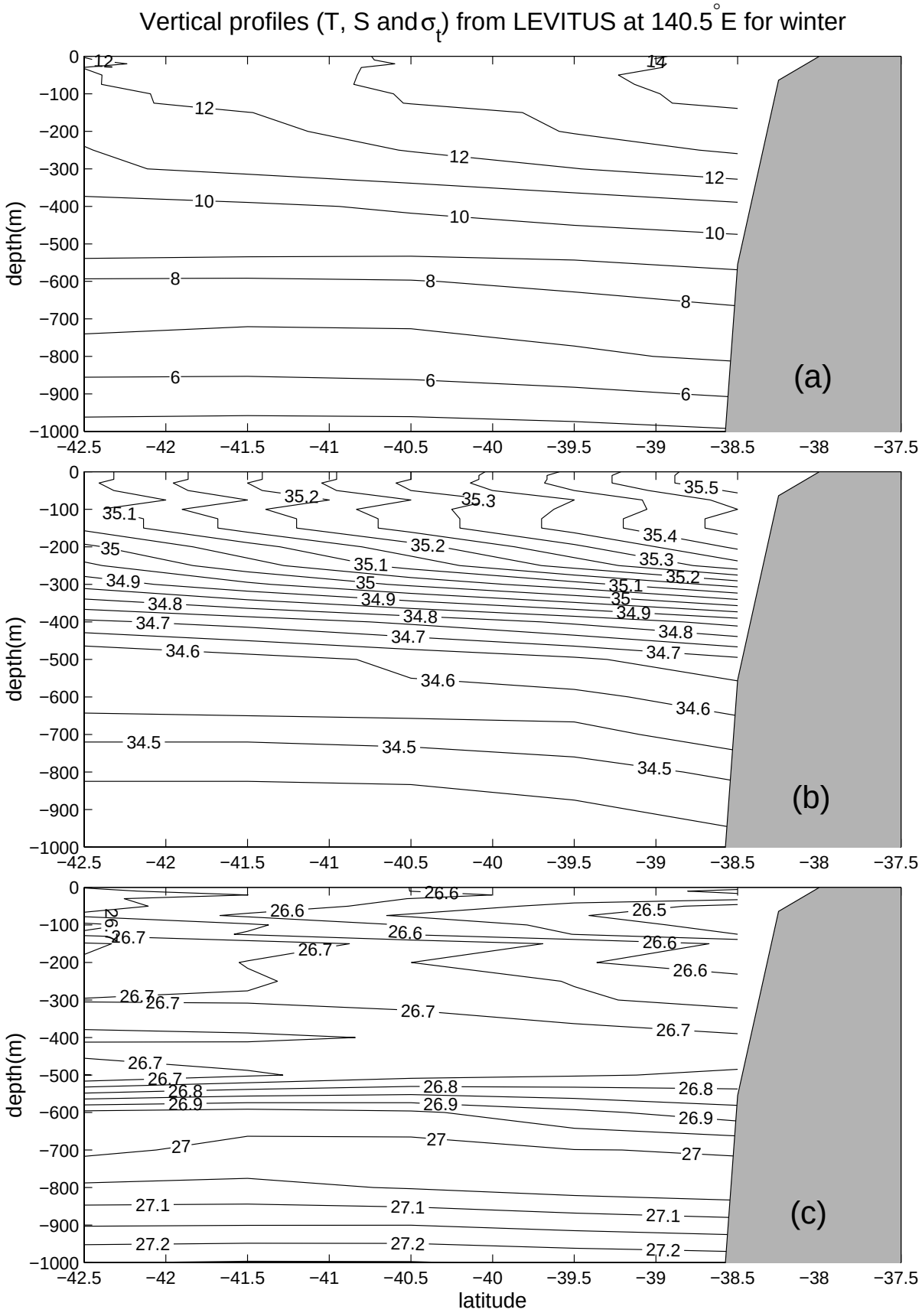

Figure B.7: *Same as Fig. B.6, but from Levitus.*

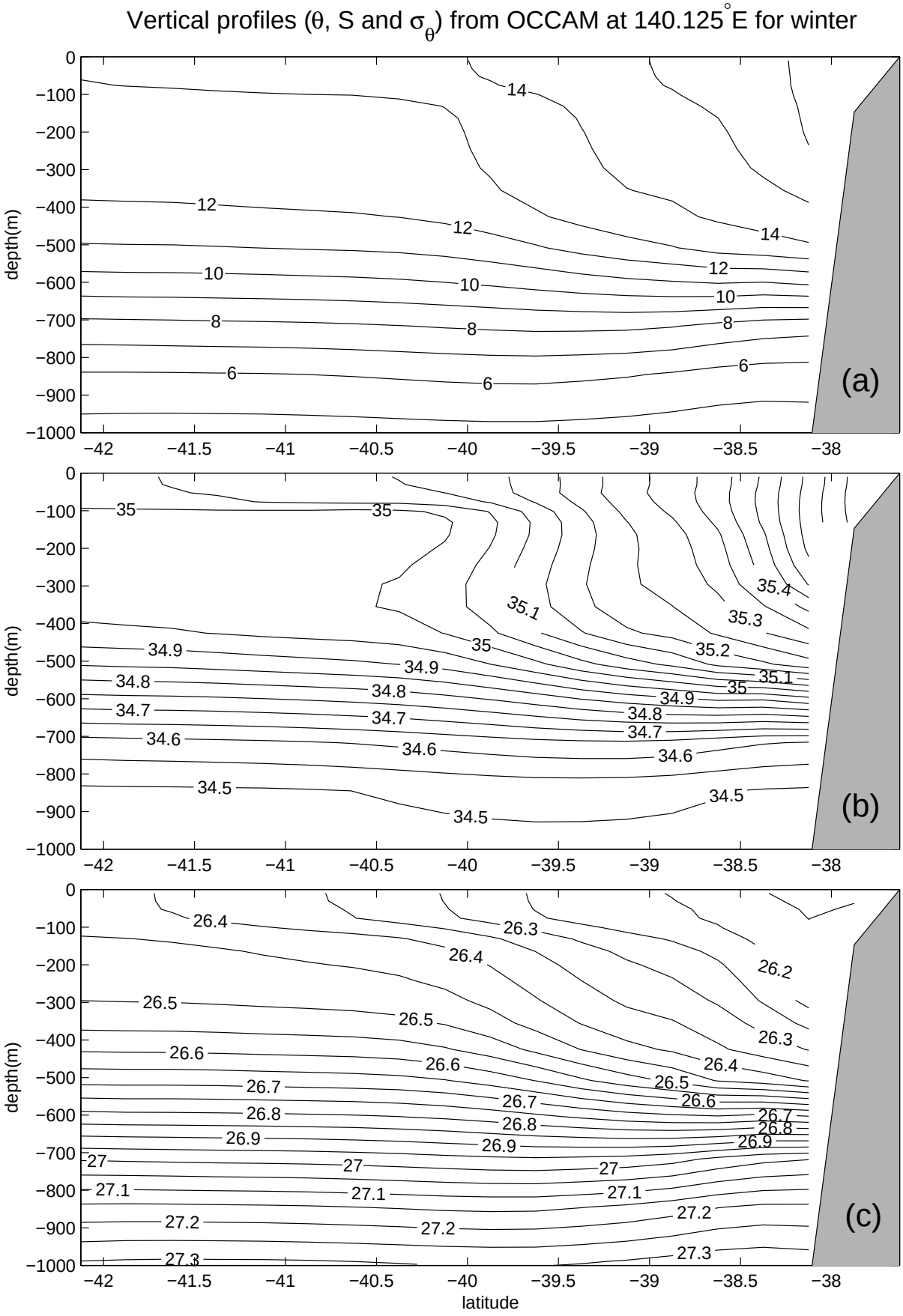

Figure B.8: *Same as Fig. B.3, but at 140°E.*

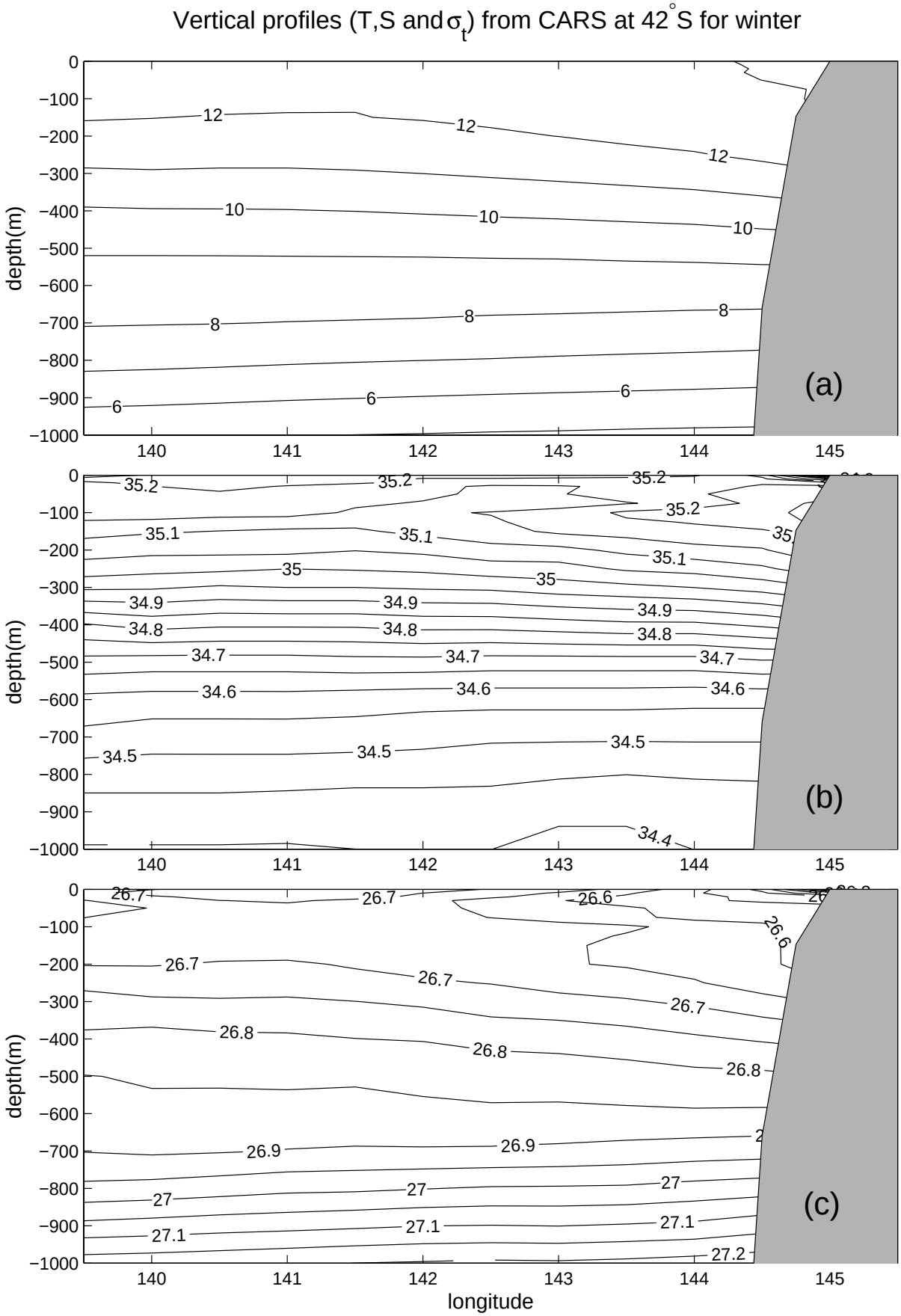

Figure B.10: *Same as Fig. B.2, but at 42°S.*

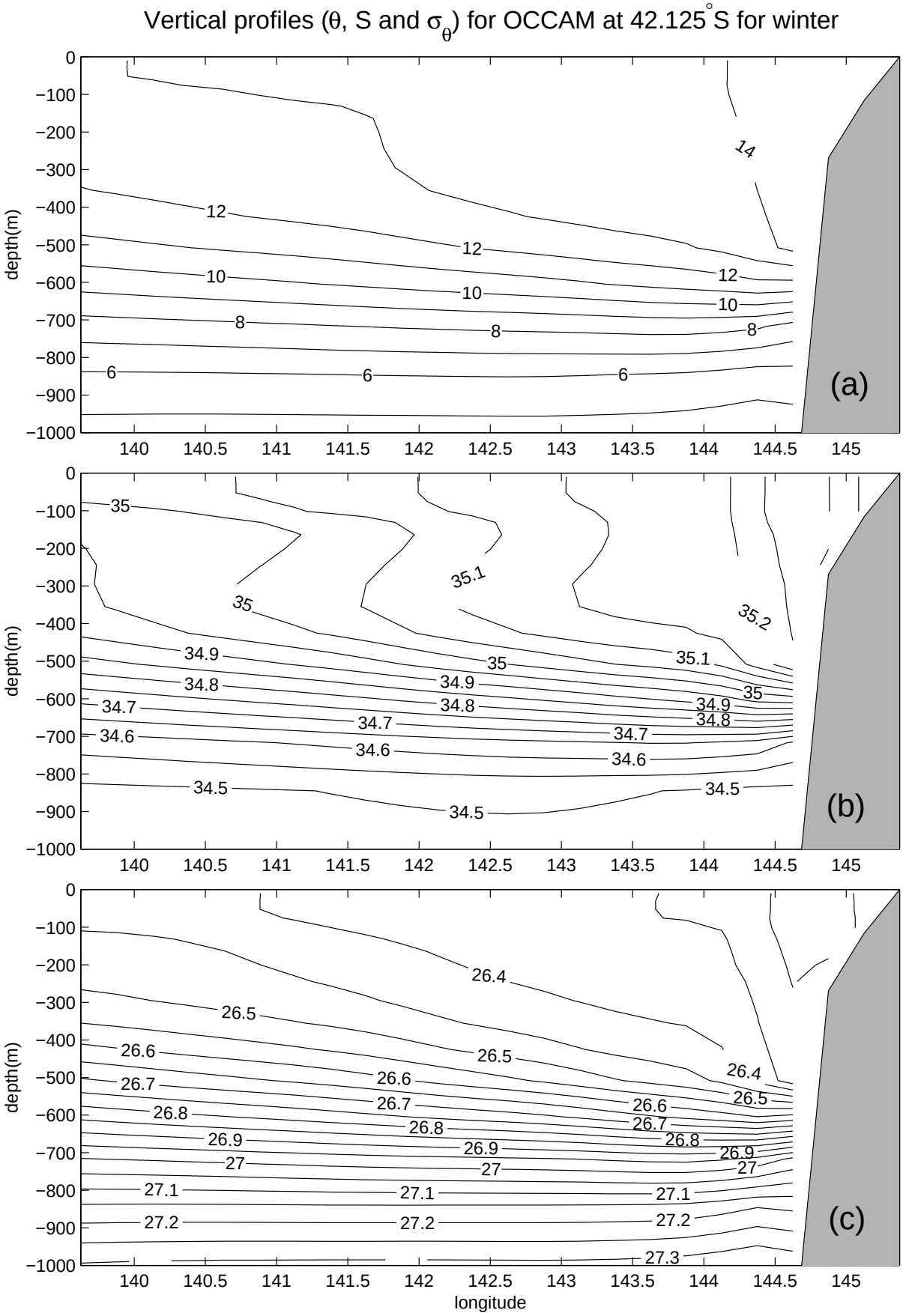

Figure B.11: *Same as Fig. B.3, but at 42°S.*

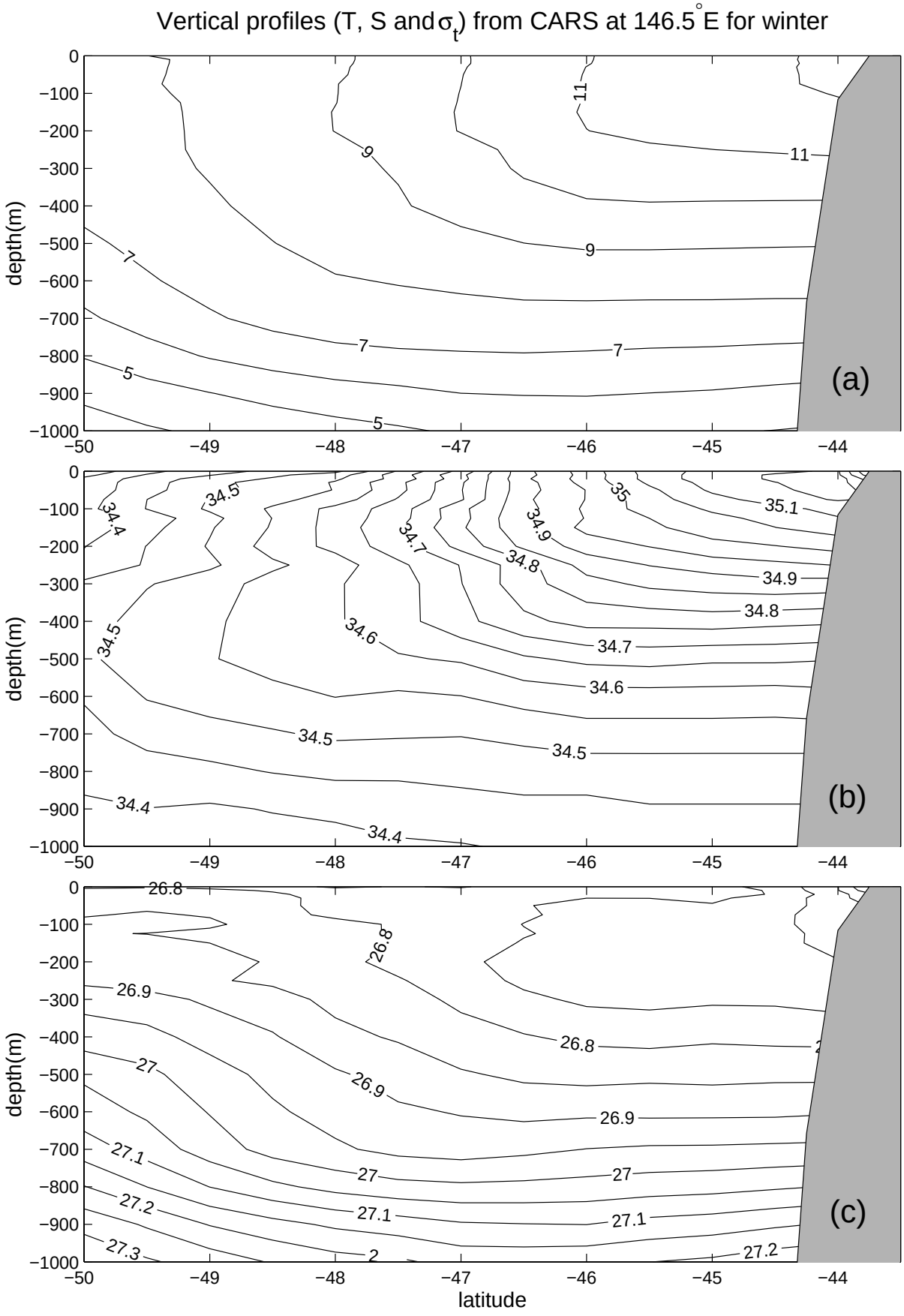

Figure B.13: *Same as Fig. B.2, but at 146.5°E.*

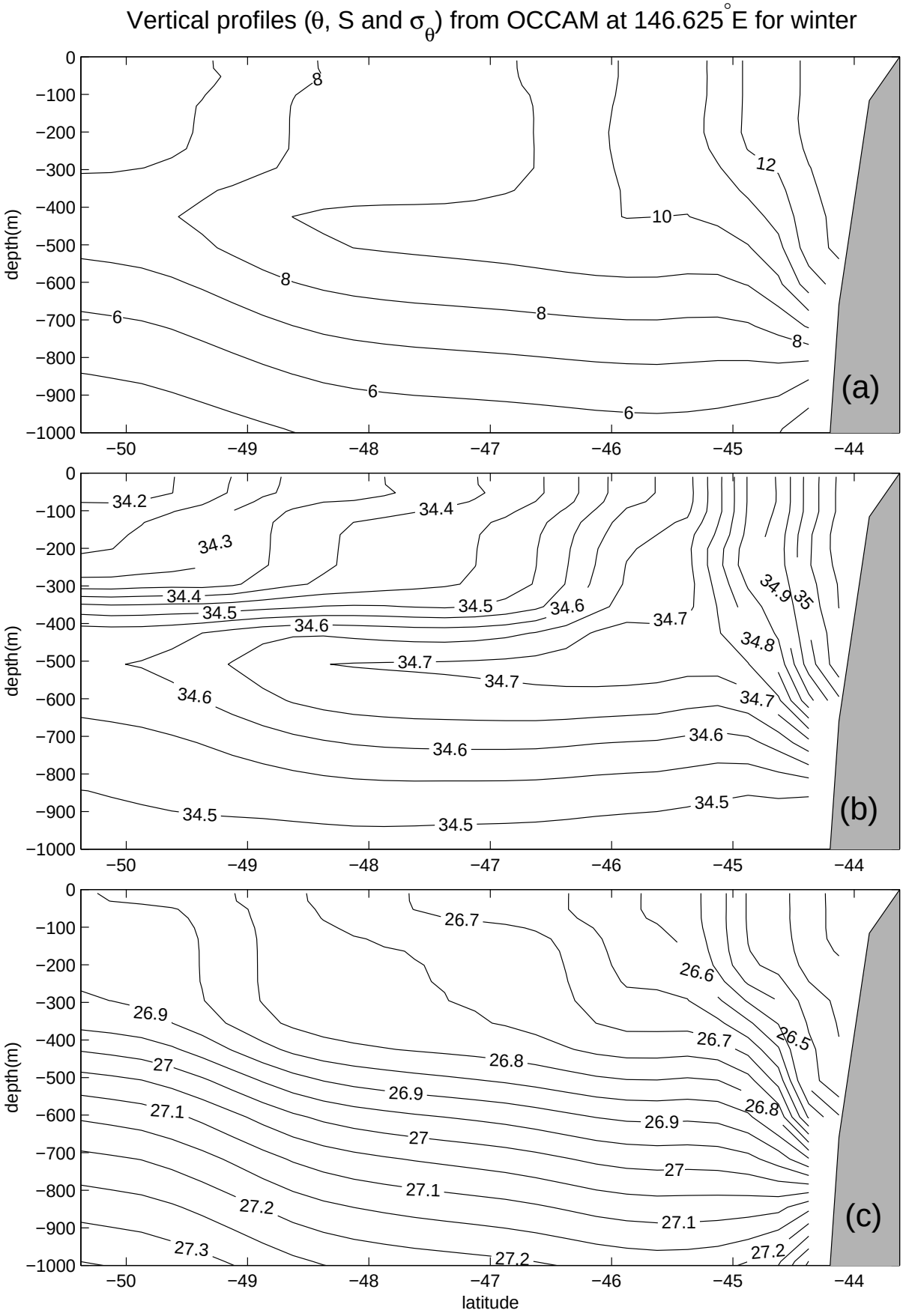

Figure B.14: *Same as Fig. B.3, but at 146.5°E.*

Appendix C

Baroclinic Instability

Baroclinic geostrophic flows in thermal wind equilibrium require the existence of a horizontal pressure gradients to occur. When the tilt of the isopycnals that govern these flows are reduced, potential energy is liberated and transformed into kinetic energy which can generate disturbances and cause the flow to become unstable. This process is called baroclinic instability. The aim of this section is to verify whether the disturbances found on the SEIO region can be generated through such a process. However in order to understand the mechanism and scales for baroclinic instability, lets first consider the response of a two layer ocean and a scaling of the equation for potential vorticity.

Fundamental dynamics

For an inviscid ocean potential vorticity has to be conserved, so that any displacement of a fluid column from its original location has to be accompanied by the generation of relative vorticity. Vertical stretching of the water column generates cyclonic relative vorticity (clockwise in the Southern Hemisphere (SH)) and vertical squashing generates anticyclonic relative vorticity (anti-clockwise in the SH). Using a two-layer diagram, Cushman-Roisin (1994) describes the physical mechanism for the generation of a baroclinic instability. Since the shelf-slope circulation of the SEIO also resembles a two-layer system, Cushman-Roisin's diagram (based on North Hemisphere) was adapted to the region and is shown in Fig. C.1.

For simplicity, Fig. C.1 is considered oriented in the north-south direction and the ocean bottom is assumed to be flat. This configuration leads to an eastward flow in the upper layer and a westward flow in the lower layer. At the upper layer, disturbances moving parcels of water northwards will cause vertical stretching in the vortex tubes and will generate cyclonic vorticity. Since the interface is not rigid it will also be raised and so will induce cyclonic vorticity in the lower layer as well. On the other hand, southward movements of parcels will induce squeezing of the vortex tubes, anticyclonic vorticity and lowering of the interface, which will also create some anticyclonic movements on the lower layer.

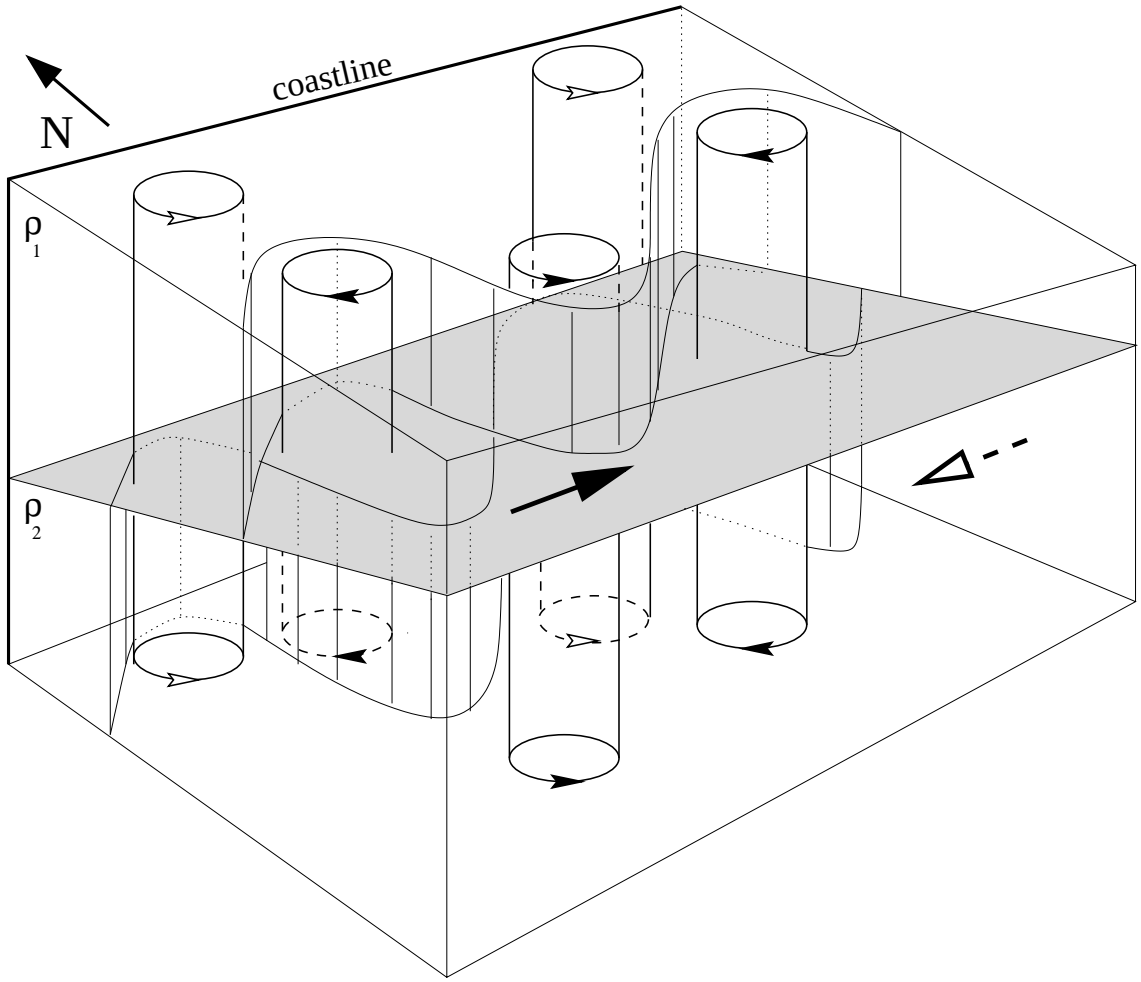

Figure C.1: *Diagram for baroclinic instabilities at the SEIO region. Motions induced by the upper layer are signed with filled head arrows, while the motions induced by the lower layer are signed with non-filled head arrows.*

If the same analogy is used for the lower layer, northward movements, now towards shallow waters, will induce vertical squeezing, anticyclonic vorticity and raising of the interface and subsequent anticyclonic vorticity in the upper layer. The opposite, vertical stretching, cyclonic vorticity and downlift of the interface causing cyclonic movements on the upper layer will occur if the movement is southwards.

The growing of a baroclinic instability is dependent on two conditions. First, there has to be a proper phase arrangements between the disturbances in the two layers. Second, the disturbances have to be of a certain wavelength where vertical stretching or squeezing of the vortex tubes is effective in generating relative vorticity. The appropriate wavelength scale (L) is obtained next by scaling the potential vorticity equation.

An equation for potential vorticity can be obtained from the quasi-geostrophic equation for nonlinear motions in a continuously stratified fluid on a β-plane (Cushman-Roisin, 1994). The transformation of the pressure field into a stream-function via $p' = \rho_0 f_0 \psi$ results in

$$\frac{\partial \overline{q}}{\partial t} + J(\psi, q) = 0 \tag{C.1}$$

where q is the potential vorticity

$$q = \underbrace{\nabla^2 \psi}_{\sim \frac{1}{L^2}} + \underbrace{\frac{\partial}{\partial z}\left(\frac{f^2}{N^2}\frac{\partial \psi}{\partial z}\right)}_{\sim \frac{f^2}{N^2 H^2}} + \beta y \tag{C.2}$$

and N and H are the Brunt-Väisälä frequency and water depth.

Now let us consider the f-plane approximation and scale the first two terms of equation (C.2). Cushman-Roisin (1994) states that " if L is much larger than $a_i = NH/f$, the relative vorticity cannot match the vertical stretching as scaled. This implies that vertical stretching will be inhibited, and the displacements in the layers will tend to be in phase in order to reduce squeezing and stretching of fluid parcels in each layer. On the other hand, if L is much shorter than a_i, relative vorticity dominates potential vorticity. The two layers become uncoupled, and there is insufficient potential energy to feed a growing disturbance. In sum, displacement wavelengths on the order of the deformation radius are the most favourable to growth." More specifically, both the continuous and two-layer Eady models (*e.g.* Gill, 1982; Holton, 1992) yields wavelengths L of preferred maximum growth rate that are around $2\pi a_i$, which is in agreement with the scaling arguments proposed above.

For the region here, the results for the Brunt-Väisälä frequency shown in Figs. C.6-C.8 below indicate depth-averaged values that range between $2 \times 10^{-3} s^{-1}$ to $3 \times 10^{-3} s^{-1}$ for water depths of 2000 and 4000 m. The corresponding internal deformation radius then ranges from 40 to 120 km. Growing waves with a scale of 250 km may then be expected.

A perturbation analysis

Here the equation determined by Gill et al. (1974) is used so as to estimate wavelengths for the baroclinic instability in the SEIO region. Gill et al. (1974) assumed that the ocean is north-south oriented, that the β-plane approximation is valid and that the only properties on which the solution is dependent are the vertical variation of the mean density field and its horizontal gradient with depth. A sloping bottom is also allowed. A mean state is specified by $\overline{U}(y,z) = -\psi_y$ and the thermal wind equation

$$f\frac{\partial \overline{U}}{\partial z} = \frac{g}{\rho_0}\frac{\partial \overline{\rho}}{\partial y} \tag{C.3}$$

with $\overline{\rho} = \overline{\rho}(y,z)$. Perturbations to this state are of the form

$$\psi(x,z,t) = Re\{\phi(z)e^{ik(x-ct)}\} \tag{C.4}$$

Substituting the equation above into Eqs. (C.1) and (C.2), the following equation results in

$$(\overline{U}-c)\left[\frac{\partial}{\partial z}\left(\frac{f^2}{N^2}\frac{\partial \phi}{\partial z}\right) - k^2\phi\right] + \frac{\partial \overline{q}}{\partial y}\phi = 0, \text{ where} \tag{C.5}$$

$$\frac{\partial \overline{q}}{\partial y} = \beta - \left[\frac{\partial}{\partial z}\left(\frac{f^2}{N^2}\frac{\partial \overline{U}}{\partial z}\right)\right] \tag{C.6}$$

and the Brunt-Väisälä frequency (N^2) is

$$N^2 = -\frac{g}{\rho_0}\frac{\partial \overline{\rho}}{\partial z} \tag{C.7}$$

Boundary conditions for equation (C.5) are obtained by assuming that the normal velocity to the surface and bottom is zero and may be written as

$$\frac{1}{\phi}\frac{\partial \phi}{\partial z} = \frac{1}{(\overline{U}-c)}\frac{\partial \overline{U}}{\partial z} \quad \text{at} \quad z = 0 \tag{C.8}$$

$$\frac{1}{\phi}\frac{\partial \phi}{\partial z} = \frac{1}{(\overline{U}-c)}\left(\frac{\partial \overline{U}}{\partial z} + s\right) \quad \text{at} \quad z = -H \tag{C.9}$$

where s is the slope factor defined by

$$s = \frac{N^2}{f}\left(\frac{\partial \overline{U}}{\partial z}\right)^{-1}\frac{\partial H}{\partial y} \tag{C.10}$$

For a given wavenumber k, equations (C.5), (C.8) and (C.9) define an eigenvalue problem for c. By taking an initial guess for c, the value of the boundary condition (C.8) can be determined. Equation (C.5) is then integrated in the vertical and the error in the boundary condition (C.9) reduced to near zero using an iterative method. The flow is considered to be baroclinically unstable if the imaginary part of the phase speed c is non-zero. The numerical scheme was validated by reproduction of the results of Gill et al. (1974). The necessary conditions for instability (Green, 1960; Charney and Stern, 1962; Gill et al., 1974) are that either

1. $\frac{\partial \overline{q}}{\partial y}$ changes sign in $-H < z < 0$, or
2. the sign of $\frac{\partial \overline{q}}{\partial y}$ is opposite to that of $\frac{\partial \overline{U}}{\partial z}$ at $z = 0$, or
3. the sign of $\frac{\partial \overline{q}}{\partial y}$ is the same as of $\frac{\partial \overline{U}}{\partial z} + s$ at $z = -H$.

Growth rates

Before moving to realistic profiles, a series of idealised curves of $\overline{U}$ and N^2 for the region was tested with the purpose of: 1) providing an idea of the growth rates, phase speed velocities and range of the wavelength for the instabilities. 2) Evaluate the importance of the β-effect and slope factor s for the SEIO solutions. The Coriolis parameter and β terms were set to -8.5×10^{-5} s^{-1} and 1.85×10^{-11} m^{-1} s^{-1} respectively.

In order to evaluate the effect of the gradient of velocity as well as the depth at which the tilt of isopycnals reverse, three different profiles were chosen (Fig. C.3a-b). A common feature of the profiles, as shown in Fig. C.2, is that they have an eastward jet with its maximum value at the surface and a subsurface westward jet that is largest at the depth of isopycnal reversal (z_{max}). Profile I and profile II will allow for the evaluation of the changes in the velocity and its derivative, while keeping the depth z_{max} unaltered. Using the third profile, the effect of changing z_{max} will be determined. For the stratification,

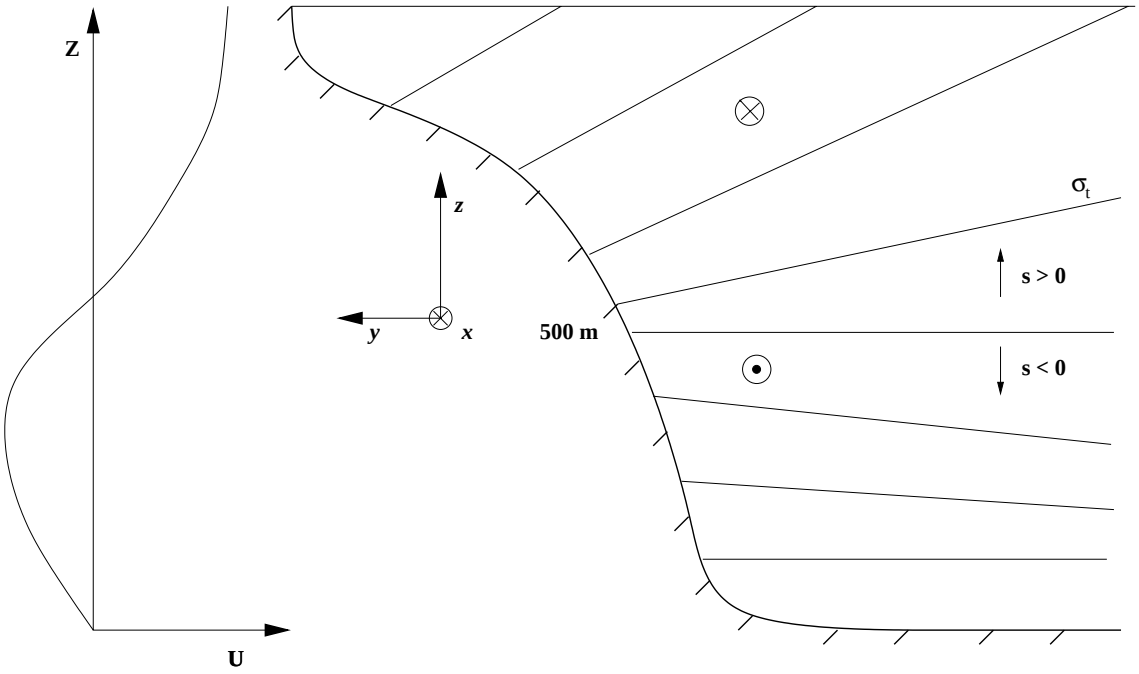

Figure C.2: *Idealised profile of the density and associated baroclinic geostrophic flow for the SEIO region.*

the maximum of the Brunt-Väisälä frequency was generally found to occur at 500 m and since the shape of the curve was reasonably similar for the region, a single curve (Fig. C.3c) was adopted in all studies.

Results for all profiles (Fig. C.4) show that instabilities have e-folding time scales growth of 20-5 days for wavenumbers between 0.03-0.205 km^{-1} (wavelengths of $\sim$ 210-30 km). Generally the growth rate increases with the wavenumber. In terms of phase speed, the maximum variation between each profile occurs at smaller wavenumbers.

Changes to $\overline{U}_z$ and thus the slope of isopycnals do alter the growth rates. Profile III, having less variations in the gradient of the velocity has the smallest relative growth rates, while Profile II with the largest changes in the velocity gradient has the highest relative growth rates (*see also* Gill et al. (1974)). It is important to mention that while all profiles have $s = 0$, no changes are found with realistic values of s (not shown). The reason for this is that the right side of the bottom boundary condition (C.9) is in all cases essentially zero when compared to that at the surface (C.8).

Profile I was also used to analyse the f-plane approximation. Changes in growth rate occur at wavenumbers smaller than 0.04 km^{-1}, where the e-folding time scale is greater

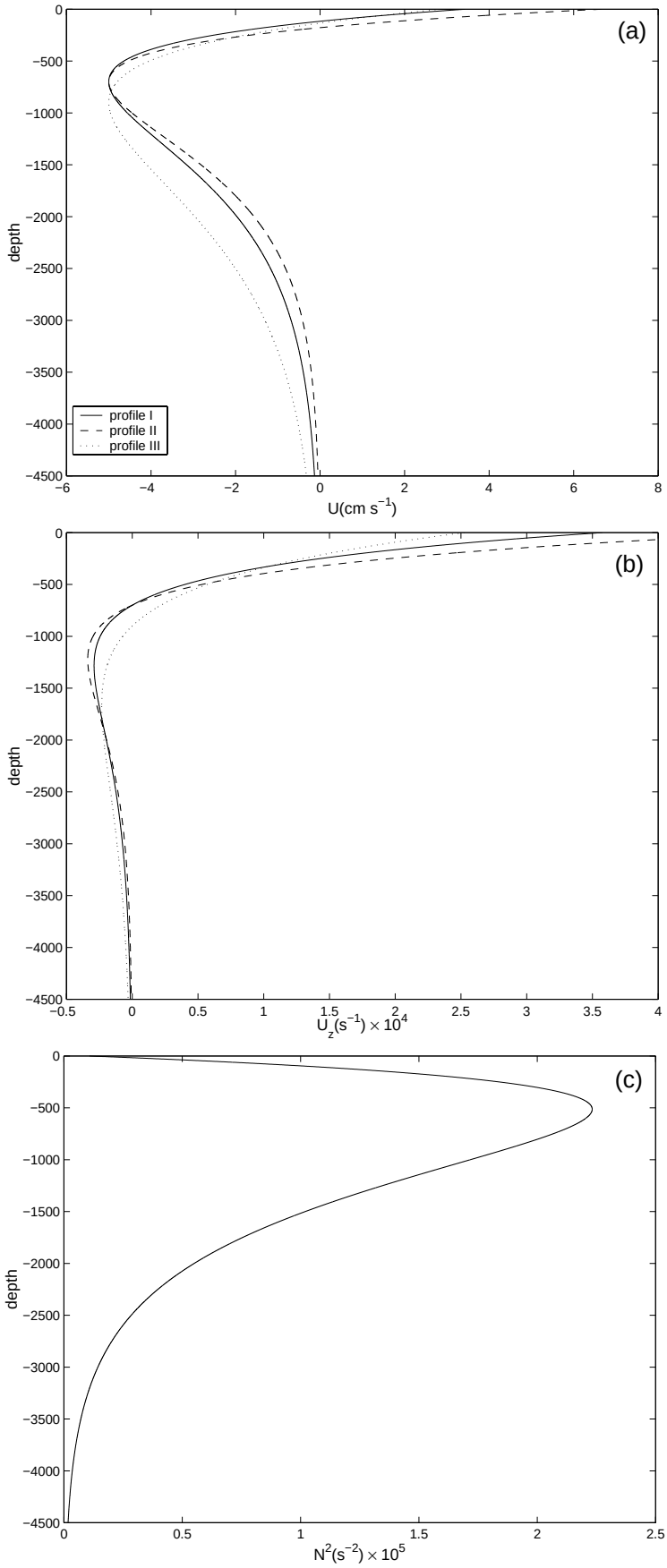

Figure C.3: *(a) Idealised curves for velocity, (b) vertical derivative of the velocity and (c) Brunt-Väisälä frequency.*

than 20 days. The phase speed velocity is more sensitive to the β-effect, but only at wavenumbers of 0.04 km^{-1}. The difference in the phase speed velocity is only 15% or so.

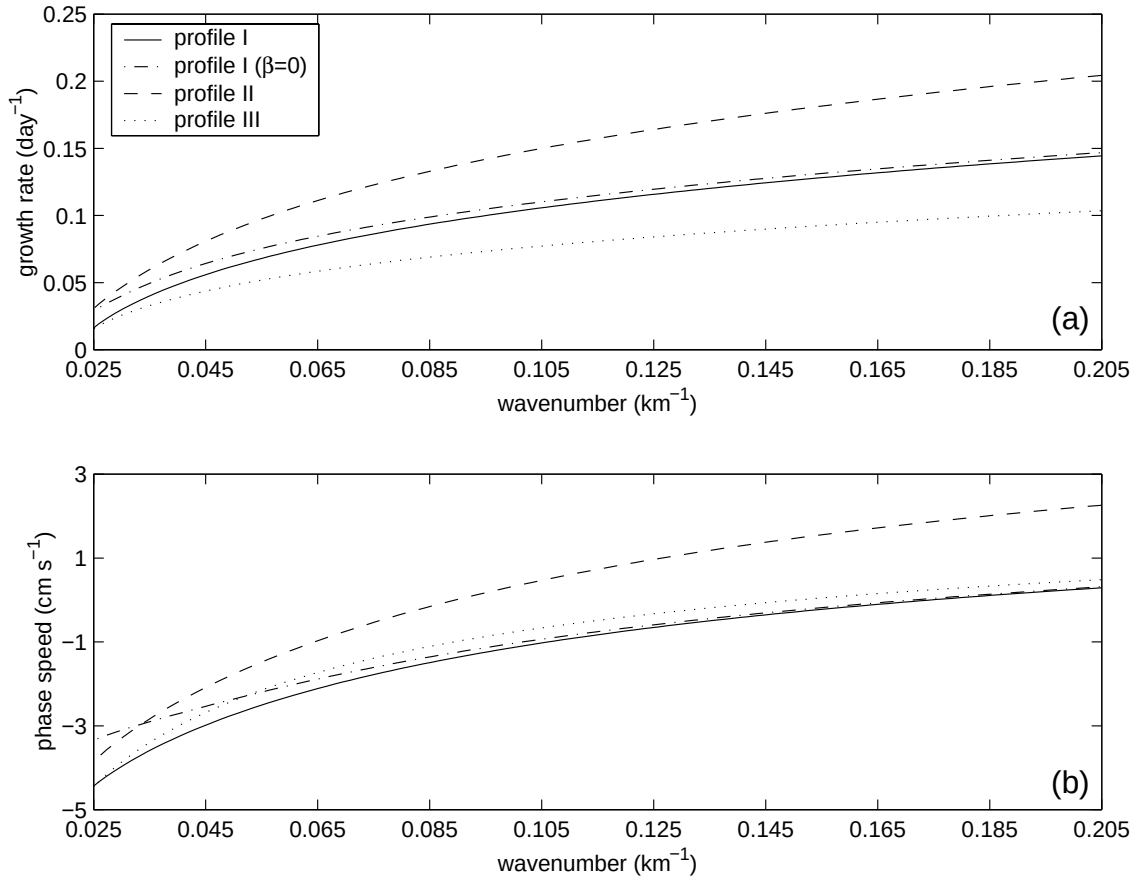

Figure C.4: *(a) Growth rate and (b) phase speed velocity for the idealised profiles. The dashed-dotted represents the the f-plane case while the other lines represent β-plane case. The x axis (wavenumber) is representative of wavelengths varying from 30-250 km.*

With a reasonable idea of the growth rates expected for the SEIO region and noting that both the β-effect and the bottom slope are generally unimportant for instabilities with time scales of the order of 1 month or less, a series of realistic profiles for $\overline{U}$ and $\overline{U}_z$ were adopted and the growth rates again determined. The initial density field for the regional model was used to infer $\overline{U}_z$ and $\overline{U}$, the along-slope shear and the velocity. Note that while $\overline{U}$ does involve an arbitrary constant, so do the solutions for phase speed in equations (C.5), (C.8) and (C.9). The f-plane approximation was again assumed. To provide a reasonable coverage of the area, three regions with two points on each one, were selected. The points were located at around 2000-2500 m and 4000-4500 m and

the regions were: (1) Kangaroo Is. (Figs. C.5 and C.6), (2) Robe (Figs. C.5 and C.7) and (3) Northwestern Tasmania (Figs. C.5 and C.8).

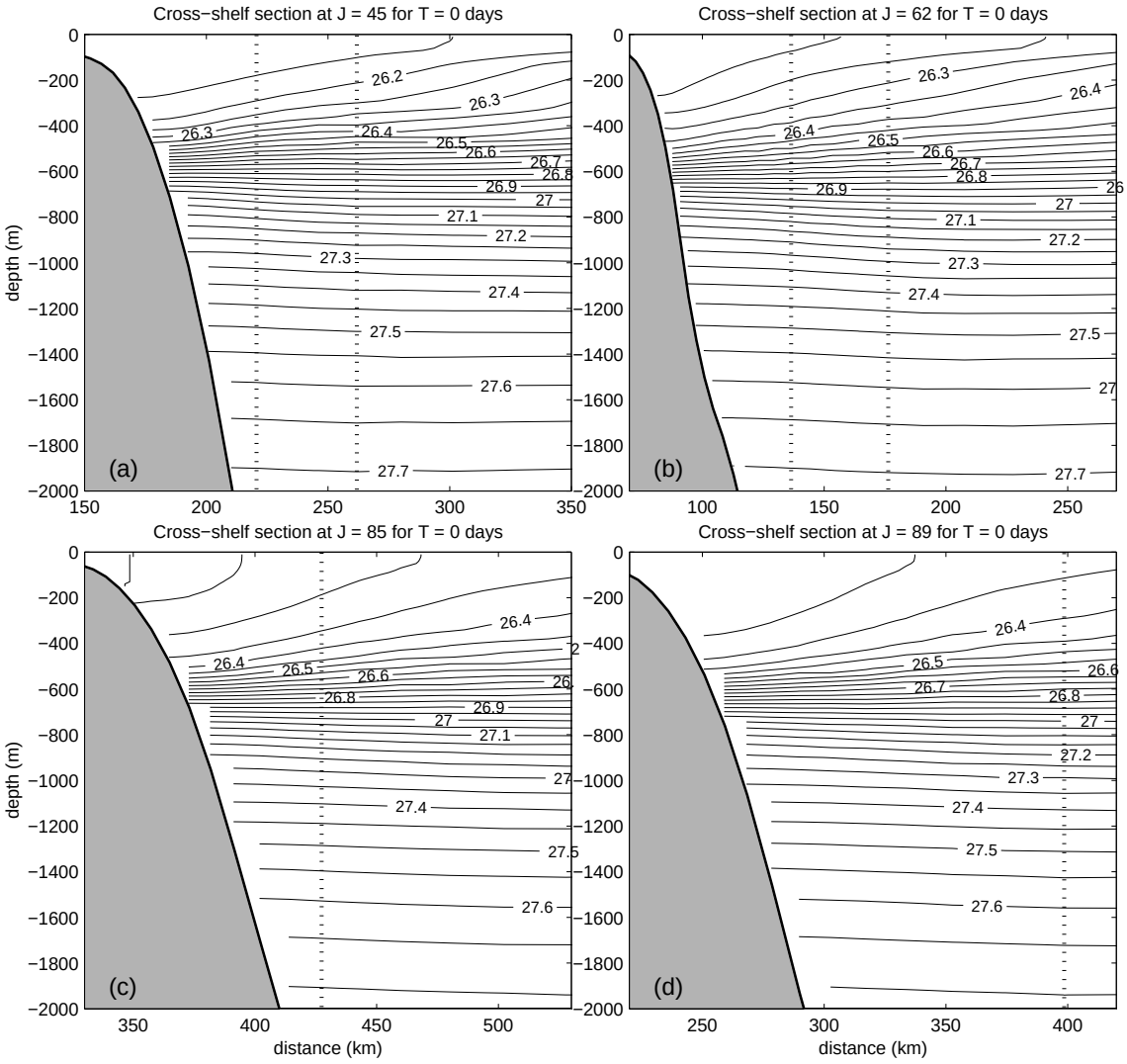

Figure C.5: *Vertical sections of the initial σ_θ for (a) region 1, (b) region 2 and (c) and (d) region 3.*

From the results presented in Figs. C.9-C.11, waves smaller than 250 km generally become unstable. Analysis of the three criteria for baroclinic instabilities show that not only $\partial\overline{q}/\partial y$ changes sign along the water column for all analysed sites (Figs. C.6-C.8), but also that the top conditions is satisfied: again the bottom condition is unimportant to the solution. The fastest growth scale of 10 days is generally reached at wavelengths of 60 km (around wavenumbers of 0.1 m^{-1}). As in the idealised profiles, the gradient of the velocity seems to be the most important factor in the growth rate of the instabilities. The sites located around the 2500 m isobath generally have higher growth rates than

the sites located at the 4500 m isobath.

The solutions for sea level after 26 days of simulation (Fig. 4.6a) show that there is a well defined sequence of high and lows systems with wavelength of around 200-250 km. The high/low system between Kangaroo Is. and Robe has such a wavelength and the instability analysis indicate an e-folding time scale of around 25 days (Fig. C.9). Such a growth rate is not inconsistent with the model results.

Although there is a good agreement with the numerical simulations, a question that remains is why the fastest growing wavelengths (60 km) are not found in the model solutions. Over 10 days, the horizontal diffusion acts to smear over a scale of $(2A_M \times$ length of time$)^{1/2}$ or 13 km. Not only that, the model is only able to resolve processes that are at least twice the minimum grid space, which defines a scale of 25-30 km.

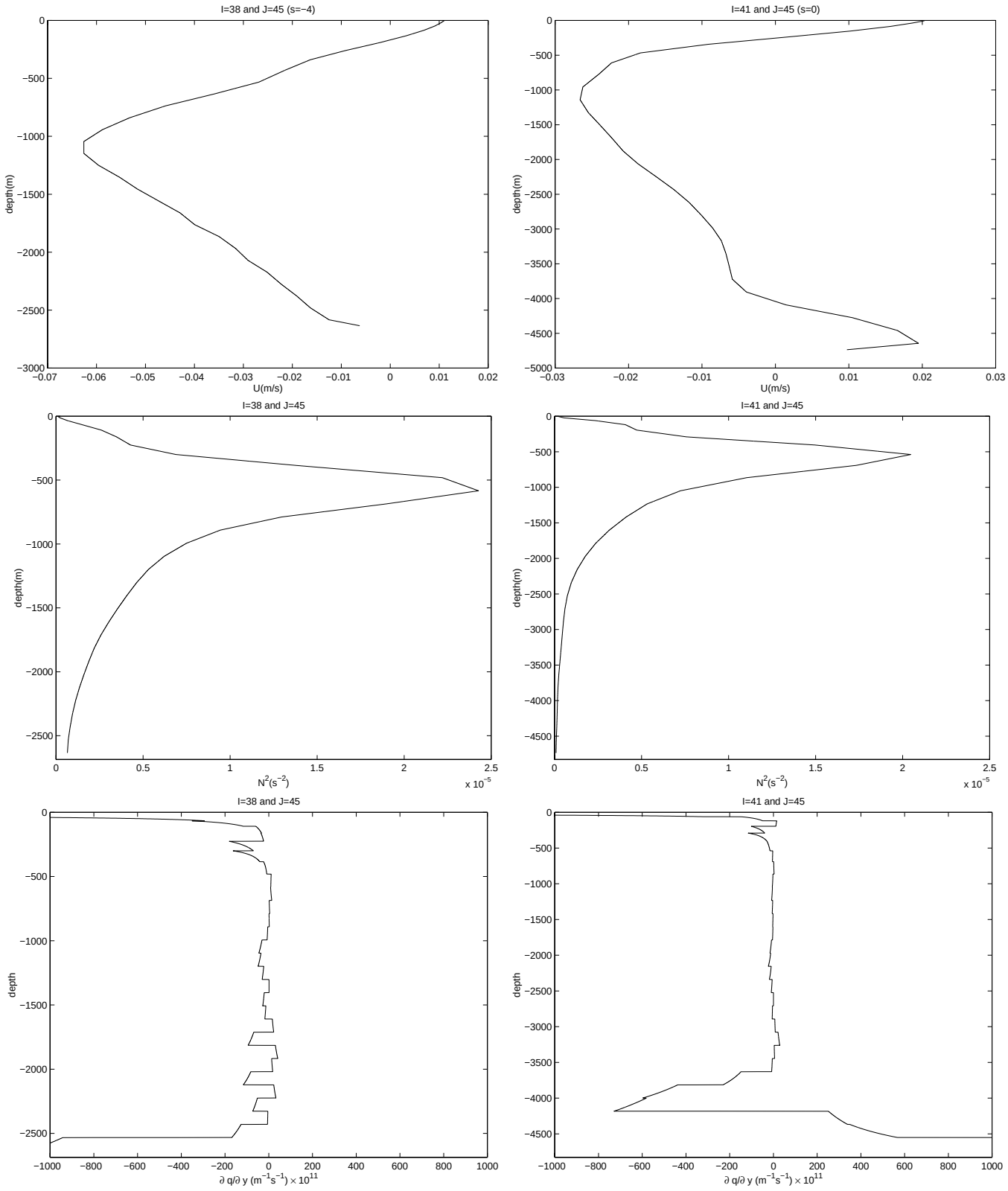

Figure C.6: *Left panels represent the velocity profile (upper), the Brunt-Väisälä frequency (middle) and $\partial\overline{q}/\partial y$ (lower) at region 1 (Fig. C.5) for a point located around the 2500 m isobath. The right panels represent the same properties, but for a point located around the 4500 m isobath.*

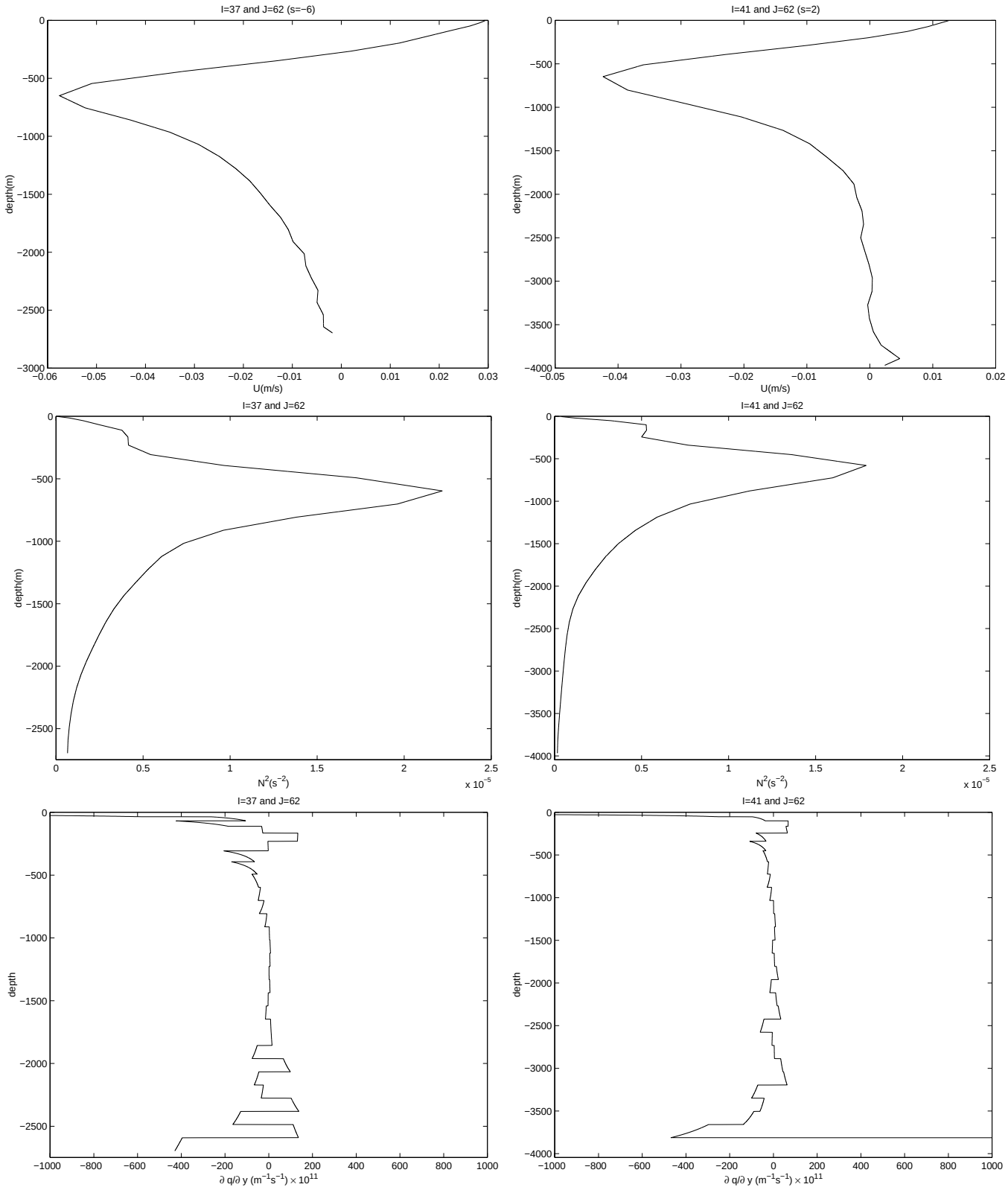

Figure C.7: *The same as Fig. C.6 but for the region 2 (Fig. C.5).*

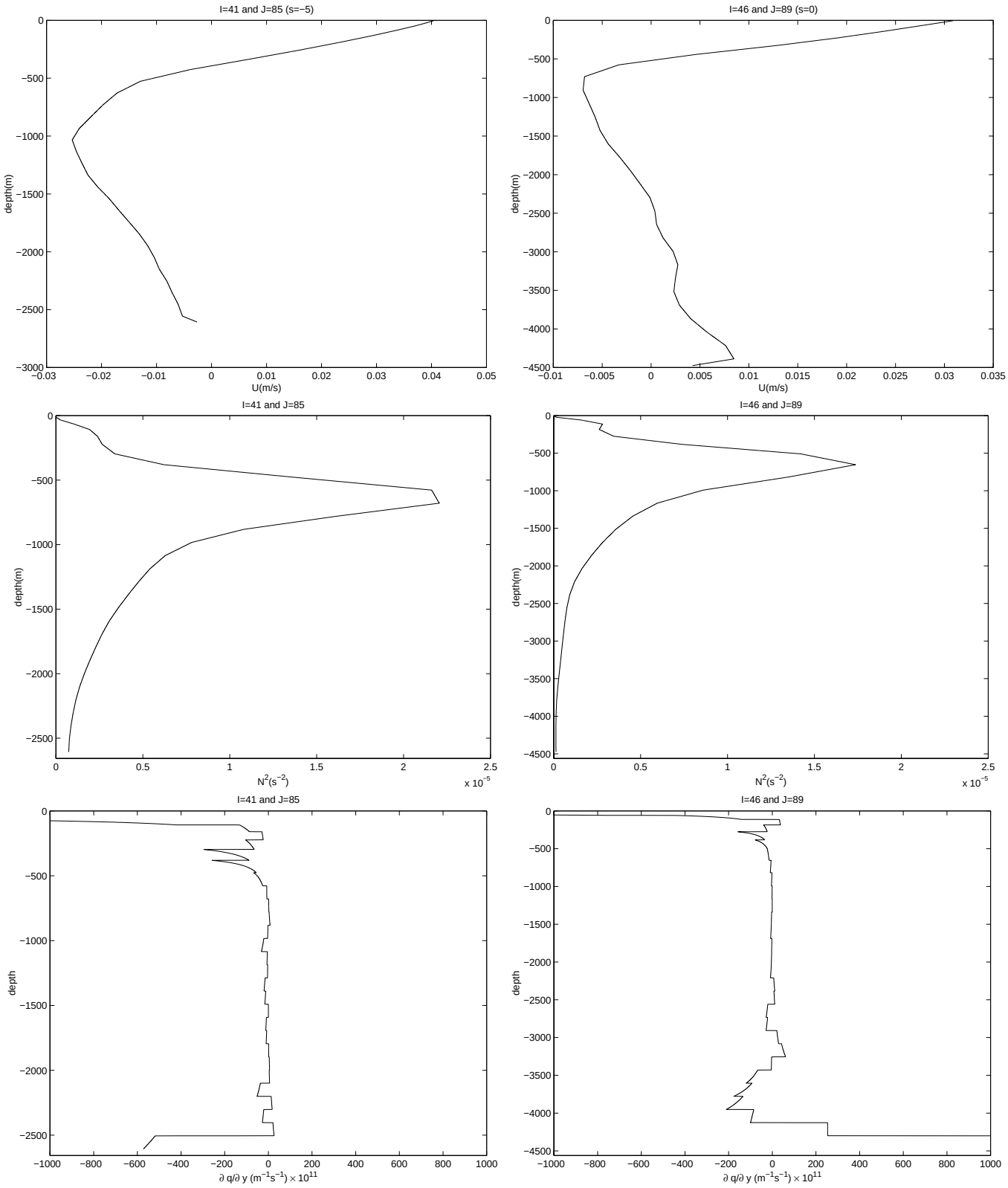

Figure C.8: *The same as Fig. C.6 but for the region 3 (Fig. C.5).*

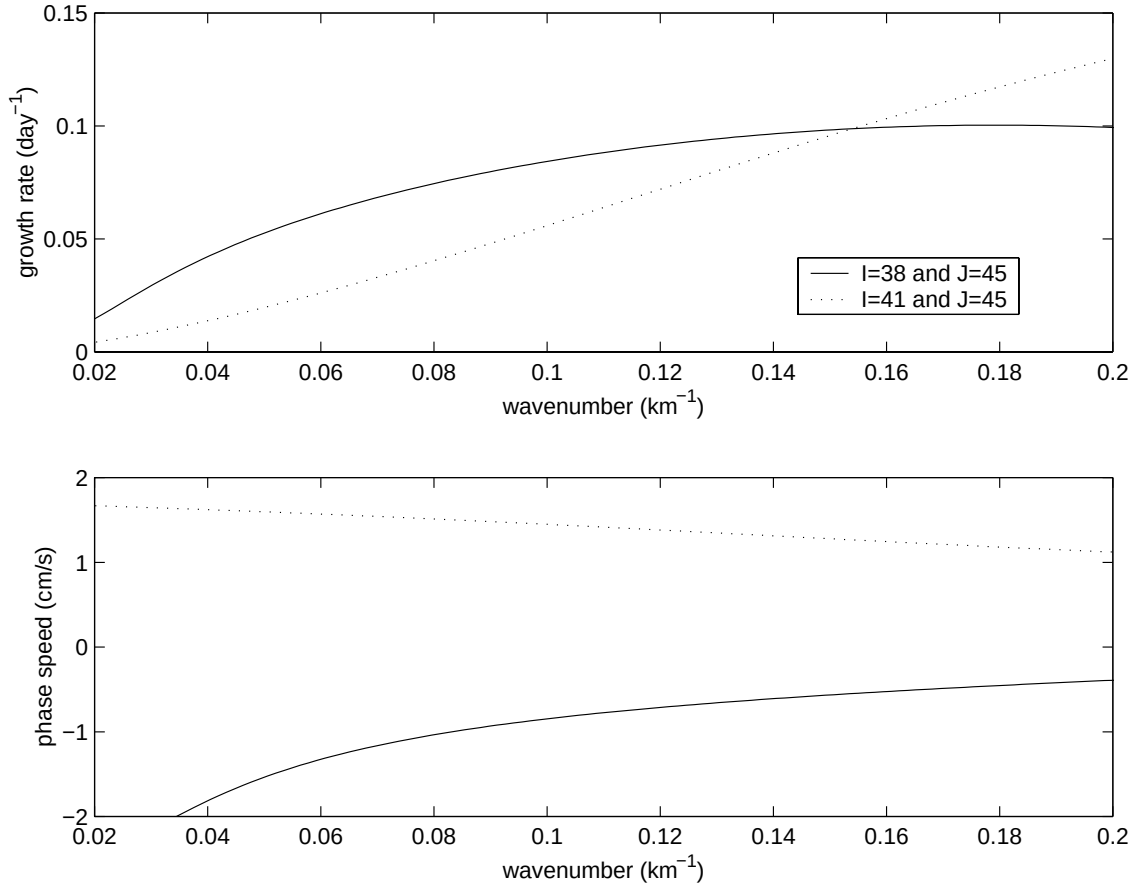

Figure C.9: *Growth rate (upper panel) and phase speed velocity (lower panel) for the points described in Fig. C.6.*

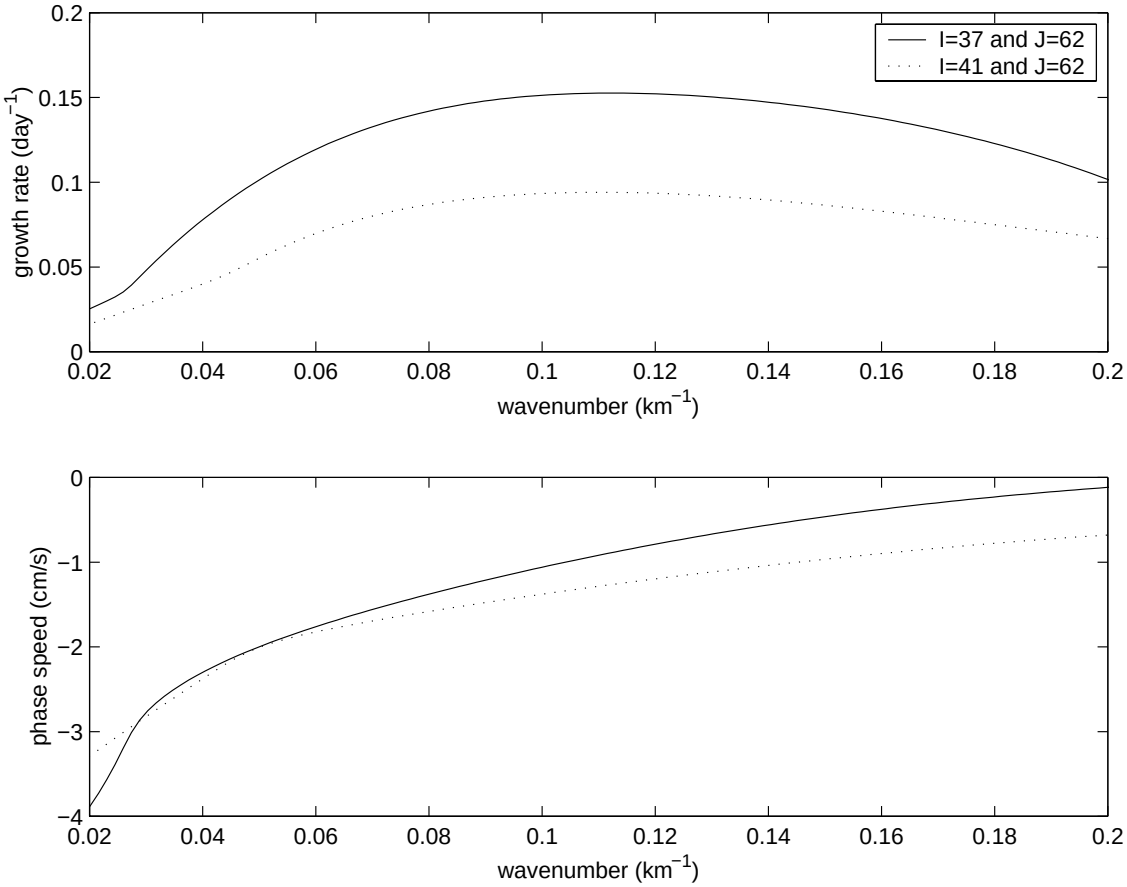

Figure C.10: *The same, but for Fig. C.7.*

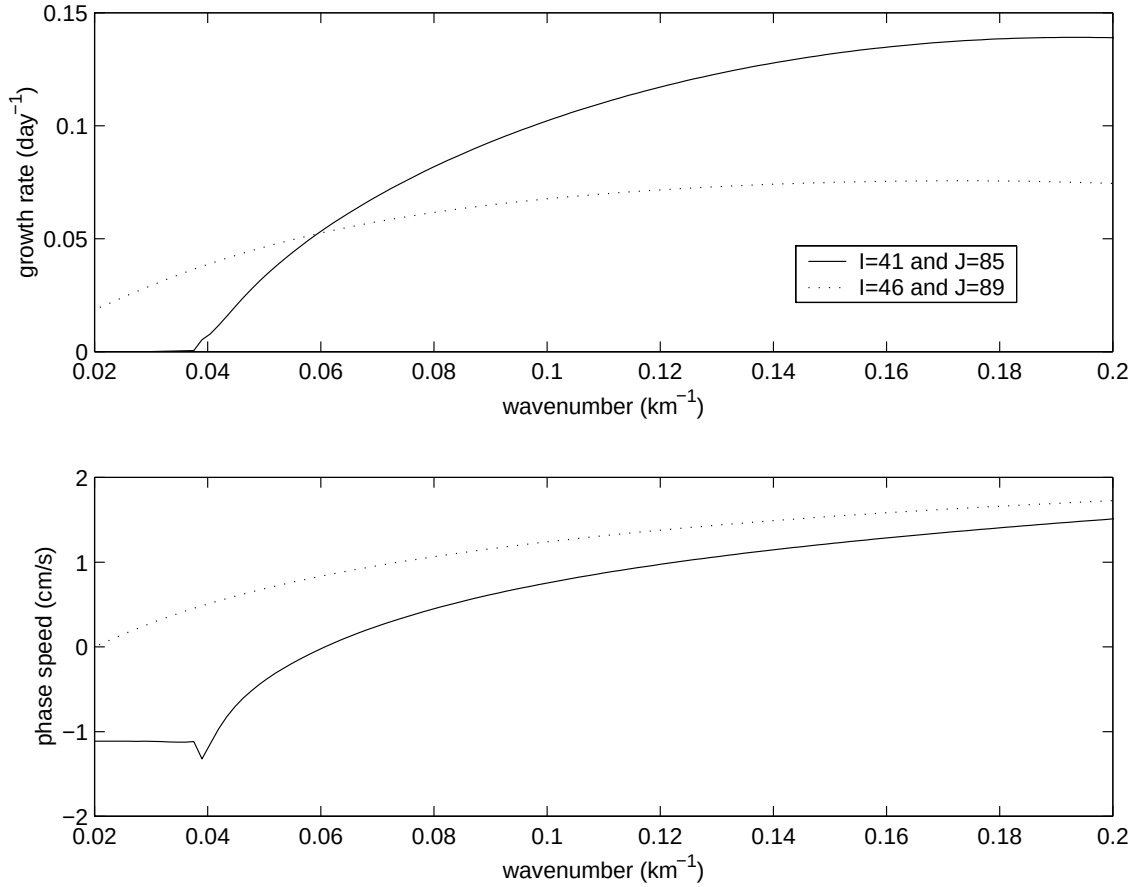

Figure C.11: *The same, but for Fig. C.8.*

Appendix D

An Idealised CTW Model

It is known that CTWs have a important role in the shelf-slope dynamics of the SEIO region (*e.g.* Freeland et al., 1986; Church and Freeland, 1987) and particularly related to the Bass Strait region (Baines et al., 1991; Middleton, 1991, 1994; Evans and Middleton, 1998).

The purpose of the idealised model described here is to provide rms bottom currents of the CTW field for use in parameterising bottom friction in the regional model. The CTWs are generated by an oscillatory zonal wind forcing over a finite fetch, where $\tau_x = \tau_0 \sin(kx - \omega t)$, $\tau_y = 0$, $\omega/k = 10$ m s^{-1}, $2\pi/\omega = 8$ days and $\tau_0 = 0.1$ Pa. The phase speed propagation of the wind system is taken from Clarke (1977) and the period of oscillation is similar to that adopted by Evans and Middleton (1998). The wind fetch is constrained by the longitudes of 125°E and 147°E, with additional 200 km cosine tapers on either side of the fetch.

The grid domain and horizontal and vertically resolution are exactly as used in the nested regional model described in Chapter 3. Since this study uses a wind field over a limited region, in analogy to Middleton and Cirano (1999), a similar set of boundary conditions for the depth-averaged velocities and elevation was adopted (see section A), while the internal boundary conditions are those described in section 3.2.3. The initial TS field is considered to be horizontally flat and was taken from the OCCAM wintertime climatology, based on a point located at the middle of the wind-forced region. The model was allowed to run for 32 days, but the rectified currents and rms bottom velocities were only obtained over the period between days 8 and 32.

In some sense, since Bass Strait is forced by local and remote winds, these results can be compared with the realistic wind simulations from Evans and Middleton (1998), where the CTW effect were included as a paddle forcing. The elevation (Fig. D.1a) and depth-averaged velocities (Fig. D.1b) for a eastward wind situation show a good agreement with their Fig. 13a,b, where an oscillatory coastal jet enters the strait between King Is. and Tasmania.

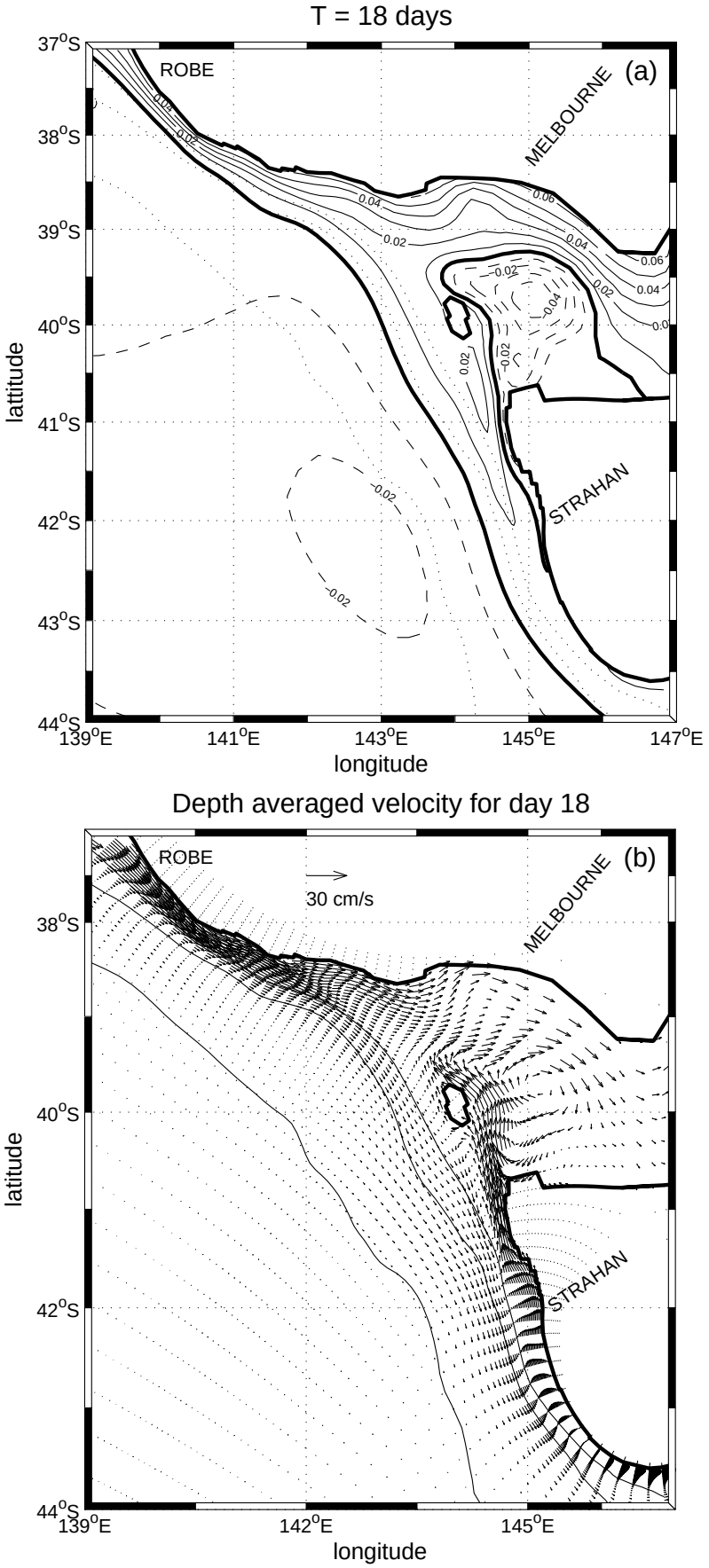

Figure D.1: *(a) Elevation and (b) depth-averaged velocities at day 18 in a eastward wind situation. Dotted (a) and solid (b) lines are the 200, 1000 and 4000 m isobaths.*

In terms of the rectified currents, they are generally small and only occur in waters inshore of the 200 m isobath. The regions that contain the strongest rectified currents (maximum of 5 cm s^{-1}) are generally off the eastern side of Kangaroo Is. (Fig. D.2a) and between King Is. and the northwestern Tasmania (Fig. D.3a). On the other hand, the rms currents, are quite large and around 30 and 18 cm s^{-1} for the South Australian region (Fig. D.2b) and Victoria-Tasmanian region (Fig. D.3b) respectively. These regions are either where the shelf narrows or where there is a abrupt change in the coastline. The magnitude of these values may have some influence on the mean circulation driven by a constant wind.

Appendix E

Comparison of Winds Within Bass Strait

To evaluate the reliability of winds within Bass Strait, twice daily wind data was obtained from the Bureau of Meteorology, Australia at a number of sites in and around Bass Strait (Figs. E.1 and E.2). Using the same drag law formulation adopted by Trenberth et al. (1989), the mean stress was calculated for June and July. For June, the Trenberth zonal mean is about 0.1 Pa (Fig. 6.9a) while that estimated from data within the strait (Fig. E.1) is around 0.85 Pa if the results for Wilsons Promontory are excluded: the promontory extends into the strait and may lead to a funnelling and increase in winds.

For July, the local winds suggest a zonal stress of about 0.12 Pa (Fig. E.2) which again is smaller than the value of about 0.14 Pa indicated by the Trenberth data (Fig 6.10a).

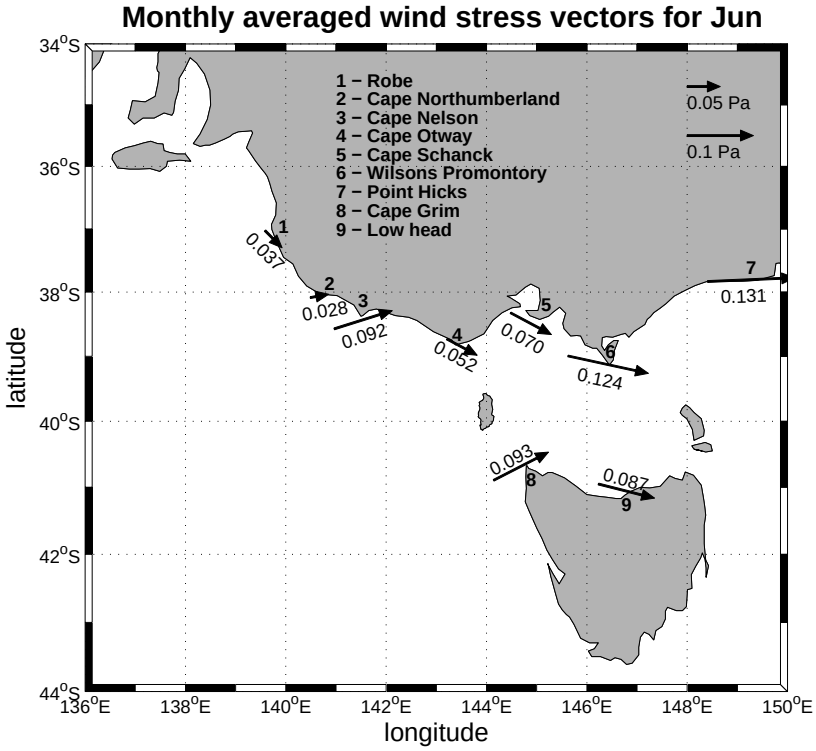

Figure E.1: *Monthly wind stress averages calculated from daily observations at several sites around South Australia, Victoria and Tasmania for Jun 1988. The data set was provided by the Bureau of Meteorology and the annual cycle can be analysed on Fig. E.3.*

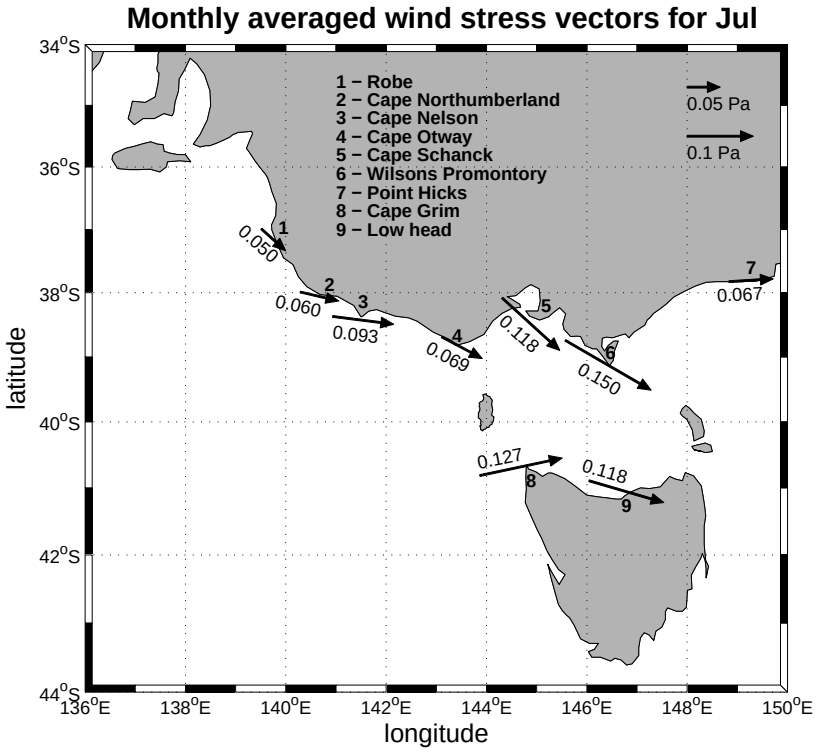

Figure E.2: *Same as Fig. E.1, but for Jul 1988.*

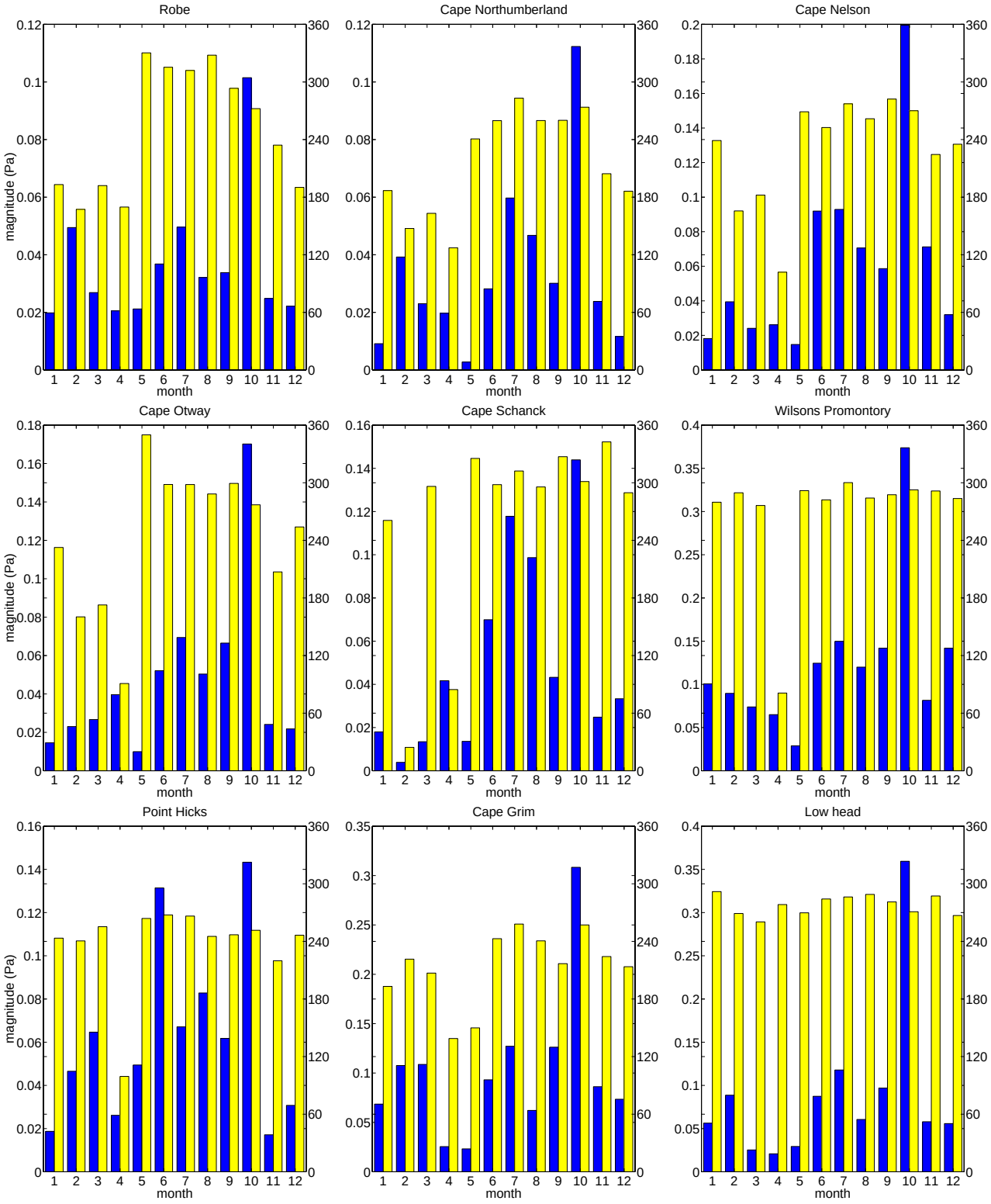

Figure E.3: *1988 cycle for the monthly wind stress averages at the sites described on Fig. E.1. The first bar (black) for each month represents the magnitude of the wind stress in Pa and the second bar (gray) represents the compass direction relative to the North.*

Bibliography

Allen, J. S. and P. A. Newberger, 1996. Downwelling Circulation on the Oregon Continental Shelf. Part I: Response to Idealized Forcing. *J. Phys. Oceanogr.*, **26**, 2011–2035.

Anderson, D. L. T. and A. E. Gill, 1975. Spin-up of a stratified ocean, with applications to upwelling. *Deep-Sea Res.*, **22**, 583–596.

Anderson, D. L. T. and P. D. Killworth, 1977. Spin-up of a stratified ocean, with topography. *Deep-Sea Res.*, **24**, 709–732.

Baines, P. G., R. J. Edwards and C. B. Fandry, 1983. Observations of a New Baroclinic Current along the Western Continental Slope of Bass Strait. *Aust. J. Mar. Freshw. Res.*, **34**, 155–157.

Baines, P. G., G. Hubbert and S. Power, 1991. Fluid transport through Bass Strait. *Cont. Shelf Res.*, **11(3)**, 269–293.

Batteen, M. L. and C. L. Butler, 1998. Modelling Studies of the Leeuwin Current off Western and Southern Australia. *J. Phys. Oceanogr.*, **28(2)**, 2199–2221.

Belkin, I. M. and A. L. Gordon, 1996. Southern Ocean fronts from Greenwich meridian to Tasmania. *J. Geophys. Res.*, **101(C2)**, 3675–3696.

Blumberg, A. F. and G. L. Mellor, 1987. A description of a three-dimensional coastal ocean circulation model. In Heaps, N. S. (Ed.), *Three-Dimensional Coastal Ocean Models*, Vol. 4 of *Coastal and Estuarine Series*, pp. 1–16. American Geophysical Union, Washington, D. C. 208 pp.

Brink, K. H. and D. C. Chapman, 1985. Programs for computing properties of coastal-trapped waves and wind-driven motions over the continental shelf and slope. Tech. rep. 85-17, Woods Wole Oceanographic Institution. 98 pp.

Bryan, K., 1969. A numerical method for the study of the circulation of the world ocean. *J. Comput. Phys.*, **4(3)**, 347–376.

Bye, J. A. T., 1972. Oceanic circulation south of Australia. In Hayes, D. (Ed.), *Antarctic Oceanology II: The Australian-New Zealand Sector*, Vol. 19 of *Antarctic Research Series*, pp. 95–100. American Geophysical Union, Washington, D. C.

Bye, J. A. T., 1983a. The General Circulation in a Dissipative Ocean Basin with Longshore Wind Stresses. *J. Phys. Oceanogr.*, **13(9)**, 1553–1563.

Bye, J. A. T., 1983b. Physical Oceanography. In Tyler, M. J. (Ed.), *Natural History of the South East*, pp. 75–84. Royal Soc. Sth. Aust., Adelaide, Australia.

Chapman, D. C., 1985. Numerical Treatment of Cross-Shelf Open Boundaries in a Barotropic Coastal Ocean Model. *J. Phys. Oceanogr.*, **15**, 1060–1075.

Chapman, D. C. and S. J. Lentz, 1997. Adjustment of Stratified Flow over a Sloping Bottom. *J. Phys. Oceanogr.*, **27(2)**, 340–356.

Charney, J. G. and M. E. Stern, 1962. On the stability of internal baroclinic jets in a rotating atmosphere. *J. Meteor.*, **4**, 135–163.

Chu, P. and C. Fan, 1997. Sixth-Order Difference Scheme for Sigma Coordinate Ocean Models. *J. Phys. Oceanogr.*, **27**, 2064–2071.

Church, J. A. and P. D. Craig, 1998. Australia's shelf seas: diversity and complexity. In Robinson, A. R. and K. H. Brink (Eds.), *The Sea*, Vol. 11, pp. 933–964. John Wiley & Sons, Inc., New York.

Church, J. A., G. R. Cresswell and J. S. Godfrey, 1989. The Leeuwin Current. In Neshyba, S. J., C. N. K. Mooers and R. L. Smith (Eds.), *Poleward Flows Along Eastern Ocean Boundaries*, Vol. 34 of *Coastal and Estuarine Studies*, pp. 230–254. American Geophysical Union, Washington, D. C. 374 pp.

Church, J. A. and H. J. Freeland, 1987. The Energy Source for the Coastal-Trapped Waves in the Australian Coastal Experiment Region. *J. Phys. Oceanogr.*, **17(3)**, 289–300.

Church, J. A., H. J. Freeland and R. L. Smith, 1986. Coastal-Trapped Waves on the East Australian Continental Shelf. Part I: Propagation of Modes. *J. Phys. Oceanogr.*, **16(11)**, 1929–1943.

Clarke, A. J., 1977. Observational and Numerical Evidence for Wind-Forced Coastal Trapped Long Waves. *J. Phys. Oceanogr.*, **4**, 231–247.

Clarke, A. J., 1991. On the Reflection and Transmission of Low-Frequency Energy at the Irregular Western Pacific Ocean Boundary. *J. Geophys. Res.*, **96**, 3289–3305.

Clarke, A. J. and X. Liu, 1994. Interannual Sea Level in the Northern and Eastern Indian Ocean. *J. Phys. Oceanogr.*, **24**, 1224–1235.

Clarke, A. J. and S. Van Gorder, 1994. On ENSO Coastal Currents and Sea Levels. *J. Phys. Oceanogr.*, **24**, 661–680.

Cox, M. D., 1984. A primitive equation 3-dimensional model of the ocean. GFDL Ocean Group Tech. rep. 1, Geophysical Fluid Dynamics Laboratory/NOAA, Princeton University, Princeton, N. J. 08542, U. S. A. 143 pp.

Cresswell, G. R., 2000. Currents of the continental shelf and upper slope of Tasmania. In *Papers and Proceedings of the Royal Society of Tasmania*.

Cresswell, G. R. and J. L. Peterson, 1993. The Leeuwin Current South of Western Australia. *Aust. J. Mar. Freshw. Res.*, **44**, 285–303.

Cushman-Roisin, B., 1994. *Introduction to Geophysical Fluid Dynamics*. Prentice-Hall, Englewood Cliffs, New Jersey. 320 pp.

da Silva, A. M., C. C. Young and S. Levitus, 1994. *Algorithms and Procedures*, Vol. 1 of *Atlas of Surface Marine Data 1994. NOAA Atlas NESDIS 6*. U. S. Department of Commerce, Washington, D. C. 84 pp.

Domingues, C. M., S. Wijffels, M. A. Tomczak and J. A. Church, 1999. Volume transports and structure of the Leeuwin Current at 22°S - WOCE ICM6. *Int. WOCE Newsletter*, **37**, 36–40.

Dunn, J. R., K. R. Ridgway and J. L. Wilkin, 2000. CARS, a new high-resolution climatology for waters around Australasia..

Edwards, R. J. and W. J. Emery, 1982. Australasian Southern Ocean Frontal Structure during Summer 1976-1977. *Aust. J. Mar. Freshw. Res.*, **33**, 3–22.

Emanuel, K. A., 1994. *Atmospheric Convection*. Oxford University Press, New York. 580 pp.

Evans, S. and J. F. Middleton, 1998. A Regional Model of Shelf Circulation near Bass Strait: A new Upwelling Mechanism. *J. Phys. Oceanogr.*, **28(7)**, 1439–1457.

Ezer, T. and G. L. Mellor, 1994. Diagnostic and prognostic calculations of the North Atlantic circulation and sea level using a sigma coordinate ocean model. *J. Geophys. Res.*, **99(C7)**, 14159–14171.

Fortunato, A. B. and A. M. Baptista, 1996. Evaluation of Horizontal Gradients in Sigma-Coordinate Shallow Water Models. *Atmos.-Ocean*, **34(3)**, 489–514.

Freeland, H. J., F. M. Boland, J. A. Church, A. J. Clarke, A. M. G. Forbes, A. Huyes, R. L. Smith, R. O. R. Y. Thompson and N. J. White, 1986. The Australian Coastal Experiment: The search for coastal trapped waves. *J. Phys. Oceanogr.*, **16**, 1230–1240.

Garrett, C., P. MacCready and P. Rhines, 1993. Boundary mixing and arrested Ekman layers. *Annu. Rev. Fluid Mech.*, **25**, 291–323.

Garrett, C. and B. Toulany, 1982. Sea Level Variability Due to Meteorological Forcing in the Northeast Gulf of St. Lawrence. *J. Geophys. Res.*, **87(C3)**, 1968–1978.

Gawarkiewicz, G. and D. C. Chapman, 1991. Formation and Maintenance of Shelfbreak Fronts in an Unstratified Flow. *J. Phys. Oceanogr.*, **21**, 1225–1239.

Gill, A. E., 1982. *Atmosphere-Ocean Dynamics*. Academic Press, New York. 662 pp.

Gill, A. E., J. S. A. Green and A. J. Simmons, 1974. Energy partition in the large-scale ocean circulation and the production of mid-ocean eddies. *Deep-Sea Res.*, **21**, 499–528.

Godfrey, J. S., 1989. A Sverdrup model of the depth-integrated flow for the world ocean allowing for island circulations. *Geophys. Astrophys. Fluid Dyn.*, **45**, 89–112.

Godfrey, J. S., 1996. The effect of the Indonesian throughflow on ocean circulation and heat exchange with atmosphere: A review. *J. Geophys. Res.*, **101(C1)**, 12217–12237.

Godfrey, J. S. and K. R. Ridgway, 1985. The Large-Scale Environment of the Poleward-Flowing Leeuwin Current, Western Australia: Longshore Steric Height Gradients, Wind Stresses and Geostrophic Flow. *J. Phys. Oceanogr.*, **15**, 481–495.

Godfrey, J. S., D. J. Vaudrey and S. D. Hahn, 1986. Observations of the Shelf-Edge Current South of Australia, Winter 1982. *J. Phys. Oceanogr.*, **16**, 668–679.

Green, J. S. A., 1960. A problem in baroclinic instability. *Quar. J. Roy. Meteor. Soc.*, **86**, 237–251.

Grewe, P. M., N. G. Elliott, B. H. Innes and R. D. Ward, 1997. Genetic population structure of southern bluefin tuna (*thunnus maccoyii*). *Mar. Biol.*, **127**, 555–561.

Haney, R. L., 1991. On the pressure gradient force over steep topography in sigma coordinate ocean models. *J. Phys. Oceanogr.*, **21**, 610–619.

Hannah, C. G., 1992. Geostrophic Control with wind-forcing: Application to Bass Strait. *J. Phys. Oceanogr.*, **22**, 1596–1599.

Hayes, D. and J. R. Conolly, 1972. Morphology of the southeast Indian Ocean. In Hayes, D. (Ed.), *Antarctic Oceanology II: The Australian-New Zealand Sector*, Vol. 19 of *Antarctic Research Series*, pp. 125–145. American Geophysical Union, Washington, D. C.

Herzfeld, M., 1997. The annual cycle of sea surface temperature in the Great Australian Bight. *Prog. Oceanogr.*, **39**, 1–27.

Herzfeld, M. and M. Tomczak, 1997. Numerical modelling of sea surface temperature and circulation in the Great Australian Bight. *Prog. Oceanogr.*, **39**, 29–78.

Hickey, B., 1989. Poleward flow near the northern and southern boundaries of the U.S. west coast. In Neshyba, S. J., C. N. K. Mooers and R. L. Smith (Eds.), *Poleward Flows Along Eastern Ocean Boundaries*, Vol. 34 of *Coastal and Estuarine Studies*, pp. 160–175. American Geophysical Union, Washington, D. C. 374 pp.

Hirst, A. C. and J. S. Godfrey, 1993. The Role of the Indonesian Throughflow in a Global Ocean GCM. *J. Phys. Oceanogr.*, **23**, 1057–1086.

Holton, J. R., 1992. *An Introduction to Dynamic Meteorology* (3th edition). Academic Press, Orlando, Florida. 507 pp.

Josey, S. A., E. C. Kent, D. Oakley and P. K. Taylor, 1996. A new global air-sea heat and momentum flux climatology. *Int. WOCE Newsletter*, **24**, 3–5.

Killworth, P. D., 1996. Time Interpolation of Forcing Fields in Ocean Models. *J. Phys. Oceanogr.*, **26**, 136–143.

Legeckis, R. and G. Cresswell, 1981. Satellite observations of sea-surface temperature fronts off the coast of western and southern Australia. *Deep-Sea Res.*, **28A(3)**, 297–306.

Levitus, S., 1982. *Climatological Atlas of the World Ocean*. NOAA professional Paper. U. S. Goverment Printing Office, Washington, D. C. 173 pp.

Levitus, S. and T. P. Boyer, 1994. *Temperature*, Vol. 4 of *World Ocean Atlas 1994. NOAA Atlas NESDIS*. U. S. Department of Commerce, Washington, D. C. 117 pp.

Levitus, S., R. Burgett and T. P. Boyer, 1994. *Salinity*, Vol. 3 of *World Ocean Atlas 1994. NOAA Atlas NESDIS*. U. S. Department of Commerce, Washington, D. C. 99 pp.

Lyne, V. D. and R. E. Thresher, 1994. Dispersal and Advection of *macruronus novaezealandiae* (Gadiformes: Merlucciidae) Larvae off Tasmania: Simulation of the Effects of Physical Forcing on Larval Distribution. In Sammarco, P. W. and M. L. Heron (Eds.), *Bio-Physics of Marine Larval Dispersal*, Vol. 45 of *Coastal and Estuarine Studies*, pp. 109–136. American Geophysical Union, Washington, D. C. 352 pp.

MacCready, P. and P. B. Rhines, 1993. Slippery Bottom Boundary Layers on a Slope. *J. Phys. Oceanogr.*, **23(1)**, 5–22.

McCartney, M. S., 1977. Subantarctic Mode Waters. *Deep-Sea Res.*, **24**, 103–119.

McCartney, M. S., 1982. The subtropical recirculation of Mode Waters. *J. Mar. Res.*, **40**, 427–464.

McCreary, J. P., 1981. A linear stratified ocean model of the coastal undercurrent. *Phil. Trans. Roy. Soc. Lond. A.*, **302**, 385–413.

McCreary, J. P. and S.-H. Chao, 1985. Three-dimensional shelf circulation along an eastern ocean boundary. *J. Mar. Res.*, **43(1)**, 13–36.

McCreary, J. P., Y. Fukamachi and P. K. Kundu, 1991. A Numerical Investigation of Jets and Eddies Near an Eastern Ocean Boundary. *J. Geophys. Res.*, **96(2)**, 2515–2534.

Mellor, G., 1986. Numerical simulation and analysis of the mean coastal circulation off California. *Cont. Shelf Res.*, **6(6)**, 689–713.

Mellor, G. L., 1973. Analytic Prediction of the Properties of Statified Planetary Surface Layers. *J. Atmos. Sci.*, **30**, 1061–1069.

Mellor, G. L., 1991. An equation of State for Numerical Models of Oceans and Estuaries. *J. Atmos. Oceanic Technol.*, **8**, 609–611.

Mellor, G. L., 1998. *User's Guide for a three-dimensional, primitive equation, numerical ocean model*. Program in Atmos. and Ocean. Sci., Princeton University, Princeton. 41 pp.

Mellor, G. L. and T. Ezer, 1991. A Gulf Stream Model and an Altimetry Assimilation Scheme. *J. Geophys. Res.*, **96(C5)**, 8779–8795.

Mellor, G. L., T. Ezer and L.-Y. Oey, 1994. The Pressure Gradient Conundrum of Sigma Coordinate Ocean Models. *J. Atmos. Oceanic Technol.*, **11(4)**, 1126–1134.

Mellor, G. L., L.-Y. Oey and T. Ezer, 1998. Sigma Coordinate Pressure Gradients Errors and the Seamount Problem. *J. Atmos. Oceanic Technol.*, **15**, 1122–1131.

Mellor, G. L. and T. Yamada, 1974. A Hierarchy of Turbulence Closure Models for Planetary Boundary Problems. *J. Atmos. Sci.*, **31**, 1791–1806.

Mellor, G. L. and T. Yamada, 1982. Development of a Turbulence Closure Model for Geophysical Fluid Problems. *Rev. of Geophys. Space Phys.*, **20**, 851–875.

Meyers, G., 1996. Variation of Indonesian throughflow and the El Ninõ - Southern Oscilation. *J. Geophys. Res.*, **101(C5)**, 12255–12263.

Middleton, J. F., 1991. Coastal-trapped Wave Scattering into and out of Straits and Bays. *J. Phys. Oceanogr.*, **21(5)**, 681–694.

Middleton, J. F., 1994. The Baroclinic Response of Straits and Bays to Coastal-Trapped Wave Scattering. *J. Phys. Oceanogr.*, **24(3)**, 521–539.

Middleton, J. F., 2000. Wind-Forced Upwelling: The Role of the Surface Mixed Layer. *J. Phys. Oceanogr.*, **30(5)**, 745–763.

Middleton, J. F. and K. P. Black, 1994. The low frequency circulation in and around Bass Strait: a numerical study. *Cont. Shelf Res.*, **14(13/14)**, 1495–1521.

Middleton, J. F. and M. Cirano, 1999. Wind-Forced Downwelling Slope Currents: a Numerical Study. *J. Phys. Oceanogr.*, **29**, 1723–1743.

Middleton, J. F. and M. Cirano, 2000. A Boundary Current along Australia's Southern Shelves: the Flinders Current. **in preparation**.

Middleton, J. F. and D. Ramsden, 1996. The evolution of the bottom boundary layer on the sloping continental shelf: A numerical study. *J. Geophys. Res.*, **101(C8)**, 18061–18077.

Middleton, J. F. and F. Viera, 1991. The Forcing of Low Frequency Motions within Bass Strait. *J. Phys. Oceanogr.*, **21(5)**, 695–708.

Neshyba, S. J., C. N. K. Mooers and R. L. Smith (Eds.)., 1989. *Poleward Flows Along Eastern Ocean Boundaries*, Vol. 34 of *Coastal and Estuarine Studies*. American Geophysical Union, Washington, D. C. 374 pp.

Newell, B. S., 1961. Hydrology of south-east Australian waters: Bass Strait and New South Wales tuna fishing areas. Tech. rep. 10, CSIRO Div. Fish. Oceanogr. 22 pp.

Oey, L.-Y. and P. Chen, 1992a. A Model Simulation of Circulation in the Northeast Atlantic shelves and Seas. *J. Geophys. Res.*, **97(C12)**, 20087–20115.

Oey, L.-Y. and P. Chen, 1992b. A Nested-Grid Ocean Model: With Application to the Simulation of Meanders and Eddies in the Norwegian Coastal Current. *J. Geophys. Res.*, **97(C12)**, 20063–20086.

Orlanski, I., 1976. A simple boundary condition for unbounded hyperbolic flows. *J. Comput. Phys.*, **21**, 251–269.

Orsi, A. H., T. Whitworth III and W. D. Nowlin Jr., 1995. On the meridional extent and fronts of the Antarctic Circumpolar Current. *Deep-Sea Res.*, **42(5)**, 641–673.

Pacanowski, R. C. and S. G. K. Philander, 1981. Parameterization of Vertical Mixing in Numerical Models of Tropical Oceans. *J. Phys. Oceanogr.*, **11**, 1443–1451.

Palma, E. D. and R. P. Matano, 1998. On the implementation of passive open boundary conditions for a general circulation model: The barotropic mode. *J. Geophys. Res.*, **103(C1)**, 1319–1341.

Pariwono, J. I., J. A. T. Bye and G. W. Lennon, 1986. Long-period variations of sea-level in Australasia. *Geophys. J. R. astr. Soc.*, **87**, 43–54.

Pedlosky, J., 1987. *Geophysical Fluid Dynamics* (2nd edition). Springer Verlag, New York. 710 pp.

Phillips, N. A., 1957. A Coordinate System Having Some Special Advantages for Numerical Forecasting. *J. Meteor.*, **14**, 184–185.

Platov, G. and J. F. Middleton, 2000. A Barotropic Model of Tides along Australia's Southern Shelves. *Mar. Freshw. Res.*, **submitted**.

Provis, D. G. and G. W. Lennon, 1981. Some Oceanographic Measurements in the Great Australian Bight. In *Proc. Fifth Aust. Conf. on Coastal and Ocean Engineering*, pp. 119–120. The Institution of Engineers.

Ramp, S. R., 1997. Moored observations of the current and temperature structure over the continental slope off central California. 1. A basic description of the variability. *J. Geophys. Res.*, **102(C10)**, 22877–22902.

Reid, J. L., 1997. On the total geostrophic circulation of the pacific ocean: flow patterns, tracers, and transports. *Prog. Oceanogr.*, **39**, 263–352.

Ribbe, J. and M. Tomczak, 1996. Some Indications of a Reversed Surface Flow Around Tasmania in the Fine Resolution Antarctic Model. *Ocean Modelling*, **111**, 2–5.

Ridgway, K. R. and J. S. Godfrey, 1997. Seasonal cycle of the East Australian Current. *J. Geophys. Res.*, **102(C10)**, 22921–22936.

Ridgway, K. R. and R. G. Loch, 1987. Mean Temperature-Salinity Relationships in Australia Waters and their Use in Water Mass Analysis. *Aust. J. Mar. Freshw. Res.*, **38**, 553–567.

Rintoul, S. R. and J. L. Bullister, 1999. A late winter hydrographic section from Tasmania to Antarctica. *Deep-Sea Res.*, **46**, 1417–1454.

Rintoul, S. R., J. R. Donguy and D. H. Roemmich, 1997. Seasonal evolution of upper ocean thermal structure between Tasmania and Antarctica. *Deep-Sea Res.*, **44(7)**, 1185–1202.

Rintoul, S. R. and S. Sokolov, 1999. Baroclinic transport variability of the Antarctic Circumpolar Current south of Australia (WOCE repeat section SR3). *J. Geophys. Res.*, **submitted**.

Rochford, D. J., 1986. Seasonal Changes in the Distribution of Leeuwin Current Waters off Southern Australia. *Aust. J. Mar. Freshw. Res.*, **37**, 1–10.

Saunders, P. M., A. C. Coward and B. A. de Cuevas, 1999. Circulation of the Pacific Ocean seen in a global ocean model: Ocean Circulation and Climate Advanced Modelling project (OCCAM). *J. Geophys. Res.*, **104(C8)**, 18281–18299.

Schahinger, R. B., 1987. Structure of Coastal Upwelling Events Observed off the Southeast Coast of South Australia during February 1983–April 1984. *Aust. J. Mar. Freshw. Res.*, **38**, 439–459.

Schodlok, M., M. Tomczak and N. White, 1997. Deep sections through the South Australian Basin and across the Australian-Antartic Discordance. *Geophys. Res. Lett.*, **24(22)**, 2785–2788.

Semtner, A. J., 1974. A general circulation model for the World Ocean. Tech. rep. 9, Department of Meteorology, University of California, Los Angeles. 99 pp.

Siefridt, L. and B. Barnier, 1993. Banque de Donnéss AVISO Vent/flux: Climatologie des Analyses de Surface du CEPMMT. Tech. rep. 91 1430 025, 43 pp.

Smith, R. L., A. Huyer, J. S. Godfrey and J. A. Church, 1991. The Leeuwin Current off Western Australia, 1986-1987. *J. Phys. Oceanogr.*, **21(2)**, 323–345.

Song, Y. T., 1998. A General Pressure Gradient Formulation for Ocean Models. Part I: Scheme Design and Diagnostic Analysis. *Mon. Wea. Rev.*, **126**, 3213–3230.

Stammer, D., R. Tokmakian, A. Semtner and C. Wunsch, 1996. How well does a $1/4^\circ$ global circulation model simulate large-scale oceanic observations?. *J. Geophys. Res.*, **101(C10)**, 25779–15811.

Suginohara, N., 1981. Propagation of Coastal-Trapped Waves at Low Latitudes in a Stratified Ocean with Continental Shelf Slope. *J. Phys. Oceanogr.*, **11**, 1113–1122.

Suginohara, N., 1982. Coastal Upwelling: Onshore–Offshore Circulation, Equatorward Coastal Jet and Poleward Undercurrent over a Continental Shelf–Slope. *J. Phys. Oceanogr.*, **12**, 272–284.

Suginohara, N. and Y. Kitamura, 1984. Long Term Coastal Upwelling over a Continental Shelf–Slope. *J. Phys. Oceanogr.*, **14**, 1095–1104.

Thompson, K. R., J. R. N. Lazier and B. Taylor, 1986. Wind-Forced Changes in Labrador Current Transport. *J. Geophys. Res.*, **91(C12)**, 14261–14268.

Thompson, R. O. R. Y., 1983. Low-Pass Filters to Supress Inertial and Tidal Frequencies. *J. Phys. Oceanogr.*, **13(6)**, 1077–1083.

Thompson, R. O. R. Y., 1984. Observations of the Leeuwin Current off Western Australia. *J. Phys. Oceanogr.*, **14(3)**, 623–628.

Tomczak, M. and J. S. Godfrey, 1994. *Regional oceanography: an introduction*. Pergamon Press, London. 422 pp.

Tomczak, M., C. James, I. Helmond and L. Pender, 2000. The Subtropical Front of the south eastern Indian Ocean during winter of 1998. *Mar. Freshw. Res.*, **submitted**.

Tomczak, M. and L. Pender, 1998. Density compensation in the Subtropical Front of the Indian Ocean south of Australia part 1: winter. http://www.es.flinders.edu.au/∼mattom/STF/fr1098.html.

Trenberth, K. E., J. C. Olson and W. G. Large, 1989. A Global Ocean Wind Stress Climatology Based on ECMWF Analyses. Tech. rep. NCAR/TN-338+STR, National Center for Atmospheric Research, Boulder, Colorado. 98 pp.

von der Borch, C. C., 1968. Submarine canyons of southern Australia: Their distribution and ages. *Mar. Geol.*, **6(4)**, 267–279.

Walker, A. E. and J. D. Wilkin, 1998. Optimal averaging of NOAA/NASA Pathfinder satellite sea surface temperature data. *J. Geophys. Res.*, **103(C6)**, 12869–12883.

Webb, D., B. A. de Cuevas and A. C. Coward, 1998. The first main run of the OCCAM global ocean model. Tech. rep. 34, Southampton Oceanography Centre. 43 pp.

Wells, N. C. and B. A. de Cuevas, 1995. Depth-Integrated Vorticity Budget of the Southern Ocean from a General Circulation Model. *J. Phys. Oceanogr.*, **25(11)**, 2569–2582.

Wright, D. G. and K. R. Thompson, 1983. Time-Averaged Forms of the Nonlinear Stress Law. *J. Phys. Oceanogr.*, **13(2)**, 341–345.

Wyrtki, K., 1971. *Oceanographic Atlas of the International Indian Ocean Expedition*. National Science Foundation, Washington, D. C. 531 pp.